Theory of Optical Transitions in π-Conjugated Polymers

Max Marcus

Magdalen College
University of Oxford



A thesis submitted for the degree of
Doctor of Philosophy
at the University of Oxford

Trinity 2017

Theory of Optical Transitions in π-Conjugated Polymers

Max Marcus
Magdalen College
University of Oxford

A thesis submitted for the degree of
Doctor of Philosophy
at the University of Oxford, Trinity 2017

Abstract

Conjugated Polymers have attracted a great deal of research interest in recent years due to their optoelectronic properties which makes them suitable for applications in organic light-emitting devices (OLEDs) and organic photovoltaics. Their properties are strongly dependent on the electron-electron and electron-nuclear interactions as well as the disorder which is present in almost all systems at finite temperatures.

In this thesis the optical properties of electronically neutral conjugated polymers will be investigated. The results obtained are general and applicable to a wide range of parameters. In order to compare these to experiment the optical properties of poly(*para*-phenylene), poly(*para*-phenylene vinylene), and derivatives have been calculated. In these polymers the primary photoexcitations are Frenkel excitons which can be described by the Frenkel-Holstein Hamiltonian, which explicitly takes into account the exciton-nuclear coupling. Disorder can be introduced into this model both as diagonal and off-diagonal disorder within the Hamiltonian.

First the optical transitions in ordered, linear conjugated polymers are investigated. It is found that the length of the polymer has a direct spectroscopic signature in the emission spectrum. When off-diagonal disorder is introduced the excitons localise on portions of the chain and the length of these portions, the conjugation length, then shows a clear emission signature. As such, a disordered polymer can be described theoretically as a chain of shorter segments, which define chromophores in a polymer context.

Following from these calculations the role of conformation was investigated and effects were observed that greatly determine the optical properties of non-linear polymers. Most notable the Herzberg-Teller effect, which renders symmetrically forbidden transitions weakly allowed and greatly affects the absorption and emission spectra. The signatures observed in these spectra allow the determination of the (coarse grained) conformation of the polymer, something that has been difficult to measure directly.

Keywords: Conjugated Polymers; Frenkel-Holstein Model; Optical Spectroscopy ■

Statement of Originality

I, Max Marcus, hereby confirm that this thesis and the work to which it refers are the results of my own efforts. Any ideas, data, images, or text resulting from the work of others (whether published or unpublished) are fully identified as such within the work and attributed to their originator in the text, bibliography, or in footnotes. This thesis has not been submitted in whole or in part for any other academic degree or professional qualification.

Date:

Signature:

Acknowledgments

Writing this thesis as undoubtedly been the biggest thing I have so far done in my life and I am acutely aware that this is by no means a single effort on my behalf. First and foremost I want to and, indeed, have to thank William Barford, for his guidance, patience, criticism, and support during the past four years as my supervisor and the year before that as my lecturer. I am well aware that I cannot have been the easiest student to supervise and most certainly not the most appreciate student to lecture to. The fact that he did take me on as a research student after I fell asleep in a one-on-one lecture during my MSc year does not speak for my abilities, but for his goodwill and sense of humour. He has been immensely supportive during my studies and I have come to see him not just as a supervisor, but also as a friend and I do hope this will continue beyond my time in Oxford for many years and decades to come.

Second in this list but not second in giving support is my family. I know they have sacrificed a lot over the past years and letting me go to study abroad in a country neither of them had been to before has been difficult, not just for them, but also for me. I cannot express my gratitude in a way that would in any way be appropriate but I do hope they know what they mean to me and how grateful I am. My grandfather commented about me gaining my doctorate and becoming a professor one day, long before I even understood what it meant. And although he made it sound like a joke, I know that he meant it. He sadly passed away less than a year before this thesis was submitted but I do hope that he is proud of me, wherever he is now.

I would also like to thank everyone in the Physical & Theoretical Chemistry Laboratory. First and foremost David Logan for having given me the chance to come up to Oxford for my MSc; Stuart Mackenzie for being a fantastic college adviser and sitting down with me more than once to talk about my DPhil and future; David Clary, for supporting me all the way and writing references for me and giving some of the most interesting lecturers I have ever had the pleasure to attend; Martin Galpin for letting me teach over the past four years, being a fantastic internal examiner. He has recently become somewhat of a star on the facebook meme scene, but I am proud to say: I knew him before he was famous (although that my be a disservice to him); David Manolopolous for the occasional pint in the Uni Club and the most unconventional lectures and discussions, oscillating between declaring something trivial and impossible so quickly, it could almost be described as a superposition; And lastly, but in no way least, Jenny Nelson from Imperial College London, for providing references for me without any obligation whatsoever and being a superb examiner.

My time in Oxford has been some of the best I have had so far and that is to a large extend thanks to the people I have met along the way, many of which I am happy and proud to call my friends. The people I spent almost every day with in the office and who had to endure me, Oliy, Josh, Alan, David, David, and David, Lachlan, Joe, Jonathan, and Jonathan, Darren, Dom, and all of the Part IIs that have come and gone over the years, Susannah, Jaymee and Djamshid, Alice, and of course Jess, as well as all others I

now forgot. Then, of course, the people I spent almost as much time with, albeit most of it out in the cold in the wee hours of the day. The boat club, MCBC, has given me a sport and hobby that I will cherish for many years to come and that is due to some exceptional people: Chris, Katherine, Jimmy and all the people from M2 in Summer VIIIs 2014; Will, Will, Rory, Joe, and everyone from M1 in various combinations over the past years; Georgia, Jane, Kaci, and everyone else from MCBC. It hasn't always been easy but I will miss every second of it. Floreat Magdalena!

I intended to give a list of the bottles of wine and spirits consumed during the making of this thesis and thank the responsible vineyards and distillers but I have, more or less unsurprisingly, lost track of the number. Let me just say that several drafts were written under the influence, and they certainly looked like it when I examined them later on. Cynics might say that parts of this thesis still look like it...

Thanks to everyone I mentioned here and everyone else I managed to forget: the following 200+ pages would not have been possible without you. The past four years were incredible and I want to finish with a quote from Magdalen's most famous almnus (probably), Oscar Wilde: 'Memory is the diary we all carry about with us.'

Magdalen College, Trinity 2017

Publications

The work presented in this thesis has led to the following publications:

- Chapters 4-6:
  1. W. Barford, M. Marcus, Perspective: Optical Spectroscopy in π-Conjugated Polymers and how it can be used to Determine Multiscale Polymer Structures, *J. Chem. Phys.* **146**, 130902 (2017).
- Chapter 4:
  2. W. Barford, M. Marcus, Theory of Optical Transitions in Conjugated Polymers. I. Ideal Systems, *J. Chem. Phys.* **141**, 164101 (2014).
  3. M. Marcus, O. R. Tozer, W. Barford, Theory of Optical Transitions in Conjugated Polymers. II. Real Systems, *J. Chem. Phys* **141**, 164102 (2014).
- Chapter 5:
  4. M. Marcus, J. Coonjobeeharry, W. Barford, Theory of Optical Transitions in Conjugated Macrocycles, *J. Chem. Phys.* **144**, 154102 (2016).
  5. W. Barford, M. Marcus, Theory of Optical Transitions in Curved Chromophores, *J. Chem. Phys* **145**, 142111 (2016).

The following published work does not form part of this thesis but was published during my DPhil studies:

6. W. Barford, M. Marcus, O. R. Tozer, Polarons in π-Conjugated Polymers: Anderson or Landau?, *J. Phys. Chem. A* **120**, 615 (2016).

Contents

Abstract ii

Statement of Originality iii

Acknowledgments iv

Publications vi

1 Introduction 1
- 1.1 Electronic Structure of Conjugated Polymers . . . 2
- 1.2 Motivation . . . 4
- 1.3 Structure of the Thesis . . . 9

2 Theoretical Framework 12
- 2.1 π-Electron Models . . . 13
  - 2.1.1 Separation of σ- and π-Electrons . . . 13
  - 2.1.2 The Pariser-Parr-Pople Hamiltonian . . . 16
  - 2.1.3 Nature of Excited States . . . 18
  - 2.1.4 Frenkel Excitons . . . 19
  - 2.1.5 Charge-Transfer Excitons . . . 20
- 2.2 Coarse-Grained Hamiltonians . . . 20
  - 2.2.1 Frenkel Hamiltonian . . . 22
    - 2.2.1.1 Types of Exciton States . . . 28
  - 2.2.2 Frenkel-Holstein Hamiltonian . . . 32
    - 2.2.2.1 Exciton-Phonon Coupling Constant . . . 34
    - 2.2.2.2 Born-Oppenheimer Regime . . . 37
    - 2.2.2.3 Momentum-Space Representation . . . 39
    - 2.2.2.4 Polaron States . . . 45

3 Computational Methods 50
- 3.1 Density Matrix Renormalisation Group . . . 50
  - 3.1.1 DMRG algorithm . . . 51
    - 3.1.1.1 Basis States and Hamiltonian Decomposition . . . 52
    - 3.1.1.2 Superblock State Calculation . . . 53
    - 3.1.1.3 Truncation . . . 54
    - 3.1.1.4 Infinite and Finite Lattice Algorithms . . . 57
- 3.2 Conjugate Gradient Routine . . . 59

3.2.1 Derivation of the Conjugate Gradient Routine 60

4 Vibronic Progression in Linear Conjugated Polymers 63
4.1 Ideal Chains 64
4.1.1 Exciton Wavefunction 64
4.1.2 Condon Allowed Transitions 66
4.1.3 The Born-Oppenheimer Regime 67
4.1.3.1 0-0 Transition 72
4.1.3.2 1-0 Absorption 74
4.1.3.3 0-1 Emission 77
4.1.3.4 Copolymers 78
4.1.4 Numerical Results 79
4.1.4.1 Periodic Boundary Conditions 80
4.1.4.2 Open Boundary Conditions 82
4.1.5 Breakdown for Long Chains 84
4.2 Disordered Chains 86
4.2.1 Disordered Model Systems 88
4.3 Summary 91

5 Vibronic Progression in Bent Chromophores and Macrocycles 94
5.1 Conjugated Macrocycles 95
5.1.1 Ordered Macrocycles 97
5.1.1.1 Temperature Effects 99
5.1.1.2 Herzberg-Teller Correction 101
5.1.2 Disordered Macrocycles 106
5.1.2.1 Herzberg-Teller Correction and Disorder 109
5.1.2.2 Summary of Effects 111
5.2 Bent Chromophores 113
5.2.1 Generalised Herzberg-Teller Correction 115
5.2.1.1 0-0 Absorption 116
5.2.1.2 1-0 Absorption 119
5.2.1.3 0-1 Emission 123
5.2.2 The Macrocycle Limit 127
5.2.3 Numerical Results 128
5.3 Summary 129

6 Modelling of Polymer Spectra 131
6.1 Poly(para-phenylene) and poly(para-phenylene vinylene) 132
6.1.1 Oligomers 134
6.1.2 Polymers 140
6.2 Poly(para-phenylene ethynelene) Macrocycles 152
6.3 Ladder-type PPP (MeLPPP) 155

7 Conclusion and Outlook 159
7.1 Summary of Results 159

7.2 Optical Spectroscopy of Conjugated Polymers and its Applications in the Future 162

Bibliography **164**

A Derivation of the Pariser-Parr-Pople Hamiltonian **175**

B Intrapolating between Adiabatic and Antiadiabatic Limits **181**

C Parameters for Polymer Modelling **184**
C.1 PPP 184
C.2 PPV 185
C.3 MeLPPP 187

D DMRG Convergence Tables **189**

1

Introduction

Since the discovery of the electroluminescent properties of phenylene-based polymers between the 1970s and 1990s the research interest in this class of compounds has risen significantly [1–4]. The semi-conducting properties of these materials, which are due to the molecular structure of the polymers, means they have the potential to replace conventional, silicon and rare earth based semiconductors. In conventional semi-conductors, the excited electrons are very loosely bound to the nuclear framework, allowing for electrical conductivity. Due to the very weak coupling of the excited electrons to the nuclei the crystal structure of the semiconductor essentially remains unchanged upon excitation [5]. This is in stark contrast to conjugated polymers: the excited electrons couple strongly to the nuclear degrees of freedom (phonons) and as such the nuclear structure readily adapts around the excited electron and as a result the energy of the system decreases. Additionally, the excited electron remains tightly bound to the hole left behind in the HOMO and the Coulomb attraction between these two charged particles also lowers the energy of the system. As such, there is a distinct difference between direct and optical band gaps in conjugated polymers, to a much larger extent than in conventional semi-conductors, making especially phenylene-based polymers absorb and emit in the UV-Vis region. This feature makes them ideal candidates for Organic Light Emitting-Diodes (OLEDs) as well as Organic Photovoltaics (OPVs). However many problems are associated with this, not least the inefficiency of OPVs and more research is needed to understand this exciting class of compounds.

In this thesis the direct effects of the electron-phonon coupling on the spectroscopic

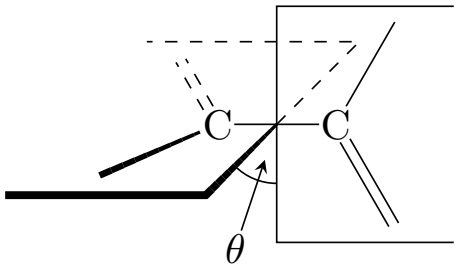


Figure 1.1.: Graphical representation of the dihedral angle, θ, between two moieties containing double bonds. The planes indicate the planes of the double bond, *i.e.* the π-orbital is perpendicular to the plane. Substituents have been omitted for clarity.

signature of conjugated polymers will be addressed and the associated questions will be developed in this chapter. First, however, the structural elements that lead to properties mentioned above will be discussed.

1.1 Electronic Structure of Conjugated Polymers

Conjugated polymers share the feature of an extended π-electron system along their backbone: unsaturated carbon atoms form a chain and each contributes one p-orbital which can overlap side-ways with the p-orbitals of neighbouring carbon atoms. This leads to a large orbital spanning, in principle, the entire polymer in the ideal case and the electrons within this orbital are delocalised over the entire chain. As a result of this delocalisation the energy of the system decreases, increasing its stability.

The geometry of the polymer has a profound effect on the extend of the conjugated system, as the overlap between neighbouring p-orbitals is a function of the dihedral angle between the planes of the respective π-orbitals, illustrated in Fig. 1.1. For $\theta = \pi/2$ the two double bonds will be perpendicular to one-another and the overlap will vanish, causing a break in the conjugated system. While it is very unlikely that the conjugation will be completely broken, it shows nevertheless that even small fluctuations in the neighbouring

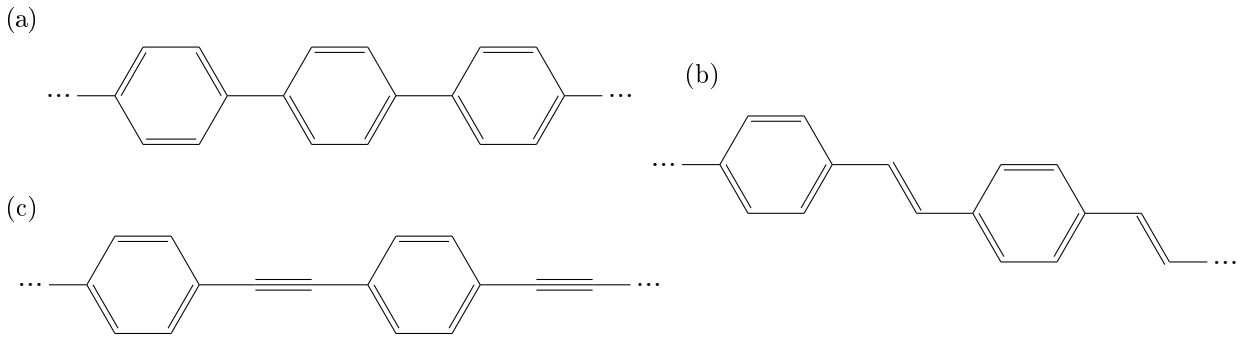


Figure 1.2.: Chemical structures of (a) poly(*para*-phenylene), (b) poly(*para*-phenylene ethylene), and (c) poly(*para*-phenylene ethynelene).

angles can have big effects. As a corollary, it seems intuitive to assume that conjugation along the polymer backbone will have a planarising effect on the molecule, while steric hindrance and kinetic energy of the molecule will prevent that. Conversely, the equilibrium structure of the polymer will be found to simultaneously minimise steric effects while maximising delocalisation under the constraint of the kinetic energy within the molecule.

Fig. 1.2 shows the basic chemical structure of the polymers under consideration in this thesis. Poly(*para*-phenylene) (PPP), poly(*para*-phenylene vinylene) (PPV), and poly(*para*-phenylene ethynylene) (PPE) are all phenylene-based polymers and, with exception of PPE, exhibit a non-zero equilibrium dihedral angle. This angle can be modified by the introduction of side- or branching chains, which do not participate in the conjugated system but planarise or twist the chain as desired. As they do not alter the properties of the π-conjugated system, they are not modelled explicitly but are taken into account via the modulation of parameters. Those systems include ladder-type PPP (MeLPPP) and methoxy-substituted PPV (MEH-PPV), which are well-investigated compounds in the literature and modelling of these systems will be performed in this thesis.

In addition to these sources of disorder, out-of-plane deformation within the systems can occur, *i.e.* PPE, for instance, can curve out of the plane of the molecular backbone.

This is necessary in order to synthesise macrocycles of the form discussed in Chapter 5. Effects on the electronic structure of the polymers via these effects are not modelled explicitly as they are taken to be negligible to the effects introduced by torsional disorder.

After introducing the motivation for this research as well as developing the questions addressed in the following section, the structure of this thesis will be set out.

1.2 Motivation

The efficiency of organic semiconductors in photoelectric applications has been increased significantly since the discovery of this property but is still significantly below those of the corresponding conventional materials. This poses a challenge especially for OPVs and the reasons for this inefficiency are manifold. A clear understanding of the processes that occur within the polymer and how these are influenced by a manifold of parameters is desirable and theoretical modelling can help, alongside experimental results, to gain a deeper insight into this class of materials.

As discussed above, the structure of a polymer has a non-negligible effect on the extended π-electron systems which underlies all photoelectric effects. This also holds true for the structure of the bulk on other length scales. In a conventional semi-conductor the electrons move more or less freely through the bulk, whereas in a molecular crystal the electrons have to migrate either along a polymer or from one polymer to another. As a consequence the direct environment of a given polymer will influence its properties and as such the structure of the bulk will determine its properties to a non-insignificant extend. To understand these structure-property relationships would allow for a more targeted approach in synthesising and manufacturing polymer-based appliances with desired properties.

Determining the structure of a polymer bulk is notoriously difficult: the bulk is usually amorphous and the nuclei tend to be very light. Conventional methods like X-ray diffraction will therefore not yield any results, while surface diffraction does not give any information of the bulk structure. If it is possible to establish structure-property relationships, the optical signature of a sample, a property that is measured very easily and quickly, can be used to determine the multi-scale structure.

This thesis sets out to understand how the local structure of a polymer determines its optical signature. With conjugated polymers being quasi-one-dimensional systems it is expected that effects which are well known in one-dimensional systems become important. It has been shown by Anderson, for instance, that random fluctuations in a potential necessarily lead to localisation in one dimension (see Sec. 2.2.2.4) [6, 7]. Local disorder in the dihedral angles between neighbouring moieties will introduce such potential fluctuations and it is therefore necessary to understand to what extend the localisation occurs and whether it is a dominant effect. The aim of this thesis is therefore to investigate the role of disorder in polymer systems and its effects on the optical signature. By deriving expression for the ordered case and generalising them for the disordered case it will be established how localisation affects the vibronic progression and how that, in return, can be used to infer local structure.

One parameter that is commonly used to describe the coupling between the excitonic and nuclear degrees of freedom is the so-called Huang-Rhys parameter, g^2 [8], which relates in a system with one nuclear normal coordinate the displacement of the equilibrium structure and the relaxation energy for electronic transitions between the corresponding states (see. Fig. 1.3). Previous studies gave indications that this parameter is a function of the number of monomers, N, in a polymer chain and that $g^2 \equiv f(N)$. If this function

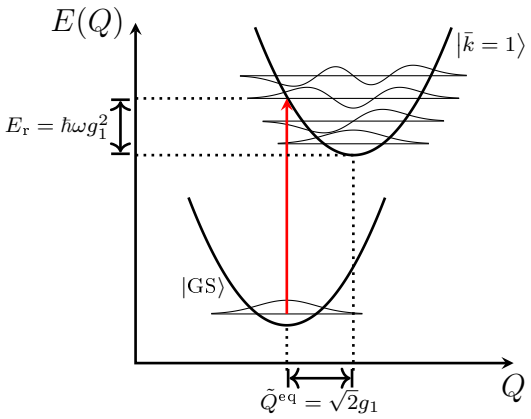


Figure 1.3.: Schematic representation of an excitation within a molecule with one normal mode. The Huang-Rhys parameter, g_1^2, is related to the displacement of the oscillator, $\tilde{Q}^\mathrm{eq}$, as well as the relaxation energy, E_r. This model can be used to study the excitations in a single monomer with one normal mode coupling dominantly to excitations, such as the symmetric stretch in vinylene or the benzoid-quinoid distortion in phenylene. g_1^2 is also the ratio of the 0-0 and 1-0 intensities in the corresponding absorption spectrum.

is known the length of the chain can be determined indirectly if g^2 can be measured. Brédas and co-workers have performed theoretical research in this field [9–11], while Yu *et al.* have shown that the vibronic progression of PPV indicates that $g_N^2 = a\exp(-N^2/b)$, where a and b are empirical parameters [12]. Chang *et al.* have also shown that a derivation of the relaxation energy associated with the nuclear rearrangement after excitation implies that $g_N^2 = 2g_1^2/(2(N+1))$, where g_1^2 is the monomeric Huang-Rhys parameter [13]. For a polymer with one normal mode per monomer these results imply that an effective Franck-Condon factor can be found, $F_{0\upsilon}(N) = (g_N^2)^\upsilon \exp(-g_N^2)/\upsilon!$, quantifying the vibronic progression and relating it to the length of the polymer via g_N^2. This also implies a mirror image relation between the absorption and emission spectrum. This is in contrast to the results by Spano and co-workers, who have studied the Frenkel-Holstein model, which is used in this thesis, and applied it first to so-called J-aggregates [14, 15] and then to polymers [16, 17]. They found that, within the anti-adiabatic limit, the mirror image relationship breaks down: for photoluminescence the ratio of the 0-1/0-0 emission

intensity ratio is a decreasing function of the chain length, while the 1-0/0-0 absorption intensity ratio is independent of the chain length. Knowing the relationship linking the intensity ratios and chain length will therefore enable us to predict one by knowing the other. In this case, the intensity ratio will return the length of a polymer if it is perfectly ordered and the excitation giving rise to the vibronic progression is delocalised along the entire chain. The length of the chain will then correspond to what is commonly known as a 'chromophore', *i.e.* the irreducible part of the chain that supports the excitation [18,19]. In a polymer with local disorder the excitations will be confined to length scales shorter than the actual polymer and as such the vibronic progression will be a function of the localisation length of the exciton. This thesis aims to establish a quantitative link between disorder, vibronic progression, and the Huang-Rhys parameter and in turn will also define what a chromophore within a polymer is.

It is not just disorder that influences the single-polymer spectrum. The conformation of the polymer does, as well. Due to symmetry selection rules certain transitions that make up the first excited state in our description will be allowed or forbidden depending on whether the polymer is linear, a ring, or anything in between. An important class of polymers to consider are macrocycles, which are polymers that form closed cycles with a diameter of up to several nanometers [20–22]. This class of polymers is widely used in nature as light antennae, for instance in chlorophyll and related compounds [23, 24]. This is partially due to their optical and electronic properties which differ significantly from linear polymers [25–37]. Additionally, macrocycles like cyclo-poly(*para*-phenylenes) (CPPPs) also form topologically the shortest carbon-nanotubes which makes them interesting compounds to investigate the basic properties of this class of compounds [38]. Due to synthetic limitations conjugated macrocycles have only recently become available and

are therefore interesting systems to perform theoretical studies on.

Between perfectly linear polymers and macrocycles bent polymers link the optical and electronic properties of these two extreme cases. Hestand and Spano have shown that the prediction for the emission intensity ratio in linear polymers fails as soon as the chain bends [39]. This is in accordance with the findings presented in this thesis and already published [40, 41] which show this to be due to the Herzberg-Teller effect [42]. In this most general case the emission and absorption intensity ratios are functions of the local disorder within the chain as well as the conformation of the polymer and the detailed functional dependence will be investigated.

All these questions will be investigated by first assuming the Condon approximation: the electronic excitation happens on a time scale much faster than nuclear relaxation and therefore the electronic and nuclear degrees of freedom decouple. However, especially for macrocycles this approximation breaks down and a post-Condon treatment needs to be developed in order to incorporate the explicit coupling of different vibronic states. This effect, which will be shown to be the Herzberg-Teller effect, enhances certain transitions which, especially in the limit of a fully ordered macrocycle, can be symmetry-forbidden and hence would not be bright within the Condon approximation.

All of the above shows that understanding the influence of the local structure of a polymer on its optical properties will help to understand the processes that occur when the polymer is excited and in turn will help to predict and engineer the properties of a polymer by changing its structure.

1.3 Structure of the Thesis

In order to gain insight into the local structure-property relationship a range of theoretical methods introduced in Chapter 2 will be employed. As will be justified, only the π-electron system within these polymers needs to be considered to capture the basic photoelectronic effects and it will be explained how they can be separated from the other electrons in the system, allowing for a theoretical modelling of a much larger systems than otherwise possible. Having restricted the Hilbert Space of the systems significantly, a semi-empirical model, the Frenkel-Model, will be introduced, which models the electronic excitation within the polymer as a single particle: a tightly-bound electron-hole pair referred to as an exciton. As the particles display a strong Coulomb-attraction they can be modelled as one quasi-particle without charge or spin, simplifying our model even further. This Frenkel-Model is then augmented to include explicit exciton-phonon coupling to give what is known as the Frenkel-Holstein model. This model itself is introduced in a semi-classical description, treating the nuclear vibrations as classic harmonic oscillators, and in a fully quantised version in which the vibrations are quantised as phonons. The general form of the eigenstates of both the Frenkel and the Frenkel-Holstein model are discussed and terminology will be introduced used throughout this thesis.

In Chapter 3 the computational methods used to solve the models are introduced, namely the Density Matrix Renormalisation Group (DMRG) which is used to solve the fully quantised model which has a Hilbert Space that in most to all cases exceeds the feasible limit for a full computation, and the Conjugate Gradient (CG) routine, which is a multidimensional minimisation protocol used at two distinct points in this thesis. Using the DMRG routine enables the calculation of larger systems with an in principle exact approach. The accuracy of the routine can be increased by increasing two convergence

parameters for which convergence tables are provided in Appendix B.

Chapter 4 will discuss the results for linear polymers. Expressions for ordered, linear chains that describe the vibronic progression in the optical spectra, are derived and these closed formulae will be checked using the DMRG routine, giving the essentially exact result. Using these results disorder will be introduced into the systems and it will be shown that the expressions derived previously can be easily amended to account for the disorder effects. As the central result of Chapter 4 it is found that the ratio of the vibronic progression gives a direct measure for the localisation length of an exciton along the polymer chain allowing an indirect determination of the local disorder.

Macrocycles will be one focus in Chapter 5 and post-Condon expressions for their coupling of vibronic states, which is especially prominent in cyclic systems owing to the symmetry, will be derived. The effects of temperature and disorder will be discussed and it will be shown that in macrocycles the post-Condon corrections become non-negligible and have a large influence on the optical signature. Following on from this the work on macrocycles and linear chains will be tied together by discussing a general, non-linear chain. In this intermediate regime most, if not all, symmetry selection rules break down and the spectra have many contributions. It is however possible, by using polarised spectroscopy, to determine the conformation of the polymer, a first step into the multi-scale structure determination of polymers using spectroscopic methods. Formulae for the vibronic progressions interpolating between linear and macrocyclic systems and therefore spanning the entire range of conformations for a given single polymer will be derived.

In Chapter 6 all of these results are used to model the spectra of some selected polymers and explain features in their spectra. For instance, a PPV derivative shows two distinct phases in the low-temperature spectra and using the previously obtained theo-

retical results allows to explain in detail what distinguishes these phases and how each contributes to the overall spectrum.

The thesis will conclude with a summary in Chapter 7 and an outlook as to where future research can be taken in order to use spectroscopy as a direct means of determining the multi-scale structure of polymers.

The appendices contain a derivative of the Pariser-Parr-Pople Hamiltonian, a model used to describe π-electrons, from first principles, results intrapolating between the adiabatic and anti-adiabatic limits, convergence tables for the DMRG code used, and tables of model parameters for various polymers.

2

Theoretical Framework

Having described the problems and questions addressed in this thesis in the previous chapter, this chapter aims to provide a concise description of the theoretical models underlying the calculations performed. Polymers contain a large number of nuclei and electrons and, due to particle-particle interactions, an exact solution of the systems (*i.e.* solving the exact Hamiltonian) is not possible. Neither is a full description of each particle at basic levels of electronic structure theory, for instance by Hartree-Fock (HF) or Density Functional Theory (DFT) methods. Due to the need to include excited states these methods become even less applicable and post-HF methods (like Configuration interaction (CI) or Coupled Cluster (CC)) or time-dependent DFT (TD-DFT) tend to be vastly more computationally expensive than HF and DFT itself. A model that (i) describes the basic and essential photophysical properties of the systems whilst (ii) being computationally accessible is therefore needed. In the course of this chapter the underlying Hamiltonian will be simplified and adapted to the point where it achieves both goals.

First it will be shown that only a heavily reduced subspace of electrons needs to be considered to capture the fundamental excitations within conjugated polymers and then the systems under investigation will be mapped onto model systems which simplify the underlying Hamiltonian so that it becomes computationally accessible. The Frenkel model will be introduced, describing a particle that can migrate on a lattice and the nature of its eigenstates will be discussed. Then explicit exciton-phonon coupling will be introduced resulting in the Frenkel-Holstein model and the effects of this coupling on the excitonic wavefunctions will be discussed. The Frenkel-Holstein model will be introduced in its

semi-classical form, treating the nuclear normal modes classically, and a fully quantized form, quantising the vibrations as phonons.

2.1 π-Electron Models

As described in Chapter 1 the defining feature of conjugated polymers is the common, extended π-electron system spanning large sections or the entirety of the polymer. It is not possible to describe all electrons within the system explicitly, especially in the polymer limit. Even just describing the valence electrons becomes computationally infeasible for moderately sized oligomers. The number of electrons considered explicitly will thus need to be reduced even further. In the following section it will be justified why the π- and σ-electrons can be separated in their treatment and how this can be exploited to derive simplified Hamiltonians which still capture the basic photophysical properties of the polymers.

2.1.1 Separation of σ- and π-Electrons

The electrons within the σ- and π-bonds form two bands which explain the photophysical properties of conjugated polymers (see Fig. 2.1). The σ-electrons form a narrow band with relatively large band gaps, usually exceeding 10 eV [43–46], while the π-electrons form a broad band with small band gaps, ranging from 2 - 4 eV [47]. The principal optical processes will thus take place involving the π-electrons and due to the difference in the energy scale it is justified to separate the treatment of both types of electrons and consider the σ-electrons only parametrically, for instance by shielding the nuclear charge. Another argument is the orthogonality of the orbitals in perfectly planar systems, indicating that even in non-planar systems the interaction will be negligible.

The simplest polymer containing an extended π-electron system, poly(acetylene), is

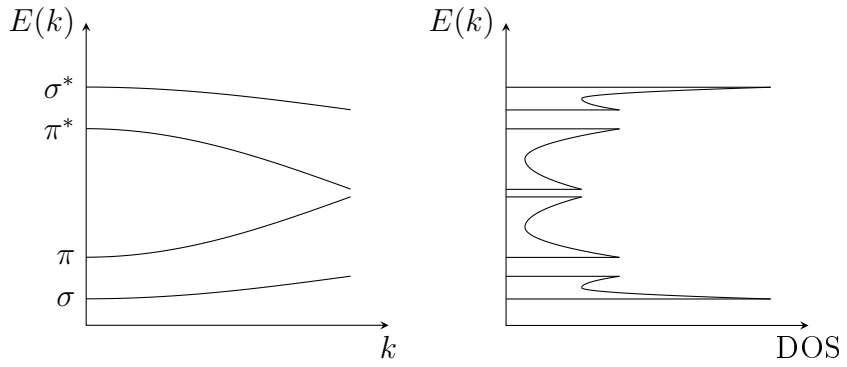


Figure 2.1.: Schematic representation of the $\sigma^{(*)}$ and $\pi^{(*)}$ bands and Density of States (DOS) in a conjugated polymer. The $\pi^* \leftarrow \pi$ band gap is significantly smaller than the $\sigma^* \leftarrow \sigma$ band gap. The optical band gap is even smaller then the direct band gap indicated here.

often taken as a model to explain basic properties of conjugated polymers. The states accessible to the π-electrons here are often described in terms of a particle-in-a-box model: the gap between energy levels (*i.e.* the band gap, as well) reduces with increasing size of the polymer, vanishing in the limit of an infinite polymer. While this is true when ignoring any particle-particle interactions, in real polymers electron-electron and electron-nucleus interactions result in a non-vanishing band gap, even in the thermodynamic limit. Especially for systems similar to poly(acetylene) (*i.e.* systems with significant electron-electron interactions) a band gap forms near the Fermi energy due to electron-electron interactions, rendering the polymer a Mott insulator [48–52]. The electron-nucleus interactions manifest themselves via two mechanisms. Firstly, one-dimensional conductors (as an ideal poly(acetylene)) are subject to Peierls distortion, leading to an alternation in bond length, a doubling in unit-cell size and hence a doubling in band numbers. This distortion also leads to a band gap at the Fermi energy, as is most easily shown for an infinite chain of hydrogen (see Fig. 2.2). This renders the polymer a Peierls insulator [5]. Lastly, at finite temperatures conjugated polymers are unlikely to be perfectly ordered, leading to a non-uniform potential and the applicability of the Anderson localisation model for insu-

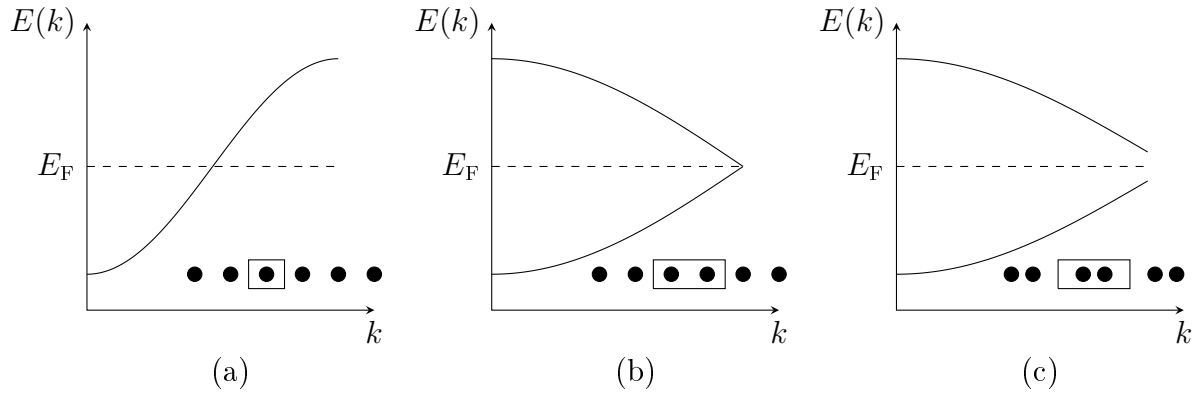


Figure 2.2.: Schematic representation of the Peierls transition in an ideal Hydrogen chain with the band gap opening up at the Fermi energy, E_{F}, after pairwise distortion (c) of the chain. The doubled unit-cell (b) causes the splitting of one band in (a) into two (bonding and anti-bonding with respect to the bond within the unit cell).

lators [6]. For *trans*-polyacetylene the Peierls distortion is not unique. The dimerisation can 'inverse', *i.e.* the single- and double bonds can 'swap' places, and lead to an equivalent structure with different single bond - double bond alternation. As these structures are equivalent in both energy and topology, the Peierls insulator model is strictly not applicable to *trans*-polyacetylene and this polymer is more accurately described as a Mott insulator [43].

This shows that because of particle-particle interactions conjugated polymers are generally insulators. However, for phenylene based polymers, like poly(*para*-phenylene) (PPP), the fundamental band gap of the $\pi^* \leftarrow \pi$ transition is of the order of 2 eV, which is relatively small and corresponds to the UV-Vis region of the electromagnetic spectrum. It is therefore that these materials are commonly described as organic semiconductors [43–47].

In the following section a Hamiltonian capable of describing the basic properties of π-electron systems in conjugated polymers is introduced. While not being used directly in this work, it serves as a benchmark to the models used and helps to parametrize the coarse-grained models [53].

2.1.2 The Pariser-Parr-Pople Hamiltonian

With the separation of $\sigma-$ and $\pi-$electrons justified in the previous section, only the $\pi-$electrons need to be considered. Every carbon atom forming part of the π-electron system contributes one electron so if the CP is made up of n carbon atoms in its σ-backbone, the π-electron system will have n electrons. A Hamiltonian suitable to describe the properties of such systems is the Pariser-Parr-Pople Hamiltonian [54–56]. Labelling the carbon nuclei by i, j the model reads,

$$\hat{H}_{\mathrm{PPP}} = \sum_{\langle ij\rangle\sigma} t_{ij}\left(\hat{c}^{\dagger}_{i\sigma}\hat{c}_{j\sigma} + \hat{c}^{\dagger}_{j\sigma}\hat{c}_{i\sigma}\right) + U\sum_{i}\left(\hat{n}_{i\uparrow} - \frac{1}{2}\right)\left(\hat{n}_{i\downarrow} - \frac{1}{2}\right) + \frac{1}{2}\sum_{i\neq j} V_{ij}\left(\hat{n}_i - 1\right)\left(\hat{n}_j - 1\right), \tag{2.1}$$

where $\hat{c}^{\dagger}_{i\sigma}$ ($\hat{c}_{i\sigma}$) creates (destroys) an electron of spin σ on site i, $\hat{n}_{i\sigma} = \hat{c}^{\dagger}_{i\sigma}\hat{c}_{i\sigma}$ is a number operator and $\hat{n}_i = \sum_{\sigma}\hat{n}_{i\sigma}$. The first term in Eq. (2.1) is the electron hopping term, with the transfer integral t_ij. The second term expands as,

$$U\sum_{i}\left(\hat{n}_{i\uparrow} - \frac{1}{2}\right)\left(\hat{n}_{i\downarrow} - \frac{1}{2}\right) = U\sum_{i}\hat{n}_{i\uparrow}\hat{n}_{i\downarrow} - U\sum_{i}\hat{n}_i + \frac{1}{4}\sum_{i}U. \tag{2.2}$$

Here, the first term describes the on-site electron-electron interaction, the second term is the on-site electron-nucleus interaction and the last term is a correction to eliminate self-interaction contributions (see Appendix A). The factor of $\frac{1}{2}$ in the third term in Eq. (2.1) prevents double counting of contributions when summing over pair of sites and the sum can be rewritten as,

$$\sum_{i\neq j} V_{ij}\left(\hat{n}_i - 1\right)\left(\hat{n}_j - 1\right) = \sum_{i\neq j} V_{ij}\hat{n}_i\hat{n}_j - 2\sum_{i\neq j} V_{ij}n_i + \sum_{i\neq j} V_{ij}, \tag{2.3}$$

where the first term denotes the off-site electron-electron interaction, the second term the off-site electron-nucleus attraction and the last term the nucleus-nucleus interaction. For a full derivation of the Hamiltonian from first principles see Appendix A.

The on-site energy is a result of the attraction (repulsion) of electrons and nuclei (electrons) on the same site. The off-site interaction follows the Coulomb-law, but often an interpolation for V_{ij} is used which recovers U for $i = j$, for example the Ohno potential [57], given as,

$$V_{ij} = \frac{U}{\sqrt{1 + \left(U\varepsilon r_{ij}/14.397\ \mathrm{C}^2\right)}}, \tag{2.4}$$

where ε is the relative dielectric constant of the material and the factor of $1/14.397$ is an empirical scaling factor to recover the Coulomb behaviour for large r_{ij}, which is the relative distance of the sites i and j.

Other Hamiltonians have been developed to treat extended π-electron systems. The most widely known and crude model is the Hückel model, which neglects all pair-wise interactions (apart from the on-site electron-nucleus interactions). Due to these drastic approximations the Hückel model is only useful to gain qualitative insight into the photophysical properties of a fermionic system (it will be shown below that its usefulness increases drastically when a bosonic system is investigated). Another model widely employed is the Su-Schrieffer-Heeger (SSH) model [58,59], which adds electron-phonon interactions to the Hückel model. The Pariser-Parr-Pople model is then the next extension to the SSH model by incorporating nuclear interactions.

In order to examine the photophysical properties of conjugated polymers the excited states of the systems have to be known as the absorption of a photon results in the promotion of an electron to a virtual orbital. The nature of these excited states (especially the ones important in this thesis) will be discussed in the next section.

2.1.3 Nature of Excited States

The absorption of a photon (a spin-1-boson) by a conjugated polymer generally results in the promotion of an electron from its ground state into an excited state. Due to the electronic structure of organic semiconductors this will be a $\pi^* \leftarrow \pi$-transition if the absorbed photon is within the ultraviolet or visible range of the electromagnetic spectrum. The electronic structure thus changes and the electrons remaining in the π-band adapt to a lack of charge. This situation can be modelled by introduction of a positively charged quasi-particle, a hole. In ideal and uniform systems the excited electron and hole posses certain symmetries which will be exploited later in this thesis. Thus, an absorption of a photon creates an electron/hole pair in the π^*/π bands, which in turn can be described as a neutral quasi-particle, called exciton.

There has been considerable discussion about the nature of these excitons within conjugated polymers [60]. If $\mathbf{r}_\mathrm{e}$ describes the position of the electron and $\mathbf{r}_\mathrm{h}$ of the hole (within the excited molecule/polymer) then the exciton can be described by these coordinates. It is, however, sometimes more convenient to describe the exciton in terms of its centre-of-mass (COM) and the spread between the electron and the hole. One can define the two coordinates,

$$\mathbf{r}_\mathrm{COM} = \frac{1}{2}\left(\mathbf{r}_\mathrm{h} + \mathbf{r}_\mathrm{e}\right); \quad \mathbf{r}_\mathrm{rel} = \mathbf{r}_h - \mathbf{r}_e \tag{2.5}$$

quantifying the exciton [19]. In the late 1990s it was generally accepted that the electron and hole form a tightly bound exciton within photoexcited conjugated polymers as there is a large, only weakly screened, Coulomb attraction between the electron and hole of about 1 eV [43, 61–63]. This has the direct consequence that the optical band gap is about 1 eV smaller than the direct band gap in these polymers.

As electrons are spin-$\frac{1}{2}$ particles, so is the hole that is created by the excitation of the electron and hence the resulting exciton can be a singlet (paired spin) or triplet (parallel spin) exciton. We limit our discussions to singlet excitons to ease the computational effort.

2.1.4 Frenkel Excitons

As mentioned above the relative separation of electron and hole in phenylene based polymers is very small, which is owing to the strong electron-hole interactions which are essentially not screened by the polymer itself due to the low relative permittivity. This means that the bound state with $\mathbf{r}_{\text{rel}} \approx 0$ is separated by a relatively large energy gap from any unbound states and as such it is reasonable to assume that for low-energy excitations the resulting exciton will be an electron-hole pair confined to the same repeat unit of the polymer [64, 65]. This phenomenological explanation of the low-energy exciton structure is also verified by the solutions to the one-dimensional Schrödinger equation. The low-energy solutions form a sub-space of the full Hilbert space in which the electron-hole pairs are tightly bound, whereas solutions with larger separations between these two particles form part of another sub-space with generally higher energies.

These excitations were first discussed by Frenkel and are thus most commonly knows as Frenkel excitons [66, 67]. It simplifies the treatment of excitons significantly as these can now be described by a wavefunction with only one variable, the centre-of-mass coordinate, which corresponds to the position of the exciton. In a group theoretical description the Frenkel excitations are the $1B_u^-$ excitation manifold of the $1A_g^+$ ground state.

Despite the electron and hole tightly bound the exciton itself can spread over the entire polymer and as such the exciton can be delocalised. In this thesis excitons not spread over the entire chain shall be termed 'localised' and the effects localisation has on the

optical properties of phenylene based polymers will be discussed.

2.1.5 Charge-Transfer Excitons

Higher excited states in phenylene-based polymers show a non-zero electron-hole separation and as such the centre of mass does not correspond to the electron and hole positions. Excitons with electron and hole separated over one or more moieties are known as charge-transfer (CT) excitons as a charge signature can be seen on the polymer. These states are, in phenylene based polymers such as PPP and PPV, high-energy excited states and can only be observed at high temperatures or by multiple photon absorption [68–70]. They correspond to the nA_g^+ states of the excited polymer and, as mentioned above, the corresponding wavefunctions form a separate sub-space of the Hilbert space. However, as shown below, CT excitons can be regarded as a perturbation on Frenkel excitons in low-energy states and are therefore important in the exact treatment of low-energy excitations. In addition, CT states are in their own right interesting to study due to multi-photon experiments and form part of proposed future research (see Chapter 7).

2.2 Coarse-Grained Hamiltonians

After introducing the full π-electron models and discussing the nature of excited states in phenylene-based polymers, coarse-grained Hamiltonians that capture the essential photophysical properties of the systems while also being computationally affordable will now be introduced.

While the electron and hole may not be localised on the same atom within a phenylene or vinylene unit, it has been shown that in polymers consisting of such moieties, like PPP and PPV, the electron-hole separation is smaller than the length scale of a moiety

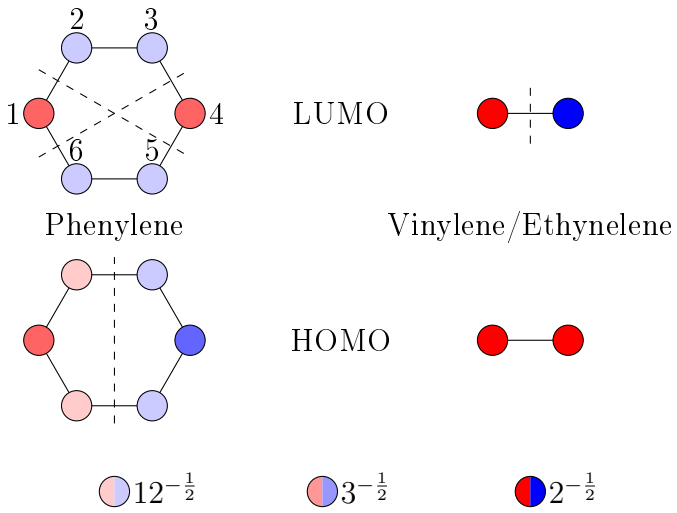


Figure 2.3.: Schematic representation of the HOMO and LUMO orbitals of phenylene and vinylene units. The colours indicate signs of the wavefunction and the shades show the amplitudes. Dashed lines indicate nodal planes within the orbitals.

and therefore such moieties are ideal for coarse graining and approximating as a site in our models [64]. From now on, 'site' shall refer to either a phenylene, a vinylene, or an ethynylene unit.

The fundamental excitations in π-conjugated polymers are from the HOMO, which is the π-orbital, to the LUMO, the π^*-orbital and as described above such excitations are not directly affected by the other orbitals in the system. Hence, our description will be limited to the valence band/HOMO and the conduction band/LUMO. The relevant orbitals are shown in Fig. 2.3.

The model Hamiltonians used in this thesis will be introduced in the following sections. First the Frenkel model, which models a single Frenkel exciton and is equivalent to the Hückel model. After discussing the nature of its eigenstates, the exciton-nuclear coupling will be reintroduced into the model and the effects of this coupling on the excitonic wavefunctions will be discussed. We will also recast the Frenkel-Holstein model in a momentum-space representation, which will be useful in the discussion of macrocycles

and bent chromophores.

2.2.1 Frenkel Hamiltonian

As detailed above, electronic excitations in extended systems can be described by two variables, $\mathbf{r}_{\mathrm{COM}}$ and $\mathbf{r}_{\mathrm{rel}}$, giving the centre-of-mass coordinates and the spread of the delocalised particles. In a one-dimensional system, such as the conjugated polymers considered in this thesis, these coordinates are scalars and form good quantum numbers (as they are preserved during the manipulations of the model within this thesis) to label excitonic states within the polymer. If $\mathbf{r}_{\mathrm{COM}} \to R$ and $\mathbf{r}_{\mathrm{rel}} \to r$ then $R - r/2$ and $R + r/2$ are the positions of the hole and excited electron, respectively. The Hilbert space of all electronic excitation is then spanned by the states $\{|R, r\rangle\}$. Frenkel-excitons are then described by the states $\{|R, 0\rangle\}$ and charge-transfer excitons by $\{|R, 1\rangle\}$, for example. The Hilbert space is described by the excitonic Hamiltonian, $\hat{H}_{\mathrm{exciton}}$, and it is assumed that it can be divided into a low-energy subspace spanned by Frenkel-excitons and a high-energy subspace spanned by CT-excitons. Each of these subspaces is associated with a projection operator, $\hat{P}_{\mathrm{F}}$ and $\hat{P}_{\mathrm{C}}$, which project a general state $|\Psi\rangle$ onto these subspaces, respectively. If we restrict ourselves to these two subspaces then,

$$\hat{P}_{\mathrm{F}} + \hat{P}_{\mathrm{C}} = \hat{1}, \tag{2.6}$$

and it follows as a corollary that,

$$\hat{P}_{\mathrm{F}}^2 = \hat{P}_{\mathrm{F}}; \quad \hat{P}_{\mathrm{C}}^2 = \hat{P}_{\mathrm{C}}. \tag{2.7}$$

Starting from the full Schrödinger equation it follows that,

$$\begin{aligned} \hat{H}_{\text{exciton}} |\Psi\rangle &= E |\Psi\rangle \\ \hat{P}_{\text{F}} \hat{H}_{\text{exciton}} |\Psi\rangle &= E \hat{P}_{\text{F}} |\Psi\rangle \end{aligned} \tag{2.8}$$

$$\begin{aligned} \hat{P}_{\text{F}} \hat{H}_{\text{exciton}} \left(\hat{P}_{\text{F}}^2 + \hat{P}_{\text{C}}^2 \right) |\Psi\rangle &= E |\Psi_{\text{F}}\rangle \\ \hat{H}_{\text{FF}} |\Psi_{\text{F}}\rangle + \hat{H}_{\text{FC}} |\Psi_{\text{C}}\rangle &= E |\Psi_{\text{F}}\rangle , \end{aligned}$$

where $\hat{P}_{\text{F}} |\Psi\rangle = |\Psi_{\text{F}}\rangle$ and $\hat{P}_{\text{F}} \hat{H}_{\text{exciton}} \hat{P}_{\text{F}} = \hat{H}_{\text{FF}}$ (and equivalent for $\hat{P}_{\text{C}}$). $\hat{H}_{\text{FF}}$ represents the part of the Hamiltonian acting in the Frenkel subspace, $\hat{H}_{\text{CC}}$ acts in the CT subspace, and $\hat{H}_{\text{FC}}, \hat{H}_{\text{CF}}$ connects the Frenkel and CT part of the Hilbert subspaces, and equivalent for other combinations.

In a similar way one can arrive at,

$$\hat{H}_{\text{CF}} |\Psi_{\text{F}}\rangle + \hat{H}_{\text{CC}} |\Psi_{\text{C}}\rangle = E |\Psi_{\text{C}}\rangle . \tag{2.9}$$

This expression can be solved for $|\Psi_{\text{C}}\rangle$,

$$|\Psi_{\text{C}}\rangle = -\frac{\hat{H}_{\text{CF}}}{\hat{H}_{\text{CC}} - E} |\Psi_{\text{F}}\rangle . \tag{2.10}$$

Then, using Eq. (2.8),

$$\left(\hat{H}_{\text{FF}} - \frac{\hat{H}_{\text{FC}} \hat{H}_{\text{CF}}}{\hat{H}_{\text{CC}} - E} \right) |\Psi_{\text{F}}\rangle = E |\Psi_{\text{F}}\rangle , \tag{2.11}$$

where the term in brackets is an effective Hamiltonian acting on the Frenkel subspace. The second term in the bracket connects the Frenkel subspace to the CT subspace.

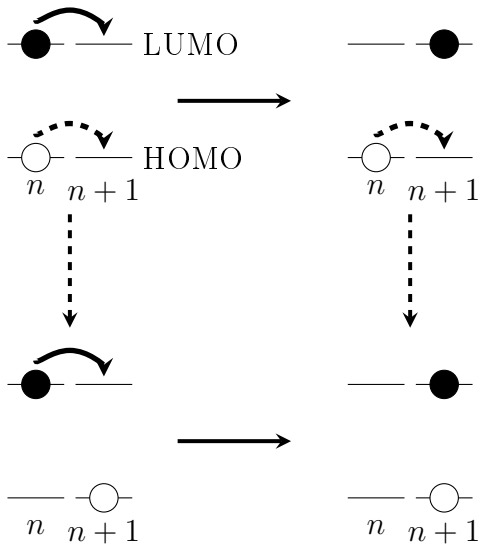


Figure 2.4.: Migration of a Frenkel exciton from site n to site $n+1$ via charge-transfer states. The migration can be realised by two equivalent mechanisms in which the electron (•, solid) or hole (∘, dashed) hops first.

$\hat{H}_{\mathrm{FC}}\left(\equiv \hat{H}_{\mathrm{CF}}^{\dagger}\right)$ can be treated as perturbation on $\hat{H}_{\mathrm{CC}}$ and $\hat{H}_{\mathrm{FF}}$ and to lowest order in perturbation theory, the effective Hamiltonian can be rewritten as,

$$\hat{H}_{\mathrm{eff}} = \hat{H}_{\mathrm{FF}} - \frac{\hat{H}_{\mathrm{FC}}\hat{H}_{\mathrm{CF}}}{\Delta E_{\mathrm{CF}}}, \tag{2.12}$$

where $\hat{H}_{\mathrm{CC}} - E$ was replaced (approximately) by $\Delta E_{\mathrm{CF}} = E_{\mathrm{C}} - E_{\mathrm{F}}$ with,

$$E_{\mathrm{F}} = \left\langle \Psi \left| \hat{H}_{\mathrm{FF}} \right| \Psi \right\rangle = \left\langle \Psi_{\mathrm{F}} \left| \hat{H}_{\mathrm{exciton}} \right| \Psi_{\mathrm{F}} \right\rangle, \tag{2.13}$$

and an equivalent expression for the CT subspace.

The resulting effective Hamiltonian contains contributions from Frenkel excitons located on a single site within the polymer and contributions from charge-transfer excitons located on neighbouring site. These charge-transfer contributions are migration terms of the Frenkel excitons, as illustrated in Fig. 2.4 as well as virtual states in which a charge migrates to a neighbouring site and back.

This real-space model can be expressed in second quantization as,

$$\hat{H}_{\text{Frenkel}} = \sum_{n=1}^{N} \varepsilon_n \hat{a}_n^\dagger \hat{a}_n + \sum_{n=1}^{N} J_{n,m} \left(\hat{a}_n^\dagger \hat{a}_m + \hat{a}_m^\dagger \hat{a}_n \right), \tag{2.14}$$

where $\hat{a}_n^\dagger$ ($\hat{a}_n$) creates (destroys) a Frenkel exciton on moiety n associated with the on-site energy ε_n. The second term describes the migration with the transfer integral $J_{n,m}$ from site n to site m.

The exciton creation operator can be written in terms of the electron creation and destruction operators as,

$$\hat{a}_n^\dagger = \hat{c}_{n,c}^\dagger \hat{c}_{n,v} = \sum_{ij} \phi_{i,c} \phi_{j,v} \hat{c}_i^\dagger \hat{c}_j, \tag{2.15}$$

with i, j labelling carbon atoms on site n and $\phi_{i,c}$ ($\phi_{j,v}$) being the electronic wavefunction of the LUMO/conduction band (HOMO/valence band) on site i (j). The terms $i = j$ have no contributions due to the orthogonality of the frontier orbitals.

The on-site energy, ε_n, is measured against the electronic ground state of the polymer and as such contains contributions from the energy difference between the HOMO and LUMO, the Coulomb interactions between the electron and the hole, and stabilising contributions from virtual charge transfer states accessible by reversible hopping of the charges to neighbouring sites. The numerical value of ε_n depends on the nature of the moiety and for phenylene can be calculated by comparing the asymptotic energy of an exciton on a uniform chain to the values obtained by the Pariser-Parr-Pople. If this value is taken to be equal for phenylene moieties in PPV the value of ε_n for vinylene units can be found by comparing results obtained by the Frenkel model to results of the Pariser-Parr-Pople model. The value found are then $\varepsilon_{\text{P}} = 6.05$ eV in the case of phenylene and $\varepsilon_{\text{V}} = 8.59$ eV for vinylene.

The contributions to the hopping parameter, $J_{n,m}$, can be classified as dipole-dipole and as superexchange interactions [71, 72]. In the case of the former the exciton transfers to neighbouring sites in a coherent fashion, electron and hole simultaneously. This contribution can be expressed as,

$$J_{n,m}^{\mathrm{DD}} = \frac{\kappa_{n,m}\mu_0^2}{4\pi\varepsilon_r\varepsilon_0 R_{n,m}^3}, \tag{2.16}$$

with μ_0 being the on-site transition dipole moment, $R_{n,m}$ the distance of the centre of the moieties n and m. $\kappa_{n,m}$ is a structure factor describing the orientation of the transition dipole moment vector, $\boldsymbol{\mu}_n$, to the vector joining the centres of the moieties, $\mathbf{R}_n$,

$$\kappa_{n,m} = 3\left(\mathbf{R}_{n,m}\cdot\boldsymbol{\mu}_m\right)\left(\mathbf{R}_{n,m}\cdot\boldsymbol{\mu}_n\right) - \boldsymbol{\mu}_m\cdot\boldsymbol{\mu}_n. \tag{2.17}$$

The dipole-dipole interaction is usually restricted to nearest-neighbour contributions due to the $R_{n,m}^3$-dependency.

The second contribution to the hopping parameter is the superexchange contribution, describing the electron and hole moving independently along the polymer and migrating the exciton as described in Fig. 2.4. Second order perturbation theory allows to relate this parameter to the parameters of the Pariser-Parr-Pople Hamiltonian as,

$$J_{n,m}^{\mathrm{SE}} = \frac{2t_n^2\left|\phi_n^i\right|^2\left|\phi_m^j\right|^2}{\Delta E}, \tag{2.18}$$

with t_n being the electron transfer integral, ϕ_n^i is the amplitude of the electronic wavefunction of the HOMO (or LUMO) on site i on moiety n, which is adjacent to a site j of moiety m, and ΔE is the energy difference between the Frenkel and charge transfer

excitons [43]. This contribution is a direct consequence of Eq. (2.18), which links the respective Hilbert sub-spaces. t_n is proportional to the cosine of the dihedral angle between adjacent moieties, $\cos\theta_n$ and hence $J^{\mathrm{SE}}_{n,n+1} = J^{\mathrm{SE}}\cos^2\theta_n$, where J^{SE} is the superexchange hopping parameter for coplanar moieties ($\theta_n = 0$). From now on, only nearest-neighbour hopping will be considered and all higher-order terms will be neglected. Fluctuations in dihedral angles between neighbouring sites are therefore a significant source of disorder in polymeric systems, having a large influence on the overall nearest-neighbour hopping parameter, $J_{n,n+1}$, which can be expressed as,

$$J_{n,n+1} \equiv J_n = J^{\mathrm{DD}} + J^{\mathrm{SE}}\cos^2\theta_n. \tag{2.19}$$

These formulae give values of 0.4 eV for PPP and 0.6 eV for PPV in the dipole-dipole hopping, J^{DD}, and 1.0 eV for PPP and 1.68 eV for PPV for the superexchange contribution, J^{SE} [62, 73].

If $|\Psi\rangle$ is an exciton centre-of-mass state (which is generally a linear combination of eigenstates of the Frenkel Hamiltonian) it can be expressed as a linear combination of single site Frenkel exciton basis states, $|n\rangle = \hat{a}_n^\dagger|0\rangle$,

$$|\Psi\rangle = \sum_{n=1}^{N} \Psi_n |n\rangle\,, \tag{2.20}$$

where Ψ_n is the exciton centre-of-mass wavefunction.

A semi-empirical approach to parametrise the model was chosen in this work. It is believed that a closer link with the physical interpretation of the parameters is retained but a fully empirical parametrisation is possible by fitting the results of the Frenkel model to experimental observables, like absorption and emission spectra [74].

The Frenkel model neglects all electron-phonon interactions. However, in contrast to conventional electronically conducting materials, conjugated polymers display large electron-nuclear coupling which has to be considered when modelling these systems. The model will therefore be augmented to result in the Frenkel-Holstein model, which couples the excitonic degrees of freedom to the nuclear vibrational normal modes. However, the nature of the eigenstates of the Frenkel model first will be discussed first.

2.2.1.1 Types of Exciton States

The eigenstates of the Frenkel model are exciton states with the ground state of the model corresponding to the lowest energy excitonic state and its eigenvalue is the energy of the exciton within the polymer. In ordered systems these exciton states correspond to the particle-in-a-box wavefunctions. When disorder is introduced into the system, either by varying the on-site energy, ε_n, or the hopping integral, J_n, the exciton states will change and adapt to the altered potential. As conjugated polymers are quasi one-dimensional the disorder in the system will lead to dynamical localisation of the excitons as described by Anderson. This process will occur in any disordered polymer, but it is a question of the other parameters if this is the main localisation process.

The various types of excitonic states will now be discussed and the concepts of local excitonic ground states (LEGSs), local excitonic excited states (LEESs), and quasi-extended excitonic states (QEESs) introduced. Following on from the discussion of the Frenkel-Holstein model in the following section, the alterations to these states when taking exciton-phonon coupling into account will then be discussed.

Local Exciton Ground States As mentioned above, on a uniform lattice the eigenstates of the Frenkel model will correspond to the particle-in-a-box states, which for open

boundary conditions are standing waves and for periodic boundary conditions will be Bloch- or plane-waves. However, by introducing disorder into such a system these states will localise and the degree of localisation grows exponentially with the disorder. This localisation always occurs in one-dimensional systems, as first described by Anderson, if the disorder is non-periodic [6,7,75] and we will explain it in more detail in Section 2.2.2.4. In polymers, it can be expected that disorder is present in almost all instances due to various reasons, which can be external or internal [76,77]. External disorder, which arises from density fluctuations in the surroundings of the polymer, causes local variations in the relative permittivity which then affects the exciton binding energy [71,77–79]. External disorder is accounted for when simulating spectra by having a non-zero homogeneous linewidth or a standard deviation in the on-site energy, σ_ε. However, the main focus will be internal disorder caused by variations in the torsional angles between neighbouring sites, which will alter the hopping integrals, J_n. This process is considered to be more important and to be the main source of disorder, as the torsional potentials around the single bonds between neighbouring sites are very shallow, and hence subject to large fluctuations at finite temperatures, and because the twisting along the molecular axis has a direct effect on the π-electron system supporting the excitations considered in this thesis. Localisation due to exciton-phonon coupling will be discussed below.

In disordered polymers, the lowest energy eigenstates of the Frenkel model will be superlocalised excitonic states which are non-overlapping, space-filling, and essentially nodeless (*i.e.* their nodes occur in regions with small exciton density). These states will be confined to a segment of the polymer chain and they are termed local exciton ground states (LEGSs) [71,80–82]. Due to their essentially nodeless character, we can identify

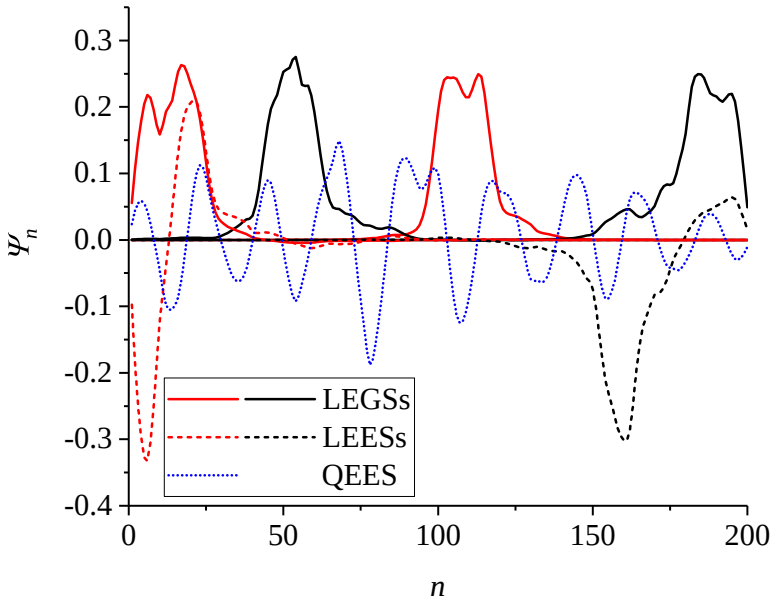


Figure 2.5.: LEGSs, LEESs, and one QEES on a disordered chain of 200 sites with open boundary conditions. Shown are four distinct LEGSs, two LEESs, and one QEES.

them by using the Signed Value Parameter, SVP,

$$\mathrm{SVP} = \left| \sum_{n=1}^{N} \Psi_n \left| \Psi_n \right| \right|, \tag{2.21}$$

where Ψ_n is the exciton centre-of-mass wavefunction. For a truly nodeless state, SVP $= 1$, but for LEGSs a cut-off of SVP ≥ 0.95 is usually chosen to account for nodes in the tail ends of the wavefunctions and numerical inaccuracies [83]. Fig. 2.5 shows all LEGSs on a disordered chain of 200 sites with open boundary conditions.

Whilst being a useful theoretical concept, LEGSs also have experimental use. In this thesis it will be argued that LEGSs are the irreducible parts of a polymer which support the absorption and emission of light and hence define chromophores within conjugated polymers [19, 40, 84].

Despite being few in number, due to their nodeless nature LEGSs account for about 50% of the overall absorption intensity from the electronic ground state to excited states calculated within the Frenkel model. Furthermore, when hot excitons can be neglected (*i.e.* at low temperatures), any higher-energy states will relax ultrafast into LEGSs and hence LEGSs are responsible for nearly the entirety of the emission in conjugated polymers and even dominate at higher temperatures.

Higher Energy Exciton States As mentioned above, the number of LEGSs is small compared to the total number of states and therefore all other states can be regarded as 'excited' exciton states. Taking the portions of the polymer that are spanned by LEGSs it is easy to imagine the polymer being cut into segments by the potential wells that localise the LEGSs. As such these boxes can support localised excited states that will be similar in nature to particle-in-a-box states. These states are known as localised excited exciton states (LEESs) [81,82] and two of these are also shown in Fig. 2.5. However, the potential wells localising the LEGSs are normally too shallow to also localise higher energy states and as such LEESs are comparatively few in number, *i.e.* not every LEGS is associated with a series of LEESs.

A more common variety of excited states are states that extend over the range of several LEGSs. While they are longer than LEGSs they are still shorter (in general) than the polymer and as such they are termed quasi-extended exciton states (QEESs).

Due to the low number of LEESs they are comparatively unimportant when considering the optical properties of polymers. Much more important are QEESs as they, due to their large number, typically carry about 50% of oscillator strength in absorption. Before de-exciting into the ground state under emission, QEESs relax into a LEGS which then decays radiatively. This conversion of QEESs into LEGSs is observed in ultrafast depolarisation

seen in polymer spectra [72, 85].

The re-introduction of exciton-nuclear interactions as well as the effects this coupling has on the excitonic wavefunctions will now be discussed.

2.2.2 Frenkel-Holstein Hamiltonian

The Holstein model was devised to couple charges to nuclear degrees of freedom in molecular assemblies [86, 87]. It is easily adapted to couple Frenkel excitons to local nuclear normal modes in conjugated polymers and the total Hamiltonian of the resulting Frenkel-Holstein model partitions into three contributions,

$$\hat{H}_{\mathrm{FH}} = \hat{H}_{\mathrm{e}} + \hat{H}_{\mathrm{n}} + \hat{H}_{\mathrm{en}}, \tag{2.22}$$

with $\hat{H}_{\mathrm{e}}$ being the pure excitonic, $\hat{H}_{\mathrm{n}}$ the pure nuclear, and $\hat{H}_{\mathrm{en}}$ the excitonic-nuclear interaction contribution. Within the Frenkel-Holstein model, $\hat{H}_{\mathrm{e}}$ is the Frenkel model described above. The nuclear part contains the kinetic and elastic energy contributions of the normal modes and can be written as,

$$\hat{H}_{\mathrm{n}} = \frac{M}{2}\sum_{n=1}^{N} P_n^2 + \frac{K}{2}\sum_{n=1}^{N} Q_n^2, \tag{2.23}$$

where P_n and Q_n are scalars proportional to the nuclear kinetic and potential energies, respectively, M is the reduced mass of the oscillator and K is the force constant of the bond(s) under consideration.

The last term in Eq. (2.22), the exciton-nuclei coupling term, couples the excitons to local normal modes of the moieties. It can be shown by simple considerations that the excitons couple most strongly to the benzoid-quinoid distortion in phenylene moieties and

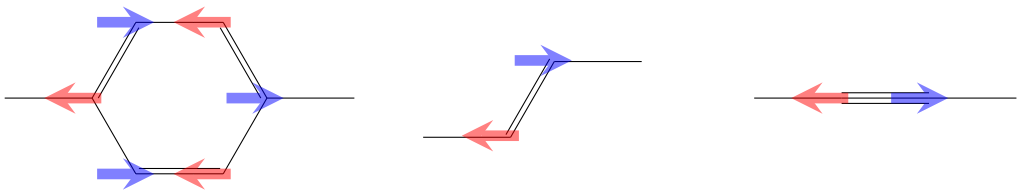


Figure 2.6.: Schematic representation of the dominant normal modes the exciton in phenylene, vinylene, and ethynylene based polymers couples to. All vibrations, the benzoid-quinoid distortion in phenylene and the stretch in vinylene and ethynylene, have a similar frequency of about 1800 cm^{-1} as confirmed by experiment and calculations.

.

to the symmetric stretch in vinylene and ethynylene units and this can also be confirmed by quantum chemical calculations. Fig. 2.6 shows the normal modes considered in this thesis and only coupling to these vibrations will be discussed subsequently.

All of these vibrations have a similar frequency of about 1800 cm^{-1} which gives an oscillator energy, $\hbar\omega$, of about 0.19 eV, a value used throughout this thesis to model real polymers. It is notable that $\hbar\omega \approx 0.2$ eV is applicable to most conjugated polymers and the dominant normal mode coupling to excitons therein.

The exciton-nuclear coupling is assumed to be linear in the oscillator displacement and the exciton density and takes the form,

$$\hat{H}_{\mathrm{en}} = -\sum_{n=1}^{N} \Gamma_n Q_n \hat{a}_n^\dagger \hat{a}_n, \tag{2.24}$$

where Γ quantifies the exciton-phonon coupling energy. The full Frenkel-Holstein model thus reads,

$$\hat{H}_{\mathrm{FH}} = \sum_{n=1}^{N} \varepsilon_n \hat{a}_n^\dagger \hat{a}_n + \sum_{n=1}^{N} J_n \left(\hat{a}_{n+1}^\dagger \hat{a}_n + \mathrm{h.c.} \right) + \frac{M}{2} \sum_{n=1}^{N} P_n^2 + \frac{K}{2} \sum_{n=1}^{N} Q_n^2 - \sum_{n=1}^{N} \Gamma_n Q_n \hat{a}_n^\dagger \hat{a}_n. \tag{2.25}$$

The nuclear contribution can be recast in dimensionless form by introducing,

$$\tilde{Q}_n = \left(\frac{M\omega}{\hbar}\right)^{\frac{1}{2}} Q_n; \quad \tilde{P}_n = \left(\frac{1}{M\hbar\omega}\right)^{\frac{1}{2}} P_n, \tag{2.26}$$

and the Hamiltonian then reads,

$$\hat{H}_{\mathrm{FH}} = \sum_{n=1}^{N} \varepsilon_n \hat{a}_n^\dagger \hat{a}_n + \sum_{n=1}^{N} J_n \left(\hat{a}_{n+1}^\dagger \hat{a}_n + \mathrm{h.c.}\right) + \frac{\hbar\omega}{2} \sum_{n=1}^{N} \left(\tilde{Q}_n^2 + \tilde{P}_n^2\right) - \hbar\omega \sum_{n=1}^{N} A_n \tilde{Q}_n \hat{a}_n^\dagger \hat{a}_n. \tag{2.27}$$

Here, A is the dimensionless exciton-nuclear coupling constant given as,

$$A_n = \frac{\Gamma_n}{\sqrt{M\hbar\omega^3}}, \tag{2.28}$$

is related to the monomeric Huang-Rhys parameter as,

$$A_n^2 = 2g_1^2(n),$$

and can be parametrised against observables like spectra or against quantum-chemical calculations as shown by Lavrentiev and Barford [88]. This method was first used to estimate the phonon-coupling constant in PPP and we will recap the method before adapting it to the model presented here.

2.2.2.1 Exciton-Phonon Coupling Constant

Starting from the Pariser-Parr-Pople Hamiltonian (Eq. (2.1)) the particle-phonon interaction can be incorporated into the model by considering the modulation of the transfer integral, t_{ij}, and the electron repulsion, V_{ij}, by the change in the bond length between atoms i and j. The dependency of t_{ij} will be considered here especially. We can set the

transfer integral up as,

$$t_{ij} = t_{\mathrm{P}} \left(1 - \delta \Delta r_{ij}\right) = t_{\mathrm{P}} - \gamma \Delta r_{ij}, \tag{2.29}$$

where t_{P} is the transfer integral between neighbouring sites in an undistorted phenylene unit, $\Delta r_{ij} = r_{ij} - r_{\mathrm{P}}$ is the deviation from the equilibrium bond length and δ is a scaling parameter. The derivative of the transfer integral with respect to the interatomic distance is then simply $\gamma = t_{\mathrm{P}}\delta$, which for phenylene units has been estimated to be $\gamma = 2.900$ eV/Å. As only excitons within the Frenkel-Holstein model are considered and the phenylene and vinylene units are approximated as sites in every model, the dependency of $\tilde{V}_{ij}$ on the normal modes can be neglected and thus the leading correction to the PPP Hamiltonian is,

$$\hat{H}_{\mathrm{en}} = \gamma \sum_{\langle ij \rangle \sigma} \Delta r_{ij} \left[\hat{c}^{\dagger}_{i\sigma} c_{j\sigma} + \mathrm{h.c.}\right], \tag{2.30}$$

where the sum runs over neighbouring sites i, j and $\hat{c}^{\dagger}_{i\sigma}$ ($\hat{c}_{i\sigma}$) creates (destroys) an electron of spin σ on site i. The spin index will now be dropped and only excitons will be considered from now on. If only one vibrational mode is considered, the atomic displacements can be related to the vibrational coordinate Q as $x_i = a^j_i Q_j$, where $\boldsymbol{a}^j$ is the eigenvector of the jth vibrational normal mode. Introducing phonon operators (see Sec. 2.2.2.2 for more detail), this can be rewritten as,

$$Q = \left(\frac{\hbar}{2M\omega}\right)^{\frac{1}{2}} \left(\hat{b} + \hat{b}^{\dagger}\right). \tag{2.31}$$

Eq. (2.30) can now be transformed into local (monomer) molecular HOMO/LUMO orbital basis and the bond length distance can be related to the phonon operators. This then

leads to,

$$\hat{H}_{\text{en}} = \sum_{n\alpha} \Gamma^{(1)}_{n\alpha} \left(\hat{n}^{\text{H}}_n - \hat{n}^{\text{L}}_n - 2 \right) Q_\alpha + \sum_{n\alpha} \Gamma^{(2)}_{n\alpha} \left(\hat{a}^{\text{H}\dagger}_{n\sigma} \hat{a}^{\text{H}}_{n+1,\sigma} - \hat{a}^{\text{L}\dagger}_{n\sigma} \hat{a}^{\text{L}}_{n+1,\sigma} + \text{h.c.} \right) Q_\alpha, \tag{2.32}$$

where $\hat{a}^{\text{H(L)}\dagger}_{n\sigma}$ ($\hat{a}^{\text{H(L)}}_{n\sigma}$) creates an electron of spin σ in the HOMO(LUMO) on monomer n and $\hat{n}^{\text{H(L)}}_n = \sum_\sigma \hat{a}^{\text{H(L)}\dagger}_{n\sigma} \hat{a}^{\text{H(L)}}_{n\sigma}$. For our model this then adapts to,

$$\hat{H}_{\text{en}} = -2 \sum_{n\alpha} \Gamma^{(1)}_{n\alpha} \hat{a}^\dagger_n \hat{a}_n Q_\alpha + \sum_{n\alpha} \Gamma^{(2)}_{n\alpha} \left(\hat{a}^{\text{H}\dagger}_{n+1,\sigma} \hat{a}^{\text{H}}_{n\sigma} - \hat{a}^{\text{L}\dagger}_{n+1,\sigma} \hat{a}^{\text{L}}_{n\sigma} + \text{h.c.} \right) Q_\alpha. \tag{2.33}$$

This then shows that $\Gamma^{(1)}_{n\alpha}$ is the (dimensionful) exciton-phonon coupling parameter in the Frenkel-Holstein model on site n and for normal mode α and $\Gamma^{(2)}_{n\alpha}$ quantifies the change in the transfer integral with the normal mode. Only $\Gamma^{(1)}$ will be considered here explicitly, which is related to the exciton-phonon coupling used above as $\Gamma_{n\alpha} = 2\Gamma^{(1)}_{n\alpha} N^{1/2}$, where N is the total number of equivalent moieties in the system over which the normal mode is delocalised and in order to correct for a factor of $N^{1/2}$ has to be introduced. $\Gamma^{(1)}_{n\alpha}$ is then in turn relates to the dimensionless exciton-phonon coupling parameter as,

$$A_{n\alpha} = \frac{\Gamma_{n\alpha}}{\sqrt{\mu\hbar\omega^3}} = \frac{2\Gamma^{(1)}_{n\alpha} N^{\frac{1}{2}}}{\sqrt{\mu\hbar\omega}}. \tag{2.34}$$

For the two normal modes considered in this thesis, the benzoid-quinoid distortion for phenylene and the symmetric stretch for vinylene and ethynylene, $\Gamma^{(1)}_n$ is then given by,

$$\Gamma^{(1)}_{\text{P}} = \gamma \left(\frac{1}{3} \left(-a^z_1 + a^z_2 - a^z_3 + a^z_4 - a^z_5 + a^z_6 \right) + \frac{\sqrt{3}}{6} \left(a^y_2 + a^y_3 - a^y_5 - a^y_6 \right) \right), \tag{2.35}$$

for vinylene,

$$\Gamma^{(1)}_{\text{V}} = \gamma \left[-a^z_1 + a^z_2 + \sqrt{3}(a^y_1 - a^y_2) \right], \tag{2.36}$$

and for ethynylene,

$$\Gamma_{\mathrm{E}}^{(1)} = \gamma \left[-a_1^z + a_2^z\right]. \tag{2.37}$$

The HOMO/LUMO wavefunctions shown in Fig. 2.3 have been used to derive these expressions and the molecular axis has been taken to be aligned with z and the yz-plane is the plane containing the phenylene ring and vinylene bond, respectively. The numbering of the sites within the phenylene unit is given in the same figure. The results of the parametrisations are presented in Appendix C and used in Chapter 6, predominantly.

2.2.2.2 Born-Oppenheimer Regime

Returning to the Frenkel-Holstein model and invoking the Born-Oppenheimer approximation, which corresponds to $\tilde{P}_n = 0$, the Hamiltonian simplifies accordingly. This model shall be referred to as semi-classical Frenkel-Holstein model due to the classical treatment of the normal modes and is given as,

$$\hat{H}_{\mathrm{FH}}^{\mathrm{BO}} = \sum_{n=1}^{N} \varepsilon_n \hat{a}_N^\dagger \hat{a}_n + \sum_{n=1}^{N} J_n \left(\hat{a}_{n+1}^\dagger \hat{a}_n + \mathrm{h.c.}\right) + \frac{\hbar\omega}{2} \sum_{n=1}^{N} \tilde{Q}_n^2 - \hbar\omega \sum_{n=1}^{N} A_n \tilde{Q}_n \hat{a}_n^\dagger \hat{a}_n. \tag{2.38}$$

It is possible to quantize the normal modes as phonons and the resulting model is a fully quantized Frenkel-Holstein model,

$$\hat{H}_{\mathrm{QFH}} = \sum_{n=1}^{N} \varepsilon_n \hat{a}_n^\dagger \hat{a}_n + \sum_{n=1}^{N} J_n \left(\hat{a}_{n+1}^\dagger \hat{a}_n + \mathrm{h.c.}\right) + \hbar\omega \sum_{n=1}^{N} \hat{b}_n^\dagger \hat{b}_n - \hbar\omega \sum_{n=1}^{N} g_1(n) \left(\hat{b}_n^\dagger + \hat{b}_n\right) \hat{a}_n^\dagger \hat{a}_n, \tag{2.39}$$

where $\hat{b}_n^\dagger$ ($\hat{b}_n$) creates (destroys) a phonon on site n and the operator is defined as,

$$\hat{b}_n^\dagger = \frac{1}{\sqrt{2}} \left(\tilde{Q}_n - \mathrm{i}\tilde{P}_n\right). \tag{2.40}$$

This also shows that, while A_n is the natural choice for the exciton-phonon coupling constant in for classical normal modes, $g_1(n)$ is the natural choice for a quantised basis.

The model is readily made more accurate by including quadratic terms in the oscillator displacement, accounting for a change of normal mode frequency in the presence of the exciton [89]. These contributions are, however, neglected as they are expected to be negligible. Moreover the model in its current form is computationally less expansive.

The model presented here couples the excitonic states to a ladder of phonon states at each site and as such, even for a small number of phonons considered, the Hilbert space of the entire system grows rapidly. For N sites, each associated with $N_{\text{phon}} + 1$ vibrational levels (to account for the vibrational ground state) the Hilbert space has, in an untruncated form, a dimensionality of $(N_{\text{phon}} + 1)^N$, which even for chains with 10 moieties and only 3 phonons per sites is in the excess of 1 000 000 eigenstates. The states themselves can be represented as a linear combination of basis states consisting of the the direct product of the excitonic wavefunction in a site representation, $|n\rangle$, and a series of vibrational states of υ phonons on site m, $\prod_m |\upsilon\rangle\rangle_m$. Thus, a general basis state of the Frenkel-Holstein model will take the form,

$$|\chi\rangle = |n\rangle \otimes \prod_m |\upsilon\rangle\rangle_m \,. \tag{2.41}$$

Due to the size of the resulting Hilbert space in order to be able to model realistic systems ($N \geq 20; N_{\text{phon}} \geq 5; N_{\text{States}} \approx 3.7 \times 10^{17}$) an approximate method has to be used to solve the model. In this thesis, the Density Matrix Renormalisation Group (DMRG) technique will be used, which is fully introduced in Section 3.1. The method truncates the Hilbert space to states that are important to calculate ground state properties and has been shown to be highly accurate for one-dimensional systems, such as conjugated

polymers, while also reducing the computational cost significantly. A size reduction of the Hilbert space in the excess of several orders of magnitude is readily achieved, making it possible to calculate the properties of larger and more realistic systems as described below.

2.2.2.3 Momentum-Space Representation

For certain applications it is convenient to recast Eq. (2.39) in a momentum-space representation, which has a few advantages, especially when considering non-linear polymers, and will be used in the discussion of these systems (Chapter 5).

For this, periodic (PCB) and open (OBC) boundary conditions have to be distinguished as the transformation made is different. While under PBC the transformation is via the standard Bloch functions and eigenstates of the particle-on-a-ring, for OBC the transformation is done by considering the particle-in-a-box eigenstates. Both cases are now described.

Periodic Boundary Conditions Under periodic boundary conditions, which are especially applicable to macrocycles (see Chapter 5) the eigenstates of the system satisfy Bloch's theorem, *i.e.*

$$\hat{T}_p \left|\Psi_\kappa\right\rangle = \mathrm{e}^{\pm \mathrm{i}\kappa p} \left|\Psi_\kappa\right\rangle , \tag{2.42}$$

where κ denotes the total momentum of the eigenstate and $\hat{T}_p$ is a translation operator denoting a displacement by p sites. A one-vibration state can be written as $|n; n+m\rangle = \hat{a}_n^\dagger \hat{b}_{n+m}^\dagger |0\rangle$, where n is the site of the exciton and m is the distance between exciton and

vibration and a general state of the system with one vibration is then given by,

$$|\Psi_\kappa(m)\rangle = \frac{1}{\sqrt{N}} \sum_{n=1}^{N} |n; n+m\rangle \, \mathrm{e}^{\mp \mathrm{i}\kappa n}, \tag{2.43}$$

with the action of the translation operator as described above,

$$\begin{aligned} \hat{T}_p \, |\Psi_\kappa(m)\rangle &= \frac{1}{\sqrt{N}} \sum_{n=1}^{n} |n+p; n+p+m\rangle \, \mathrm{e}^{\mp \mathrm{i}\kappa n} \\ &= \frac{1}{\sqrt{N}} \sum_{n'=1}^{N} |n'; n'+m\rangle \, \mathrm{e}^{\mp \mathrm{i}\kappa (n'-p)} = \mathrm{e}^{\pm \mathrm{i}\kappa p} \, |\Psi_\kappa(m)\rangle \, . \end{aligned} \tag{2.44}$$

Using now the electronic part of Eq. (2.39) (*i.e.* Eq. (2.14)) and using uniform parameters to represent a translationally invariant system (*i.e.* $\varepsilon_n = \varepsilon_0, J_n = J_0 \forall n$), it is found that,

$$\begin{aligned} \hat{H}_\mathrm{e} \, |\Psi_\kappa(m)\rangle &= \frac{\varepsilon_0}{\sqrt{N}} \sum_{n=1}^{N} |n; n+m\rangle \, \mathrm{e}^{\mp \mathrm{i}\kappa n} + \frac{J_0}{\sqrt{N}} \sum_{n=1}^{N} \left[|n+1; n+m\rangle + |n-1; n+m\rangle \right] \mathrm{e}^{\mp \mathrm{i}\kappa n} \\ &= \varepsilon_0 \, |\Psi_\kappa(m)\rangle + \frac{J_0}{\sqrt{N}} \sum_{n'} \left[|n', n'+m-1\rangle \, \mathrm{e}^{\mp \mathrm{i}\kappa (n'-1)} + |n', n'+m+1\rangle \, \mathrm{e}^{\mp \mathrm{i}\kappa (n'+1)} \right] \\ &= \varepsilon_0 \, |\Psi_\kappa(m)\rangle + J_0 \left[\mathrm{e}^{\pm \mathrm{i}\kappa} \, |\Psi_\kappa(m-1)\rangle + \mathrm{e}^{\mp \mathrm{i}\kappa} \, |\Psi_\kappa(m+1)\rangle \right] . \end{aligned} \tag{2.45}$$

The Hamiltonian has the standard Bloch solutions as eigenstates, i.e.,

$$\begin{aligned} |\Psi_{\kappa,q}\rangle &= \frac{1}{\sqrt{N}} \sum_{m=0}^{N} |\Psi_\kappa(m)\rangle \, \mathrm{e}^{\mathrm{i}qm} \\ &= \frac{1}{N} \sum_{n=1}^{N} \sum_{m=0}^{N} |n; n+m\rangle \, \mathrm{e}^{\mp \mathrm{i}\kappa n} \mathrm{e}^{\pm \mathrm{i}qm}, \end{aligned} \tag{2.46}$$

with the eigenvalues,

$$\hat{H}_{\mathrm{e}} \left|\Psi_{\kappa,q}\right\rangle = \left(\varepsilon_0 + 2J\cos(\kappa - q)\right)\left|\Psi_{\kappa,q}\right\rangle = \left(\varepsilon_0 + 2J\cos(k)\right)\left|\Psi_{\kappa,q}\right\rangle . \tag{2.47}$$

q is the momentum of the phonon and it follows that $k = \kappa - q$ is the momentum of the exciton. As such, the excitonic energy does only depend on the exciton momentum, as expected. In fact, it can be easily shown that the excitonic energy remains the same regardless of the number of phonons in the system. Eq. 2.47 thus allows us to re-write the excitonic Hamiltonian in momentum space using the excitonic momentum, k, as,

$$\hat{H}_{\mathrm{e}} = \sum_k \left(\varepsilon_0 + 2J\cos k\right)\tilde{a}_k^\dagger \tilde{a}_k, \tag{2.48}$$

where $\tilde{a}_k^\dagger$ ($\tilde{a}_k$) creates (destroys) an exciton with momentum k in the system. The destruction operator $\hat{a}_n$ can then be written as a Bloch transform,

$$\hat{a}_n = \frac{1}{\sqrt{N}} \sum_k \tilde{a}_k \mathrm{e}^{\mathrm{i}kn}, \tag{2.49}$$

and similarly for the creation operator. Using this form then gives for the phonon destruction operator,

$$\hat{b}_n = \frac{1}{\sqrt{N}} \sum_q \tilde{b}_q \mathrm{e}^{\mathrm{i}qn}, \tag{2.50}$$

and this allows for the rewriting of the phonon part of Eq. (2.39) as,

$$\hat{H}_{\mathrm{p}} = \frac{\hbar\omega}{N} \sum_n \sum_{qq'} \tilde{b}_q^\dagger \tilde{b}_{q'} \mathrm{e}^{-\mathrm{i}qn} \mathrm{e}^{\mathrm{i}q'n} = \frac{\hbar\omega}{N} \sum_n \sum_{qq'} \tilde{b}_q^\dagger \tilde{b}_{q'} \mathrm{e}^{\mathrm{i}(q'-q)n} = \frac{\hbar\omega}{N} \sum_n \sum_q \tilde{b}_q^\dagger \tilde{b}_q = \hbar\omega \sum_q \tilde{b}_q^\dagger \tilde{b}_q. \tag{2.51}$$

This leaves the exciton-phonon term to be recast. Using Eqs. (2.49) and (2.50) it

follows that,

$$\begin{aligned}\hat{H}_{\mathrm{ep}} &= -g_1\hbar\omega\sum_{n=1}^{N}\hat{a}_n^\dagger\hat{a}_n\left(\hat{b}_n+\hat{b}_n^\dagger\right)\\ &= -\frac{g_1\hbar\omega}{N\sqrt{N}}\sum_{n=1}^{N}\sum_{kk'q}\tilde{a}_k^\dagger\tilde{a}_{k'}\mathrm{e}^{-\mathrm{i}(k-k')n}\left(\tilde{b}_q\mathrm{e}^{\mathrm{i}qn}+\tilde{b}_q^\dagger\mathrm{e}^{-\mathrm{i}qn}\right)\\ &= -\frac{g_1\hbar\omega}{\sqrt{N}}\sum_{kq}\left(\tilde{a}_k^\dagger\tilde{a}_{k-q}\hat{b}_q+\tilde{a}_k^\dagger\tilde{a}_{k+q}\tilde{b}_q^\dagger\right).\end{aligned} \tag{2.52}$$

This expression can be rewritten by considering the $q=0$ case explicitly, i.e.,

$$\begin{aligned}\hat{H}_{\mathrm{ep}} &= -\frac{g_1\hbar\omega}{\sqrt{N}}\left(\sum_k\tilde{a}_k^\dagger\tilde{a}_k\right)\left(\tilde{b}_0+\tilde{b}_0^\dagger\right)-\frac{g_1\hbar\omega}{\sqrt{N}}\sum_{k,q\neq0}\left(\tilde{a}_k^\dagger\tilde{a}_{k-q}\tilde{b}_q+\tilde{a}_k^\dagger\tilde{a}_{k+q}\tilde{b}_q^\dagger\right)\\ &= -\frac{g_1\hbar\omega}{\sqrt{N}}\left(\tilde{b}_0+\tilde{b}_0^\dagger\right)-\frac{g_1\hbar\omega}{\sqrt{N}}\sum_{k,q\neq0}\left(\tilde{a}_k^\dagger\tilde{a}_{k-q}\tilde{b}_q+\tilde{a}_k^\dagger\tilde{a}_{k+q}\tilde{b}_q^\dagger\right),\end{aligned} \tag{2.53}$$

where $\sum_k\tilde{a}_k^\dagger\tilde{a}_k=1$ (only one exciton in the system) was used. This shows that the $q=0$ mode decouples explicitly from the excitons in periodic systems.

The total Hamiltonian in momentum-space representation for periodic boundary conditions and translationally invariant systems then reads,

$$\begin{aligned}\hat{H}_{\mathrm{QFH}}^{\mathrm{PBC}} = &\sum_k\left(\varepsilon_0+2J\cos k\right)\tilde{a}_k^\dagger\tilde{a}_k+\hbar\omega\sum_q\tilde{b}_q^\dagger\tilde{b}_q-\frac{g_1\hbar\omega}{\sqrt{N}}\left(\tilde{b}_0+\tilde{b}_0^\dagger\right)\\ &-\frac{g_1\hbar\omega}{\sqrt{N}}\sum_{k,q\neq0}\left(\tilde{a}_k^\dagger\tilde{a}_{k-q}\tilde{b}_q+\tilde{a}_k^\dagger\tilde{a}_{k+q}\tilde{b}_q^\dagger\right).\end{aligned} \tag{2.54}$$

This process can be repeated using the classical treatment of the normal modes. The Hamiltonian then reads,

$$\hat{H}_{\mathrm{FH}}^{\mathrm{PBC}}=\sum_k\left(\varepsilon_0+2J\cos k\right)\tilde{a}_k^\dagger\tilde{a}_k+\frac{\hbar\omega}{2}\sum_q\left|\tilde{Q}_q\right|^2-\frac{A\hbar\omega\tilde{Q}_0}{\sqrt{N}}-\frac{A\hbar\omega}{\sqrt{N}}\sum_{k,q\neq0}\tilde{a}_k^\dagger\tilde{a}_{k-q}\tilde{Q}_q. \tag{2.55}$$

Open Boundary Conditions For non-cyclic systems open boundary conditions are more realistic and the process described above can be repeated for these conditions. Taking Eq. (2.49) and (2.50) and rewriting these with the solutions of the particle-in-a-box rather than the solutions of the particle-on-a-ring gives,

$$\hat{a}_n = \sqrt{\frac{2}{N+1}} \sum_{k=1}^{N} \sin(nk)\, \tilde{a}_k; \quad k = \frac{\pi \bar{k}}{N+1}, \tag{2.56}$$

$$\hat{b}_n = \sqrt{\frac{2}{N+1}} \sum_{q=1}^{N} \sin(nq)\, \tilde{b}_q; \quad q = \frac{\pi \bar{q}}{N+1}. \tag{2.57}$$

Using these transformations the pure excitonic and nuclear parts of Eq. (2.39) are rewritten easily as,

$$\hat{H}_{\mathrm{e}} = \sum_{k=1}^{N} \left(\varepsilon_0 + 2J\cos(k)\right) \tilde{a}_k^{\dagger} \tilde{a}_k, \tag{2.58}$$

$$\hat{H}_{\mathrm{n}} = \hbar\omega \sum_{q=1}^{N} \tilde{b}_q^{\dagger} \tilde{b}_q. \tag{2.59}$$

The exciton-phonon coupling term can be rewritten as,

$$\hat{H}_{\text{e-p}} = -g_1 \hbar\omega \left(\frac{2}{N+1}\right)^{\frac{3}{2}} \sum_{n} \sum_{k,k',q=1}^{N} \underbrace{\sin(nk)\sin(nk')\sin(nq)}_{=\bar{X}(k,k',q)} \tilde{a}_k^{\dagger} \tilde{a}_{k'} \left(\tilde{b}_q^{\dagger} + \tilde{b}_q\right). \tag{2.60}$$

The term $\bar{X}(k,k',q)$ can be rewritten using the trigonometric identity

$$\sin\alpha \sin\beta = \frac{1}{2}\left(\cos(\alpha-\beta) - \cos(\alpha+\beta)\right), \tag{2.61}$$

in three different ways, all of which have to be equal. We can thus write,

$$\begin{aligned}\bar{X}(k,k',q) = \frac{1}{6}\{&[\mathrm{c}(k-k') - \mathrm{c}(k+k')]\,\mathrm{s}(q) + [\mathrm{c}(k-q) - \mathrm{c}(k+q)]\,\mathrm{s}(k') \\ &+ [\mathrm{c}(k'-q) - \mathrm{c}(k'+q)]\,\mathrm{s}(k)\}\,,\end{aligned} \tag{2.62}$$

where $\mathrm{c}(x) = \cos(nx)$ and $\mathrm{s}(x) = \sin(nx)$ are shorthands. This can again be rewritten using,

$$\cos\alpha \sin\beta = \frac{1}{2}\left[\sin(\alpha+\beta) - \sin(\alpha-\beta)\right], \tag{2.63}$$

and then,

$$\begin{aligned}\bar{X}(k,k',q) = \frac{1}{12}\{&\mathrm{s}(k-k'+q) - \mathrm{s}(k-k'-q) - \mathrm{s}(k+k'+q) + \mathrm{s}(k+k'-q) \\ &+ \mathrm{s}(k+k'-q) - \mathrm{s}(k-k'-q) - \mathrm{s}(k+k'+q) + \mathrm{s}(k-k'+q) \\ &+ \mathrm{s}(k+k'-q) - \mathrm{s}(-k+k'-q) - \mathrm{s}(k+k'+q) + \mathrm{s}(-k+k'+q)\} \\ = \frac{1}{4}\{&\mathrm{s}(k-k'+q) + \mathrm{s}(-k+k'+q) - \mathrm{s}(k+k'+q) + \mathrm{s}(k+k'-q)\}\,.\end{aligned} \tag{2.64}$$

This expression can now be summed over all sites n and using Lagrange's trigonometric summation formulae [90,91] this results in,

$$\begin{aligned}X(k,k',q) \equiv \sum_n \bar{X}(k,k',q) = \frac{1}{4}\Bigg\{&\cot\left(\frac{k-k'+q}{2}\right) + \cot\left(\frac{-k+k'+q}{2}\right) \\ &+ \cot\left(\frac{k+k'-q}{2}\right) - \cot\left(\frac{k+k'+q}{2}\right)\Bigg\}\,.\end{aligned} \tag{2.65}$$

For a general expression, $\cot\left(\frac{\pi(\alpha+\beta+\gamma)}{2(N+1)}\right)$, it follows that $\alpha+\beta+\gamma$ has to be odd due to the pole structure of the cotangent. Hence, if $\bar{k}+\bar{k}'$ is odd $\bar{q}$ has to be even and vice-versa.

With this result we can write the total Hamiltonian for an ordered system under open

boundary conditions in the momentum-space representation as,

$$\begin{aligned}\hat{H}_{\mathrm{QFH}}^{\mathrm{OBC}} = &\sum_{k=1}^{N}\left[\varepsilon_0 + 2J\cos(k)\,\tilde{a}_k^\dagger\tilde{a}_k\right] + \hbar\omega\sum_{q=1}^{N}\tilde{b}_q^\dagger\tilde{b}_q \\ &- g_1\hbar\omega\left(\frac{2}{N+1}\right)^{\frac{3}{2}}{\sum_{k,k',q=1}^{N}}' X(k,k',q)\tilde{a}_k^\dagger\tilde{a}_{k'}\left(\tilde{b}_q^\dagger + \tilde{b}_q\right),\end{aligned} \tag{2.66}$$

where the primed sum indicates the restrictions on the values of k, k', q mentioned above.

Once again, the model can also be written treating the normal modes classically. The Hamiltonian then reads,

$$\begin{aligned}\hat{H}_{\mathrm{FH}}^{\mathrm{OBC}} = &\sum_{k=1}^{N}\left[\varepsilon_0 + 2J\cos(k)\,\tilde{a}_k^\dagger\tilde{a}_k\right] + \frac{\hbar\omega}{2}\sum_{q=1}^{N}\left|\tilde{Q}_q\right|^2 \\ &- A\hbar\omega\left(\frac{2}{N+1}\right)^{\frac{3}{2}}{\sum_{k,k',q=1}^{N}}' X(k,k',q)\tilde{a}_k^\dagger\tilde{a}_{k'}\tilde{Q}_q.\end{aligned} \tag{2.67}$$

Having described the Frenkel-Holstein model the corresponding eigenstates will now be reviewed.

2.2.2.4 Polaron States

Due to the exciton-phonon coupling introduced explicitly above, the eigenstates of the Frenkel-Holstein model will be direct products of distorted excitonic states (distorted eigenstates of the Frenkel model) and phonon states, which will be taken as the eigenstates of the harmonic oscillator. The nuclei of the polymer will adapt to the change in electronic structure and as the exciton moves along the chain, so will the phonons associated with the nuclear distortion. This effect was first observed for charges in lattices and the resulting quasiparticles, consisting of the charge and the lattice distortion, were called polarons [92, 93]. The nomenclature will be adapted here for (uncharged) excitons surrounded by

a cloud of phonons. As the excitons are delocalised over the entire polymer or segments of it, so will be the nuclear distortion associated with it and these two processes which lead to localisation of polarons will now be described.

Landau Polarons Due to the coupling of the excitons to the phonons, the resulting polaron will have a larger effective mass than the exciton or phonons alone [94]. This process, of the exciton acquiring a cloud of phonons, is referred to as self-trapping, as it can be thought of as a deepening of the potential around the exciton due to the nuclear distortion [95, 96]. This is a distinct process from self-localisation, which, in an ordered system, will subsequently occur if the potential well due to the self-trapping is deep enough to localise the exciton to smaller region than the entire system. This process was first observed by Landau in his investigation of thermo-radiative effects in solids. Polarons primarily localised by their self-trapping are thus referred to as Landau polarons [94]. Landau polarons are solutions to the Frenkel-Holstein model in the continuum limit [86,97] and the associated wavefunctions are given as,

$$\Psi_n = \left(\frac{\lambda}{2}\right)^{\frac{1}{2}} \operatorname{sech} \lambda(n - n_0), \tag{2.68}$$

with

$$\lambda = \frac{g^2 \hbar\omega}{2J_0}, \tag{2.69}$$

where J_0 is the exciton hopping term for an ordered system. Ψ_n describes a polaron self-localised on site n_0 and the spatial extent can be quantified by,

$$l_c = 2\lambda^{-1} = \frac{4J_0}{g^2 \hbar\omega}, \tag{2.70}$$

where it is assumed that $\lambda < 1$. This implies that for any $g > 0$ the ground state of the Frenkel-Holstein model within the Born-Oppenheimer approximation is a polaron of spread l_{c} [43].

Anderson Polarons Anderson localisation is a well-known phenomenon in one-dimensional lattices subject to random disorder. First introduced in 1958 [6], it has been shown to be universally true for lattices in one and two dimensions. Substantial progress has been made since that discovery [98] of which only the essential key features regarding the work in this thesis will be reviewed here. According to single-parameter scaling theory the localisation length of a free particle (*i.e.* uncoupled particle, g=0) close to the band edge on a one-dimensional lattice subject to random Gaussian disorder with standard deviation σ scales as,

$$l_0 \simeq \left(\frac{J_0}{\sigma}\right)^{2/3}. \tag{2.71}$$

The localisation length when phonon coupling is present will differ from this free length scale by a factor determined by the ratio of the free particle bandwidth and the modulated bandwidth due to the coupling. The effective mass, m^*, of a particle at the bottom of a parabolic band is proportional to the inverse band width and hence the localisation length of a polaron by Anderson localisation can be defined as,

$$l_{\mathrm{s}} = \left(\frac{m_0}{m^*}\right)^{2/3} l_0, \tag{2.72}$$

where m_0 is the mass of the free particle such that $l_s(m^* = m_0) = l_0$. Weak-coupling perturbation theory allows the calculation of the effective mass depending on the coupling

and the energy of the phonons as [99],

$$\frac{m^*}{m_0} = 1 + \frac{g_1^2}{8}\sqrt{\frac{\hbar\omega}{J_0}} = 1 + \frac{g_1^2\bar{\omega}^{1/2}}{8}, \tag{2.73}$$

for $\hbar\omega/J_0 \ll 1$ and $\lambda \ll 1$ and hence,

$$l_\mathrm{s} = \left(\frac{8}{8 + g_1^2\bar{\omega}^{1/2}}\right)^{2/3} l_0. \tag{2.74}$$

It now depends on the values of l_s, l_c, and l_0 which localisation mechanism is the dominant one given the system parameters.

Polaron Localisation The process of self-localisation competes with localisation by disorder as described above. It has been shown in recent work, that Anderson localisation is always present as soon as disorder is introduced into polymer systems and that, moreover, Anderson localisation is the primary source of localisation in these systems. In fact, Landau polarons only form in a very narrow parameter regime [100,101]. The authors have identified three regimes within the disorder/phonon energy parameter space that describe the localisation of the polaron. The regime for which the Landau polaron description is most appropriate is very narrow and does normally not fall within the parameter regime appropriate for conjugated polymers. Thus, in the system under consideration in this thesis the Anderson localisation description is most appropriate.

This has direct computational consequences. If self-localisation is an important localisation process, the exciton wavefunction in the presence of a non-zero number of phonons, Ψ_n^v, will be very different from the excitonic wavefunction which is not coupled to any phonons , Ψ_n^0. However, due to the fact that in parameter regimes applicable to polymers Anderson localisation is much more important, the true excitonic wavefunctions, are very

similar to these undistorted states, especially (but not limited to) one-phonon excitonic states, Ψ_n^1, *i.e.*

$$\Psi_n^1 \approx \Psi_n^0 \approx \Psi_n^{\text{vert}}, \tag{2.75}$$

where Ψ_n^{vert} is the exciton wavefunction associated with vertical excitation (*i.e.* without nuclear relaxation). This means that, for most polymeric systems, the (true) Frenkel-Holstein excitonic wavefunction can be approximated by the Frenkel excitonic wavefunction without too much loss in accuracy. Moreover, for long chains the approximation will become more valid, as the average distortion of the nuclei decreases with chain length [84]. When calculating the optical properties of polymers this will be made use of as it allows the efficient calculation of longer chains without large sacrifices in accuracy.

3

Computational Methods

Having introduced the models used in this thesis in the previous chapter, this chapter is concerned with the computational methods employed to solve our models. While the semi-classical Frenkel-Holstein model (Eq. (2.25)) is easy to solve by full diagonalization due to the small Hilbert space, which scales as N^2, where N is the number of sites in the polymer, the fully quantized Frenkel-Holstein model (Eq. (2.39)), due to its large Hilbert space scaling as $(N_{\text{phon}}+1)^N$, is not solvable by full diagonalization for large systems in a reasonable time. Approximations have to be made either in the model or in the way the model is solved. The latter approach is adopted here and the Density Matrix Renormalisation Group (DMRG) algorithm, which has been shown to work particularly well for one-dimensional systems such as the polymers in this thesis, will be used here.

This chapter will first introduce the DMRG technique and its adaptation to our models. How DMRG approximates the exact solution and how these are computed will be discussed. Following this, the conjugate gradient routine used to (i) find the states within the DMRG routine and (ii) optimise modelling parameters to fit experimental observations will be introduced.

3.1 Density Matrix Renormalisation Group

The Density Matrix Renormalisation Group (DMRG) was developed by White and Noack [102] as an approximate method to solve models that the Numerical Renormalisation Group [103–105] could not solve due to the node structure of the solutions of these models [106–110]. In recent years the mathematical background of DMRG has been extended and

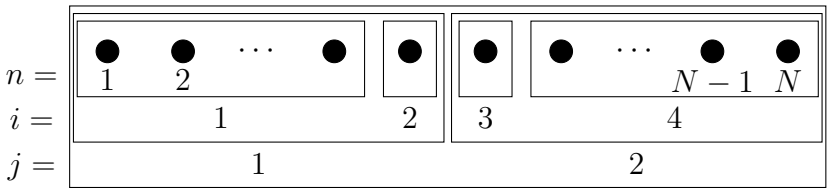


Figure 3.1.: Schematic representation of the blocking used in the DMRG routine of a system with N sites under open boundary conditions. n labels the sites, i the primitive blocks, and j the augmented blocks. The overall system of N sites is called superblock. For periodic boundary conditions the primitive blocks 3 and 4 are exchanged.

the connection to Matrix Product States [111–114] and, more generally, Tensor Network States [115–117], has been established. A comprehensive review of the DMRG method and its connection to Matrix Product States was provided by Órus and Schollwöck [118–120]. The key features of DMRG will be reviewed in the following section placing particular emphasis on the aspects relevant to the models in this thesis.

3.1.1 DMRG algorithm

Central to the DMRG routine is the sectioning of the system into two blocks which themselves are split into two. The entire system itself is divided into a 'system' and an 'environment' block [121], which are referred to as augmented blocks. For the purposes of this thesis the system of interest is comprised of both a 'system' ($j = 1$) and 'environment' ($j = 2$) block, as shown in Fig. 3.1, the so called superblock. The augmented blocks are divided into smaller (primitive) blocks, one of which only contains a single site ($i = 2, 3$) and the other block containing the rest of the sites in the respective augmented block ($i = 1, 4$).

The routine itself can be decomposed into three steps: first the superblock basis states are found by augmenting the primitive blocks after which the Hamiltonian in this basis is diagonalised to find the superblock eigenstates. In our case the target states are low in

energy in their respective symmetry (see below) and thus diagonalisation routines can be used that find the low-energy states. Once the states are found the reduced density matrix is constructed which allows for the rotation and truncation of the operators retaining the optimal basis for the target states in the augmented block basis while significantly reducing the size of the Hilbert space.

3.1.1.1 Basis States and Hamiltonian Decomposition

Each primitive block, i, in our systems can be classified by two quantum numbers: k, specifying the 'doping' of the block, *i.e.* if and what particle resides on the block, and n, a running index of the state associated with k. The basis states then take the form $\left\{|k_i, n_i\rangle^{(i)}\right\}$.

Each state of the augmented blocks can be constructed from these basis states by direct multiplication. Using the same quantum numbers,

$$|k_{\mathrm{L}}, n_{\mathrm{L}}\rangle\rangle^{(\mathrm{L})} = |k_1, n_1\rangle^{(1)} \otimes |k_2, n_2\rangle^{(2)}\,, \tag{3.1}$$

where the double-ket denotes augmented block states. This is a basis state for the left augmented block, whereas,

$$|k_{\mathrm{R}}, n_{\mathrm{R}}\rangle\rangle^{(\mathrm{R})} = |k_3, n_3\rangle^{(3)} \otimes |k_4, n_4\rangle^{(4)}\,, \tag{3.2}$$

is a basis state of the right augmented block. As only single excitations are considered in this thesis certain restrictions are imposed on the values of k both for the augmented block and the primitive blocks making up the augmented block, *i.e.* $k_{\mathrm{L}} + k_{\mathrm{R}} = 1$.

The superblock states are then constructed in a similar way as,

$$\begin{aligned} |n_{\mathrm{S}}\rangle &= |k_{\mathrm{L}}, n_{\mathrm{L}}\rangle\rangle^{(\mathrm{L})} \otimes |k_{\mathrm{R}}, n_{\mathrm{R}}\rangle\rangle^{(\mathrm{R})} \\ &= |k_1, n_1\rangle^{(1)} \otimes |k_2, n_2\rangle^{(2)} \otimes |k_3, n_3\rangle^{(3)} \otimes |k_4, n_4\rangle^{(4)} . \end{aligned} \tag{3.3}$$

The nature of the Hamiltonians and the construction of the superblock states allows the decomposition of the Hamiltonian into intra-block and inter-block Hamiltonians,

$$\begin{aligned} \hat{H}_{\mathrm{S}} &= \hat{H}_{\mathrm{L}} + \hat{H}_{\mathrm{LR}} + \hat{H}_{\mathrm{R}} \left(+\hat{H}_{\mathrm{RL}}\right) \\ &= \underbrace{\hat{H}_1 + \hat{H}_{12} + \hat{H}_2}_{\hat{H}_{\mathrm{L}}} + \underbrace{\hat{H}_{23}}_{\hat{H}_{\mathrm{LR}}} + \underbrace{\hat{H}_3 + \hat{H}_{34} + \hat{H}_4}_{\hat{H}_{\mathrm{R}}} \left(+ \underbrace{\hat{H}_{41}}_{\hat{H}_{\mathrm{RL}}} \right) , \end{aligned} \tag{3.4}$$

where the terms in brackets only contribute under periodic boundary conditions. The matrix elements of the Hamiltonian in the primitive block basis can then be calculated and stored. This decomposition is generally true for all operators used in this thesis.

3.1.1.2 Superblock State Calculation

Each iteration of the DMRG routine begins by calculating the superblock states using the Hamiltonian in the primitive block basis as described above. Expanding a general state $|\Psi\rangle$ in the superblock basis as,

$$|\Psi\rangle = \sum_{n_{\mathrm{S}}} \Psi(n_{\mathrm{S}}) \, |n_{\mathrm{S}}\rangle \, , \tag{3.5}$$

allows the use of a conjugate gradient routine [122] in which the target state is found by repeated multiplication of $|\Psi\rangle$ with the Hamiltonian constructed from the (truncated) primitive block states. In each step small changes are made to the wavefunction $\Psi(n_{\mathrm{S}})$ to minimise the energy of the state until it is converged. The first state obtained in

this manner is the ground state of the model and higher states can be calculated by projecting out the state(s) found previously in each step. In our work a Gram-Schmidt orthogonalisation [123] was used,

$$|\Phi\rangle = |\Psi\rangle - \sum_{i=1}^{n} \frac{\langle \Psi | i \rangle}{\langle i | i \rangle} |i\rangle \,, \tag{3.6}$$

where $|i\rangle$ is one of the n states already found and $|\Phi\rangle$ is the orthogonalised version of $|\Psi\rangle$. This way, in theory, all states of the system can be found. However, due to the truncation of the augmented block bases to states most important to the ground state, the method becomes less accurate the higher in energy the state is. To overcome this, other states can be targeted by imposing additional restraints on them, not just the lowest energy. By targeting a certain parity of state, for instance, it is possible to calculate higher excited states with equal accuracy.

So far, the method is exact and is equivalent to full diagonalisation of the full Hamiltonian. In order to reduce the computational effort, the augmented block bases are truncated and the operators are rotated into the new basis.

3.1.1.3 Truncation

Assuming the target superblock state is a pure state it can be written within the augmented block bases as,

$$|\Psi\rangle = \sum_{l=1}^{N_{\mathrm{L}}} \sum_{r=1}^{N_{\mathrm{R}}} \Psi_{lr} |l\rangle |r\rangle \,, \tag{3.7}$$

where $\{|l\rangle\}$ and $\{|r\rangle\}$ are the full bases of the left and right augmented block in a simplified notation. The aim is now to reduce the number of states, N_{L} and N_{R}, in this representation to a pre-set number of M (it is assumed that this number is the same for all blocks, but

it is a trivial generalisation to have different numbers for each block). The M states $|u_\alpha\rangle = \sum_l u_\alpha^l |l\rangle$, for the left block, and $|v_\alpha\rangle = \sum_r v_\alpha^r |r\rangle$, for the right block, that best approximate the superblock wavefunction,

$$|\Psi\rangle \approx |\tilde{\Psi}\rangle = \sum_{\alpha=1}^{M} c_\alpha |u_\alpha\rangle |v_\alpha\rangle , \tag{3.8}$$

are of interest.

Different approaches can be taken to make the approximation as good as possible. One approach is to maximise the overlap between the approximation and the target wavefunction, $\langle\tilde{\Psi}|\Psi\rangle$. Another approach uses the minimisation of the square deviation,

$$D = \left| |\Psi\rangle - |\tilde{\Psi}\rangle \right|^2 = \sum_{lr} \left(\Psi_{lr} - \sum_{\alpha=1}^{M} c_\alpha u_\alpha^l v_\alpha^r \right)^2 . \tag{3.9}$$

To solve this problem, rewrite $\mathbf{\Psi}$ as,

$$\mathbf{\Psi} = \mathbf{U}\mathbf{D}\mathbf{V}^{\mathrm{T}}, \tag{3.10}$$

where $\mathbf{D}$ is a diagonal matrix with entries c_α and $\mathbf{U}$ and $\mathbf{V}$ are formed of the eigenvectors u_α^l and v_α^r, respectively. This method is known as Singular Value Decomposition and is closely related to diagonalisation of a matrix.

The problem described above is then equivalent to finding the eigenstates of the reduced density matrix with the largest eigenvalues of one of the augmented blocks (conventionally the left one). This matrix is given as (for the left augmented block),

$$[\boldsymbol{\rho}_{\mathrm{L}}]_{ll'} = \sum_r \Psi_{lr}\Psi_{l'r}. \tag{3.11}$$

The resulting matrix is diagonalised by $\mathbf{U}$,

$$\boldsymbol{\rho}_{\mathrm{L}} = \mathbf{U}\mathbf{D}^2\mathbf{U}^{\mathrm{T}}, \tag{3.12}$$

and the eigenvalues of the reduced density matrix are then $\omega_\alpha = c_\alpha^2$, giving the probability of the left block being in state $|u_\alpha\rangle$, which imposes the restriction,

$$\sum_{\alpha=1}^{N_{\mathrm{L}}} \omega_\alpha = 1. \tag{3.13}$$

The states of the left block with the largest values of ω_α will contribute most to the superblock states closest to the target state and these states are therefore the ones that will be retained. The sum of the eigenvalues of the discarded states is a measure for the accuracy of the truncation.

When attempting to find more than one superblock state, the state $|\Psi\rangle$, will be a superposition of the eigenstates of the system, *i.e.*

$$|\Psi\rangle = \sum_m P_m |\Psi_m\rangle , \tag{3.14}$$

and hence,

$$[\boldsymbol{\rho}]_{ll'} = \sum_m P_m \sum_r \Psi_{lr}^m \Psi_{l'r}^m, \tag{3.15}$$

which has the eigenvalues,

$$\omega_\alpha = \sum_m P_m \left(c_\alpha^m\right)^2 . \tag{3.16}$$

This allows us to use the superblock eigenstates which have been found by diagonalising the Hamiltonian matrix to find the optimal augmented block states to keep in the next DMRG iteration. The earlier calculated augmented block operators are then rotated into

this new basis as,

$$\left\langle k, \tilde{n}'_{\mathrm{L}} \left| \hat{O} \right| k, \tilde{n}_{\mathrm{L}} \right\rangle = \sum_{n_{\mathrm{L}}, n'_{\mathrm{L}}} \langle k, \tilde{n}'_{\mathrm{L}} | k, n'_{\mathrm{L}} \rangle \left\langle k, n'_{\mathrm{L}} \left| \hat{O} \right| k, n_{\mathrm{L}} \right\rangle \langle k, n_{\mathrm{L}} | k, \tilde{n}_{\mathrm{L}} \rangle \,, \tag{3.17}$$

where the first and third term on the right-hand side are the coefficients of the eigenstates of the reduced density matrix. This procedure can also be used on the right augmented block.

If the system is symmetric only one augmented block has to be calculated. However, by introducing disorder this symmetry breaks down and symmetry arguments are not used explicitly in this work.

3.1.1.4 Infinite and Finite Lattice Algorithms

The augmented blocks resulting from the procedure above will have one more site than the previous primitive blocks $i = 1, 4$. If these blocks are then taken as the new primitive blocks $i = 1, 4$ two new sites have to be inserted between these blocks as primitive blocks $i = 3, 4$ and the overall system will grow by two sites. With this new setup, the DMRG routine can be repeated. This algorithm, which grows the system by two sites in each step, is known as the infinite lattice algorithm and is the first algorithm used in our DMRG calculations to grow the system to the target size. Due to the setup of the algorithm, the minimal system size is $N = 4$, while the target size has to be an even number. The Hilbert space size is kept constant once the augmented block states exceed the pre-set truncation value, M. Hence, any system size can be calculated using this routine, which gives it its name. However, if this was the only algorithm employed, the results would become less accurate as the system grows. Moreover, when disorder is introduced the potential energy surface will have many local minima in addition to the global minimum.

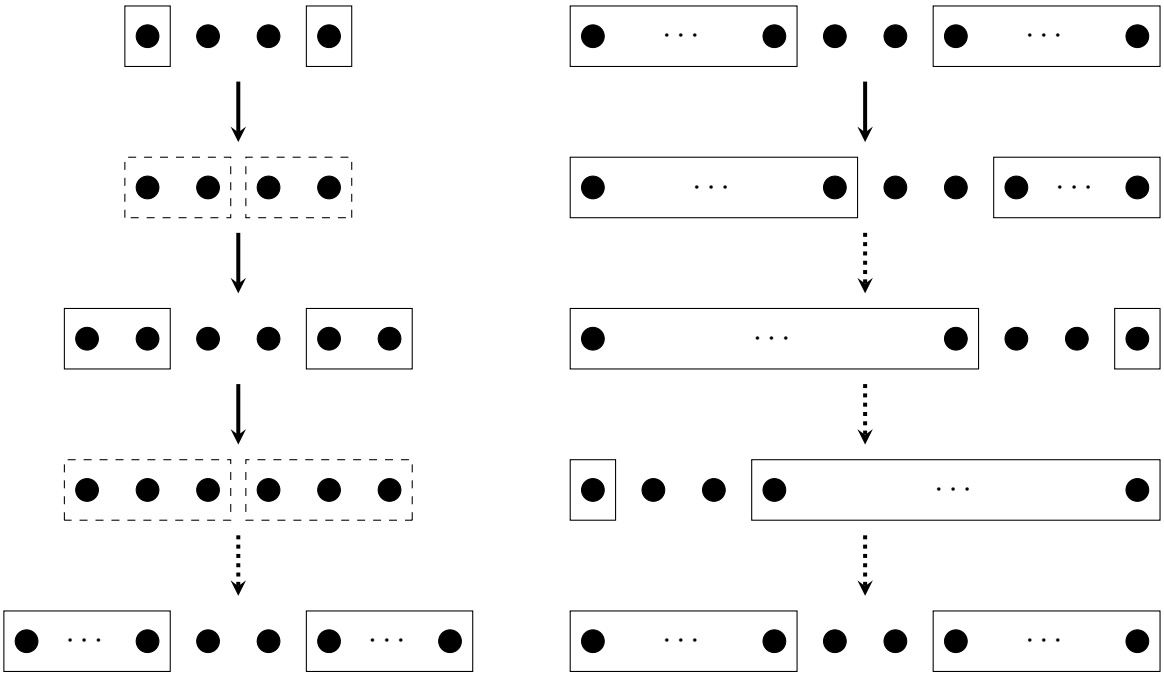


Figure 3.2.: Schematic representation of the infinite (left) and finite (right) lattice DMRG algorithms. The right scheme shows one sweep within the finite lattice routine.

As a result, due to discarding a large number of states, the algorithm can converge on a local rather than the global minimum.

In order to overcome this problem, a second algorithm is used once the system has grown to its target size. This algorithm, the finite lattice routine (see Fig. 3.2), grows one block on the expense of the other, *i.e.* while, for instance, the primitive blocks 1 and 2 are augmented and the resulting block is being taken as the new primitive block 1, the primitive block 4 is being shrunk by one site, to retain the general blocking of the system. The eigenstates of the shrunken primitive block will have been found during the infinite lattice routine, while the other block has been augmented and rotated as described above. This procedure is repeated until the primitive block 4 has reached a size of one site (when it cannot be shrunken any further) and then it is reversed, *i.e.* block 4 is grown on the expense of block 1. When using symmetry, this procedure can be stopped when

the initial, symmetric state of the superblock, is reached. As symmetry is not used in the calculations presented here, block 4 is being grown on expense of block 1 until that block has reached the size of one site and then the direction is reversed again to reach the initial state. This whole procedure, known as a sweep, can be repeated multiple times to improve convergence as in every sweep the single site states are being re-investigated to optimise the truncation of the augmented blocks. It has been found that a single sweep is usually enough to converge the results to reasonable accuracy while keeping the computational cost low (see App. D).

The basics of the Conjugated Gradient procedure will now be introduced before presenting the results in the subsequent chapters.

3.2 Conjugate Gradient Routine

The conjugate gradient routine is used in two distinct instances in this thesis: firstly, it is used in the DMRG routine to find the lowest (second lowest,...) eigenstate of the Hamiltonian by minimising the energy. Secondly, it is used in an automated parametrisation technique for the Frenkel-Holstein model and the conjugate gradient routine will be discussed in that context.

To parametrise the model against experimental spectra, the difference between the latter and the calculated spectra is used as a metric to judge the quality of the parameters. If E^{00}_{exp} and E^{10}_{exp} are the 0-0 and 1-0 absorption energies and R_{exp} the corresponding intensity ratio, then the calculated spectra are fitted to these quantities by reducing the squared error, *i.e.* the sum of the squared differences between experiment and calculation.

The conjugate gradient routine then determines a series of steps to be taken to optimise the parameters, $\mathbf{x}$, such that the metric chosen reaches a (local) minimum.

3.2.1 Derivation of the Conjugate Gradient Routine

Having established the metric to be minimised and the associated parameters, $\mathbf{x}$, it is assumed that there exists one set of parameters, $\mathbf{x}_*$, for which $f(\mathbf{x}_*) \simeq 0$, or, more generally, $\nabla_{\mathbf{x}} f(\mathbf{x}_*) = 0$ for which the function has a minimum. The procedure is iterative and determines conjugate directions along which the function is minimised until the gradient vanishes.

If the initial values of the parameters, $\mathbf{x}_0$, are chosen then the function f can be approximated by its Taylor series expansion as,

$$f(\mathbf{x}) = f(\mathbf{x}_0) + \sum_i \frac{\partial f}{\partial x_i} x_i + \frac{1}{2} \sum_{ij} \frac{\partial^2 f}{\partial x_i \partial x_j} x_i x_j + \ldots \approx c - \mathbf{b} \cdot \mathbf{x} + \frac{1}{2} \mathbf{x} \cdot \mathbf{A} \cdot \mathbf{x}, \qquad (3.18)$$

with $c \equiv f(\mathbf{x}_0)$ is the functional value at the expansion point, $\mathbf{b} \equiv -\nabla f(\mathbf{x}_0)$ is the negative gradient at the expansion point, and $[\mathbf{A}]_{ij} = \left.\frac{\partial^2 f}{\partial x_i \partial x_j}\right|_{\mathbf{x}_0}$ is the matrix of second partial derivatives (the so called Hessian Matrix or just Hessian) at the expansion point. Within this approximation the gradient of the function can be calculated as,

$$\nabla f = \mathbf{A} \cdot \mathbf{x} - \mathbf{b}, \qquad (3.19)$$

and finding an extremum then corresponds to solving the equation $\mathbf{A} \cdot \mathbf{x} = \mathbf{b}$. If the solution is denoted as $\mathbf{x}_*$, a set of n vectors can defined, $\{\mathbf{p}_i\}$, in which the solution can be expanded as,

$$\mathbf{x}_* = \sum_{i=1}^{n} \alpha_i \mathbf{p}_i. \qquad (3.20)$$

This can solved for α_i in the following way:

$$\begin{aligned} \mathbf{A}\mathbf{x}_* &= \sum_{i=1}^{n} \alpha_i \mathbf{A}\mathbf{p}_i \\ \mathbf{p}_k^{\mathrm{T}} \mathbf{A}\mathbf{x}_* &= \sum_{i=1}^{N} \alpha_i \mathbf{p}_k^{\mathrm{T}} \mathbf{A}\mathbf{p}_i \\ \langle \mathbf{p}_k, \mathbf{b} \rangle &= \alpha_k \langle \mathbf{p}_k, \mathbf{A}\mathbf{p}_k \rangle = \alpha_k \langle \mathbf{p}_k, \mathbf{p}_k \rangle_{\mathbf{A}} , \end{aligned} \tag{3.21}$$

where (without loss of generality) it is required that $\mathbf{p}_i^{\mathrm{T}} \mathbf{A}\mathbf{p}_j = C\delta_{ij}$, *i.e.* the vectors of the set $\{\mathbf{p}_i\}$ are *conjugate*. With the result above, the solution of $\mathbf{x}_*$ can be found once $\mathbf{A}$ as well as the conjugate basis is known. The latter, however, is mostly not even necessary: by knowing a sufficient subset it is often possible to get very accurate estimates of $\mathbf{x}_*$ and thus it makes more sense to view the conjugate gradient method as an iterative method in which the directions $\{\mathbf{p}_i\}$ are found successively until the solution is reached.

The routine then follows the following steps:

1. Choose the starting values for the parameters, $\mathbf{x}_0$, and calculate the function value, $f(\mathbf{x}_0)$, and the gradient, $\mathbf{g}_0 \equiv \nabla f(\boldsymbol{x}_0)$ and $\mathbf{h}_0 \equiv \mathbf{g}_0$. This initialises the routine and sets the negative gradient of the function as the first search direction.

2. Minimise $f(\mathbf{x})$ along $\mathbf{h}_0$ to find a new point, $\mathbf{x}_1 = \mathbf{x}_0 + \alpha_0 \mathbf{h}_0$.

3. Set $\mathbf{g}_1 = -\nabla f(\mathbf{x}_1)$ and calculate,

$$\gamma_0 = \frac{\mathbf{g}_1 \cdot \mathbf{g}_1}{\mathbf{g}_0 \cdot \mathbf{g}_0} = \frac{|-\nabla f(\mathbf{x}_1)|^2}{|-\nabla f(\mathbf{x}_0)|^2}. \tag{3.22}$$

4. Set $\mathbf{h}_1 = \mathbf{g}_1 + \gamma_i \mathbf{h}_0$ and minimise the function along this line to find $\mathbf{x}_2$. Repeat until the gradient vanishes (or is smaller than a predetermined threshold).

This routine ensures that the function f is minimised along a set of directions, $\{\mathbf{h}_i\}$, that are conjugate with respect to the Hessian, *i.e.* $\mathbf{h}_i \cdot \mathbf{A} \cdot \mathbf{h}_j = 0$ for any i, j.

4

Vibronic Progression in Linear Conjugated Polymers

Conjugated polymers show a variety of possible conformations as the chains are generally very flexible and can also be deformed due to internal defects, such as *cis-trans* defects in polymers containing vinylene and related units. For phenylene-based polymers, the most simple conformation is that of a linear chain and this also tends to be the conformation of lowest energy and is therefore of particular interest for applications.

In this chapter the optical properties of such polymers will be investigated, using the coarse-grained Frenkel and Frenkel-Holstein models described in Chapter 2. Ideal chains, *i.e.* chains that are uniform and show no disorder or defects in their structure, will be discussed first. The discussion of such chains will be general, assuming generic parameters for the models and general trends will be established. Invoking the Born-Oppenheimer (or adiabatic) approximation [124], analytical expressions will be derived for the principal transition dipole moments in such polymers and these predictions will be tested and confirmed with the Frenkel-Holstein model and DMRG routine.

Following this, the effects of disorder on the optical properties will be described and investigated. As has been shown in previous work [19, 83], random disorder will cause the localisation of excitons to segments of the chain and the main result of this section is that these segments form the principal molecular unit supporting an electronic excitation and hence act as chromophores within the extended polymer. The results in this chapter will be used in Chapter 6 to predict the absorption and emission spectra of various oligomers and polymers of the poly(*para*-phenylene) (PPP) and poly(*para*-phenylene

vinylene) (PPV) family. The effect of conformational changes on the optical properties will be discussed in greater detail in Chapter 5. The chapter will finish with a brief summary.

4.1 Ideal Chains

Linear chains of polymers are susceptible to random disorder, especially in the torsional angles as the torsional potentials around the moiety-moiety single bonds are very shallow (see Appendix D). Hence, even for very low temperatures, the polymers will display disorder which significantly alters the optical properties. However, ideal, non-disordered chains form excellent model systems and are easily understood and as such are worthwhile investigating in their own right. Moreover, polymers in solids and thin films, when produced correctly, show much less disorder than in solution. In the next section it will be shown that ordered chains can be regarded as irreducible segments of disordered, longer chains.

The exciton wavefunctions on linear, ordered polymers will be discussed before deriving analytical expressions within the Born-Oppenheimer limit and subsequently testing them numerically using the Frenkel-Holstein model and DMRG routine. At the end of this section the breakdown of the predictions will be discussed before introducing disorder in Section 4.2.

4.1.1 Exciton Wavefunction

Linear π-conjugated polymers have a quasi-one-dimensional π-electron system with an effective potential generated by the screening of the nuclear charges by the σ-electrons in the polymer backbone. In an ordered, uniform polymer this potential is (within the coarse grained site model) uniform along the chain and increases steeply at the boundaries of the

π-electron system. Such a potential is very similar to the particle-in-a-box model and the wavefunctions describing a particle in such a π-system will be very similar to the particle-in-a-box wavefunctions if particle-particle interactions are neglected. It is therefore useful to refer to the excitonic centre-of-mass wavefunctions in terms of the particle-in-a-box (quasi)momentum, k, or their quantum number, $\bar{k}$, which is a good quantum number in ordered (and low-disorder) linear polymers. Under open boundary conditions (OBC) the excitonic ground state of an ordered polymer will thus be similar to the $\bar{k} = 1$ state of the particle-in-a-box and will be nodeless spanning the entire π-system. Similarly the $\bar{k} = 2(3, 4, ...)$ state will have one(two,three,...) node(s). This model also holds true for periodic boundary conditions (PBC) and the first state ($\bar{k} = 0$) will have no node, the two degenerate first excited states ($\bar{k} = \pm 1$) will have two, and so on.

By treating low-energy excitons in conjugated polymers as Frenkel excitons (*i.e.* $\mathbf{r}_{\text{rel}} \approx 0$, see Section 2.1.4) the centre-of-mass wavefunction becomes identical to the exciton wavefunction. As each excitonic state is associated with a vibronic progression specified by the number of excited phonons, vibronically excited states in an ordered (or low-disorder) polymer can be classified by two quantum numbers, $\bar{k}$ and υ, the latter giving the number of phonons.

Using this analogy between the particle-in-a-box states and a Frenkel exciton on a linear, ordered polymer, excitonic states can be classified as bright or dark states, *i.e.* if the associated transitions from and to the ground state are visible in the absorption or emission spectra, respectively. This classification makes use of the Condon approximation [125–127], which assumes that the electronic excitation occurs on a faster timescale than the associated nuclear relaxation. As will be shown in Chapter 5, this approximation is violated by the simple fact that excitonic and nuclear degrees of freedom are

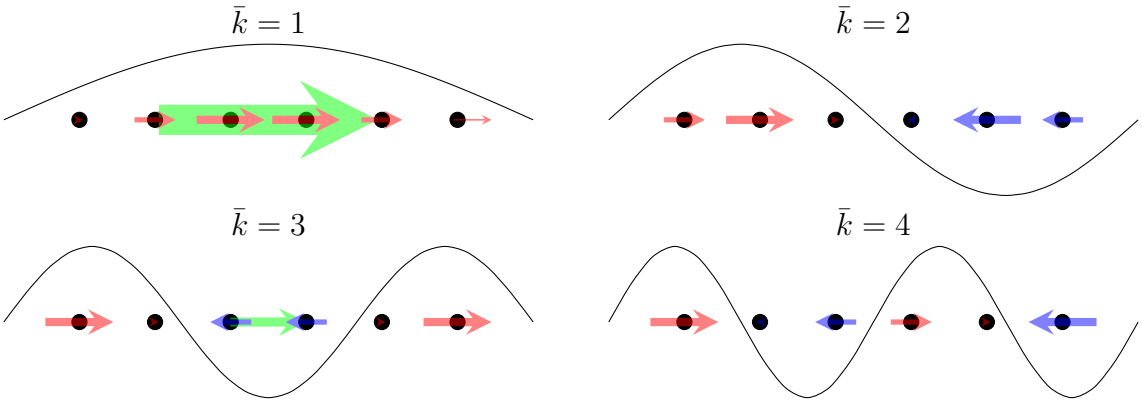


Figure 4.1.: Illustration of the transition dipole moments in a chain with 6 sites under OBC. The overall TDM (green) is the sum of the site TDMs (red and blue, respectively), whose phase is determined by the sign of the excitonic wavefunction.

coupled within the Frenkel-Holstein model. However, the predictions made using this approximation are still widely applicable.

4.1.2 Condon Allowed Transitions

The transition dipole moment in a linear, ordered polymer is, within the line-dipole approximation, directly proportional to the number of sites of the polymer [128, 129]. This can be understood when every site in the polymer is associated with an on-site transition dipole moment, which is a vector quantity aligned on the molecular axis. The direction of these on-site transition dipole moments depends on the sign of the excitonic wavefunction and it is then the modulus of the resulting transition dipole moment that determines the intensity of the observed transition.

Fig. 4.1 visualises this situation for a chain of 6 sites and open boundary conditions. It can be seen that within the Condon approximation only states with odd $\bar{k}$ are bright target states and only these will be observed in absorption and emission spectra. One can also see that the intensity of the transitions is expected to decrease monotonically if it is proportional to the norm of the resulting TDM.

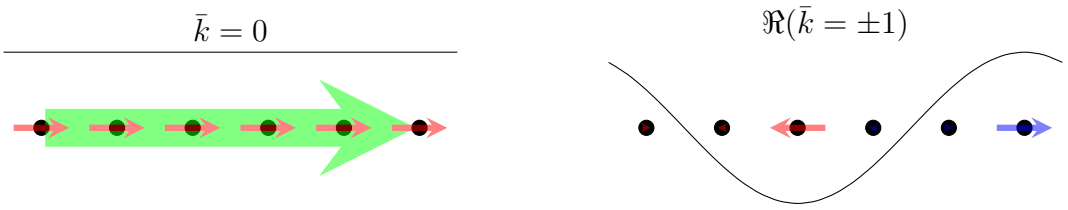


Figure 4.2.: Illustration of the transition dipole moments in a chain with 6 sites under PBC for $\bar{k} = 0$ and $\bar{k} = \pm 1$. The overall TDM (green) is the sum of the site TDMs (red and blue, respectively), whose phase is determined by the sign of the excitonic wavefunction.

For periodic boundary conditions the case simplifies even more, as the only bright transition is into the $k = 0$ state, as illustrated in Fig. 4.2.

In the following section expression for the transition dipole moments will be derived using the Born-Oppenheimer and Condon approximations, before being compared to numerical results obtained with the Frenkel-Holstein model and the DMRG routine.

4.1.3 The Born-Oppenheimer Regime

The Born-Oppenheimer (or adiabatic) approximation is valid when the nuclear motion is much slower than electronic processes and as a result the energy scale of the excitonic state separation is much larger than the vibrational state separation. This can be quantified by the quotient $\hbar\omega/|J|$, giving the ratio of the nuclear and electronic kinetic energy scales. Generally, in conjugated polymers, $\hbar\omega/|J| \sim 0.1$ and the approximation is therefore assumed to be valid. The Born-Oppenheimer *limit* is reached for $\omega \to 0$ while $\mu\omega \to \infty$, where μ is the reduced mass and ω the angular frequency of the oscillator. Within this regime, which will be loosely defined as $\hbar\omega/|J| \ll 1$, closed formulae for the transition dipole moments and other properties can be derived, which will be compared to numerical results.

The Frenkel-Holstein model in the adiabatic regime has been introduced in Sec. 2.2.2.2

and reads for a uniform chain (parameters become site-independent) with no on-site energy,

$$\hat{H}_{\mathrm{FH}}^{\mathrm{BO}} = J\sum_{n=1}^{N}\left(\hat{a}_{n+1}^{\dagger}\hat{a}_n + \hat{a}_n^{\dagger}\hat{a}_{n+1}\right) - A\hbar\omega\sum_{n=1}^{N}\tilde{Q}_n\hat{a}_n^{\dagger}\hat{a}_n + \frac{\hbar\omega}{2}\sum_{n=1}^{N}\tilde{Q}_n^2. \tag{4.1}$$

Expressed in a site-basis, $|n\rangle$, a general excitonic state will have the form,

$$|\Psi\rangle = \sum_{n=1}^{N}\Psi_n|n\rangle\,, \tag{4.2}$$

with Ψ_n being the excitonic centre-of-mass wavefunction. For linear, ordered chains these wavefunctions will resemble the wavefunctions of a particle-in-a-box with appropriate boundary conditions.

The equilibrium normal coordinates, $\left\{\tilde{Q}_n^{\mathrm{eq}}\right\}$, can be determined by minimising the expectation value of the energy, which is a function of the nuclear coordinates. The expression,

$$\begin{aligned} E\left(\left\{\tilde{Q}_n\right\}\right) &= \left\langle\Psi\left|\hat{H}_{\mathrm{FH}}^{\mathrm{BO}}\right|\Psi\right\rangle \\ &= \sum_{n=1}^{N}\left(J\left(\Psi_{n+1}^{*}\Psi_n + \Psi_n^{*}\Psi_{n+1}\right) - A\hbar\omega\tilde{Q}_n|\Psi_n|^2 + \frac{\hbar\omega}{2}\tilde{Q}_n^2\right), \end{aligned} \tag{4.3}$$

has thus to be minimised. Using the Hellmann-Feynman theorem [130, 131],

$$\frac{\partial\left\langle\Psi\left|\hat{H}\right|\Psi\right\rangle}{\partial X} = \left\langle\Psi\left|\frac{\partial\hat{H}}{\partial X}\right|\Psi\right\rangle. \tag{4.4}$$

This then implies that if $\partial E\left(\left\{\tilde{Q}_n\right\}\right)/\partial\tilde{Q}_n = 0$,

$$\tilde{Q}_n^{\mathrm{eq}} = A|\Psi_n|^2\,. \tag{4.5}$$

This shows that the nuclear displacement is proportional to the exciton density, which results in the self-trapping of the exciton as the nuclear potential around the exciton will adapt to the change in electronic structure leading to the formation of an exciton-polaron. The exciton is not self-localised by the trapping as the system is uniform in the absence of disorder, leading to delocalisation, and as such the kinetic energy (the first term in Eq. (4.3)) will not be affected. The relaxation energy associated with the lattice deformation (in the presence of one exciton) is then given as,

$$\begin{aligned} E_{\mathrm{r}} &= -\sum_n \left(A\hbar\omega \tilde{Q}_n^{\mathrm{eq}} \left|\Psi_n\right|^2 + \frac{\hbar\omega}{2} \left(\tilde{Q}_n^{\mathrm{eq}}\right)^2 \right) \\ &= \frac{A^2\hbar\omega}{2} \sum_n \left|\Psi_n\right|^4 \\ &= \hbar\omega g_N^2, \end{aligned} \tag{4.6}$$

where an effective Huang-Rhys parameter for a polymer/chromophore of N moieties has been defined as,

$$g_N^2 = \frac{A^2}{2} \left(\sum_n \left|\Psi_n\right|^4 \right). \tag{4.7}$$

The term in brackets can be related to the spatial extent of the corresponding wavefunction and the participation number, PN, can be defined as,

$$\mathrm{PN} = \frac{1}{\sum_n \left|\Psi_n\right|^4}. \tag{4.8}$$

The value of PN depends on the nature of the exciton wavefunction.

Localised Exciton If the exciton is localised on one monomer PN = 1 and then,

$$g_N^2 = \frac{A^2}{2} = g_1^2. \tag{4.9}$$

Plane-wave exciton For translationally invariant excitons,

$$\Psi_n^{(\bar{k})} = \frac{1}{\sqrt{N}} \exp\left(\mathrm{i}2\pi\bar{k}/N\right), \tag{4.10}$$

and then $\mathrm{PN} = N$, giving,

$$g_N^2 = \frac{g_1^2}{N}. \tag{4.11}$$

Standing-wave excitons For standing-wave solutions,

$$\Psi_n^{(\bar{k})} = \left(\frac{2}{N+1}\right)^{\frac{1}{2}} \sin\left(\frac{n\pi\bar{k}}{N+1}\right), \tag{4.12}$$

$\mathrm{PN} = 2(N+1)/3$ and therefore,

$$g_N^2 = \frac{3g_1^2}{2(N+1)}; \quad N > 1. \tag{4.13}$$

In the following sections it will be shown that this effective Huang-Rhys parameter is of central importance when considering electronic excitations in conjugated polymers.

Within the Born-Oppenheimer approximation the total wavefunction of the systems is the direct product of the electronic and nuclear wavefunctions. In the true ground state the system is characterized by the absence of any electronic or vibrational excitations, *i.e.* ,

$$|\mathrm{GS}; 0\rangle = |0\rangle \otimes \prod_m |0\rangle\rangle_m, \tag{4.14}$$

where $|0\rangle$ is the electronic ground state, and $|0\rangle\rangle_m$ is the vibrationally unexcited state of

the monomer at site m. Similarly, the excitonic ground state can be written as,

$$|\mathrm{EX};0\rangle = \left|\Psi^0\right\rangle \otimes \prod_m |0'\rangle\rangle_m \,, \tag{4.15}$$

where $|\Psi^0\rangle$ is the electronically excited state without any vibrational excitation expanded in the site basis, and $|0'\rangle\rangle_m$ is the vibrationally unexcited oscillator at site m, which is displaced due to the presence of the exciton.

In a continuous one-dimensional system the transition dipole operator, $\hat{\boldsymbol{\mu}}$, is defined as,

$$\hat{\boldsymbol{\mu}} = \boldsymbol{\mu}_0 \hat{x}, \tag{4.16}$$

where $\boldsymbol{\mu}_0$ is the single-site dipole moment and $\hat{x}$ is the (dimensionless) position operator. Within the coarse-grained model the expectation value of the position operator corresponds to the site (normalized to the inter-site distance) the exciton is located on. This can be expressed by substituting $\hat{x} \to \left(\hat{a}_n^\dagger + \hat{a}_n\right)$, and by taking the general case that the single-site transition dipole moment is site-dependent, the expression can be re-written as,

$$\hat{\boldsymbol{\mu}} = \sum_{n=1}^{N} \boldsymbol{\mu}_n \left(\hat{a}_n^\dagger + \hat{a}_n\right). \tag{4.17}$$

The absorption transition dipole moment for an ordered chain with N monomers is thus given by,

$$\boldsymbol{\mu} = \sum_{n=1}^{N} \boldsymbol{\mu}_n \left\langle \mathrm{EX} \left| \hat{a}_n^\dagger \right| \mathrm{GS} \right\rangle. \tag{4.18}$$

When introducing disorder (see below) the excited state wavefunction will be localised to a given segment of the chain and hence only these on-site transition dipole moments will contribute to the overall transition dipole moment.

4.1.3.1 0-0 Transition

The 0-0 transition band is comprised of all transitions from the true ground state to the electronically excited states without any excited vibrations, *i.e.* all excitonic states with odd $\bar{k}$ and $\upsilon = 0$ under OBC. The associated matrix element for a given $\bar{k}$ is thus,

$$a_n^{00} = \left\langle \mathrm{EX}; 0 \left| \hat{a}_n^\dagger \right| \mathrm{GS}; 0 \right\rangle = \left\langle \Psi^0 \left| \hat{a}_n^\dagger \right| 0 \right\rangle \prod_{mm'} {}_{m'}\langle\langle 0' | \, 0 \rangle\rangle_m = \Psi_n^0 \prod_{mm'} {}_{m'}\langle\langle 0' | \, 0 \rangle\rangle_m \,, \quad (4.19)$$

which is the transition density on site n. The choice of the oscillator basis is arbitrary and hence, without loss of generality, it will be assumed that the oscillators on different monomers are orthogonal, ${}_{m'}\langle\langle 0' | \, 0 \rangle\rangle_m = \delta_{mm'} \, {}_m\langle\langle 0' | \, 0 \rangle\rangle_m$. The self-overlap of the oscillator in the two different electronic states is quantified by the Huang-Rhys parameter, $g_1^2(m)$, as ${}_m\langle\langle 0' | \, 0 \rangle\rangle_m = \exp\left(-g_1^2(m)/2\right)$ and hence,

$$a_n^{00} = \Psi_n^0 \prod_m \exp\left(-\frac{g_1^2(m)}{2}\right) = \Psi_n^0 \exp\left(-\frac{1}{2}\sum_m g_1^2(m)\right). \quad (4.20)$$

The Huang-Rhys parameter also quantifies the displacement of the potential energy minimum with respect to a normal mode: in a system with one nuclear degree of freedom it is related to the difference in equilibrium distances in the two electronic states (see Sec 1.2). Analytically it is given as,

$$g_1^2(m) = \frac{\left(\tilde{Q}_m^{\mathrm{eq}}\right)^2}{2} = \frac{A^2 \left|\Psi_m^0\right|^4}{2}, \quad (4.21)$$

where Eq. (4.5) was used. Eq. (4.20) can thus be rewritten as,

$$a_n^{00} = \Psi_n^0 \exp\left(-\frac{A^2}{4}\sum_m \left|\Psi_m^0\right|^4\right), \quad (4.22)$$

and thus,

$$\boldsymbol{\mu}_{00} = \left(\sum_n \boldsymbol{\mu}_n \Psi_n^0 \right) \exp\left(-\frac{A^2}{4} \sum_m \left| \Psi_m^0 \right|^4 \right). \tag{4.23}$$

The intensity of an optical transition is proportional to the square modulus of the transition dipole moment, *i.e.* ,

$$I_{00} \propto \left| \boldsymbol{\mu}_{00} \right|^2 = \left(\sum_n \boldsymbol{\mu}_n \Psi_n^0 \right)^2 \exp\left(-\sum_m \frac{A^2 \left| \Psi_m^0 \right|^4}{2} \right) = \mu(N)^2 \exp\left(-g_N^2 \right), \tag{4.24}$$

with g_N^2 being an effective Huang-Rhys parameter for the entire chain and,

$$\mu(N) = \left| \sum_n \boldsymbol{\mu}_n \Psi_n^0 \right|^2. \tag{4.25}$$

For a one-dimensional chain of identical sites it is reasonable to make the approximation that $\boldsymbol{\mu}_n \equiv \mu_1$ and hence $\mu(N)^2$ only depends on the nature of the excitonic wavefunction. Using particle-in-a-box wavefunctions, for periodic boundary conditions the result is trivial as,

$$\Psi_n^0 = \psi_k^{\mathrm{PBC}}(n) = N^{-\frac{1}{2}} \exp\left(-\mathrm{i}kn \right), \tag{4.26}$$

which leads to

$$\mu(N)^2 = \begin{cases} \mu_1^2 N & \text{for } \bar{k} = 0, \\ 0 & \text{otherwise.} \end{cases} \tag{4.27}$$

This shows that for a linear chain under PBC the only absorbing exciton state is the $\bar{k} = 0$ (uniform) state (cf. above). Under open boundary conditions,

$$\Psi_n^0 = \psi_k^{\mathrm{OBC}}(n) = \sqrt{\frac{2}{N+1}} \sin\left(\frac{\bar{k}\pi n}{N+1} \right), \tag{4.28}$$

which in turn gives,

$$\mu(N)^2 = \begin{cases} \mu_1^2 \frac{2}{N+1} \cot^2\left(\frac{\pi j}{2(N+1)}\right) & \text{for odd } \bar{k}, \\ 0 & \text{otherwise,} \end{cases} \tag{4.29}$$

i.e. only absorption into excitonic states with odd $\bar{k}$ occurs in periodic boundary conditions when assuming the Condon approximation (cf. above).

The vibrational contribution to the transition dipole moment is quantified by the second term in Eq. (4.24), which is an effective Franck-Condon factor, $F_{00}(N)$. Hence,

$$I_{00} \propto |\boldsymbol{\mu}_{00}|^2 = \mu(N)^2 F_{00}(N). \tag{4.30}$$

4.1.3.2 1-0 Absorption

The absorptions from the vibronic groundstate into the first vibrationally excited state of electronically excited states make up the 1-0 absorption transition. Eq. (4.14) is no required but for the excited states,

$$|\mathrm{EX}; 1, q\rangle = \left|\Psi^1\right\rangle \otimes |1', q\rangle\rangle\,, \tag{4.31}$$

where $|\Psi^1\rangle = \sum_n \Psi^1 |n\rangle$ is the excitonic wavefunction in the presence of one phonon and,

$$|1', q\rangle\rangle = \sum_m \phi_{q,m} |1'_m\rangle\rangle\,, \tag{4.32}$$

represents a phonon of momentum q of a single displaced oscillator. $\phi_{q,m}$ is the wavefunction for the qth mode of a phonon on site m and,

$$|1'_m\rangle\rangle = \hat{b}'^{\dagger}_m \prod_{m'} |0'\rangle\rangle\,, \tag{4.33}$$

is a single displaced oscillator on site m. Each site can have one vibrational excitation and thus in a system of N sites there are N states making up $|\mathrm{EX};1,q\rangle$.

Rewrite Eq. (4.31) as,

$$|\mathrm{EX};1,q\rangle = \sum_m \phi_{q,m} |\mathrm{EX};1,q\rangle = \sum_m \phi_{q,m} \left\{ \left|\Psi^1\right\rangle \otimes |1'_m\rangle\rangle \right\}. \tag{4.34}$$

With this the calculation of the matrix elements is possible,

$$\begin{aligned} a_n^{01_m} &= \left\langle \mathrm{EX};1_m \left| \hat{a}_n^{\dagger} \right| \mathrm{GS};0 \right\rangle \\ &= \Psi_n^1 g_1(m) \exp\left(-\frac{1}{2} \sum_{m'} g_1^2(m') \right). \end{aligned} \tag{4.35}$$

It has been shown that the difference between the excitonic wavefunction in the phonon vacuum, Ψ^0, and the perturbed wavefunction in the presence of one phonon, Ψ^1, is very small (*i.e.* the exciton-polaron does not self-localise) [100, 101], especially in the Born-Oppenheimer limit and thus, without large sacrifices in accuracy, and using Eq. (4.21),

$$a_n^{01_m} = \Psi_n^0 \left(\frac{A}{\sqrt{2}} \left|\Psi_m^0\right|^2 \right) \exp\left(-\frac{A^2}{4} \sum_{m'} \left|\Psi_{m'}^0\right|^4 \right). \tag{4.36}$$

This expression describes the transition dipole moment between the electronic and vibrational ground state and the first vibrationally excited state of a given exciton state with the vibration on site m and the exciton on site n and it is exact within the Born-Oppenheimer

limit.

Thus, the 1-0 absorption transition density for the transition to the one-phonon vibronic state with momentum q is given by,

$$a_n^{01_q} = \left\langle \mathrm{EX}; 1, q \left| \hat{a}_n^\dagger \right| \mathrm{GS}; 0 \right\rangle = \sum_m \phi_{q,m} a_n^{01_m}, \tag{4.37}$$

and the intensity of the 1-0 absorption band is then proportional to,

$$\left| \boldsymbol{\mu}_{01}^{\mathrm{A}} \right|^2 = \sum_q \left| \sum_n \boldsymbol{\mu}_n a_n^{01_q} \right|^2 . \tag{4.38}$$

The value of this depends on the chosen phonon basis, $\phi_{q,m}$.

Localised Phonons For a localised phonon basis $\phi_{q,m} = \delta_{\bar{q},m}$,

$$\left| \boldsymbol{\mu}_{01}^{\mathrm{A}} \right|^2 = \frac{A^2}{2} \sum_q \left| \Psi_q^0 \right|^4 \left| \sum_n \boldsymbol{\mu} \Psi_n^0 \right|^2 \exp\left(-\frac{A^2}{2} \sum_n \left| \Psi_n^0 \right|^4 \right). \tag{4.39}$$

Comparing this to Eq. 4.23 then gives,

$$\left| \boldsymbol{\mu}_{01}^{\mathrm{A}} \right|^2 = g_N^2 \left| \boldsymbol{\mu}_{00} \right|^2 . \tag{4.40}$$

Delocalised Phonons Phonons have a very narrow bandwidth within conjugated polymers due to their coupling to the exciton. Hence, for translationally invariant systems,

$$\phi_{q,m} = \frac{1}{\sqrt{N}} \exp\left(\mathrm{i} q m \right), \tag{4.41}$$

and only the $q = 0$ mode is optically active. Thus,

$$a_n^{01_{q=0}} = \frac{1}{\sqrt{N}} \sum_m a_n^{01_m} \tag{4.42}$$

and then,

$$\left|\boldsymbol{\mu}_{01}^{\mathrm{A}}\right|^2 = \frac{A^2}{2N} \left|\boldsymbol{\mu}_{00}\right|^2 . \tag{4.43}$$

As the band is very narrow even small amounts of disorder will localise the phonons and it is thus expected that expression Eq. (4.40) is more accurate. Thus,

$$\left|\boldsymbol{\mu}_{01}^{\mathrm{A}}\right|^2 = \mu(N)^2 g_N^2 \exp[-g_N^2], \tag{4.44}$$

which implies an effective Franck-Condon factor for the 1-0 absorption for a chain of N monomers as,

$$F_{01}(N) = g_N^2 \exp[-g_N^2]. \tag{4.45}$$

4.1.3.3 0-1 Emission

The 0-1 emission is made up of the transitions from the electronically excited states in their vibrational ground state to the electronic groundstate in its first vibrationally excited state. The states,

$$|\mathrm{EX}; 0\rangle = \left|\Psi^0\right\rangle \otimes |0'\rangle\rangle \,, \tag{4.46}$$

and

$$|\mathrm{GS}; 1, q\rangle = |0\rangle \otimes |1, q\rangle\rangle \,, \tag{4.47}$$

with equivalent definitions as above, are thus required. And as,

$$ {}_m\langle\langle 0' \,|1\rangle\rangle_m = {}_m\langle\langle 1' \,|0\rangle\rangle_m \,, \tag{4.48} $$

all expressions for the 1-0 absorption hold true for the 0-1 emission, as well, with the only exception that Ψ_m^1 is replaced by Ψ_m^0. In the ground state there is no coupling of phonons to excitons and hence within the Frenkel-Holstein model it is only reasonable to assume a localised phonon basis and hence,

$$ \left|\boldsymbol{\mu}_{01}^{\mathrm{E}}\right|^2 = \mu(N)^2 g_N^2 \exp[-g_N^2], \tag{4.49} $$

which is identical to the expression for $\left|\boldsymbol{\mu}_{10}^{\mathrm{A}}\right|$.

The expressions derived above indicate that within the Born-Oppenheimer and Condon approximations the 1-0 absorption and 0-1 emission transition dipole moments are the same and moreover that,

$$ \frac{\left|\boldsymbol{\mu}_{10}^{\mathrm{A}}\right|^2}{\left|\boldsymbol{\mu}_{00}\right|^2} \approx \frac{\left|\boldsymbol{\mu}_{01}^{\mathrm{E}}\right|^2}{\left|\boldsymbol{\mu}_{00}\right|^2} = g_N^2, \tag{4.50} $$

i.e. the intensity ratios for the two observed bands in the absorption and emission spectra are identical and only a function of the chain length and the Huang-Rhys parameter.

4.1.3.4 Copolymers

For polymers with alternating moieties supporting Frenkel excitations (for CT-supporting polymers see below) small modifications have to be made to the results, namely the average Huang-Rhys parameter. The effective Huang-Rhys parameter, $\bar{g_1^2}$, is then defined as,

$$ g_N^2 = \sum_{n=1}^{N} g_1^2(n) \left|\Psi_n\right|^4 = \bar{g_1^2} \sum_{n=1}^{N} \left|\Psi_n\right|^4 , \tag{4.51} $$

i.e. each moiety is weighted by the square of the exciton density. In addition,

$$E_r = \sum_{n=1}^{N} \hbar\omega_n g_1^2(n) \left|\Psi_n\right|^4 = \hbar\omega g_N^2, \tag{4.52}$$

where the last identity only holds true if $\hbar\omega_n$ is the same for each moiety (as is assumed in this thesis for PPP and PPV).

Numerical results will now be discussed and compared to the predictions made here.

4.1.4 Numerical Results

The fully-quantised Frenkel-Holstein model (Eq. (2.39)) and the DMRG routine was used to verify the predictions made above. It has been found that for small $\hbar\omega$ the results converge for 10 phonon levels and about 100 block states were used which then leads to about 300 000 superblock states. At least one sweep was performed and the DMRG routine is explained in more detail above. For a full convergence table see Appendix D.

The groundstate of the Frenkel-Holstein Hamiltonian is the electronically first excited state without vibrational excitation, *i.e.* $|\mathrm{EX};0\rangle$. For $\hbar\omega/|J| \ll 1$ the first N excited states of the Frenkel-Holstein model will correspond to the one-phonon vibrational manifold. For $\hbar\omega/|J| \gg 1$ (*i.e.* the anti-adiabatic limit) higher excited states with $\bar{k} > 1$ will become lower in energy than vibrationally excited states and the one-phonon states will not necessarily be in order, any more.

The transition dipole moments were calculated as $\left\langle \mathrm{EX};\alpha \left|\hat{a}_n^\dagger\right| \mathrm{GS}\right\rangle$, where $|\mathrm{GS}\rangle$ is the excitonic and vibrational vacuum and α labels the eigenstates of the Frenkel-Holstein model. As described above in the Born-Oppenheimer limit, $\alpha = 1$ will be the first exciton state without vibrational excitation, giving rise to the 0-0 transition, whereas $2 \leq \alpha \leq N+1$ will be the N quasi-degenerate one-phonon states. Summing the transition

dipole moments to these states then gives the overall transition dipole moment for the 1-0 absorption.

The emission transition dipole moments are calculated from the first excited state, $|\mathrm{EX};\alpha=1\rangle$ to the vibrational manifolds of the electronic ground state via $\left\langle \mathrm{EX};\alpha=1\left|\hat{a}_n^\dagger\right|\mathrm{GS},\upsilon_m\right\rangle$, where in the ground state υ_m vibrational excitations are on moiety m. The dipole moment is then calculated using either a plane wave or localised phonons. To test the predictions in the Born-Oppenheimer limit as described above parameters generally applicable to conjugated polymers were used, namely $\hbar\omega/|J|=0.1$ and $g_1^2=A^2/2=1$. The on-site energy is set to 0 as it just acts as energy offset and has no effect on the transition dipole moments.

4.1.4.1 Periodic Boundary Conditions

For translationally invariant chains the exciton wavefunctions are given as plane-waves, *i.e.*

$$\psi_n^{(k)}=\frac{1}{\sqrt{N}}\exp\left(\pm \mathrm{i}kn\right);\quad k=\frac{2\pi\bar{k}}{N};\quad -\frac{N}{2}\leq\bar{k}\leq\frac{N}{2}, \tag{4.53}$$

with energies

$$E^{(k)}=2J\cos(k). \tag{4.54}$$

Fig. 4.3(a) shows the evolution of the 0-0 absorption transition dipole moment with increasing chain length. Also shown is the result expected from the Born-Oppenheimer expressions (Eq. (4.30)), as well as the sum rule, $|\mu_{00}/\mu_1|^2=N$ [132], which shows deviations due to the intensity of higher-order transitions. It can be seen that the Born-Oppenheimer expression reproduces the DMRG results very accurately, especially for short chains. However, for longer chains a slight overestimation of the transition dipole moment can be seen. The discrepancy to the sum rule also becomes larger for longer

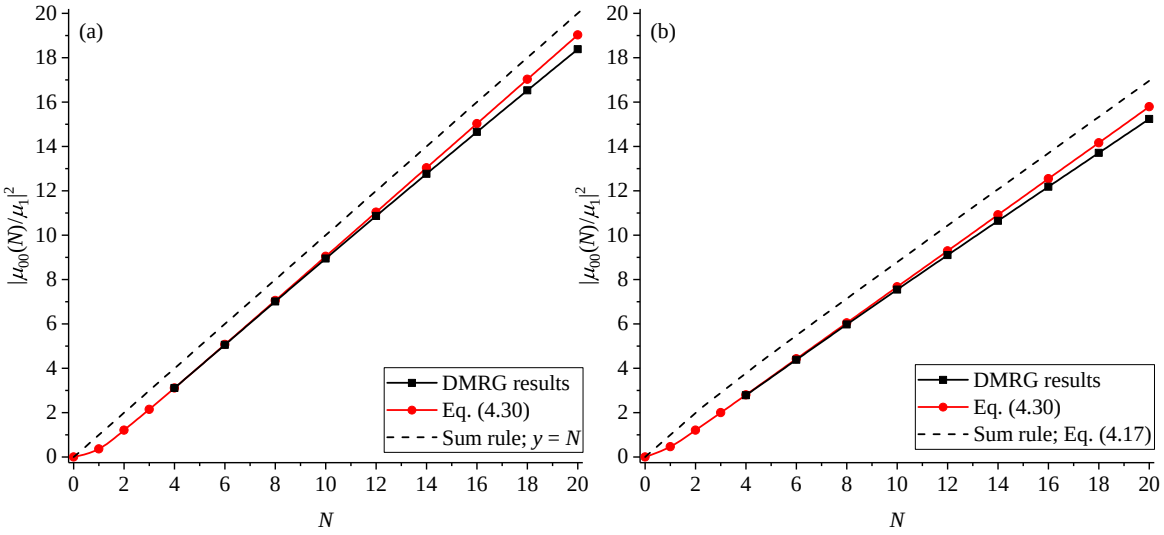


Figure 4.3.: The 0-0 squared transition dipole moment versus chain length, N, in the adiabatic regime for linear chains with (a) periodic and (b) open boundary conditions. $\hbar\omega/|J| = 0.1, g_1^2 = 1$. The results were obtained using 7 phonons per site and 60 states per augmented block. Note that ehe minimum chain size for DMRG calculations in $N = 4$ (see Chapter 3).

chains, indicating a transfer of oscillator strength to higher-energy transitions. Overall it becomes obvious that for longer chains the Born-Oppenheimer expressions break down. This will be discussed in more detail below.

Table 4.1 shows the results for 0-0 transitions, as well as for 1-0 absorption and 0-1 emission transition dipole moments. Within the one-phonon vibronic manifold one state is identified as carrying the oscillator strength for this transitions. In the code this is the $\alpha = N + 1$ state. The calculated values of $\left|\mu_{10}^{A}(\alpha = N + 1)/\mu_{00}\right|^2$ are in perfect agreement with Eq. (4.43). The value of the 0-1 emission transitions dipole moment is independent of the phonon basis, as shown above, and $\left|\mu_{10}^{\mathrm{A}}(\alpha = N + 1)\right|^2 = \left|\mu_{01}^{\mathrm{E}}\right|^2$, which is in agreement to the prediction of equal 1-0 and 0-1 transition dipole moments within the Condon approximation (see Eq. (4.50)).

N	Eq. (4.30)	$\lvert\mu_{00}/\mu_1\rvert^2$	α	$\lvert\mu^{\mathrm{A}}_{10}/\mu_1\rvert^2$	$\delta E(\alpha)/\hbar\omega$	$\lvert\mu^{\mathrm{E}}_{01}/\mu_1\rvert^2$
4	3.1152	3.1106	5	0.7777	1.00	0.7777
6	5.0789	5.0608	7	0.8435	1.00	0.8435
8	7.0600	7.0122	9	0.8765	1.00	0.8765
10	9.0484	8.9501	11	0.8950	1.00	0.8950
12	11.0405	10.8693	13	0.9058	1.00	0.9058

Table 4.1.: Comparison of $\lvert\mu_{00}/\mu_1\rvert^2$ obtained with BO-expressions, Eq. (4.30), and DMRG results. N is the number of monomers, α labels the eigenstate obtained with the DMRG routine, $\Delta E(\alpha)$ is the energy of state α relative to the 0-0 transition, μ^{A}_{10} and μ^{E}_{01} are the 1-0 absorption and 0-1 emission transition dipole moments, respectively. $\hbar\omega/J = 0.1, g_1^2 = 1$. The results were calculated using 7 phonons per site and 60 states per augmented block.

4.1.4.2 Open Boundary Conditions

The exciton centre-of-mass wavefunctions for ordered chains with open boundary conditions are given as,

$$\psi_n^{(k)} = \sqrt{\frac{2}{N+1}}\sin(nk)\,; \quad k = \frac{\pi\bar{k}}{N+1}; \quad 1 \leq \bar{k} \leq N. \tag{4.55}$$

Fig. 4.3(b) shows the results for the 0-0 transition dipole moment against the Born-Oppenheimer prediction (Eq.(4.30)) and the sum rule (Eq. (4.29)). As in the case for periodic boundary conditions the results deviate from the Born-Oppenheimer predictions for longer chains. Also observed is once again the deviation from the sum rule, showing the contribution of higher-energy transitions, becoming more pronounced for longer chains.

Tab. 4.2 shows the calculated 0-0, 1-0 absorption, and 0-1 emission transition dipole moments. For a chain of N segments there are $N/2$ bright states contributing to the 1-0 absorption transition dipole moment, with the $\alpha = N + 1$ state having the largest contribution. The 0-1 emission intensity now depends on the choice of the phonon basis. For plane wave phonons is is found that the 0-1 emission intensity is equal or very close

N	Eq. (4.30)	$\lvert\mu_{00}/\mu_1\rvert^2$	α	$\lvert\mu_{10}^{\mathrm{A}}(\alpha)/\mu_1\rvert^2$	$\Delta E(\alpha)/\hbar\omega$	$\left\lvert\mu_{01}^{\mathrm{E(P)}}/\mu_1\right\rvert^2$	$\left\lvert\mu_{01}^{\mathrm{E(L)}}/\mu_1\right\rvert^2$
4	2.8069	2.7866	3	0.1545	0.98	*0.6966*	**0.8364**
			5	*0.6966*	1.00		
			3-5	**0.8511**			
6	4.4266	4.3841	3	0.1273	0.98	*0.7307*	**0.9340**
			5	0.1063	0.99		
			7	*0.7306*	1.00		
			3-7	**0.9642**			
8	6.0502	5.9717	3	0.1464	0.97	*0.7465*	**0.9819**
			5	0.0530	0.99		
			7	0.0867	1.00		
			9	*0.7464*	1.00		
			3-9	**1.0325**			
10	7.6741	7.5449	3	0.1669	0.97	*0.7545*	**1.0060**
			5	0.0447	0.99		
			7	0.0443	0.99		
			9	0.0716	1.00		
			11	*0.7547*	1.00		
			3-11	**1.0822**			

Table 4.2.: Same as Tab. 4.1 but for chains with open boundary conditions. $\left\lvert\mu_{01}^{\mathrm{E(P)}}/\mu_1\right\rvert^2$ and $\left\lvert\mu_{01}^{\mathrm{E(L)}}/\mu_1\right\rvert^2$ refer to 0-1 emission transition dipole moments calculated assuming a plane wave or localised phonon basis, respectively.

in value to the 1-0 absorption intensity of the $\alpha = N + 1$ state, while for a localised phonon basis the summed 1-0 absorption intensity is very close in value to the 0-1 emission intensity. The equality of the 1-0 absorption and 0-1 emission intensities assuming a plane wave phonon basis has previously been observed by Spano and Yamagata, who also confirm that this equivalence holds true in the adiabatic and anti-adiabatic regime (see below) [17]. However, the values diverge for longer chains, *i.e.* when the approximations of the Born-Oppenheimer expressions break down. This, in turn, leads to the assumption that for $\hbar\omega/J \to 0$, *i.e.* within the adiabatic limit in which the Born-Oppenheimer expressions were derived, the approximation $\left\lvert\boldsymbol{\mu}_{10}^{\mathrm{A}}\right\rvert^2 \approx \left\lvert\boldsymbol{\mu}_{01}^{\mathrm{E(L)}}\right\rvert^2$ indeed becomes an equality.

For the localised phonon basis it has been shown that within the Born-Oppenheimer

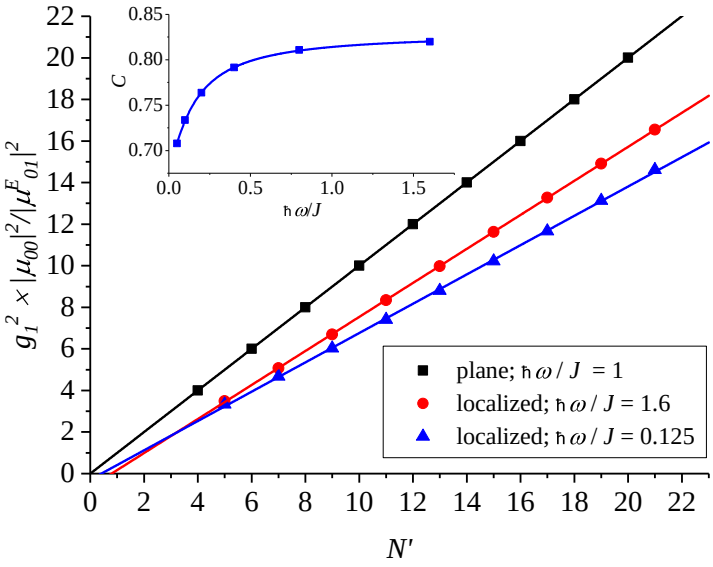


Figure 4.4.: Scaled emission intensity, $g_1^2 \times |\mu_{00}|^2/|\mu_{01}^{\mathrm{E}}|^2$, ratio for linear chains with open boundary conditions against N'. For a plane-wave phonon basis, $N' = N$, and $y = N$ for any value of $\hbar\omega/|J|$. For localised phonons, $N' = N + 1$ and $y = C(N + 1)$ with $C = 2/3$ for $\hbar\omega/|J| \to 0$ and $C = 5/6$ for $\hbar\omega/|J| \gg 1$ as shown in the inset.

approximation (cf. Eq. (4.13) and (4.40)),

$$\frac{|\mu_{00}|^2}{\left|\mu_{01}^{\mathrm{E(L)}}\right|^2} = \frac{C \times (N+1)}{g_1^2}, \tag{4.56}$$

where $C = 2/3$. However, C is found to be a weak function of the adiabaticity of the system, *i.e.* of $\hbar\omega/|J|$. In the adiabatic limit, $\hbar\omega/|J| \to 0$, $C \to 2/3$, as expected. However, for $\hbar\omega/|J| \gg 1$, $C \to 5/6$, as shown in Fig. 4.4. The same figure also shows the result for plane-wave phonons, which is independent of $\hbar\omega/|J|$.

4.1.5 Breakdown for Long Chains

As shown by the numerical results above, the Born-Oppenheimer expressions that have been derived are generally valid in the Born-Oppenheimer regime, *i.e.* $\hbar\omega \ll |J|$. However,

N	$\lvert\mu_{00}/\mu_1\rvert^2$	α	$\lvert\mu^{\mathrm{A}}_{10}/\mu_1\rvert^2$	$\Delta E(\alpha)/\hbar\omega$
8	6.907	9	0.8634	1.0
		11	0.0268	1.8
12	10.589	13	0.8795	1.0
		18	0.1622	1.7
16	14.185	17	0.8865	1.0
		22	0.4798	1.5
		17+22	1.366	
20	17.748	21	0.8865	1.0
		30	0.7671	1.4
		21+30	1.654	
24	21.301	25	0.8865	1.0
		38	1.009	1.3
		25+38	1.896	

Table 4.3.: Same as for Tab. 4.1, but $\hbar\omega/J = 0.2$.

even in that limit the approximations break down for long chains, *i.e.* large N. This is attributed to a reduction of the energy gaps between different exciton centre-of-mass states as the chain lengths increases. As the energy gaps decrease and get close to the energy gap between phonon states the Born-Oppenheimer approximation breaks down. For translationally invariant systems the exciton energies are given by Eq. (4.54) and hence, if,

$$N \sim \frac{2\pi}{\arccos\left(1 - \frac{\hbar\omega}{2|J|}\right)}, \tag{4.57}$$

or $N \sim 2\pi\,(2|J|/\hbar\omega)^{1/2}$ the $(\bar{k} = 1, \upsilon = 0)$ state becomes quasi-degenerate with the $(\bar{k} = 0, \upsilon = 1)$ state. This breakdown can be seen in the results above which deviate from the Born-Oppenheimer prediction, indicating a transfer of oscillator strength to higher energy transitions. When increasing the ration $\hbar\omega/|J|$ the effect becomes more pronounced and Tab. 4.3 shows the absorption transition dipole moments for $\hbar\omega/|J| = 0.2$.

For $\hbar\omega/|J| = 0.2$, Eq. (4.57) predicts a breakdown of the Born-Oppenheimer expressions for $N \sim 14$. While the state $\alpha = N + 1$ has the intensity predicted by Eq. (4.43), a

higher lying bright state appears and for increasing chain length its energy decreases and for $N > 14$ the energy is within the 1-0 absorption window, $\hbar\omega/2 \leq \Delta E \leq 3\hbar\omega/2$. For longer chains the 1-0 absorption now increases sub-linearly.

It is therefore predicted that for long chains the absorption-emission symmetry is lost. While the 0-0 and 0-1 emission intensities still satisfy the relationships detailed above, the 0-0 and 1-0 absorption intensity ratio grows sub-linearly with N for long chains. However, the Born-Oppenheimer breakdown for long chains is not as severe as the breakdown in the anti-adiabatic limit, *i.e.* $\hbar\omega/|J| \gg 1$.

4.2 Disordered Chains

Having discussed the optical transitions in ordered chains both theoretically and numerically, disorder will now be introduced into the systems which will make them more comparable to experimental structures. The potentials for torsions of moieties around the molecular axis are typically very shallow for phenylene based polymers and as such even a small increase in temperature will result in large fluctuations within the torsional angles of neighbouring moieties, ϕ_n. These fluctuations will alter the transition integrals between sites, as described above, namely,

$$J_n = J^{\mathrm{DD}} + J^{\mathrm{SE}} \cos^2 \phi_n, \tag{4.58}$$

where ϕ_n will be set up as Gaussian random variable with mean ϕ_0 and standard deviation σ_ϕ. In some cases it is more convenient and/or interesting to treat J_n as Gaussian random variable with mean J_0 and standard deviation σ_J. While not as physically accurate it allows a more precise investigation of certain effects. It will be clear from the context

which approach has been used for the simulations for introducing disorder.

The participation number, as defined previously (cf. Eq. (4.8)),

$$\mathrm{PN} = \left(\sum_{n=1}^{N} |\Psi_n|^4 \right)^{-1}, \tag{4.59}$$

is closely related to the spread of the exciton and, recalling the results above (Eqs. (4.9)-(4.13)),

$$g_N^2 = \sum_{n=1}^{N} g_1^2(n) \, |\Psi_n|^4 = \frac{\bar{g_1^2}}{\mathrm{PN}}, \tag{4.60}$$

and

$$E_r = \hbar\omega g_N^2 = \hbar\omega \frac{\bar{g_1^2}}{\mathrm{PN}}, \tag{4.61}$$

where $\bar{g_1^2}$ is an average monomeric Huang-Rhys parameter, which for homo-moiety polymers is the respective g_1^2 for the monomer species and for copolymers is an average of the monomeric parameters weighted by the exciton density of the respective moiety type, as defined in Sec. 4.1.3.4.

It has been shown that fluctuations in the potential along a chain will invariably lead to Anderson localisation of the exciton and as such the exciton will be confined to a number of moieties smaller than the chain length, N [6, 83]. There is a second kind of localisation, Landau localisation, which is associated with the self-trapping of excitons in phonon clouds which will then lead to localisation, as described above. Despite only being important in a very narrow parameter regime [101], both localisation mechanisms have the same effect on the optical properties and it shall not be discriminated between these two processes in the following.

4.2.1 Disordered Model Systems

The model systems described in this section have no physical or chemical relevance other than investigating the behaviour of the optical properties when introducing disorder. For ordered chains it has been found that,

$$\frac{|\boldsymbol{\mu}_{00}|^2}{|\boldsymbol{\mu}_{01}^{\mathrm{E}}|^2} = \frac{1}{g_N^2} = \frac{N}{g_1^2}, \tag{4.62}$$

in the case of translationally invariant systems. For disordered systems, following the definitions of Eq. (4.60), it is now predicted that,

$$\frac{|\boldsymbol{\mu}_{00}|^2}{|\boldsymbol{\mu}_{01}^{\mathrm{E}}|^2} = \frac{1}{g_N^2} = \frac{\mathrm{PN}}{\bar{g_1^2}}, \tag{4.63}$$

for a given emissive state on a chain. Each chain is now expected to support more than one LEGS and to reduce statistical noise, an ensemble average is taken,

$$\frac{\left\langle |\boldsymbol{\mu}_{00}|^2 \right\rangle}{\left\langle |\boldsymbol{\mu}_{01}^{\mathrm{E}}|^2 \right\rangle} = \frac{1}{\langle g_N^2 \rangle} = \frac{\langle \mathrm{PN} \rangle}{\langle \bar{g^2} \rangle}. \tag{4.64}$$

This equation was derived by Spano and Yamagata in a different way from ours. In their work $N_{\mathrm{coh}} \equiv \langle \mathrm{PN} \rangle$ and $\lambda^2 \equiv g^2$ [15, 17]. The emissive states in disordered chains are, according to Kasha's rule, the lowest energy excited states for a given part of the chain. These correspond to the LEGSs of a polymer and will be the main focus the discussion.

As laid out above, LEGSs can be defined by the value of their signed value parameter, SVP, satisfying,

$$\mathrm{SVP} = \left| \sum_n \Psi_n^\alpha \left| \Psi_n^\alpha \right| \right| \geq 0.95, \tag{4.65}$$

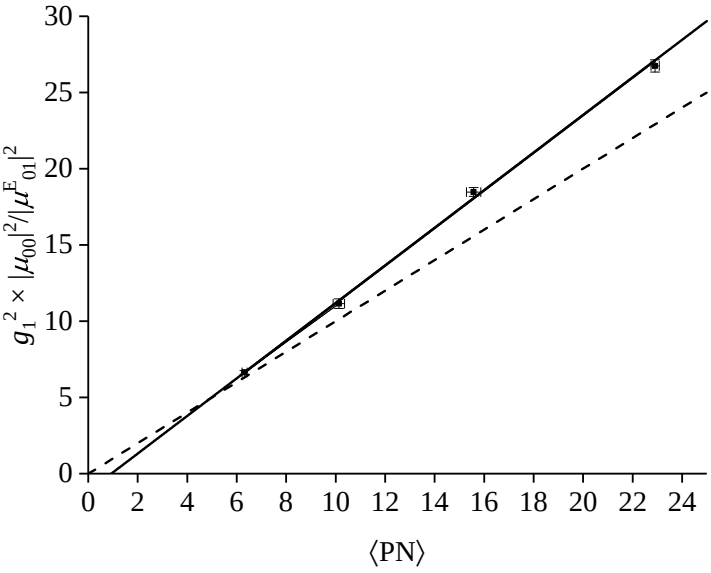


Figure 4.5.: Plot of $g^2 \times |\boldsymbol{\mu}_{00}|^2 / \left|\boldsymbol{\mu}_{01}^{\mathrm{E}}\right|^2$ against the average PN with linear fit (solid line) and prediction (dashed line). Note that PN cannot be smaller than 1 due to its definition and the normalisation constraint on allowed wavefunctions.

where α labels the state. The spatial extent or conjugation length of a LEGS can be defined as,

$$\mathrm{CL} = \left(\frac{12\pi^2}{\pi^2 - 6}\right)^{\frac{1}{2}} \left(\left\langle n^2 \right\rangle - \left\langle n \right\rangle^2\right)^{\frac{1}{2}}, \tag{4.66}$$

with

$$\left\langle n^p \right\rangle = \sum_n n^p \left|\Psi_n^\alpha\right|^2, \tag{4.67}$$

and the prefactor (≈ 5.6) was introduced such that for an ordered system the $\alpha = 1$ state spans the entire chain, *i.e.* $\mathrm{CL} = N$. Because a LEGS is the irreducible unit supporting an emission, the length of a LEGS corresponds to the length of a chromophore.

Fig. 4.5 shows the results obtained using the fully quantised Frenkel-Holstein model and the DMRG routine. The disorder was introduced modelling J_n directly as a Gaussian random variable with varying values of σ_J and N to achieve multiple values of PN which were then averaged for a given (N,σ_J) combination. The calculations were performed in

the Born-Oppenheimer regime with $\hbar\omega/|J_0| = 0.02$ and the number of phonons per site was $N_{\text{phon}} = 15$ with 60 states retained per augmented block in the DMRG routine.

The solid black line shows the linear fit (with $R^2 = 0.99855$) as,

$$g_1^2 \frac{|\boldsymbol{\mu}_{00}|^2}{|\boldsymbol{\mu}_{01}^{\text{E}}|^2} = (1.23344 \pm 0.02717)\,\langle \text{PN} \rangle + (-1.14969 \pm 0.27764)\,. \tag{4.68}$$

Also shown is the theoretical prediction, Eq. (4.64). While it as clear that the results scale linearly with $\langle \text{PN} \rangle$, they diverge, especially for large PN, from the theoretical prediction. A large value of $\langle \text{PN} \rangle$ corresponds, necessarily, to a value of $N \geq \langle \text{PN} \rangle$ and it is a central observation in this thesis, that the Born-Oppenheimer predictions break down for large N (see above). For small $\langle \text{PN} \rangle$, which corresponds to small N or large σ_J, the prediction is accurate and even for the whole range shown in Fig. 4.5 the simple model performs reasonably well.

The linearity of the results in Fig. 4.5 strongly resembles the results for ordered chains and as such shows that disorder localises excitons to portions of the chain and these segments each act as emissive entity, defining a chromophore. A polymer, segmented by disorder, is thus very similar to an ensemble of ordered molecules showing the same $\langle \text{PN} \rangle$. As the PN is related to the chromophore length, CL, it is possible to determine the average length of a chromophore directly from the emission intensity ratio readily observed in the photoluminescence spectrum. For low disorder, which normally corresponds to low temperatures, it is even possible to give a lower boundary of the overall polymer length, given that $\text{CL} = N$ for ordered systems.

4.3 Summary

A theoretical description of the fundamental absorption and emission bands observed in linear conjugated polymers has been presented and the predictions have been compared to numerical results using the Frenkel-Holstein model and a DMRG routine. The predictions are based on three assumptions: i) the low-energy excitations within the polymer are described by Frenkel-Holstein model as Frenkel excitons coupling to local normal modes; ii) the adiabatic limit is applicable to conjugated polymers, *i.e.* $\hbar\omega \ll J$; iii) the Condon approximation, *i.e.* the exciton-polaron wavefunction is independent of the normal modes.

Using these approximations an expression for an effective Huang-Rhys parameter for a chain (or, more generally, a chromophore) of length N has been derived as $g_N^2 = \bar{g_1^2}/\mathrm{PN}$, where $\bar{g_1^2}$ is an averaged monomer Huang-Rhys parameter for the moieties present in the system, and PN is the participation number, given as $\mathrm{PN} = \left(\sum_n |\Psi_n|^4\right)^{-1}$, where Ψ_n is the exciton centre-of-mass wavefunction. As PN is directly related to the chromophore length, the effective Huang-Rhys parameter decreases with the length of the chromophore.

The effective Huang-Rhys parameter has, as in small molecules, two interpretations. Firstly, it is related to the relaxation energy of the exciton due to the adaptation of the nuclear geometry, as $E_\mathrm{r} = \hbar\omega g_N^2$. Secondly, it appears in the definition of an effective Franck-Condon factor as $F_{\upsilon 0} = (g_N^2)^\upsilon \exp\left[-g_N^2\right]/\upsilon!$, for the υth vibronic manifold. A chromophore of N isolated normal modes can thus be regarded as one effective normal mode with Huang-Rhys parameter g_N^2.

Within the Born-Oppenheimer limit is has been shown that the 0-0 transitions, 1-0 absorption, and 0-1 emission intensities are proportional to $F_{00}(N)$ and $F_{10}(N) \equiv F_{01}(N)$, respectively, thus the 0-0 and 1-0/0-1 intensity ratios are proportional to g_N^2. It is predicted that the effective Franck-Condon factor does decrease with increasing chain length

and this result is in agreement with previous work [9–13]. In contrast to results obtained in the anti-adiabatic regime by Spano and co-workers [14–17], nearly symmetric absorption and emission spectra are predicted.

These analytical results are checked against DMRG calculations on the Frenkel-Holstein model and the predictions are found to be valid for emission in the adiabatic regime and exact in the adiabatic limit ($\hbar\omega/|J| \to 0$). The same is true for absorption in the case of short chains, however for chains longer than a given N the vibrational ground state of higher-lying excitonic states becomes quasi-degenerate with the first vibrational state of the excitonic ground state. This leads to a mixing of the electronic and nuclear states causing a breakdown of the Born-Oppenheimer approximation. This effect will be discussed in more detail in the next chapter, as well as the effect the conformation of a polymer has on the optical properties, as these two mechanisms are closely linked. For $\hbar\omega/|J| \approx 0.1$, a value generally applicable to conjugated polymers, however, the critical chain length is about 20 moieties and as is has been shown, disorder renders the chromophore length normally shorter than 20 moieties and as such the breakdown will not be observed in linear polymers.

When introducing disorder the emission intensity ratio is proportional to the average IPR in the system,

$$\frac{I_{01}^{\mathrm{E}}}{I_{00}} = \frac{\bar{g}_1^2}{\langle \mathrm{PN} \rangle} \left(\frac{E_{01}^{\mathrm{E}}}{E_{00}} \right)^3 . \tag{4.69}$$

This shows that disorder localises the excitons to segments of the chain which each support an exciton, defining a chromophore in a conjugated polymer. The relationship shown above directly links experimental observables to the PN and hence to the length of a chromophore. This result is found to be independent of chromophore shape within the Condon approximation as a result of the Born-Oppenheimer factorization of the many-

body wavefunction. In the next Chapter it will be shown that this result breaks down when taking post-Condon effects into account. The results obtained here are generally are in good agreement with the results of Spano and co-workers [15, 17, 39].

In the next chapter the effect the conformation of a polymer has on the optical spectra will be discussed by considering curved chromophores and macrocycles. This will require a post-Condon treatment of the transitions due to the exciton-phonon coupling, which renders Condon-forbidden transitions allowed. In Chapter 6 results of explicit polymer modelling will be presented which will also be compared to experimental results.

5

Vibronic Progression in Bent Chromophores and Macrocycles

Having discussed the conformationally easiest class of polymers, linear chains, the results will now be generalised to include the effects on the optical properties due to conformation. It will be shown that in non-linear polymers the Condon approximation breaks down and post-Condon effects have to be considered.

First discussed will be conjugated macrocycles which are, in principle, large circular polymers which can have diameters of up to several nanometers and are interesting due to their application in light harvesting systems, such as chlorophyll. Porphyrin rings and its derivatives from a class of conjugated macrocycles, for instance. Expressions will be derived for the post-Condon effects in macrocycles from the real-space Frenkel-Holstein model using a perturbation theory approach. The introduction of disorder, which naturally leads to curved, non-cyclic chromophores due to the localisation of the excitons to segments of the chain, as described above, then follows.

After this, by allowing any bent angle of the chain the effect of conformation on the optical properties can be discussed more easily and general expressions for the absorption and emission intensities using the momentum-space representation of the Frenkel-Holstein model will be used. These expressions recover the results for linear chains and macrocycles

very conveniently.

5.1 Conjugated Macrocycles

Macrocycles have attracted increased research interest in recent years. Especially cyclo(poly(*para*-phenylene)) ([n]CPPP) has only been synthetically accessible in the last couple of years. These rings form, topologically, the shortest possible nanotubes and are therefore interesting in order to study nanotube properties. Their applications in technology also includes novel molecular switches.

There are important similarities to linear polymers, especially regarding the applicability of the models used above. As in linear polymers, the electronic excitations couple to high-energy phonons and the low-energy excitations are Frenkel excitons. Furthermore, disorder in the system can be introduced by external or internal factors, as above. Again, fluctuations in the torsional angles are considered as the main source of internal disorder. The Frenkel-Holstein model therefore remains applicable.

Torsional disorder will, as in linear polymers, localise the excitons resulting in Anderson polarons, as described above. Once again, Landau polarons, *i.e.* localisation by self-trapping, is only applicable in a very narrow parameter regime, but the optical properties are affected in the same way by either form of localisation.

The biggest difference to linear polymers it the conformation, which has a profound effect on the optical properties. Within the Condon picture, only the $\bar{k} = \pm 1$ states (under PBCs) are optically active as shown in Fig. 5.1. This means that in ordered macrocycles in the absorption spectrum only one vibronic progression (of the $\bar{k} = \pm 1$) states is expected to be observed, while the emission spectrum should vanish (due to Kasha's rule). It will shown that this is not the case and that post-Condon effects couple different vibronic states and in this way transfer oscillator strength to normally dark states

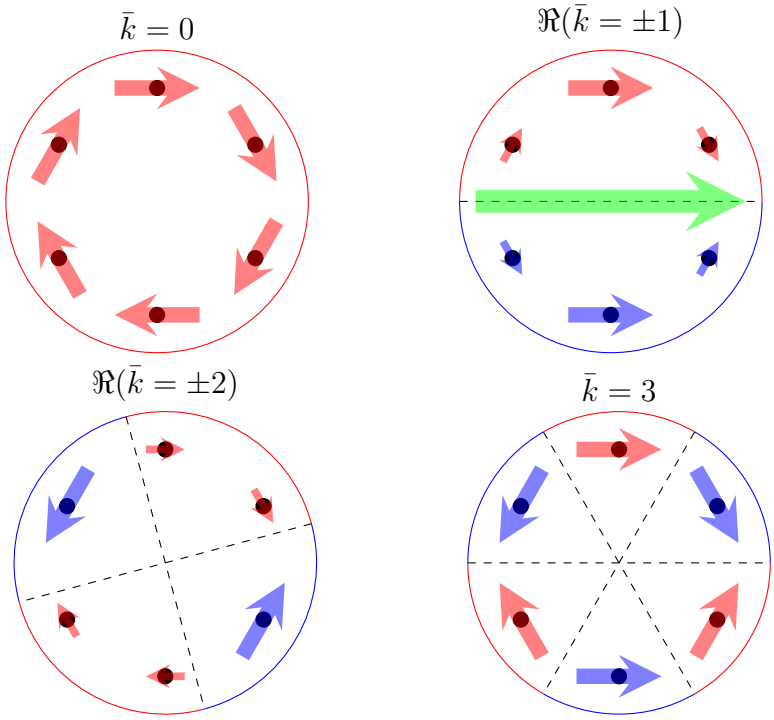


Figure 5.1.: Schematic representation of the alignment and magnitude of site transition dipole moments in a macrocycle with 6 sites. The red (blue) circles represent the phase of the excitonic wavefunction determining the alignment and the dashed lines show nodal planes. The green arrow is the resulting transition dipole moment for the $\bar{k} = \pm 1$ states.

so they become weakly allowed.

This section is organised as follows: first the role of temperature on the optical properties will be investigated and how state population affects the oscillator strengths of the transitions. Following from this the Herzberg-Teller effect, which makes dark states weakly allowed, will be introduced and analytical expressions for this effect within the Born-Oppenheimer limit will be derived and the fully quantized Frenkel-Holstein model with the DMRG routine will be used to verify these expressions numerically. Disorder is then introduced into the system by variation of the torsional angles and the effects on the optical spectra investigated. In Chapter 6 modelled spectra of cyclo(poly(*para*-phenylene ethynylene)) ([n]CPPE) are presented and compared to experimental results to verify the

predictions of this chapter.

5.1.1 Ordered Macrocycles

On a uniform macrocycle the total angular momentum is conserved and the states can be labelled by a quantum number, $\bar{\kappa}$, where $-N/2 < \bar{\kappa} \leq N/2$. The ground state of the system can then be expressed as $|\mathrm{GS};\kappa\rangle$, where the angular momentum is carried by the phonons alone. Equivalently, for the excited states, $|\mathrm{EX};\kappa'\rangle$, where the angular momentum is the sum of the exciton, k, and phonon, q, momenta. The transition dipole moment is then given as,

$$\boldsymbol{\mu} = \langle \mathrm{EX};\kappa' \left|\hat{\boldsymbol{\mu}}\right| \mathrm{GS};\kappa\rangle \,. \tag{5.1}$$

Symmetry arguments presented above then imply that $\boldsymbol{\mu} \neq 0$ if $|\bar{\kappa} - \bar{\kappa}'| = 1$.

It is now assumed that the entire angular momentum is carried by the exciton ($\kappa = k$) and that the polymer is a homomoiety polymer, *i.e.* the sites within the coarse-grained model are all identical. In that case, within a site basis,

$$|\mathrm{EX};k\rangle = \sum_n \Psi_k(n)\,|n\rangle \,, \tag{5.2}$$

with

$$\Psi_k(n) = \frac{1}{\sqrt{N}} \exp\left(\mathrm{i}\frac{2\pi n\bar{k}}{N}\right) = \frac{1}{\sqrt{N}} \exp\left(\mathrm{i}kn\right) , \tag{5.3}$$

being the Frenkel exciton centre-of-mass wavefunction with the energy,

$$E_k = \varepsilon_0 + 2J\cos\left(k\right) , \tag{5.4}$$

and

$$|n\rangle = \hat{a}_n^\dagger |0\rangle \,, \tag{5.5}$$

represents a Frenkel exciton on moiety n. In the limit of a ring with $N \to \infty$ the system forms part of the $D_{\infty h}$ point group and the wavefunctions can be classified accordingly. The $\bar{k} = 0$ state is then of A_{1g} symmetry, while $\bar{k} = \pm 1$ states are degenerate within the E_{1u} irreducible representation. Assuming the electronic ground state is of A_{1g} symmetry, transitions to the $\bar{k} = 0$ state are dipole forbidden, while transitions to the $\bar{k} = \pm 1$ states are allowed (and are the only ones that are allowed). In fact, using Eq. (4.25),

$$\boldsymbol{\mu}_k(N) = \sum_{n=1}^{N} \boldsymbol{\mu}_n \Psi_k(n), \tag{5.6}$$

and the wavefunctions above for the $\bar{k} = 0$ state, the associated transition dipole moment vanishes. For the $\bar{k} = \pm 1$ states, which are degenerate, the wavefunctions can be combined as,

$$\Psi_\pm = \frac{1}{\sqrt{2}} \left(\Psi_{\bar{k}=+1} \pm \Psi_{\bar{k}=-1} \right), \tag{5.7}$$

to give purely real and imaginary parts, *viz.*,

$$\Psi_+ = \sqrt{\frac{2}{N}} \cos(kn), \tag{5.8}$$

$$\Psi_- = \mathrm{i}\sqrt{\frac{2}{N}} \sin(kn). \tag{5.9}$$

Placing the ring (arbitrarily) in the xy-plane and centered at the origin, the transition dipole moment takes the form,

$$\boldsymbol{\mu}_\pm(N) = \mu_1 \sum_{n=1}^{N} \left[\cos(\phi_n)\hat{\mathbf{i}} + \sin(\phi_n)\hat{\mathbf{j}} \right] \Psi_\pm(n), \tag{5.10}$$

where ϕ_n is the (arbitrary) angle of site n with the x-axis. Evaluating these expressions then returns,

$$\boldsymbol{\mu}_{\pm} = \mu_1 \sqrt{\frac{N}{2}}. \tag{5.11}$$

As the oscillator strength of a transition is proportional to the square of the transition dipole moment, the contributions from the transition to the $\bar{k} = \pm 1$ add up to $\mu_1 N$, which is the sum rule for an ordered chain of N equal absorbers. This confirms the symmetry analysis that all other transitions are dark or, indeed, dipole forbidden as the entire available oscillator strength is associated with the transitions to the $\bar{k} = \pm 1$ states.

This simple analysis shows that absorption occurs into the $\bar{k} = \pm 1$ electronic states. Additionally, if relaxation into the $\bar{k} = 0$ state is assumed, emission is Condon-forbidden under Kasha's rule.

It will now be shown how this simple model breaks down, first by temperature effects, and then by introducing post-Condon effects, namely the Herzberg-Teller effect.

5.1.1.1 Temperature Effects

For large N, *i.e.* large macrocycles, the energies of the $\bar{k} = 0$ and $\bar{k} = \pm 1$ states can be expressed as a truncated Taylor expansion,

$$E_0 = \varepsilon_0 + 2J; \quad E_{\pm 1} = \varepsilon + 2J - \frac{8\pi^2 J}{2N^2} + \ldots, \tag{5.12}$$

which then gives the energy gap between the states as,

$$\Delta E_{01} \approx \frac{4\pi^2 |J|}{N^2}; \quad N \gg 1. \tag{5.13}$$

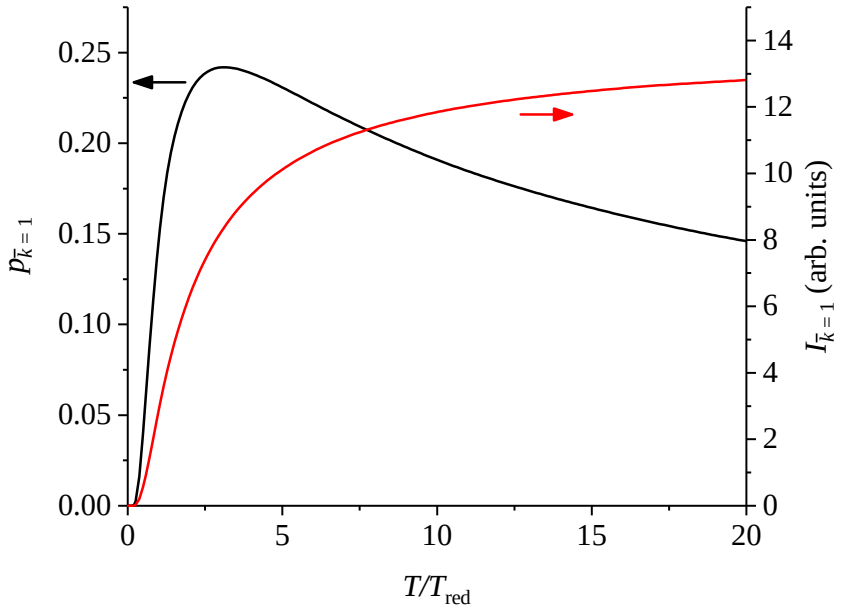


Figure 5.2.: Relative thermal population (black, left) and emission intensity (red, right) of the $\bar{k} = 1$ level of an ordered macrocycle against T/T_{red}. T_{red} is defined in the text. The semi-classical Frenkel-Holstein model was used here.

A reduced temperature can thus be defined as,

$$T_{\mathrm{red}} = \frac{4\pi^2 J}{k_{\mathrm{B}} N^2}, \tag{5.14}$$

to quantify temperature effects. Using Boltzmann statistics and the semi-classical Frenkel-Holstein model, Fig. 5.2 shows the relative population of the $\bar{k} = \pm 1$ levels against the reduced temperature. The population reaches a maximum for $T/T_{\mathrm{red}} \approx 3$ before decreasing for higher T/T_{red}. The energy spectrum is bounded and hence $p_{\bar{k}=1} \to 1/N$ for $T \gg T_{\mathrm{red}}$.

Within the Condon approximation only the $\bar{k} = \pm 1$ levels emit and hence the associated emission intensity is simply $N \times p_{\bar{k}=1}$, as also shown in Fig. 5.2. For large T or small T_{red} (*i.e.* large N) the intensity becomes independent of both T and N. Note that for the

intensity both the abscissa and ordinate are dependent on N and hence the maximum visible in the relative population vanishes.

5.1.1.2 Herzberg-Teller Correction

Within the Condon approximation the electronic transition dipole moment is taken to be independent of the nuclear normal modes. If coupling to one normal mode, $Q^{(q)}$, is considered, as is done in the Frenkel-Holstein model, the electronic transition dipole moment can be expanded in a Taylor series around the equilibrium, $Q_0^{(q)}$ as,

$$\boldsymbol{\mu}\left(Q^{(q)}\right) = \boldsymbol{\mu}\left(Q_0^{(q)}\right) + \left.\frac{\partial \boldsymbol{\mu}}{\partial Q^{(q)}}\right|_{Q_0^{(q)}} \left(Q^{(q)} - Q_0^{(q)}\right) + \dots . \tag{5.15}$$

The Condon approximation is then equivalent to only considering the leading term. The linear term is the so-called Herzberg-Teller correction and this term will be considered in the following.

Within the Born-Oppenheimer approximation the ground and excited state wavefunctions can be factorised as,

$$|\mathrm{GS}, \upsilon\rangle = \Psi_{\mathrm{GS}}\left(\boldsymbol{r}; Q^{(q)}\right) \phi_{\upsilon}^{\mathrm{GS}}\left(Q^{(q)}\right), \tag{5.16}$$

$$|\mathrm{EX}_k, \upsilon'\rangle = \Psi_{\mathrm{EX}}^{(k)}\left(\boldsymbol{r}; Q^{(q)}\right) \phi_{\upsilon'}^{\mathrm{EX}}\left(Q^{(q)}\right), \tag{5.17}$$

where υ and υ' are the vibrational levels and Ψ and ϕ are the electronic and nuclear wavefunctions, respectively. This allows for the expression of the transition dipole moment

as,

$$\begin{aligned}\boldsymbol{\mu}_{\upsilon'\upsilon} &= \langle \mathrm{GS}, \upsilon \left| \hat{\boldsymbol{\mu}} \right| \mathrm{EX}_k, \upsilon' \rangle \\ &= \int \boldsymbol{\mu}_{\mathrm{e}}^{k} \left(Q^{(q)} \right) \phi_{\upsilon}^{\mathrm{GS}} \left(Q^{(q)} \right) \phi_{\upsilon'}^{\mathrm{EX}} \left(Q^{(q)} \right) \mathrm{d}Q^{(q)},\end{aligned} \tag{5.18}$$

where $\boldsymbol{\mu}_{\mathrm{e}}^{k} \left(Q^{(q)} \right)$ is the electronic transition dipole moment given as,

$$\boldsymbol{\mu}_{\mathrm{e}}^{k} \left(Q^{(q)} \right) = \int \Psi_{\mathrm{GS}} \left(\boldsymbol{r}; Q^{(q)} \right) \hat{\boldsymbol{\mu}} \Psi_{\mathrm{EX}}^{k} \left(\boldsymbol{r}; Q^{(q)} \right) \mathrm{d}\boldsymbol{r}. \tag{5.19}$$

Using Eq. (5.15) for $\boldsymbol{\mu}_{\mathrm{e}}^{l} \left(Q^{(q)} \right)$ then gives,

$$\begin{aligned}\boldsymbol{\mu}_{\upsilon\upsilon'} = \boldsymbol{\mu}_{\mathrm{e}}^{k} \left(Q_0^{(q)} \right) & \int \phi_{\upsilon}^{\mathrm{GS}} \left(Q^{(q)} \right) \phi_{\upsilon'}^{\mathrm{EX}} \left(Q^{(q)} \right) \mathrm{d}Q^{(q)} \\ + \left. \frac{\partial \boldsymbol{\mu}_{\mathrm{e}}^{k}}{\partial Q^{(q)}} \right|_{Q_0^{(q)}} & \int \phi_{\upsilon}^{\mathrm{GS}} \left(Q^{(q)} \right) \left(Q^{(q)} - Q_0^{(q)} \right) \phi_{\upsilon'}^{\mathrm{EX}} \left(Q^{(q)} \right) \mathrm{d}Q^{(q)} \\ + \ldots .\end{aligned} \tag{5.20}$$

If the first term vanishes due to symmetry arguments (as described above), the linear term becomes the leading term and this term does not vanish for non-totally symmetric modes, *i.e.* for modes with $q \neq 0$. This term is the Herzberg-Teller correction and this contribution can be analysed further within the model using perturbation theory.

Mixing between the ground state and the first excited ($\bar{k} = 0$) state is not considered due to the large energy gap. However, the second excited states ($\bar{k} = \pm 1$) will mix with the first excited state and will render it non-totally symmetric, causing a breakdown of the Condon approximation. In the model, the perturbation causing this mixing is the exciton-phonon coupling,

$$\hat{V} = -A\hbar\omega \sum_{n=1}^{N} Q_n \hat{a}_n^{\dagger} \hat{a}_n, \tag{5.21}$$

in the semi-classical form. The local displacement, Q_n, for cyclic systems can be expressed using the Bloch transform as,

$$Q_n = \sum_k Q^{(q)} \frac{\exp\left(-\mathrm{i}qn\right)}{\sqrt{N}}. \tag{5.22}$$

Using perturbation theory, the $\bar{k} = 0$ exciton wavefunction can be expressed as,

$$\Psi_0\left(Q^{(q)}\right) = \Psi_0 + \sum_{\bar{k}=\pm 1} \frac{\left\langle \Psi_0 \left| \hat{V} \right| \Psi_{\bar{k}} \right\rangle}{\Delta E_{0\bar{k}}} \Psi_{\bar{k}} + \ldots. \tag{5.23}$$

The matrix element can be evaluated using Eq. (5.3),

$$\left\langle \Psi_0 \left| \hat{V} \right| \Psi_{\bar{k}=\pm 1} \right\rangle = -\frac{A\hbar\omega}{\sqrt{N}} Q^{(q')}, \tag{5.24}$$

where $q' = \pm 2\pi$ are the only contributing phonon modes due to symmetry. Hence,

$$\Psi_0\left(Q^{(q')}\right) \approx \Psi_0 - \sum_{\bar{k}=\pm 1} \frac{A\hbar\omega}{\sqrt{N}\Delta E_{0\bar{k}}} Q^{(q')} \Psi_j. \tag{5.25}$$

Using Eq. (5.6) then yields,

$$\boldsymbol{\mu}_{\mathrm{e}}^0\left(Q^{(q')}\right) = -\frac{A\hbar\omega}{\sqrt{N}\Delta E_{0\bar{k}}} Q^{(q')} \times \frac{\boldsymbol{\mu}_1\sqrt{N}}{2}, \tag{5.26}$$

which in turn gives the electronic contribution to the Herzberg-Teller term as,

$$\frac{\partial \boldsymbol{\mu}_{\mathrm{e}}^0}{\partial Q^{(q)}} = -\frac{\boldsymbol{\mu}_1 A\hbar\omega}{2\Delta E_{0\bar{k}}}. \tag{5.27}$$

Expressing the energy difference for long chains (*i.e.* $N \gg 1$) as a Taylor series,

$$\Delta E_{0\bar{k}} = 2J\left(1 - \cos\left(\frac{2\pi}{N}\right)\right) \approx J\left(\frac{2\pi}{N}\right)^2; \quad N \gg 1. \tag{5.28}$$

This allows the prediction of the Herzberg-Teller contribution (which is the only contribution in the case of an ordered macrocycle) to the intensity as,

$$I_{01}^{\mathrm{HT}} = |\boldsymbol{\mu}_{01}|^2 \propto |\boldsymbol{\mu}_1|^2 A^2 \left(\frac{\hbar\omega}{J}\right)^2 N^4 \times \mu_{\mathrm{vib}}, \tag{5.29}$$

where μ_{vib} is the vibrational contribution to the overall transition dipole moment given by the matrix element,

$$\mu_{\mathrm{vib}} = \int \phi_{\upsilon}^{\mathrm{GS}}\left(Q^{(q)}\right)\left(Q^{(q)} - Q_0^{(q)}\right)\phi_{\upsilon'}^{\mathrm{EX}}\left(Q^{(q)}\right)\mathrm{d}Q^{(q)}. \tag{5.30}$$

The matrix element, $\left\langle \Psi_0 \left| Q^{(q)} \right| \Psi_0 \right\rangle = 0$ for any $q \neq 0$, and as such the energy potential surface for a given non-totally symmetric normal mode is not displaced relative to the ground state and the integral given above evaluates as,

$$\mu_{\mathrm{vib}} = \left(\frac{\upsilon}{2}\right)^{\frac{1}{2}} \delta_{\upsilon,\upsilon'+1}. \tag{5.31}$$

For the 0-1 emission ($\upsilon = 0; \upsilon' = 1$) this then results in,

$$I_{01}^{\mathrm{HT}} \propto N^4 |\boldsymbol{\mu}_1|^2 A^2 \left(\frac{\hbar\omega}{J}\right)^2. \tag{5.32}$$

The validity of this equation will now be discussed. As it is only valid to second order in

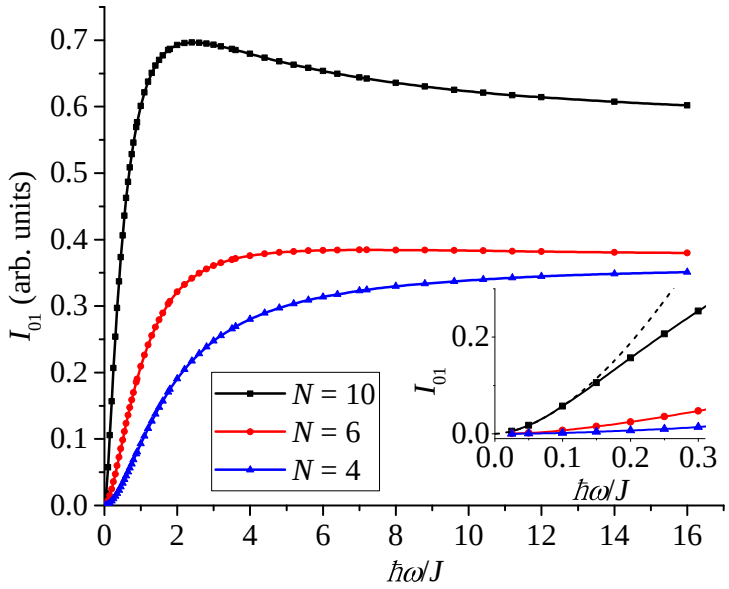


Figure 5.3.: Evolution of the 0-1 emission intensity for macrocycles of varying size against the $\hbar\omega/|J|$. The inset also shows parabolic fits (dashed), which for $N = 4$ and $N = 6$ are identical with the numerical results and only deviates for $N = 10$ as $\hbar\omega/|J| > 0.15$. These results are calculated using the (essentially exact) fully quantised Frenkel-Holstein model and the DMRG routine.

perturbation theory, it is expected to hold true only if,

$$\left|\frac{A\hbar\omega}{\sqrt{N}}Q^{(q)}\right| \ll \Delta E_{0\bar{k}}, \tag{5.33}$$

or

$$\left(\frac{\hbar\omega}{J}\right)\frac{A}{N^{3/2}} \ll 1. \tag{5.34}$$

Fig. 5.3 shows the dependence of the 0-1 emission intensity as a function of $\hbar\omega/|J|$ in ordered macrocycles of different size. For $\hbar\omega/|J| \leq 0.15$ the square-dependence of I_{01} is clearly reproduced confirming that the effect is indeed the Herzberg-Teller correction. As the expansion is only correct up to second order in perturbation theory, it is unsurprising that the prediction breaks down relatively quickly. Notably, however, it is valid for

$\hbar\omega/|J| = 0.1$, a value applicable for most conjugated polymers. The figure also shows that in the anti-adiabatic limit ($\hbar\omega/|J| >> 1$) the intensity becomes independent of $\hbar\omega/|J|$. As the macrocycles are ordered this is behaviour shows the antiadiabatic limit of the Herberg-Teller effect.

As will be discussed below, when disorder is introduced to the system the lowest energy transitions in the macrocycle become allowed and the 0-1 transitions intensity is enhanced by the Condon contributions. However, it will be shown that the Herzberg-Teller term remains a major contribution even in disordered systems.

5.1.2 Disordered Macrocycles

In the previous sections the importance of incorporating post-Condon effects when treating macrocycles has been discussed as well as the effect of temperature. In this discussion, temperature was merely taken to populate the $\bar{k} = \pm 1$ level. However, in real systems, temperature will cause disorder within the macrocycle. This is, just as it was the case in linear polymers, due to the shallow dihedral energy potentials. The disorder within the system localises the excitons to sections of the chain, just as it was the case in linear polymers, with the lowest energy excitations forming a space-filling, non-overlapping, and quasi-nodeless subset of these states, which have been referred to as LEGSs above. As a consequence of the localisation, the symmetry of the system is broken rendering more (and in most cases all) transitions symmetry-allowed. In the case of the conjugation length being smaller than the circumference of the macrocycle, the chromophores are bent and the properties of these will be discussed in greater detail in the next section.

The localisation of the LEGSs can be quantified by calculating the average participation number, $\langle \mathrm{PN} \rangle$, as defined above, over an ensemble for a given amount of disorder. We expect the PN to go down as the disorder increases, leading to shorter conjugation lengths

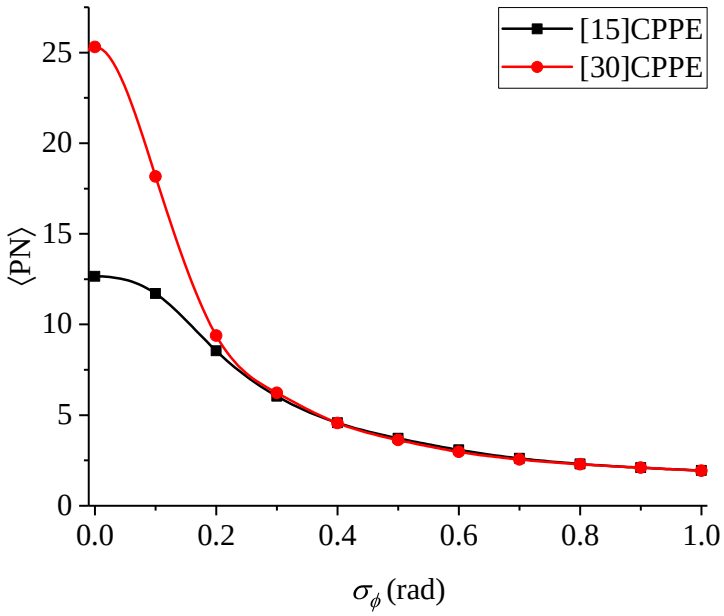


Figure 5.4.: Average Participation Number for [15]CPPE and [30]CPPE against disorder, σ_ϕ. The PN is given in monomer units and the values were averaged over 1000 different rings.

within the chromophores. Moreover, once the PN becomes smaller than the circumference of the ring, it is expected that the PN becomes independent of the ring size, *i.e.* for large σ_ϕ the PN will not be a function of the ring size, any more. This is shown in Fig. 5.4. It can be clearly seen that for $\sigma_\phi \approx 0.2$ rad the average PN is independent of the ring size and moreover that disorder has a more pronounced effect for large macrocycles. This is a consequence of Anderson localisation as discussed in Sec. 2.2.2.4.

The resulting localisation is expected to have profound effects on the transition dipole moments of the various excitonic states. While the $\bar{k} = 0$ state is dark for ordered systems, the $\bar{k} = \pm 1$ states will carry almost all of the oscillator strength. With increasing σ_ϕ the oscillator strength of the $\bar{k} = 0$ state is expected to increase on the expense of the $\bar{k} = 1$ states and ultimately tending towards to the same value for large σ_ϕ. It has to be noted that for disordered systems $\bar{k}$ is not a good quantum number any more (as the breaking

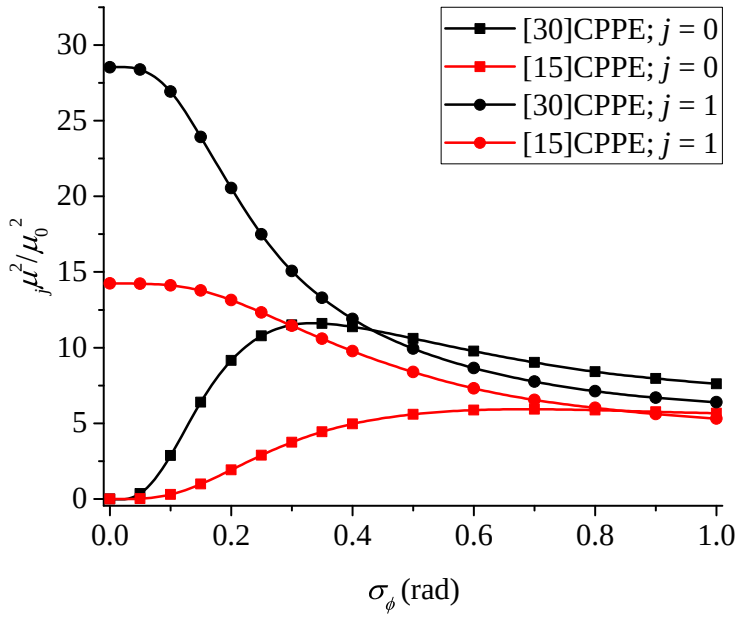


Figure 5.5.: Evolution of the squared transition dipole moments for the two lowest-energy purely excitonic states in [15]CPPE (red) and [30]CPPE (black) against disorder *within the Condon approximation*. For $\sigma_\phi = 0$ the states correspond to the $\bar{k} = 0$ (squares) and $\bar{k} = 1$ (circles) states of a particle on a ring.

of the symmetry leads to states that are more appropriately described by OBCs) and the notation is only to simplify the discussion. In fact, the $\bar{k} = 0$ and $\bar{k} = \pm 1$ states will become LEGSs for large σ_ϕ and will thus be almost degenerate. In this limit, the discussion of the Herzberg-Teller effect breaks down as perturbation theory becomes non-applicable. Regardless, Fig. 5.5 shows the evolution of the associated transition dipole moments for the lowest two states for different ring sizes. As was the case for the average PN, the $\bar{k} = \pm 1$ transition dipole moment decreases with increasing disorder, owing to localisation. The oscillator strength is transferred to the now dipole allowed $\bar{k} = 0$ state. For large disorder, the oscillator strengths tend towards the same value, emphasising the quasi-degeneracy of the LEGSs originating in the various excitonic states.

This discussion explains the distribution of oscillator strength in disordered macro-

cycles and that, for large σ_ϕ (or T), the optical properties become near-independent of the ring size. Moreover, it shows that the Herzberg-Teller correction is predominantly a low-T effect, which is more or less washed out for large disorder. The combined effects of temperature and curvature on the optical spectra of macrocycles will now be discussed before modelling the spectra of realistic systems in Chapter 6.

5.1.2.1 Herzberg-Teller Correction and Disorder

Combining the role of disorder, which breaks the symmetry and thus, within the Condon approximation, makes the transition to the $\bar{k} = 0$ state dipole allowed, and the Herzberg-Teller correction, which enhances the 0-1 emission transition of this state, allows the discussion of the relative importance of these effects. To quantify this, the ratio of the average conjugation length of a LEGS and the total circumference of the ring measured by the number of moieties, N, is introduced. Then,

$$\theta = 2\pi \frac{\langle \mathrm{CL} \rangle}{N}, \tag{5.35}$$

is the angle corresponding to the spread of the LEGS. $\theta \to 0$ indicates progressing linearisation of the LEGS, whereas $\theta = 2\pi$ is a fully closed circular LEGS.

As shown in Sec. 4.2.1, the emission intensity ratio within the Condon approximation evaluates as,

$$\frac{\langle I_{00} \rangle}{\langle I_{01} \rangle} = \frac{\langle \mathrm{PN} \rangle}{g_1^2}, \tag{5.36}$$

which is independent of the geometry of the LEGSs. As Kasha's law is assumed, the ensemble averages are taken over all (equally populated) LEGSs. This expression clearly fails for circular chromophores as $I_{00} \to 0$ as $\theta \to 2\pi$ while I_{01} remains finite due to the

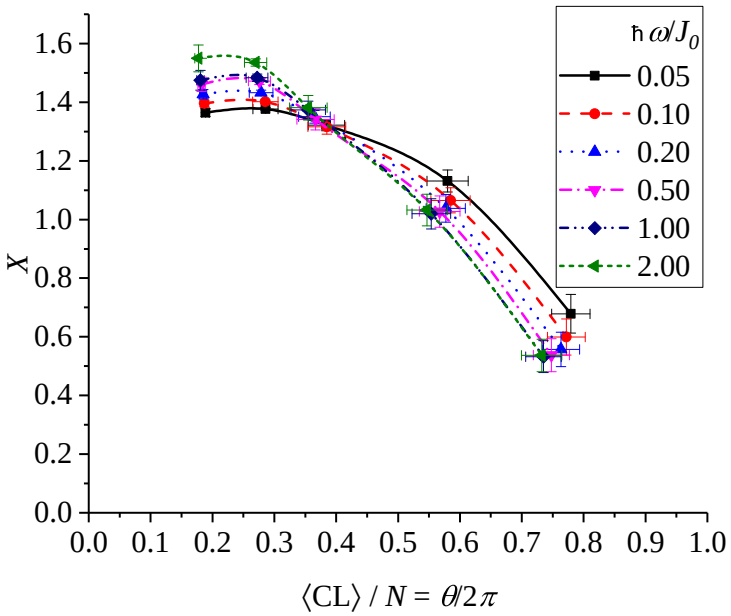


Figure 5.6.: Scaled emission intensity ratio, X, against curvature for varying values of $\hbar\omega/J_0$ where $J_0 = J_{\mathrm{DD}} + J_{\mathrm{SE}}\cos^2(0)$. The results were obtained using the DMRG routine and therefore contain both, Condon and Herzberg-Teller contributions.

Herzberg-Teller correction. A quantity, X, can now be defined as,

$$X = \frac{\langle I_{00}\rangle}{\langle I_{01}\rangle \langle \mathrm{PN}\rangle}, \tag{5.37}$$

which, for a perfect observation of the Condon approximation, is a constant $(1/g_1^2)$. Any deviation of this expression is due to post-Condon effects, namely the Herzberg-Teller correction.

Fig. 5.6 shows the evolution of X against the curvature of the chromophore measured by $\theta/2\pi$ for different values of $\hbar\omega/|J_0|$, where J_0 is the transfer integral for a planar system, *i.e.* $J_0 = J_{\mathrm{DD}} + J_{\mathrm{SE}}\cos^2(0) = J_{\mathrm{DD}} + J_{\mathrm{SE}}$. In the adiabatic limit, $\hbar\omega \to 0$ the prediction that X is a constant independent of the curvature is well reproduced for chromophores with $\theta/2\pi \gtrsim 0.3$. For large curvatures the value of X decreases and reaches 0 for a fully

circular chromophore as $I_{00} \to 0$ while I_{01} remains finite. The same general trend holds true for larger values of $\hbar\omega/J_0$ although the value for $\theta/2\pi \to 0$ increases with $\hbar\omega/J_0$ and the decrease with increasing curvature is more pronounced. If scaled appropriately, the curves are expected to collapse onto one (see Sec. 5.2.1). It is also noteworthy, that the results presented in Fig. 5.6 do not depend on any other parameters. A more formal discussion of these results and effects is presented in Sec. 5.2.1 when discussing bent chromophores.

The shown results are in qualitative agreement with Hestand and Spano [39], who predicted the effect of the curvature on the emission intensity ratio and other optical properties. Their predictions are made within the anti-adiabatic regime, while the resulst presented are obtained within the adiabatic regime. As a consequence no quantitative agreement is found.

Fig. 5.7 shows the total $0-1$ emission intensity normalised to the Herzberg-Teller correction for a fully circular chromophore. With increasing disorder in the system the overall intensity increases due to Condon contributions from now allowed transitions due to the breaking of the symmetry, before approaching a constant value for large values of disorder when the system becomes saturated with LEGSs. Simultaneously, due to the localisation of the exciton the curvature of the chromophores reduces with increasing disorder and the intensity due to the Herzberg-Teller correction decreases, *i.e.* the gain in intensity with increasing disorder occurs at the same time as the reduction of the Herzberg-Teller intensity, I_{01}^{HT}.

5.1.2.2 Summary of Effects

A short overview of the effects discussed above will now be given before turning to the more general class of bent chromophores.

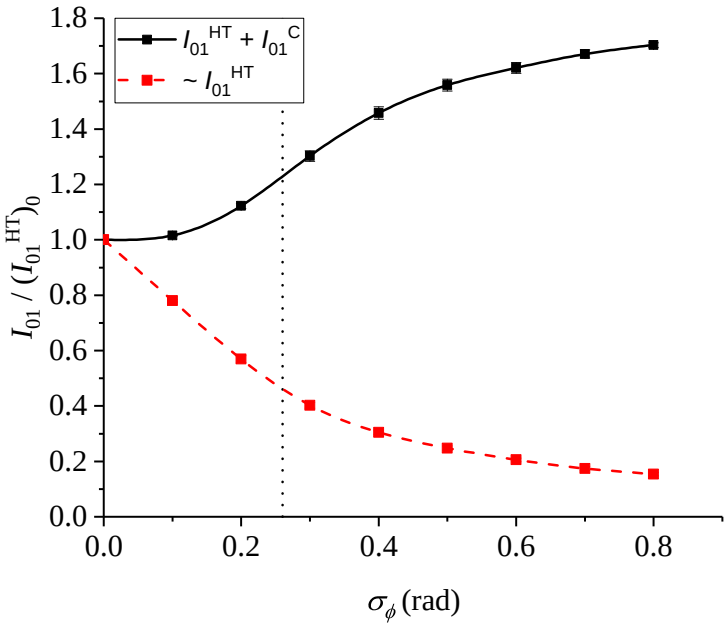


Figure 5.7.: Evolution of the 0-1 emission intensity of a [15]CPPE with disorder normalised to the intensity for a perfectly ordered ring, $(I_{01}^{\mathrm{HT}})_0$, as well as the Herzberg-Teller contribution which is proportional to the chromophore length as measured by the CL or the PN. The dotted line indicated disorder at room temperature for CPPE.

Perfectly ordered macrocycles (at $T = 0$) display, contrary to the Condon prediction, an emission spectrum with a distinctive peak arising from the mixing of states causing a breakdown of the symmetry restrictions. namely, the $\bar{k} = 1, \upsilon = 1$ state mixes with the non-totally symmetric $\bar{k} = 1, \upsilon = 0$ state, transferring oscillator strength to the former which gives rise to a 0-1 emission signal. This so-called Herzberg-Teller effect also enhances the 1-0 absorption signal by mixing the same state as above. As in emission, the 0-0 $\bar{k} = 0$ transition for absorption is forbidden. For absorption, this will give rise to a signal which looks like the 0-0 $\bar{k} = 0$ signal, but the spacing to the following peaks is too close for it to be the corresponding vibronic progression. The signal observed is in fact the 0-1 $\bar{k} = 0$ signal with the other signal belonging to the $\bar{k} = 1$ (and higher) manifold.

By increasing disorder (*i.e.* T) the symmetry of the system breaks down and the $\bar{k} = 0$

transitions become Condon allowed. This will naturally enhance the 0-1 peak and the 0-0 $\bar{k} = 0$ peak will appear and become more pronounced for increasing disorder. In the absorption spectrum, this will be observed as an emerging shoulder on the low-energy side of the spectrum, while for the emission spectrum it will be an emerging peak on the high-energy side. Simultaneously, the Herzberg-Teller correction will become less important. The 0-1 emission will continue to increase, implying that a large amount of oscillator strength is transferred to the $\bar{k} = 0$ state.

5.2 Bent Chromophores

In order to discuss the photophysics of bent chromophores the momentum space representation of the Frenkel-Holstein model introduced in Section 2.2.2.1 will be used. Bent chromophores occur in highly disordered macrocycles (if the conjugation length is less than the circumference of the ring) and in disordered chains, especially if *cis-trans* defects are involved (as they are in PPV, for instance). In contrast to perfectly linear chains and macrocycles the symmetry selection rules are heavily relaxed due to a lack of symmetry in the systems, generally. However, as the Herzberg-Teller correction introduced earlier is an effect of the curvature of the chain, it will also be present in bent chromophores, albeit to a significantly lesser extent, as discussed previously for heavily disordered macrocycles.

In bent chromophores a multitude of transitions into essentially every exciton centre-of-mass state, labelled by $\bar{k}$, can be observed. Fig. 5.8 shows schematically the transitions into the first four states under open boundary conditions. For bent chromophores the choice of boundary conditions has no effect on which transitions are allowed due to the relaxation of the symmetry selection rules, solely the intensity of a transition is influenced. For either boundary conditions, the transition dipole moment of the first transition (into

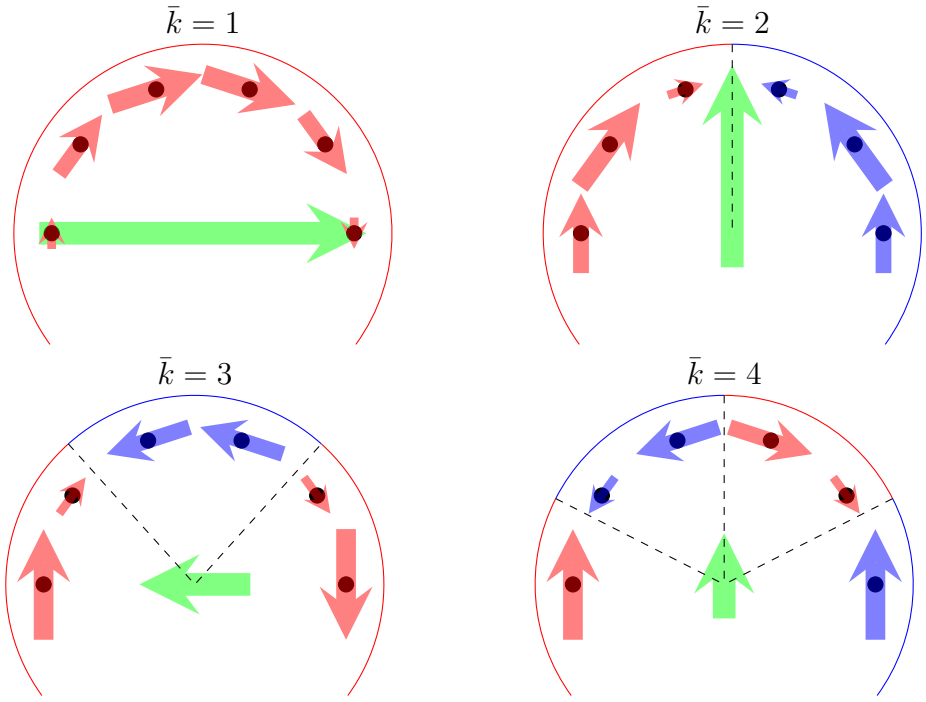


Figure 5.8.: Schematic representation of the total transition dipole moments (green) of the first four exciton states of a six-site bent chromophore under open boundary conditions. The outer arcs represent the phase of the excitonic wavefunctions and the on-site transition dipole moments are represented by scaled arrows. The alternating x- and y-polarisation of the TDM is clearly visible.

the $\bar{k} = 0$ or $\bar{k} = 1$ state) is aligned with the chord joining the ends of the bent chromophore. For periodic boundary conditions all other transitions are aligned with the axis perpendicular to the chord, while for open boundary conditions the alignment alternates, as shown. The local coordinate along the chord will be referred to as the x-axis, while the perpendicular direction is the y-axis. In this language, under PBCs the transition dipole moment of the first transition is x-aligned (or the transition is x-polarised), while all others are y-aligned (y-polarised). For OBCs we observe alternating alignment.

Expressions for the transition intensities will now be derived and the contributions of post-Condon effects discussed.

5.2.1 Generalised Herzberg-Teller Correction

For this discussion the momentum space representation of the Frenkel-Holstein model as introduced in Section 2.2.2.3 will be used, again. The fully quantised Hamiltonian for periodic and open boundary conditions reads, respectively,

$$\begin{aligned}\hat{H}_{\mathrm{QFH}}^{\mathrm{PBC}} = &\sum_k \left(\varepsilon_0 + 2J\cos k\right) \tilde{a}_k^\dagger \tilde{a}_k + \hbar\omega \sum_q \left(\tilde{b}_q^\dagger \tilde{b}_q + \frac{1}{2}\right) - \frac{A\hbar\omega}{\sqrt{2N}}\left(\tilde{b}_0 + \tilde{b}_0^\dagger\right) \\ &- \frac{A\hbar\omega}{\sqrt{2N}} \sum_{k,q\neq 0} \left(\tilde{a}_k^\dagger \tilde{a}_{k-q} \tilde{b}_q + \tilde{a}_k^\dagger \tilde{a}_{k+q} \tilde{b}_q^\dagger\right); \quad k = \frac{2\pi\bar{k}}{N}.\end{aligned} \tag{5.38}$$

$$\begin{aligned}\hat{H}_{\mathrm{QFH}}^{\mathrm{OBC}} = &\sum_k^N \left(\varepsilon_0 + 2J\cos k\right) \tilde{a}_k^\dagger \tilde{a}_k + \hbar\omega \sum_q^N \left(\tilde{b}_q^\dagger \tilde{b}_q + \frac{1}{2}\right) \\ &- \frac{2A\hbar\omega}{(N+1)^{3/2}} \sum_{k,k',q}{}' X(k,k',q) \tilde{a}_k^\dagger \tilde{a}_{k'} \left(\tilde{b}_q^\dagger + \tilde{b}_q\right); \quad k = \frac{\bar{k}\pi}{N+1}.\end{aligned} \tag{5.39}$$

First order perturbation theory is now employed to derive the effect of excited state mixing on the optical spectra. For this purpose the purely excitonic and phononic parts will be taken to be the unperturbed Hamiltonian, $\hat{H}_0$, while the exciton-phonon coupling term will be the perturbation, $\hat{H}_1$, causing the mixing of the states.

The unperturbed Hamiltonian has the exact Born-Oppenheimer eigenstates,

$$|k; n_{q_1}, n_{q_2}, \ldots, n_{q_N}\rangle^{(0)} = |k\rangle \otimes |n_{q_1}, n_{q_2}, \ldots, n_{q_N}\rangle\rangle\,, \tag{5.40}$$

where,

$$|k\rangle = \tilde{a}_k^\dagger |0\rangle\,, \tag{5.41}$$

and,

$$|n_q\rangle\rangle = \frac{\left(\tilde{b}_q^\dagger\right)^{n_q}}{\sqrt{n_q!}} |0\rangle\rangle\,. \tag{5.42}$$

$|0\rangle$ and $|0\rangle\rangle$ are the exciton and phonon vacuums, respectively. Such an unperturbed state has the eigenenergy,

$$E^{(0)}\left(k; n_{q_1}, n_{q_2}, \ldots, n_{q_N}\right) = \varepsilon_0 + 2J\cos k + \hbar\omega \sum_q \left(n_q + \frac{1}{2}\right), \tag{5.43}$$

with k appropriately chosen for the corresponding boundary conditions.

The different contributions for the 0-0 absorption and emission, as well as for the 1-0 absorption and the 0-1 emission, arising from the unperturbed Hamiltonian and the exciton-phonon coupling, will now be analysed.

5.2.1.1 0-0 Absorption

As stated before, the transition dipole moment associated with the 0-0 absorption into the jth exciton state is given by,

$$\boldsymbol{\mu}_k^{00} = {}^{(0)}\left\langle k; n_q = 0 \left| \hat{\boldsymbol{\mu}} \right| \mathrm{GS}; 0 \right\rangle, \tag{5.44}$$

where,

$$|\mathrm{GS}; 0\rangle = |0\rangle \otimes |0\rangle\rangle, \tag{5.45}$$

is the true excitonic and phononic groundstate. Assuming the chromophore to be in the xy-plane with the corresponding unit vectors $\hat{\mathbf{i}}$ and $\hat{\mathbf{j}}$, the transition dipole operator is given as,

$$\hat{\boldsymbol{\mu}} = \mu_0 \sum_{n=1}^{N} \left(\hat{\mathbf{i}}\cos\theta_n + \hat{\mathbf{j}}\sin\theta_n\right)\left(\hat{a}_n + \hat{a}_n^\dagger\right), \tag{5.46}$$

in a site basis. This then gives the contributions in the respective directions as,

$$\mu^{00}_{x,\bar{k}} = \begin{cases} 0, & \bar{k} = \bar{k}' \\ \mu_0 \sum_n \Psi^{\bar{k}}_n \cos\theta_n, & \bar{k} = \bar{k}'', \end{cases} \tag{5.47}$$

and

$$\mu^{00}_{y,\bar{k}} = \begin{cases} \mu_0 \sum_n \Psi^{\bar{k}}_n \sin\theta_n, & \bar{k} = \bar{k}' \\ 0, & \bar{k} = \bar{k}'', \end{cases} \tag{5.48}$$

with $\Psi^{\bar{k}}_n$ being the wavefunction of the kth exciton state on the nth side under given boundary conditions. For periodic boundary conditions, $\bar{k}' = 0$ and $\bar{k}''$ is any other integer, while for open boundary conditions $\bar{k}'$ is even, while $\bar{k}''$ is odd. That shows again that for open boundary conditions the direction of the transition dipole moment is alternating with $\bar{k}$, while for periodic boundary conditions every transition dipole moment is perpendicular to the $\bar{k} = 0$ dipole moment.

Using these expressions the absorption intensity contributions for the 0-0 transition can be defined as (for OBCs),

$$A^{00}_x = \left(\mu^{00}_{x,\bar{k}=1}\right)^2, \tag{5.49}$$

$$A^{00}_y = \left(\mu^{00}_{y,\bar{k}=2}\right)^2, \tag{5.50}$$

for open boundary conditions ignoring any multiplicative factors. The evolution of these intensities as a function of bent angle is plotted in Fig. 5.9 for two chains, $N = 4$ and $N = 100$, for which the observed behaviour is close to the thermodynamic limit, as well as their sum, normalised to the chain length.

Especially for linear chains ($\varphi/2\pi = 0$) the absorption is dominated by the 0-0 transitions and solely by the $\bar{k} = 1$ state, as expected (the $\bar{k} = 2$ state is dark for a linear

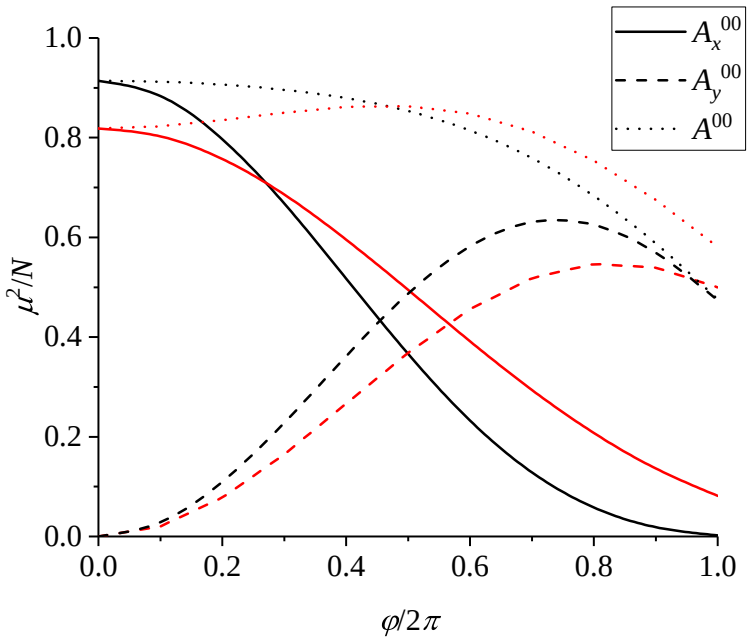


Figure 5.9.: Evolution of the x and y contributions to the 0-0 absorption in unperturbed bent chromophores as a function of the bent angle, φ, for chromophores with $N = 4$ (black) and $N = 100$ (red) under open boundary conditions. A_x^{00} (solid line) arises from the $\bar{k} = 1$ state, while A_y^{00} (dashed line) is absorption into the $\bar{k} = 2$ state. The dotted line shows the sum of these two contributions. Note that A_x^{00} does not vanish for the 4-site ring, but becomes very small.

chain). With increasing $\varphi/2\pi$, A_x^{00} decreases as the ends of the chain get closer and the chord length, which is proportional to the transition dipole moment, decreases. For long chains the intensity doesn't vanish due to surface affects arising for OBCs; it vanishes for closed chains of any length under PBCs. The y-contribution arising from the $\bar{k} = 2$ state becomes significant for bent chains but for almost closed chains it decreases again. This is due to the alignment of the two contributions towards this transition dipole moment. These are proportional to the connection line from the end of the chains to the mid-point.

The summed contributions show clearly that the absorption spectrum is dominated by the two shown transitions and the discussion will be restricted to these two and their respective vibronic progressions from now on.

For the emission it is found that I_x^{00} is proportional to both, A_x^{00} and I_y^{00}, assuming Kasha's rule.

5.2.1.2 1-0 Absorption

The transition dipole operator (Eq. 5.46) does not contain any phonon creation or annihilation operators and as such the matrix element ${}^{(0)}\langle k; n_q = 1 | \hat{\boldsymbol{\mu}} | \mathrm{GS}; 0\rangle$ vanishes due to the orthogonality of the phonon states. The 1-0 absorption intensity is thus due to the mixing of states by the perturbation, $\hat{H}_1$, which is the exciton-phonon coupling. Expanding to first-order in perturbation theory,

$$|k; n_q = 1\rangle \simeq |k; n_q = 1\rangle^{(0)} - \sum_{k'} \frac{{}^{(0)}\left\langle k'; n_q = 0 \left| \hat{H}_1 \right| k; n_q = 1 \right\rangle^{(0)}}{\Delta E_{k';k,q}} |k'; n_q = 0\rangle^{(0)}, \quad (5.51)$$

where

$$\Delta E^{(0)}_{k';k,q} = E^{(0)}(k'; n_q = 0) - E^{(0)}(k; n_q = 1). \quad (5.52)$$

Fig. 5.10 shows the available vibronic states for a system and the principal coupling between states. The states comprising the $\bar{k} = 1, \upsilon = 1$ level can couple to the $\bar{k} = 1, \upsilon = 0$ state, which is associated with an x-polarised transition and to the $\bar{k} = 2, \upsilon = 0$ level associated with a y-polarised transition.

x-Polarised Transition The mixing between the $\left|\bar{k} = 1, n_q = 1\right\rangle^{(0)}$ and $\left|\bar{k} = 1, n_q = 0\right\rangle^{(0)}$ states occurs via $\hat{H}_1$ and using Eq. (5.51) and,

$${}^{(0)}\left\langle \bar{k} = 1; n_q = 0 \left| \hat{H}_1 \right| \bar{k} = 1; n_q = 1 \right\rangle^{(0)} = -\frac{2A\hbar\omega}{N+1}^{3/2} X(1,1,q), \quad (5.53)$$

$$\Delta E_{1;1,q} = -\hbar\omega, \quad (5.54)$$

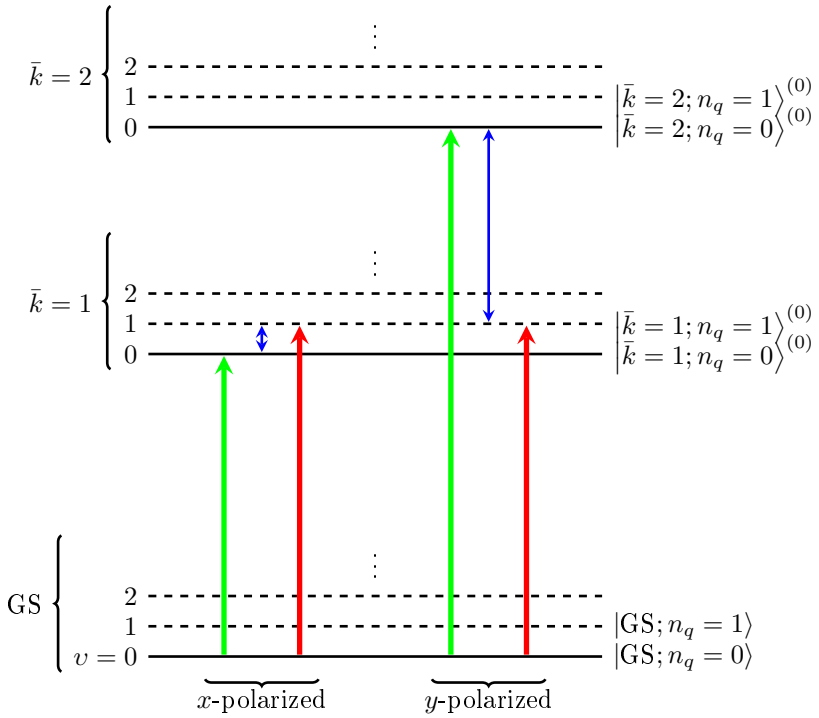


Figure 5.10.: x- and y-polarised absorption transitions for the perturbed system. The Condon-forbidden transitions (red) gain oscillator strength by mixing with states associated with Condon-allowed transitions (green) and become allowed due to Herzberg-Teller coupling (blue). The x- and y-contributions to the 1-0 absorption have different magnitudes and are thus a probe of the local structure of the chromophore (OBCs apply). For all $\bar{k}$, $\frac{\pi}{N+1} \leq q \leq \frac{N\pi}{N+1}$.

thus,

$$\left|\bar{k}=1;n_q=1\right\rangle \simeq \left|\bar{k}=1;n_q=1\right\rangle^{(0)} - \frac{2A}{(N+1)^{3/2}} X(1,1,q) \left|\bar{k}=1;n_q=0\right\rangle^{(0)}; \quad \bar{q} \text{ is odd.} \tag{5.55}$$

The associated transition dipole moment is then,

$$\mu^{01}_{x,\bar{k}=1}(q) = \left\langle \bar{k}=1, n_q=1 \left| \hat{\boldsymbol{\mu}} \right| \mathrm{GS};0 \right\rangle = \begin{cases} 0, & \bar{q} \text{ is even,} \\ -\mu^{00}_{x,1} \frac{2A}{(N+1)^{3/2}} X(1,1,q), & \bar{q} \text{ is odd.} \end{cases} \tag{5.56}$$

Summing over all phonon modes will then give the total x-polarised 1-0 absorption intensity as,

$$A_x^{01} = \sum_q \left(\mu_{x,1}^{01}(q)\right)^2 = A_x^{00} \frac{4A^2}{(N+1)^3} \sum_q X^2(1,1,q). \tag{5.57}$$

It can be shown numerically that,

$$\left(\frac{2}{N+1}\right)^3 \sum_q X^2(1,1,q) = \frac{3}{2(N+1)} \equiv \frac{1}{\mathrm{PN}}, \tag{5.58}$$

with PN being the Participation Number as defined previously. It follows then directly that,

$$A_x^{01} = A_x^{00} \frac{A^2}{2\mathrm{PN}} = A_x^{00} \frac{g_1^2}{\mathrm{PN}}, \tag{5.59}$$

or

$$\frac{A_x^{00}}{A_x^{01}} = \frac{g_1^2}{\mathrm{PN}} = g_N^2, \tag{5.60}$$

where g_N^2 is the effective Huang-Rhys parameter for a chromophore of size N. This is precisely the same result as obtained for linear polymers via a real-space approach in Chapter 4. This shows the equivalence of both approaches, albeit the latter being more elegant. This expression was also confirmed numerically in Chapter 4.

y-Polarised Transition Fig. 5.13 shows that a y-contribution to the absorption arises from coupling the $\bar{k} = 1, \upsilon = 1$ states with the $\bar{k} = 2, \upsilon = 0$ state via $\hat{H}_1$. This mixing is equivalent to the Herzberg-Teller correction introduced in the previous section: a vibronic state ($\bar{k} = 1, \upsilon = 1$) mixes with a purely excitonic state ($\bar{k} = 2, \upsilon = 0$) of the same symmetry. As the latter is a bright state, the vibronic state will acquire intensity with the same polarisation, namely in y-direction. This polarisation is orthogonal to the $\bar{k} = 1$ 0-0 transition and its associated vibronic progression and can serve as a probe for the

local chromophore structure.

Following the same procedure as above,

$$\left|\bar{k}=1;n_q=1\right\rangle \simeq \left|\bar{k}=1;n_q=1\right\rangle^{(0)} + \frac{2A}{(N+1)^{3/2}}\frac{\hbar\omega}{\Delta E_{21}^{(0)}-\hbar\omega}X(2,1,q)\left|\bar{k}=2;n_q=0\right\rangle^{(0)}, \tag{5.61}$$

for any even $\bar{q}$ (as X vanishes for odd $\bar{q}$) and with,

$$\begin{aligned}\Delta E_{21}^{(0)} &= E^{(0)}(\bar{k}=2;n_q=0) - E^{(0)}(\bar{k}=1;n_q=0)\\ &= 2|J|\left[\cos\left(\frac{\pi}{N+1}\right) - \cos\left(\frac{2\pi}{N+1}\right)\right].\end{aligned} \tag{5.62}$$

Hence,

$$A_y^{01} = A_y^{00}\frac{A^2}{2}\left(\frac{\hbar\omega}{\Delta E_{21}^{(0)}-\hbar\omega}\right)^2\left(\frac{2}{N+1}\right)^3\sum_q X^2(2,1,q), \tag{5.63}$$

and it can be shown numerically that,

$$\left(\frac{2}{N+1}\right)^3\sum_q X^2(2,1,q) = \frac{1}{N+1} = \frac{2}{3\mathrm{PN}}. \tag{5.64}$$

inserting this into Eq. (5.63), using Eq. (4.13), and rearranging then yields,

$$\frac{A_y^{01}}{A_y^{00}} = \frac{2g_N^2}{3}\left(\frac{\hbar\omega}{\Delta E_{21}^{(0)}-\hbar\omega}\right)^2. \tag{5.65}$$

Note that this expression breaks down if the exciton bandwidth ($4|J|$) is numerically similar to the phonon energy ($\hbar\omega$) due to the fact that in this case the mixing states become quasi-degenerate. For a general conjugated polymer $\hbar\omega/4|J| \simeq 0.025 \ll 1$.

5.2.1.3 0-1 Emission

As Kasha's rule is assumed, emission will occur from the lowest-energy dipole-allowed excited state. This is the $\left|\bar{k}=1;n_q=0\right\rangle^{(0)}$ state to zeroth order and it has a non-zero transition dipole moment only to the vibrationally unexcited ground state, $|\mathrm{GS};0\rangle$. The vibronic progression of the emission occurs from mixing $\left|\bar{k}=1,n_q=0\right\rangle^{(0)}$ with the $|j;\{n_q\}\rangle^{(0)}$ manifold via $\hat{H}_1$. Using perturbation theory once again and this time requiring the expansion,

$$\left|\bar{k}=1;n_q=0\right\rangle \simeq \left|\bar{k}=1;n_q=0\right\rangle^{(0)} - \sum_{\bar{k}} \frac{^{(0)}\left\langle \bar{k}';n_q=1\left|\hat{H}_1\right|\bar{k}=1;n_q=0\right\rangle^{(0)}}{\Delta E^{(0)}_{\bar{k}',q;\bar{k}}} \left|\bar{k}';n_q=1\right\rangle^{(0)}. \tag{5.66}$$

Fig. 5.11 shows the transitions and associated couplings between the states and expressions for the Herzberg-Teller contributions will now be derived.

x-Polarised Transition The transition acquires oscillator strength by mixing the $\bar{k}=1,\upsilon=0$ state with the $\bar{k}=1,\upsilon=1$ manifold. Hence,

$$\left|\bar{k}=1;n_q=0\right\rangle \simeq \left|\bar{k}=1;n_q=0\right\rangle^{(0)} + \frac{2A}{(N+1)^3/2} X(1,1,q)\left|\bar{k}=1;n_q=1\right\rangle^{(0)}, \tag{5.67}$$

and the associated transition dipole moment is then given as,

$$\begin{aligned}\mu^{01}_{x,\bar{k}=1}(q) &= \left\langle \bar{k}=1;n_q=0\left|\hat{\boldsymbol{\mu}}\right|\mathrm{GS};n_q=1\right\rangle \\ &= \begin{cases} 0, & \bar{q} \text{ is even}, \\ \mu^{00}_{x,1}\frac{2A}{(N+1)^{3/2}}X(1,1,q), & \bar{q} \text{ is odd}. \end{cases}\end{aligned} \tag{5.68}$$

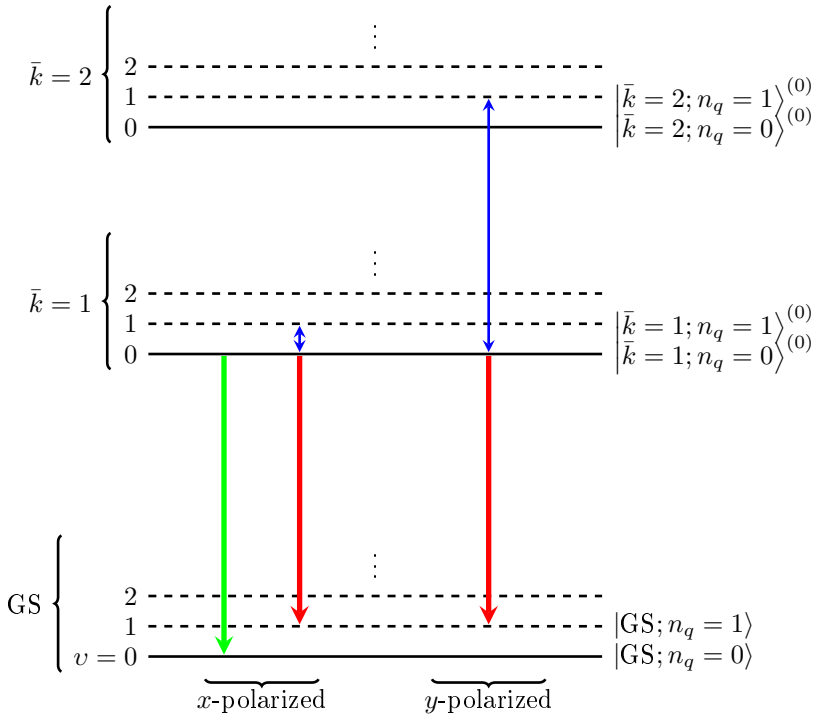


Figure 5.11.: x- and y-polarised emission transitions for the perturbed system. The Condon-forbidden transitions (red) gain oscillator strength by mixing with states associated with Condon-allowed transitions (green) and become allowed due to Herzberg-Teller coupling (blue). The x- and y-contributions to the 0-1 emission have different magnitudes and are thus a probe of the local structure of the chromophore (OBCs apply). For all $\bar{k}$, $\frac{\pi}{N+1} \leq q \leq \frac{N\pi}{N+1}$.

Summing over all q then gives the total squared transition dipole moment as,

$$\left(\mu_{x,1}^{01}\right)^2 = \sum_q \left(\mu_{x,1}^{01}(q)\right)^2 = \left(\mu_{x,1}^{00}\right)^2 g_N^2, \tag{5.69}$$

implying that,

$$I_x^{01} = I_x^{00} g_N^2 = I^{00} g_N^2, \tag{5.70}$$

assuming $\hbar\omega \ll E^{(0)}(\bar{k}=1;n_q=0)$.

This expression is exactly the expression derived in Chapter 4 for linear polymer chains. An equivalent expression was derived by Spano and co-workers [15–17]. Once again, this expression can be used to determine the size of the chromophore and thus infer the local

structure of the polymer directly.

y-Polarised Transition Mixing can also occur between the $\bar{k}=1,\upsilon=0$ state and the $\bar{k}=2,\upsilon=1$ manifold, giving rise to a y-polarised 0-1 emission contribution. Using the same procedure as above it is found that,

$$\left(\mu^{01}_{y,\bar{k}=1}\right)^2 = \sum_q \left(\mu^{01}_{y,\bar{k}=1}(q)\right)^2 - \left(\mu^{00}_{y,\bar{k}=2}\right)^2 \frac{2g_N^2}{3}\left(\frac{\hbar\omega}{\Delta E^{(0)}_{21}+\hbar\omega}\right)^2 \tag{5.71}$$

Total Emission Intensity Ratio Using the results obtained in the previous paragraphs, expressions for the total emission intensity ratio, I^{00}/I^{01}, can be derived. Define,

$$I^{00} = I^{00}_x = (E_{\bar{k}=1})^3 \left(\mu^{00}_{x,\bar{k}=1}\right)^2 = (E_{\bar{k}=1})^3 A^{00}_x, \tag{5.72}$$

$$I^{01}_x = (E_{\bar{k}=1})^3 \left(\mu^{01}_{x,\bar{k}=1}\right)^2, \tag{5.73}$$

$$I^{01}_y = (E_{\bar{k}=1})^3 \left(\mu^{01}_{y,\bar{k}=1}\right)^2, \tag{5.74}$$

and

$$I^{01} = I^{01}_x + I^{01}_y, \tag{5.75}$$

then it follows directly that,

$$\frac{I^{00}}{I^{01}} g_N^2 = \left[1 + \frac{2}{3}\left(\frac{A^{00}_y}{A^{00}_x}\right)\left(\frac{\hbar\omega}{\Delta E^{(0)}_{21}}\right)^2\right]^{-1}. \tag{5.76}$$

In the adiabatic limit, *i.e.* $\hbar\omega/|J| \to 0$, $\hbar\omega/\Delta E^{(0)}_{21} \to 0$ and then,

$$\frac{I^{00}}{I^{01}} g_N^2 \to 1: \quad \hbar\omega/|J| \to 0, \tag{5.77}$$

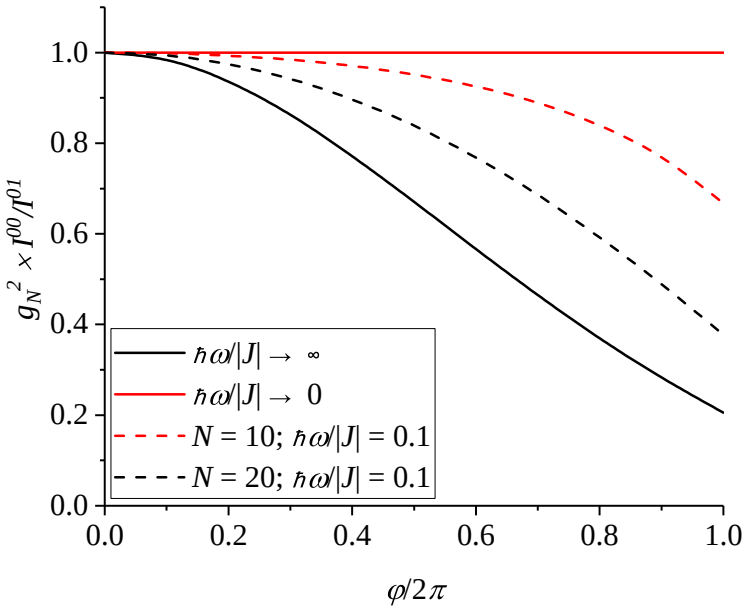


Figure 5.12.: $g_N^2 \times I^{00}/I^{01}$ as a function of the curvature, $\phi/2\pi$, for the two limits and two different chromophore lengths using Eq. (5.76) (evaluated numerically). For a fixed $\hbar\omega/|J|$ the behaviour is closer to the anti-adiabatic limit for longer chromophores, in line with previous results.

while in the anti-adiabatic limit,

$$\frac{I^{00}}{I^{01}} g_N^2 \to \frac{3A_x^{00}}{3A_x^{00} + 2A_y^{00}} : \quad \hbar\omega/|J| \to \infty. \tag{5.78}$$

Note that the last limit is also reached for $N \to \infty$, *i.e.* very large chromophores.

Fig. 5.12 shows the evolution of the scaled emission intensity ratio as a function of curvature of the chromophore. In the adiabatic limit the ratio is independent of the curvature as the Herzberg-Teller contributions vanish, while in the anti-adiabatic limit the ratio becomes a function of the curvature and can thus be used to determine the local structure. In accordance with previous results (Sec. 5.1.2.1), the adiabatic limit breaks down for longer chains for a fixed $\hbar\omega/|J|$ due to excitonic states becoming quasi-degenerate. Fig. 5.6 shows the same behaviour for disordered macrocycles, indicating

that they behave identically to the bent chromophores. The two different limits are also seen in that figure, albeit less pronounced. The intrapolation from the adiabatic to the anti-adiabatic limit is discussed in more detail in App. B. In the following section this theoretical result derived using perturbation theory within the Born-Oppenheimer limit is compared with essentially exact calculations using the fully-quantised Frenkel-Holstein model and the DMRG routine. First, however, it will be shown that the macrocycle limit, as introduced earlier in this chapter by other means, is recovered.

5.2.2 The Macrocycle Limit

The procedure outlined above can be repeated for periodic boundary conditions, which is equivalent to the treatment of macrocycles performed in Section 5.1.1.2 within the Born-Oppenheimer approximation. It is then found that, firstly the 1-0 absorption into the $k = 0$ state vanishes, as expected, while for the 1-0 absorption into the $\bar{k} = 1$ state,

$$\mu^{10}_{\bar{k}=1} = \frac{2g\hbar\omega}{\sqrt{N}\Delta E_{01}}\mu^{00}_{\bar{k}=1}. \tag{5.79}$$

This then gives the intensity ratio,

$$\frac{I^{01}}{I^{00}} \propto \frac{g^2(\hbar\omega)^2}{\Delta E^2_{01}}, \tag{5.80}$$

and using a Taylor series expansion for the energy difference of the states in question and assuming that $\hbar\omega/|J| \ll 1$, this leads to,

$$\frac{I^{01}_{\mathrm{HT}}}{I^{00}} \propto g^2\left(\frac{\hbar\omega}{J}\right)^2 : \quad \hbar\omega \ll |J|. \tag{5.81}$$

Comparing this to Eq. (5.32) shows the equivalence of the two approaches. Furthermore, in the anti-adiabatic limit, *i.e.* $\hbar\omega \gg |J|$ (which is strictly speaking not applicable in the expansion) it is found that,

$$\frac{I^{01}_{\mathrm{HT}}}{I^{00}} \propto g^2 : \quad \hbar\omega \gg |J|, \tag{5.82}$$

which is, remarkably, in agreement with the results presented in Fig. 5.3. The intensity ratio does indeed become independent of $\hbar\omega/|J|$.

5.2.3 Numerical Results

Define,

$$X \equiv \frac{I^{00}}{I^{01}} g_N^2, \tag{5.83}$$

then the deviation of the theoretical prediction from the exact result can be calculated as,

$$R = 2\frac{X_{\mathrm{theory}} - X_{\mathrm{DMRG}}}{X_{\mathrm{theory}} + X_{\mathrm{DMRG}}}, \tag{5.84}$$

i.e. the value of R is bounded from above and below ($R \in [-2; 2]$) where positive (negative) values correspond to an overestimation (underestimation) by the Born-Oppenheimer limit result.

Fig. 5.13 shows R for varying values of $\hbar\omega/|J|$, N, and φ. The calculations were found to be quasi-independent of A, with only very minor changes to the absolute values, while reproducing the trends.

It can be seen that the in the adiabatic regime the relative error is $|R| \lesssim 15\%$ and the theoretical description is fairly accurate. For larger values of $\hbar\omega/|J|$ the prediction breaks down, however, and the severity depends on the curvature. Long chains are better described for large φ, while for small φ the dependence on the chain length is less

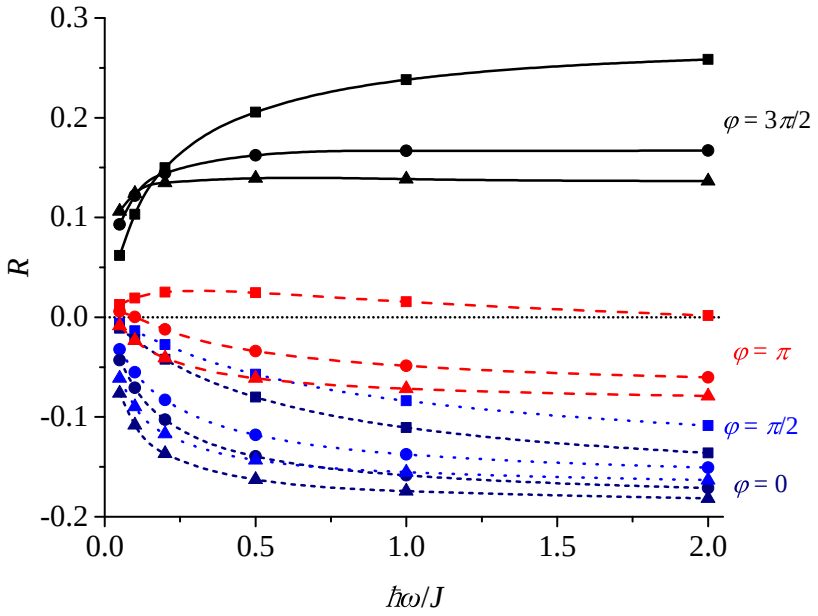


Figure 5.13.: R against $\hbar\omega/|J|$ for various angles and chain lengths. $\phi = 3\pi/2$ (black, solid curves); $\phi = \pi$ (red, dashed curves); $\phi = \pi/2$ (blue, dotted curves); $\phi = 0$ (navy, short-dashed curves); and different chain lengths, $N = 10$ (squares); $N = 20$ (circles); $N = 30$ (triangles). The short-dotted line indicates the 0-line and for all calculations $A = \sqrt{2}$.

pronounced, albeit shorter chains being predicted better. This is due to the fact that for large chromophores the curvature is smaller for a given φ then for short chromophores. It can thus be deduced that the curvature of the chromophore is the determining factor for the accuracy of the theoretical prediction. For the adiabatic limit, however, especially $\hbar\omega/|J| \simeq 0.1$, the predictions are fair to good for all φ and N.

The findings of this chapter will now be summarised, especially in light of the results of Chapter 4 before modelling realistic systems in Chapter 6.

5.3 Summary

In this chapter it has been shown that the optical signature of a conjugated polymer contains information of the local disorder within the chain: due to Anderson localisation

the excitons occupy certain regions within the polymer. The model has been extended to include non-Condon contributions within the optical signature arising from the conformation of the polymer and the local structure of the chromophore. By bending the chain, more transitions become bright and due to the coupling of states, Condon-forbidden transitions become allowed by mixing via the exciton-phonon coupling. Closed expressions have been derived for the fundamental transitions within a chromophore using perturbation theory within the adiabatic limit. The results are applicable over a wide range of parameters (with reasonable accuracy) and can be used to determine the local chromophore structure from its optical spectra.

Following on, realistic systems will be modelled using the results of the previous chapters and compared to experimental data.

6

Modelling of Polymer Spectra

In this chapter spectra obtained using the theoretical methods developed in the preceding chapters will be presented. The focus will be PPP and PPV systems and an important derivative of PPP, MeLPPP (methyl-substituted ladder-type poly(*para*-phenylene)). The latter differs from PPP only by the addition of side chains, while the π-electron system is not directly affected. MeLPPP is shown in Fig. 6.1. The side chains alter the torsional structure of the polymer, *i.e.* the equilibrium angles and force constants. The calculation of these parameters from first principles is tabled in App. C.

First PPP and PPV will be discussed, using both, the semi-classical Frenkel-Holstein model as well as the fully quantised DMRG code. The latter is computationally expensive and can therefore only be used on relatively short chains. As has been shown previously, the Born-Oppenheimer limit is generally a reasonable approximation for conjugated polymers and will be used together with the Herzberg-Teller correction to model the spectra of polymers.

After discussing these basic compounds calculations of MeLPPP will be compared with experimental data which as been provided by the research group of Prof A Köhler from

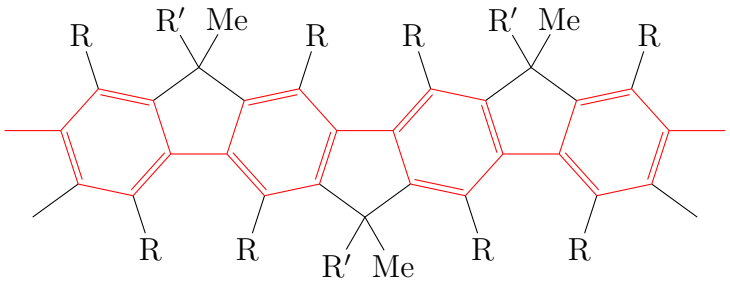


Figure 6.1.: Structure of MeLPPP with R= n-C_6H_{13} and R'=1,4-C_6H_4-n-$C_{10}H_{21}$. The underlying PPP structure is highlighted in red.

the University of Bayreuth, Germany.

6.1 Poly(para-phenylene) and poly(para-phenylene vinylene)

The fully quantised Frenkel-Holstein model is used to compute the spectra of oligomers using the DMRG routine, while for polymers the Frenkel model and the Born-Oppenheimer expressions are employed due to computational limitations.

To introduce disorder the torsional angle between sites, ϕ_n, is taken as a Gaussian random variable as described above. In addition, diagonal disorder is introduced to account for differences in density within condensed phases of polymers, which will be quantified by σ_ε, the standard deviation in on-site energy corresponding to the homogeneous line width.

The absorption and emission spectra can be modelled by,

$$A(E) \propto \sum_k \sum_\upsilon E^{\mathrm{A}}_{k,\upsilon 0} \left|\boldsymbol{\mu}^{\mathrm{A}}_{k,\upsilon 0}\right|^2 \delta\left(E - E^{\mathrm{A}}_{k,\upsilon 0}\right), \tag{6.1}$$

$$I(E) \propto \sum_k \sum_\upsilon \left(E^{\mathrm{E}}_{k,0\upsilon}\right)^3 \left|\boldsymbol{\mu}^{\mathrm{E}}_{k,0\upsilon}\right|^2 \delta\left(E - E^{\mathrm{E}}_{k,0\upsilon}\right), \tag{6.2}$$

where $\delta(x - x_0)$ is a line shape function, which is taken to be a Lorentzian. For oligomers the energies, $E^{\mathrm{A}}_{k,\upsilon 0}$ and $E^{\mathrm{E}}_{k,0\upsilon}$, were calculated directly using the DMRG routine, while for polymers,

$$E^{\mathrm{A}}_{k,\upsilon 0} = E_{k,00} + \upsilon\hbar\omega, \tag{6.3}$$

and

$$E^{\mathrm{E}}_{k,0\upsilon} = E_{k,00} - \upsilon\hbar\omega, \tag{6.4}$$

using the Frenkel model.

Tab. 6.1 shows the various parameters used in the calculation of the oligomer and

Monomer Parameters (X = P,V)		
Parameter	Phenylene, P	Vinylene, V
$\varepsilon_0^{\mathrm{X}}$ / eV	6.05	8.59
A_{X}	2.7	4.0
$g_1^2(X)$	3.65	8.0
System Parameters (X = PPP,PPV)		
Parameter	PPP	PPV
$J_{\mathrm{X}}^{\mathrm{SE}}$ / eV	-1.30	-1.68
$J_{\mathrm{X}}^{\mathrm{DD}}$ / eV	-0.40	-0.60
$\phi_{0,\mathrm{s}}^{(\mathrm{X})}$	0.47 (27°)	0.26 (15°)
$\phi_{0,\mathrm{aq}}^{(\mathrm{X,GS})}$	0.70 (40°)	0.47 (27°)
$\phi_0^{(\mathrm{EX})}$	0	
K / eV rad^{-2}	0.53	0.46

Table 6.1.: Parameters used for the simulation of oligomer and polymer PPP and PPV spectra. In addition to the ones listed above, $\hbar\omega = 0.19$ eV and $\sigma_\varepsilon = 0.065$ eV for all systems, and $g_1^2(\mathrm{PPV}) = 2.53$.

polymer spectra. They were obtained via a mixture of ab-initio methods (see App. C), experimental results, and fitting procedures.

The torsional disorder of polymer systems in solution can be related to temperature if the torsional force constant, K, is known as [88],

$$\sigma_\phi = \left(\frac{k_{\mathrm{B}}T}{K}\right)^{\frac{1}{2}}. \tag{6.5}$$

K was computed as described in Chapter 3. for both PPP and PPV, using the harmonic approximation and the Gaussian09 [133] program package at 6-311G//B3LYP DFT level [134–138].

The equilibrium dihedral angles between moieties are different in the ground and excited states as confirmed by experiment and simulation. This has a direct effect on the energy of the systems as the transition integrals will change. The excited state is generally more planarised than the ground state due to an increase in double-bond character bet-

ween moieties, which has also a stiffening effect of these bonds. As the absorption is from the ground state with (relatively) large dihedrals and the emission from the excited state with (relatively) small dihedrals, the emission will be shifted to lower energies (redshift) in comparison to the absorption and this change in geometry of the systems is the primary cause for the observed Stokes' shift in these systems. There are other causes which are related to the environment of the polymers (bathochromic effects), but as isolated systems are simulated these effects are not considered in this work.

6.1.1 Oligomers

As mentioned in Chapter 4, oligomeric systems were investigated using the fully quantised Frenkel-Holstein model and the DMRG technique. Investigated was the effect of chain length and temperature for [n]PPP and [n]PPV oligomers in solution and solids, where n is the total number of monomers (*i.e.* for PPV the total number of sites is $2n$).

First, the effect of chain length was investigated in solution for [4]PPP and [6]PPP at room temperature ($T = 298$ K) and for [3]PPV and [4]PPV at 77 K in order to be able to compare it to experimental spectra.

Figs. 6.2 and 6.3 show the results for PPP and PPV, respectively. The spectra were averaged over 20 unique realisations of disorder to reduce statistical noise. For the emission spectra, only the 0-0 and 0-1 peaks were calculated for computational reasons and for the absorption spectra the high-energy tail was not calculated as the states involved are not computed accurately by the DMRG method.

For the emission in both systems a high resolution of the emission bands is seen, showing the 0-0 and 0-1 transitions. For [4]PPP both peaks are of roughly the same height ($|\boldsymbol{\mu}_{00}|^2 \,/\, \left|\boldsymbol{\mu}^{\mathrm{E}}_{01}\right|^2 \approx 0.92$), whereas for [4]PPP the 0-0 band is clearly more intense ($|\boldsymbol{\mu}_{00}|^2 \,/\, \left|\boldsymbol{\mu}^{\mathrm{E}}_{01}\right|^2 \approx 1.24$). Using Eq. (4.63) this estimates the PNs of the polymers to 3.4

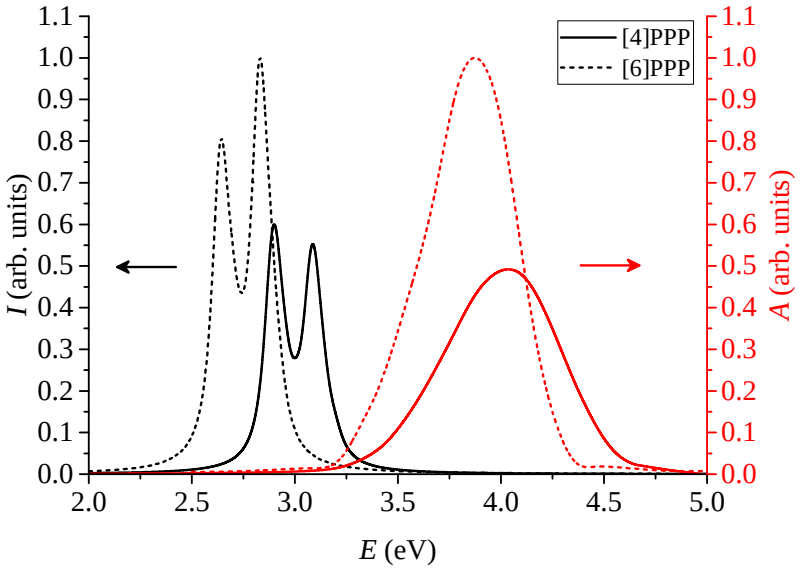


Figure 6.2.: Absorption (red) and emission (black) spectra for [4]PPP (solid) and [6]PPP (dashed) at 298 K in solution. The scales are normalised to the most intense peak for absorption and emission, respectively. $\phi_0^{\mathrm{GS}} = 40°, \phi_0^{\mathrm{EX}} = 0°, \sigma_\phi = 8.6°$. The spectra were calculated using the fully quantised Frenkel-Holstein model and the DMRG routine.

and 4.5, respectively.

The absorption spectra are in all cases feature-less (any features observed are due to the sample size of the average and are expected to smear out if the sample size is increased). For both, PPP and PPV, the absorption shows a redshift with increasing chain length, which can be explained by the spread of the LEGSs increasing. The chain lengths used here are expected to be too short to support more than one LEGS and as such the absorption energy will decrease with the chain length for short oligomers. The absorption cannot be analysed further due to the missing high-energy tail.

The obtained spectra can be compared to experimental results and the values of the main observables are tabulated in Tab. 6.2 [11, 139] and example spectra of oligo(*para*-phenylenes) are shown in Fig. 6.4. The 0-0 absorption energies, E_{00}^{A}, are, across the board, generally very well reproduced with an average deviation of 0.17 eV. The emission energies,

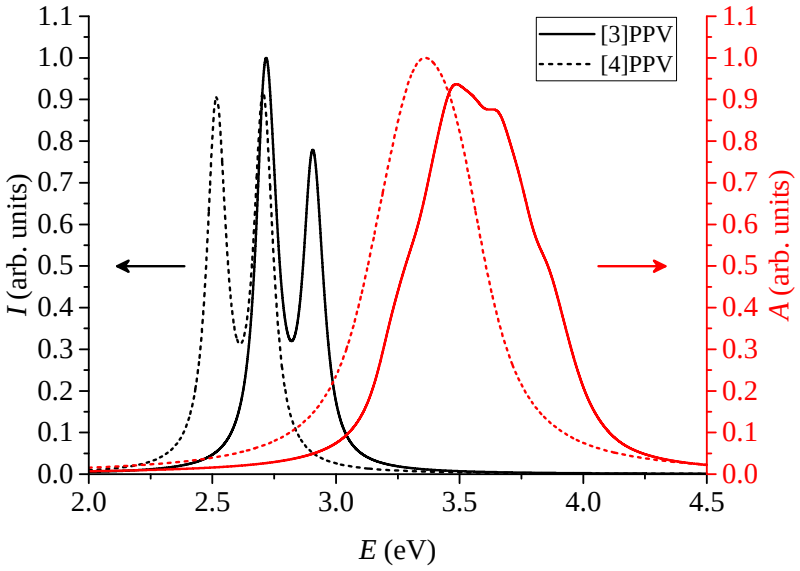


Figure 6.3.: Absorption (red) and emission (black) spectra for [3]PPV (solid) and [4]PPV (dashed) at 77 K in solution. The scales are normalised to the most intense peak for absorption and emission, respectively. $\phi_0^{\mathrm{GS}} = 27°, \phi_0^{\mathrm{EX}} = 0°, \sigma_\phi = 6.8°$. The spectra were calculated using the fully quantised Frenkel-Holstein model and the DMRG routine.

E_{00}^{E} and E_{01}^{E} on the other hand are underestimated in all cases. While the spacing of the lines is correct (confirming the value for $\hbar\omega$) the energies are on average underestimated by about 0.32 eV. This can be easily explained by the neglect of any interactions of the polymer with its surroundings. The Stokes' shifts are accurately reproduced for the PPP oligomers, however, for the PPV systems the discrepancy is close to or exceeds a factor of 2. It is thought to be again due to the neglect of any solvent effects and other interactions. The energy calculation for the excited state can easily be improved by changing the on-site exciton energy in the model, which seems to be underestimated with the parameters chosen. These values were corrected when fitting theoretical spectra to experimental results (see Section 6.3), however here we are more interested in the reproduction of general trends.

While some of the transition intensities compare favourably to experimental results,

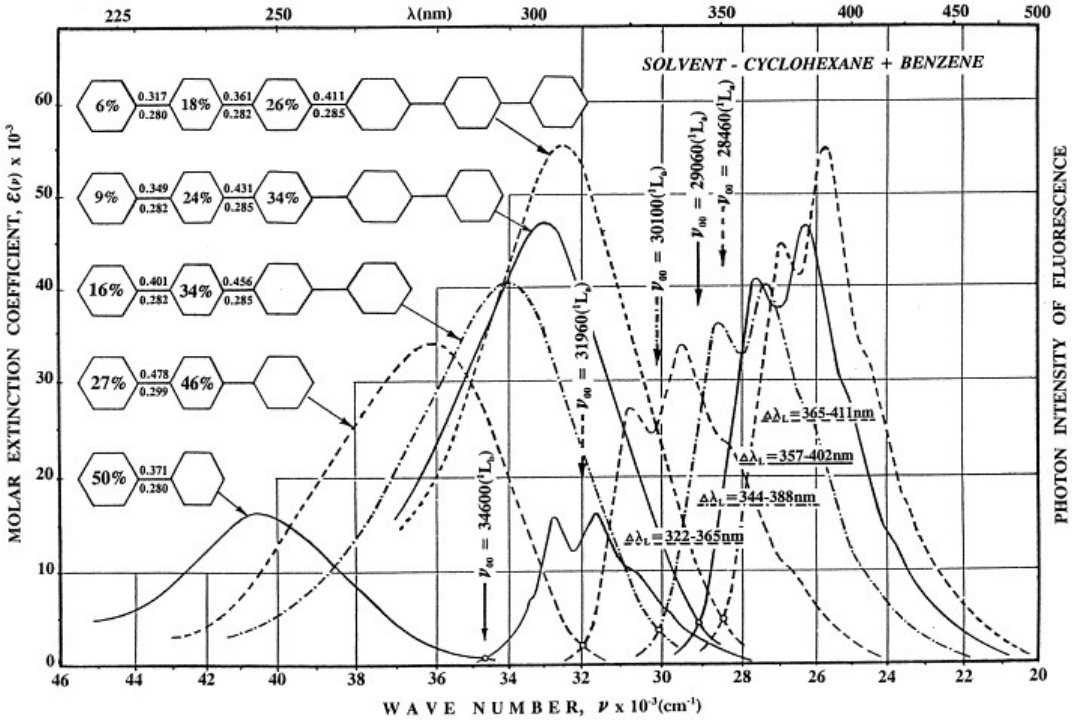


Figure 6.4.: Example of experimental absorption and emission spectra for oligo(*para*-phenylenes). Reproduced from [139] with kind permission from Elsevier.

others do not. The relative absorption intensities are quite accurately reproduced and so are most emission intensities with the exception of [6]PPP in which case the prediction is the exact opposite from experiment. This is partially due to the neglect of the 0-2 emission transitions which, due to broadening, will contribute to the 0-1 emission peak.

	[4]PPP		[6]PPP		[3]PPV		[4]PPV	
	calc.	exp. [139]	calc.	exp. [139]	calc.	exp. [11]	calc.	exp. [11]
E_{00}^{A} / eV	4.04	4.22	3.86	4.06	3.49	3.41	3.36	3.16
E_{00}^{E} / eV	3.09	3.53	2.83	3.33	2.91	3.08	2.71	2.83
E_{01}^{E} / eV	2.90	3.37	2.64	3.16	2.72	2.90	2.52	2.65
E_{Stokes} / eV	1.14	0.95	1.03	0.91	0.77	0.33	0.65	0.33
I_{00}^{A}	0.51	0.72	1.00†	1.00†	0.94	1.00	1.00†	1.00
I_{00}^{E}	0.55	0.66	1.00†	0.81	0.78	1.00	0.92	1.00
I_{01}^{E}	0.60	0.73	0.81	1.00†	1.00†	1.00	0.90	1.00
I_{00}^{E}/I_{01}^{E}	0.92	0.90	1.24	0.81	0.78	1.00	1.02	1.00

Table 6.2.: Comparison of calculated and experimental values of spectroscopic observables for polymers in solution. †: most intense peak for absorption/emission; all other peaks normalised to it.

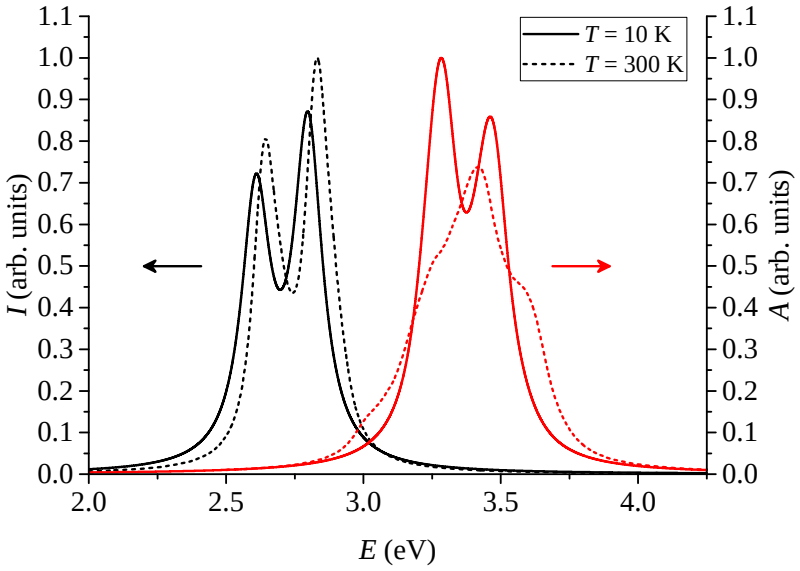


Figure 6.5.: Absorption (red) and emission (black) spectra for [6]PPP at 10 K (solid) and 300 K (dashed) in a solid/thin film. The scales are normalised to the most intense peak for absorption and emission, respectively. $\phi_0^{\mathrm{GS}} = 27°, \phi_0^{\mathrm{EX}} = 0°, \sigma_\phi(T = 10\ \mathrm{K}) = 1.6°, \sigma_\phi(T = 300\ \mathrm{K}) = 8.6°$. The spectra were calculated using the fully quantised Frenkel-Holstein model and the DMRG routine.

It is therefore predicted that all of the 0-1 emission peaks are underestimated, which is confirmed by the experimental data. The intensity ratio on the other hand is reproduced very well for [4]PPP and [4]PPV, being essentially exact.

In addition to the oligomers of different length in solution, oligomers of equal length at different temperatures in a solid, such as a thin film commonly used for organic optoelectronics, were investigated. The absorption and emission spectra of [6]PPP in a solid at 10 K and 300 K were calculated and the results are shown in Fig. 6.5.

As expected, for higher temperatures (*i.e.* higher disorder) the spectra have lower resolution. This is especially true for the absorption spectrum, which almost loses all vibronic finestructure. The emission spectrum is affected to a much lesser extent and it is discussed below why this is the case. For low temperatures the mirror-image symmetry for emission and absorption spectra, which has not been observed so far, can also be

seen. This implies that even relatively low disorder quickly destroys this symmetry in the systems investigated. Another effect observed is a redshift with increasing temperature, much more so for the emission spectrum, indicating a larger effect of disorder on the relaxed excited state. Again, this will be discussed in greater detail below.

As above, these results can be compared to experimental data [140]. The broadening and loss of vibronic features for higher temperatures, especially for absorption, is seen but, as discussed above, due to the neglect of higher order absorption transitions the spectra cannot be compared directly. The same holds true for emission: due to the neglect of 0-2 and higher emission transitions, the intensity ratio is not reproduced correctly. However, a slight redshift is observed in the experiment for higher temperatures, which is in agreement with the calculations.

As mentioned earlier, disorder localises the excitons on a polymer and the LEGSs that from as a consequence define a chromophore of length, L, which can be modelled as an ordered polymer of length L. Therefore, for disordered polymers, it is expected that their spectra converge with the spectra of ordered oligomers as the oligomer size approaches the average chromophore length within the polymer. To this end the spectra of $[n]$PPV oligomers and PPV polymers with $2n = 1000$ moieties have been calculated using the Frenkel model and Born-Oppenheimer expressions derived above. At room temperature, *i.e.* $\sigma_\phi = 8.6°$ for PPV, the average chromophore length was found to be 39 monomers and as shown in Fig. 6.6 the spectra for [39]PPV and the polymer are essentially the same.

The intensity ratio of $I_{00}/I_{01}^{\mathrm{E}} = 5.9$ is larger than the values obtained by experiment, which are typically 3.3 (MEH-PPV in toluene at 77 K) and 1.8 (MEH-PPV in toluene at room temperature), giving a conjugation length of 12 and 7, respectively [141]. These con-

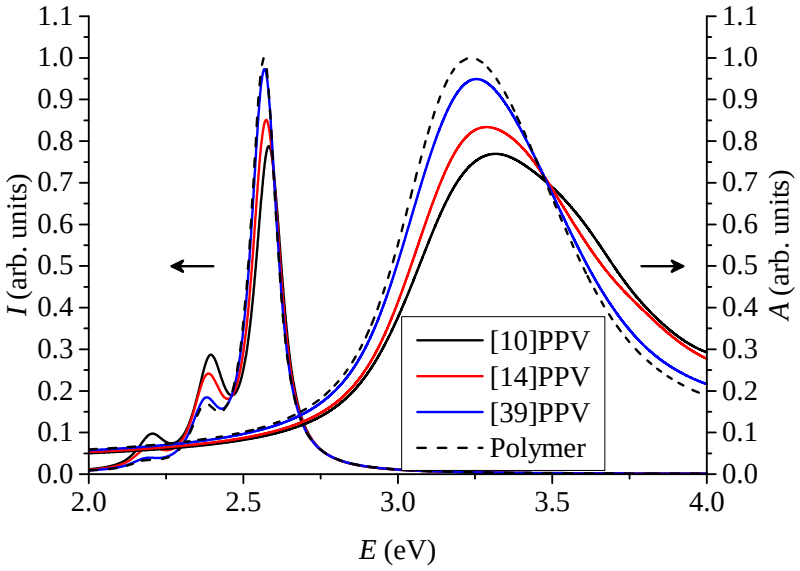


Figure 6.6.: Absorption (right) and emission (left) spectra for various PPV oligomers and a PPV polymer in solution at 77 K. The spectra were normalised to their area (summed oscillator strength) to account for varying numbers of chromophores. $\phi_0^{\mathrm{GS}} = 27°, \phi_0^{\mathrm{EX}} = 0°, \sigma_\phi = 6.8°$. The spectra were obtained using the Frenkel model.

jugation lengths are in agreement with the observation that the [9]PPV emission spectrum has the same intensity ratio as the polymer. The assumption of complete planarisation is likely to be the cause for the overestimation of the conjugation length as this is unlikely in real systems. However, the graph above shows the same qualitative result as the experiment in that it means disordered polymers can be regarded as an ensemble of chromophores that can be modelled as ordered polymers of that length.

6.1.2 Polymers

Calculations with the fully quantized Frenkel-Holstein model on realistic systems are limited to about 20 moieties due to computational restrictions. In order to model polymers the Frenkel model will therefore be used as outlined above and the Born-Oppenheimer expressions derived earlier. To model polymer properties $N = 1000$ and the average over

200 realisations of disorder when considering non-ordered systems is taken. Some basic properties of the Frenkel model will be reviewed briefly before using it to model polymeric systems.

The eigenvalues of the Frenkel model correspond to vertical transition energies, $\{E_{\text{vert}}\}$, from the electronic and vibrational ground state to electronically excited states. As such, they do not include the vibrational relaxation energy or the zero-point energy. Hence, the energies of the vibrational ground state of the electronically excited states are given as,

$$E_{00}^{k} = E_{\text{vert}}^{k} - E_{\text{r}}^{k} + \frac{\hbar\omega}{2}, \tag{6.6}$$

where E_{r}^{k} is given by Eq. (4.61). The eigenfunctions, $\{\Psi_{\text{vert}}\}$ are vertical exciton centre-of-mass functions in a vibrationally unrelaxed system. It has been shown that self-localisation of the exciton is basically non-existent in conjugated polymers and that the vertical wavefunctions closely resemble the relaxed wavefunctions [101]. It is therefore reasonable to approximate the relaxed wavefunctions obtained with the Frenkel-Holstein model with the vertical eigenfunctions of the Frenkel model, *i.e.*

$$\Psi_{n}^{0} \approx \Psi_{n}^{1} \approx \Psi_{n}^{\text{vert}}. \tag{6.7}$$

Eqs. (4.60) and (4.25) can be used to calculate the effective Huang-Rhys parameter and transition dipole moments.

Some properties of disordered polymers will now be predicted before discussing their spectra.

Chromophore Size The average PN of LEGSs and the associated chromophore size, $\langle \text{CL} \rangle$, will decrease with increasing disorder if the torsional angle is modelled as a Gaussian

random variable as,

$$\langle \mathrm{PN} \rangle \sim \left(\frac{\langle J \rangle_\phi}{\sigma_J} \right)^{\frac{2}{3}}, \tag{6.8}$$

with $\langle J \rangle_\phi$ being the exciton transfer integral averaged over the dihedral angles. From Eq. (4.58) it then follows that,

$$\langle J \rangle_\phi \approx J(\phi_0) - J^{\mathrm{SE}} \sigma_\phi^2 \cos 2\phi_0, \tag{6.9}$$

and

$$\sigma_J \approx J^{\mathrm{SE}} \sigma_\phi \sin 2\phi_0. \tag{6.10}$$

For sufficiently small σ_ϕ it then follows that,

$$\langle \mathrm{PN} \rangle \propto \left(\frac{J(\phi_0)}{J^{\mathrm{SE}} \sigma_\phi \sin 2\phi_0} \right)^{\frac{2}{3}}, \tag{6.11}$$

showing that the chromophore size decreases with increasing torsional disorder. It furthermore shows that the chromophore size increases with planarity of the system, *i.e.* $\phi_0 \to 0°$, as the effective disorder ($\sigma_\phi \sin 2\phi_0$) decreases and $J(\phi_0)$ increases.

Fig. 6.7 shows a plot of the mean PN and conjugation length, $\langle \mathrm{CL} \rangle$, for PPP and PPV in the solid state ($\phi_0^{\mathrm{PPP}} = 27°, \phi_0^{\mathrm{PPV}} = 15°$). As predicted both, the conjugation length and Participation Number, decrease with increasing disorder before saturating for high σ_ϕ. To a good approximation $\langle \mathrm{CL} \rangle = 2 \langle \mathrm{PN} \rangle$ and for $\sigma_\phi = 10°$ the predicted chromophore sizes are about 20 and 13 monomer units, respectively.

Similarly, Fig. 6.8 shows the variation of the chromophore length with disorder for different mean angles. It is evident that for a given disorder polymers with a smaller mean torsional angle support longer chromophores. For the high and no disorder limit,

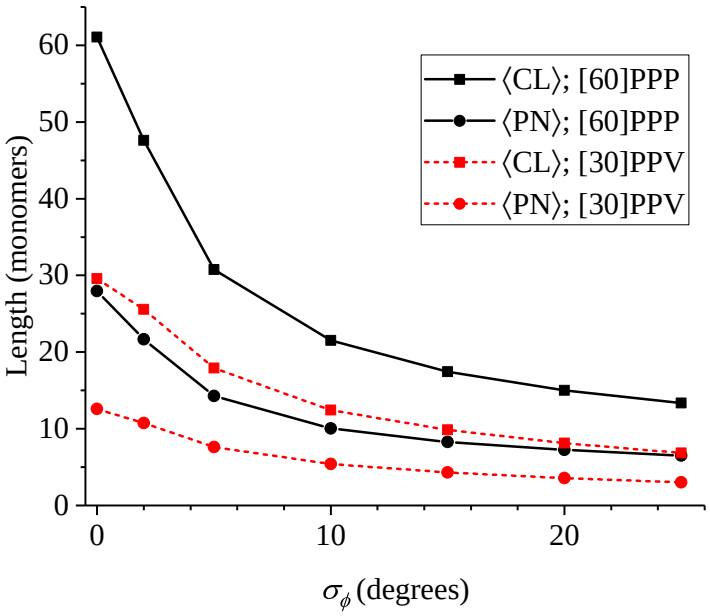


Figure 6.7.: Mean chromophore size, $\langle \mathrm{CL} \rangle$, and participation number, $\langle \mathrm{PN} \rangle$, for [60]PPP and [30]PPV against disorder for mean dihedral angles of $\phi_0^{\mathrm{PPP}} = 27°$ and $\phi_0^{\mathrm{PPV}} = 15°$, respectively. The results were obtained with the Frenkel model.

the chromophore lengths are independent of the mean angle.

Density of States Having considered the effect of disorder on the mean chromophore size, it will now be discussed how planarization and disorder affects the density of states (DOS) in polymers. Static disorder affects the density of states directly in three ways. Firstly, with increasing disorder the DOS becomes wider which is mainly due to exchange narrowing and hence enhances the low-energy (Lifshitz) tail of the DOS. Secondly, increased disorder reduces the average inverse participation ratio and therefore increases the relaxation energy as $E_{\mathrm{r}} = \hbar\omega g_1^2/\mathrm{PN} \sim \sigma_\phi^{2/3}$. These two effects lead to a reduction of energy of the LEGSs in the low-energy tail of the DOS. However, with increasing disorder the energy of the excited states increases and this effect dominates for large disorder. This is due to the increase in energy of the nominal band edge, $\varepsilon_0 - 2\left|\langle J \rangle_\phi\right|$, and can be

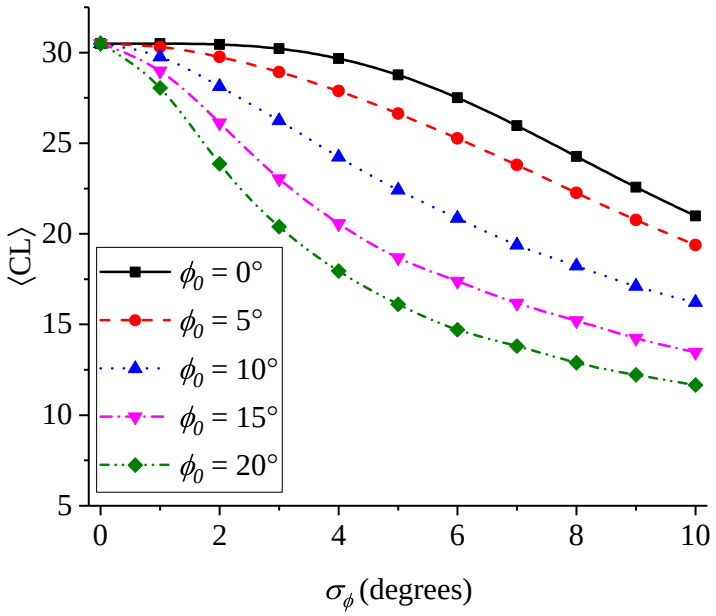


Figure 6.8.: Mean chromophore size, $\langle \mathrm{CL} \rangle$ for [30]PPV at different mean angles, ϕ_0, for varying amounts of disorder. The results were obtained using the Frenkel model, averaging over 1000 realisations of disorder.

understood by considering the dependency of the transfer integral on the disorder, given as,

$$J = \langle J \rangle_\phi + \sigma_J, \tag{6.12}$$

where $\langle J \rangle_\phi$ is given by Eq. (6.9) and σ_J by (6.10). It then is obvious that for $0 \leq \phi_0 \leq 45°$ J decreases with increasing disorder as σ_ϕ^2, which implies a reduced exciton bandwidth.

Fig. 6.9 shows the mean 0-0 transition energy, $\langle E_{0-0} \rangle$, and minimum transition energy of the LEGSs, $\langle E_{\mathrm{min}} \rangle$ (*i.e.* the bottom edge of the exciton band), in an ensemble of disordered [60]PPP and [30]PPV. It can be seen that both energies initially decrease with disorder before increasing. However, the mean energy increases for smaller values of disorder when the band edge is still being blueshifted.

The increase of ϕ_0 will also result in a blueshift of $\langle E_{0-0} \rangle$ and $\langle E_{\mathrm{min}} \rangle$, which can be

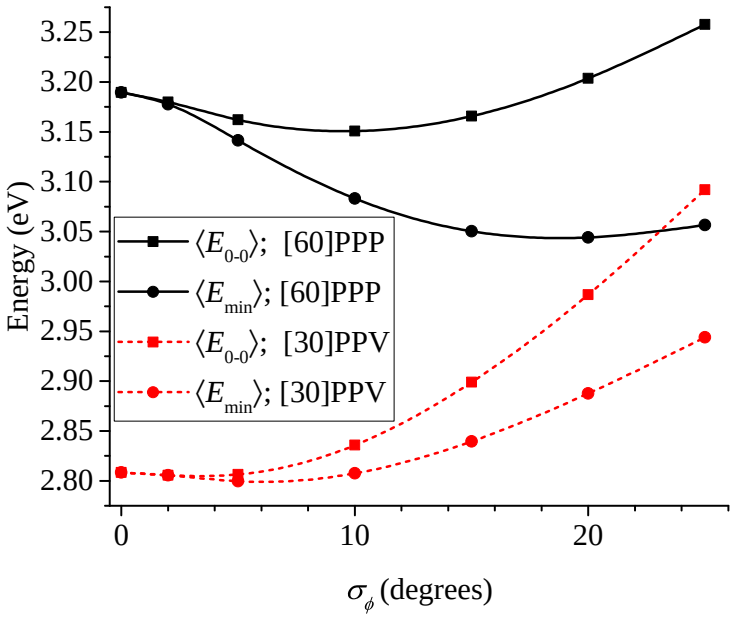


Figure 6.9.: The mean 0-0, $\langle E_{0\text{-}0}\rangle$, and minimum, $\langle E_{\text{min}}\rangle$, transition energies for [60]PPP and [30]PPV for varying disorder; $\phi_0 = 27°$ and $\phi_0 = 15°$, respectively. The results were obtained using the Frenkel model and were averaged over 1000 realisations of disorder.

understood by the way J depends on ϕ but also by considering the potential energy surface that is the basis for this dependency. It is assumed (implicitly) that the transfer integral is most stabilising when the adjacent sites have a torsional angle of 0 as in that case the overlap of the p-orbitals constituting the π-electron system is maximised. As a corollary from this, an increase in ϕ_0 will lead to an increase in energy as the stabilising effect is minimised.

Fig. 6.10 shows the evolution of the relative average 0-0 energy, $\langle E_{0-0}\rangle - E_{0-0}\,(\sigma_\phi = 0)$, with disorder. For small mean angles ϕ_0 disorder results in a redshift for any value of σ_ϕ, whereas for larger values of the mean angle the introduction of disorder results in a blueshift first before reverting into a redshift.

The results presented here can be summarized in the following way: the transition

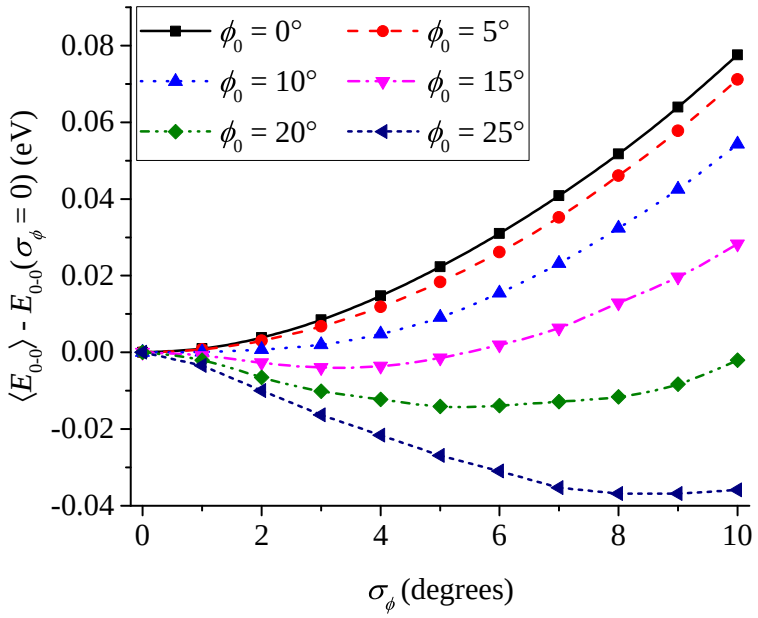


Figure 6.10.: The mean 0-0, $\langle E_{0\text{-}0} \rangle$, normalised to the 0-0 energy for no disorder, for PPV against disorder, σ_ϕ, for different values of the mean dihedral angle, ϕ_0. The results were obtained using the Frenkel model averaged over 1000 realisations of disorder.

energies are redshifted by planarisation and the chromophore length increases. Disorder decreases the chromophore size and affects the transition energies non-monotonically. For a fixed mean torsional angle and disorder shorter chromophores have a lower transition energy. For fixed disorder a more planar polymer will support longer chromophores with lower transition energies. Thus, in morphologically complex systems, such as thin film polymers, the observation that longer chromophores have lower transition energies merely implies a larger degree of planarisation in this region. This shows particularly well in polymers with polychromism, such as MEH-PPV which as a blue and a red phase corresponding to more coiled and more planarised morphologies [142–144].

Having discussed the principal effects of disorder and morphology on the LEGSs and their energies in linear polymers the absorption and emission spectra of PPP and PPV po-

lymers will now be modelled using the Frenkel model and Born-Oppenheimer expressions derived previously.

Poly(*para*-phenylene) Fig. 6.11 shows the emission and absorption spectra of PPP polymers at varying amounts of disorder. Room temperature corresponds to about $\sigma_\phi = 0.15$ and $T = 77$ K is between $\sigma_\phi = 0.05$ and 0.10. To calculate the absorption spectra, it is assumed that the polymer absorbs into every available state, while for emission Kasha's rule is assumed, *i.e.* that every state relaxes into the LEGSs for the respective part of the chain before decaying radiatively. If a LEGS is not populated via absorption it is furthermore assumed that it is via ultra-fast conversion from QEESs or LEESs overlapping with the respective LEGS. This, and the difference in the definition of the absorption and emission spectra, leads to a breakdown of the mirror-image relationship of the spectra. While reasonably accurate for the ordered chains, it breaks down as soon as disorder is introduced.

As expected from the discussion above, an increase in disorder leads to a loss of intensity in the 0-0 band, while higher order transitions, especially the 1-0 absorption and 0-1 emission, are enhanced. This suggests a decrease in $I_{00}/I_{01}^{\mathrm{E}}$ ratio which in turn implies a shortening of the chromophores. Also observed is the inhomogeneous broadening on the low-energy side of the absorption spectrum as well as the initial redshift of the 0-0 transition which is followed by a blueshift for large disorder. In both spectra the vibronic progression becomes unresolved for $\sigma_\phi \gtrsim 5°$.

As before, the spectra can be compared to experimental results [145, 146]. The absorption spectrum at room temperature is reproduced accurately, with a complete loss of vibronic finestructure. The energy is underestimated by about 0.4 eV, however. The emission spectra, on the other hand, show significant differences to the experimental results.

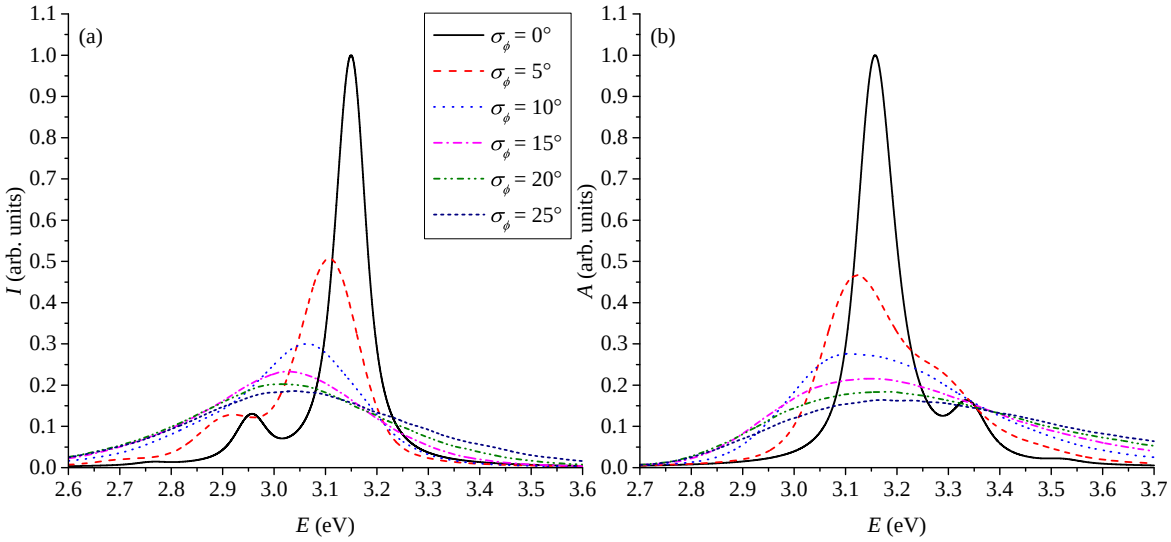


Figure 6.11.: Emission (a) and absorption (b) spectra of PPP polymers for various amounts of disorder using the parameters given above. The spectra were obtained from polymers of 1000 sites and averaged over 200 realisations of disorder using the Frenkel model and Born-Oppenheimer expressions.

While the energies are overestimated by about 0.3 eV it is especially the intensities that are not reproduced accurately. While the broadening with disorder/temperature is calculated correctly, the intensity ratios are wrong. This can have many reasons, firstly it can be due to the neglect of higher-order corrections to the intensity calculation, such as the Herzberg-Teller correction (see below) and secondly, torsional relaxation is not explicitly considered. With the results shown above, however, some qualitative predictions can be made regarding its influence on the optical properties. Excited states of phenylene-based polymers generally exhibit stiffer torsional potentials, which leads to greater planarisation of the polymer while also reducing torsional fluctuations due to temperature. This is, according to the results presented above, expected to red-shift the transition energies, narrow the inhomogeneous broadening, and increase the chromophore size. It is, however, expected that torsional relaxation has a smaller influence in polymers than it does in oligomers due to the decrease of exciton-phonon coupling with the inverse square of

the chromophore size. Lastly, in the solid state exciton migration to lower energy LEGSs before de-excitation is ignored.

Poly(*para*-phenylene vinylene) In contrast to PPP poly(*para*-phenylene vinylene) can be intrinsically non-linear due to *cis-trans* defects along the chain. While the electronic properties are not affected by this as the overlap between p-orbitals is symmetric with respect to these defects, the optical properties are heavily affected, partially because the site transition dipole moments will align in a different way resulting in a different overall transition dipole moment. The effects of curvature were discussed in great detail in Chapter 5 and the discussion here is limited to the results obtained with the Frenkel model used in Chapter 4 and a simplistic approach to the curvature will be used. A more sophisticated approach using the results of Chapter 5 is used below.

The *cis-trans* defects will limit the length of the statistical or Kuhn segments in a polymer. The length of such a segment, the Kuhn length, for a random-flight polymer is given as,

$$m = \frac{6R_{\mathrm{g}}^2}{Sa}, \tag{6.13}$$

where R_{g} is the radius of gyration, S is the polymer contour length and a is the monomer size. The value of m decreases as the polymer becomes more coiled. It is the chromophore curvature that greatly influences the optical properties in addition to the chromophore size and it is convenient to introduce a different metric to measure the chromophore curvature. The radius of gyration can be calculated directly and it will be used as a proxy for the Kuhn length. Define a quantity, ρ, as

$$\rho = \frac{\langle R_g^2 \rangle^{\frac{1}{2}}}{\langle \mathrm{CL} \rangle}, \tag{6.14}$$

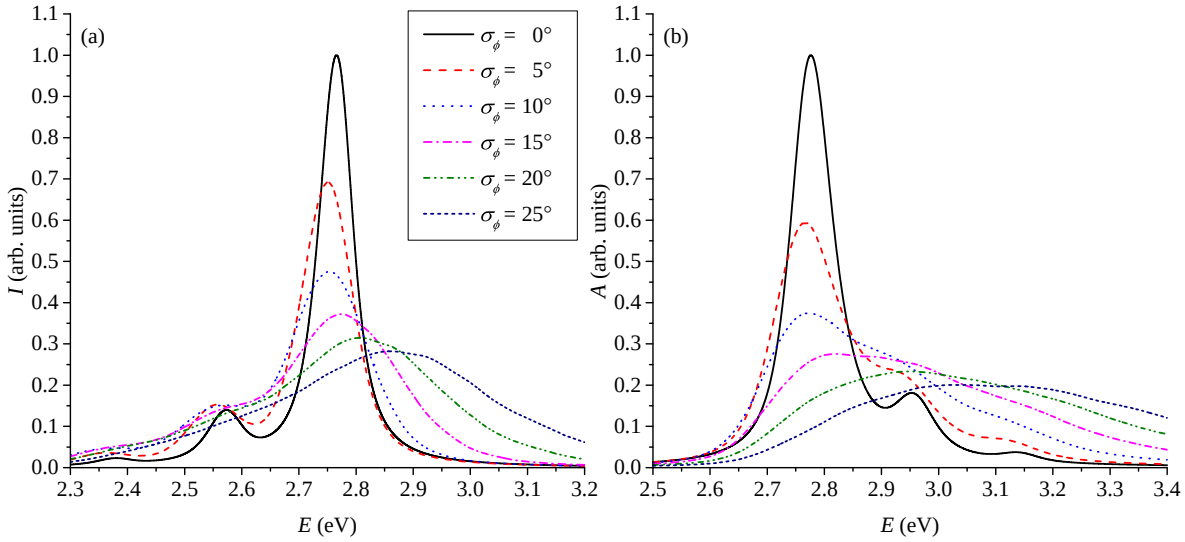


Figure 6.12.: Emission (a) and absorption (b) spectra of all-*trans* PPV polymers for various amounts of disorder using the parameters given above. The spectra were obtained form polymers of 1000 sites and averaged over 200 realisations of disorder using the Frenkel model and Born-Oppenheimer expressions.

where CL is the chromophore length as used above. Again, the value of ρ decreases as the polymer becomes more coiled. $\rho \geq 1$ implies a virtually straight polymer.

Fig. 6.12 shows the emission and absorption spectra for all-*trans* PPV for different values of disorder averaged over 200 polymers with 1000 moieties each using the Frenkel model and Born-Oppenheimer expressions. The trends for increasing disorder are identical to the discussion of PPP above and will not be repeated here.

The spectra will now be discussed as function of the Kuhn length within the Born-Oppenheimer and Condon approximations using the Frenkel model. In Chapter 5 is has been shown that this treatment is not entirely accurate and that post-Condon effects have to be included in the discussion. However, the results obtained with this low-cost method are qualitatively correct and therefore useful for further discussion.

As Fig. 6.13 shows, as the polymer becomes more coiled the absorption spectrum broadens which corresponds to transfer of oscillator strength to higher order transitions. This

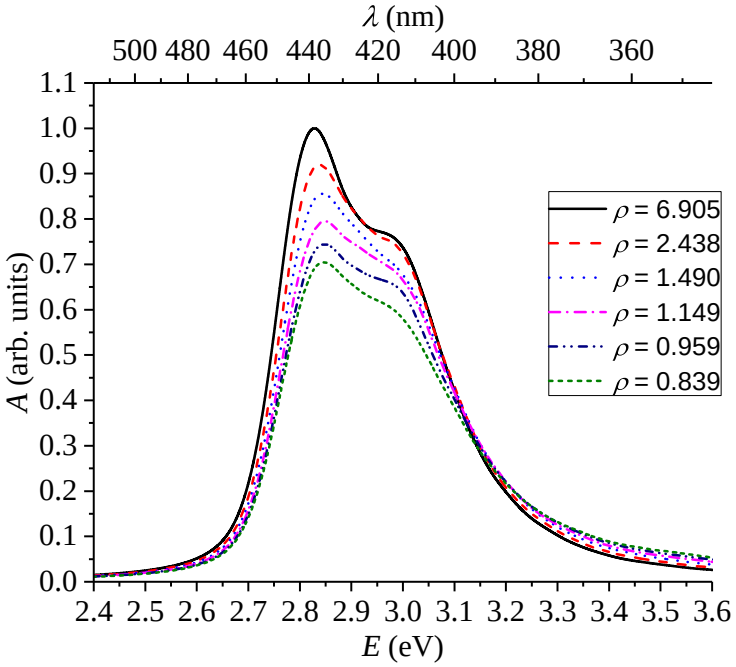


Figure 6.13.: Absorption spectrum for PPV polymers of different conformation as expressed by ρ; $\phi_0 = 15°$, $\sigma_\phi = 10°$. Other parameters as above.

is to be expected, as will be shown below, even within the Born-Oppenheimer and Condon approximations, as more states become optically active within non-linear polymers. It is noticeable that both, torsional disorder and *cis-trans* defects lead to inhomogeneous broadening of the absorption spectra. As it is assumed that emission only occurs from the LEGSs on the polymer, the curvature does not have an effect on the emission spectra within the approximations made here. In Chapter 5 is has been shown that the curvature does in fact have an effect on these spectra, but it is due to post-Condon effects.

The experimental emission intensity ratio, I_{00}/I_{01} for MEH-PPV in solution ranges from 1.5 - 3.5, [13,76,77,141,147,148] in particular 2.9 and 1.7 for the red and blue phases of MEH-PPV, respectively, at 110 K, implying conjugation lengths of 11 and 7 monomer units using $\bar{g_1^2} = 2.53$. The computed values of this ratio are larger, which is partially due to the fact that MEH-PPV has a larger mean dihedral angle of 30° due to steric hindrance

Monomer Parameters (X=P,E)		
Parameter	Phenylene, P	Ethynylene, E
ε_0^X / eV	6.05	10.4
A_X	1.7	2.4
$g_1^2(X)$	1.45	2.88
System Parameters		
Parameter	CPPE	
J^{SE} / eV	1.68	
J^{DD} / eV	0.6	
ϕ_0	0	
K / eV rad^{-2}	0.38	

Table 6.3.: Parameters used in the modelling of CPPE macrocycles. As before for PPP and PPV, $\hbar\omega = 0.19$ eV and $\sigma_\varepsilon = 0.065$ eV.

of the side chains and as discussed above a larger ϕ_0 cause a blue shift of the spectra and shorter conjugation lengths.

6.2 Poly(para-phenylene ethynelene) Macrocycles

Cyclo(*para*-phenylene ethynelene) (CPPE) is a commonly investigated conjugated macrocycle as the ethynelene units allow for a greater degree of flexibility within the polymer. The parameters used for the modelling of these systems are listed in Tab. 6.3.

The spectra are first evaluated using a tight-binding Frenkel model, which assumes the Condon approximation (*i.e.* neglects the Herzberg-Teller contributions) and discuss the primary effects of temperature and disorder on these spectra before turning to calculations using the fully quantised Frenkel-Holstein model and the DMRG routine for an (essentially) correct modelling.

Within the Condon Approximation Fig. 6.14 shows the calculated spectra for [15]CPPE with varying amounts of disorder/Temperatures. Room temperature corresponds to $\sigma_\phi \approx 0.25$ rad. For the emission spectrum Kasha's rule has been adopted, *i.e.*

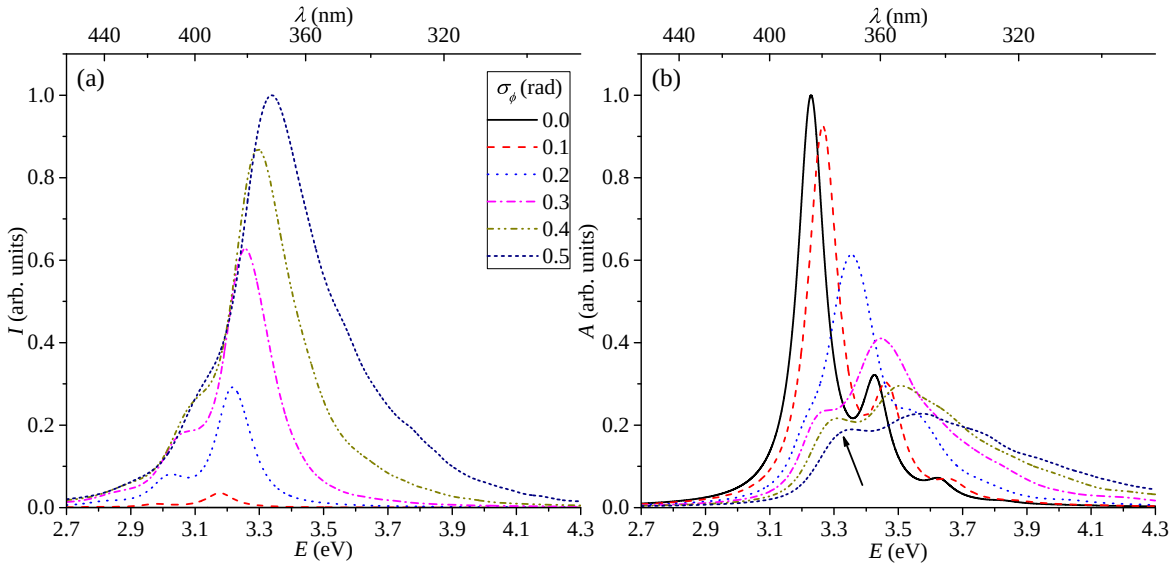


Figure 6.14.: Emission (a) and Absorption (b) spectrum of [15]CPPE for different amounts of disorder, as quantified by σ_ϕ, calculated within the Condon approximation. The arrow indicates the emerging $j = 0$ 0-0 transition peak for increasing disorder.

the emission only occurs from LEGSs, while absorption occurs into all states.

For the emission the vanishing of the entire spectrum for ordered systems can be observed due to the transition becoming completely dark because of disorder. With increasing disorder the emission becomes more intense and the spectral features vanish due to broadening of the peaks. In addition, a blueshift is observed, which is in agreement with previous results. The mean dihedral angle is taken to be 0 and hence any amount of disorder, while localising the exciton, will increase its energy. The absorption spectrum shows the $\bar{k} = 1$ vibronic progression for an ordered system as the $\bar{k} = 0$ transition is dark. For increasing disorder the peaks broaden and smear out, however, for $\sigma_\phi \gtrsim 0.2$ rad, a low-energy shoulder emerges (arrow) which gains in intensity relatively to the rest of the spectrum with increasing disorder. This is the $\bar{k} = 0$ 0-0 transition which becomes allowed due to a breaking of symmetry. As was the case for the emission spectrum, a blueshift can be observed due to the introduction of disorder.

Fully Quantised Model The DMRG method to solve the fully quantised model has also been used. The results are averaged over 40 different realisations of disorder (in contrast to 1000 above) owing to computational costs. The 35 lowest energy states were computed in this approach. State 1 is the $\bar{k} = 0, v = 0$ state, states 2 and 3 are the $\bar{k} = \pm 1, v = 0$ state and the states 4-33 form the $\bar{k} = 0, v = 1$ manifold, *i.e.* only the 0-0 and 0-1 transitions are computed, both in absorption as well as in emission.

Fig. 6.15 shows the computed spectra. In emission the difference to the Condon spectra is immediately obvious: the spectrum does not vanish for a perfectly ordered system but shows a distinct peak at about 2.9 eV. This is the $\bar{k} = 0$ 0-1 emission transition which is rendered Herzberg-Teller allowed by coupling to the $\bar{k} = 1$ manifold. With increasing disorder a peak appears about 0.2 eV higher in energy than the 0-1 peak, which decreases in intensity and broadens. The emerging 0-0 peak continues to increase with disorder and the 0-0/0-1 ratio does so, too. This implies a shrinking LEGSs size, in accordance with previous results for linear chains, albeit now shown by an increase in 0-0 intensity, rather than a decrease in 0-1 intensity.

The effect of the Herzberg-Teller correction can be seen in the absorption spectrum, as well. For an ordered chain two distinct peaks can be seen, which could be interpreted as the 0-0 and 0-1 peaks of the same $\bar{k}$, however their energetic separation is distinctively smaller than the vibrational energy, namely about 0.1 eV (in contrast to 0.19 eV). The peaks observed are the $\bar{k} = 1$ 0-0 transition (~ 3.2 eV) and the $\bar{k} = 0$ 0-1 transition (~ 3.3 eV), which is now an allowed transition due to coupling to the $\bar{k} = 1$ manifold.

With increasing disorder the usual broadening of the peaks and the blue-shift of the spectrum is observed. For $\sigma_\phi \gtrsim 0.2$ rad the $\bar{k} = 0$ 0-0 transition starts to emerge on the low-energy shoulder of the spectrum, being now an allowed transition due to the breaking

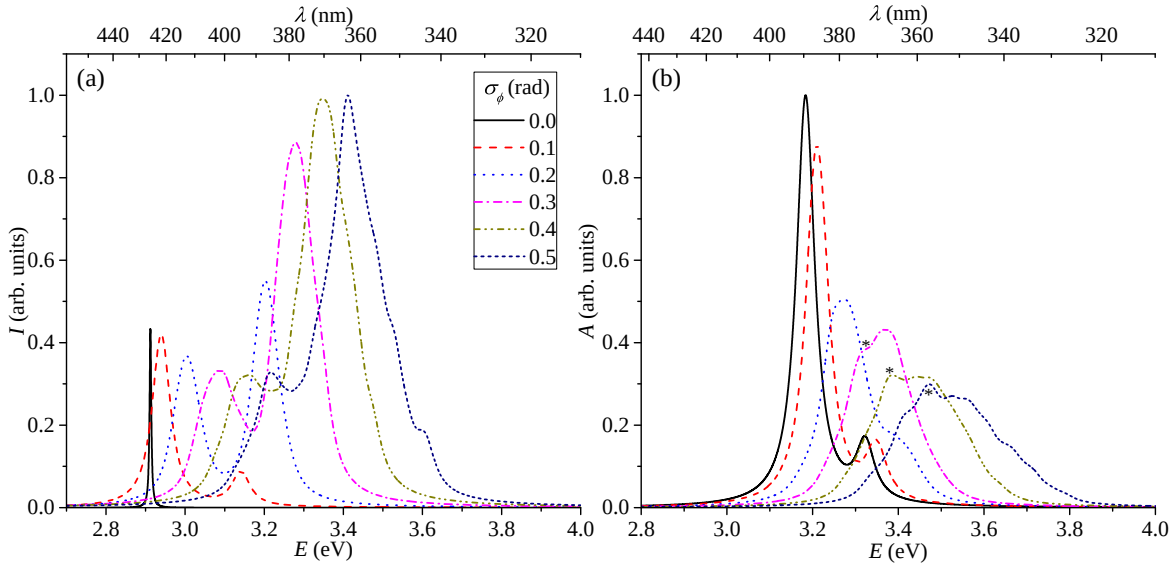


Figure 6.15.: Emission (a) and Absorption (b) spectrum of [15]CPPE for different amounts of disorder, as quantified by σ_ϕ, calculated with the fully quantised model. The asterisks indicate the emerging $\bar{k} = 0$ 0-0 absorption with increasing disorder.

of symmetry of the system and is marked in the spectra with an asterisk. This also means that the $\bar{k} = 0$ 1-0 absorption gains intensity due to the Condon contribution. The shown spectra are, especially for high disorder, not smooth due to the comparatively low number of chains the spectra are averaged over.

6.3 Ladder-type PPP (MeLPPP)

MeLPPP (see Fig. 6.1) is a derivative of PPP which stands out due to its torsional rigidity. The bridging CRR' units that link neighbouring phenylene units have two effects on the structure of the polymer: (i) due to the strain they exert on the phenylene units these organise in a more planar structure than unsubstituted PPP and (ii) for the same reason the torsional force constant is significantly larger, leading to less disorder in the system. As such it is an ideal system to perform structural studies on and test the theories

developed in this thesis in a proof-of-principle approach.

The polymer itself can be manufactured in a very precise way leading to virtually no defects within the polymer (such as a-tactic staggering of the phenylene rings). Spun in a thin film spectra were measured by the Köhler Group in Bayreuth at various temperatures and permission was kindly given to use these results in this thesis. Observations in this system are similar to those made previously: (i) the 0-0/1-0 absorption intensity increases with increasing temperature indicating shorter chromophores; (ii) the spectra display a blueshift with increasing temperature. However, due to the structural rigidity smearing of the absorption spectrum is almost not observed leading to a clear resolution of the absorption peaks for the entire temperature range from 80 K to 310 K.

The spectrum at 80 K was used as template to fit the parameters of the system to. As it is a PPP derivative, $\varepsilon_)$, J_{DD}, and J_{SE} were chosen to be the values of PPP (see Tab. 6.1 and [43]) while g_1^2, K, and ϕ_0 were optimised. In addition to the purely empirical optimisation, electronic structure calculations were performed to confirm the optimised values for ϕ_0 and K (see App. C). For subsequent temperatures the value of g_1^2 was held constant (as it is assumed to be temperature independent) and only the geometric parameters, ϕ_0 and K, acting as a proxy for disorder, were optimised. While the torsional force constant itself is not expected to be temperature dependent, the disorder of the system will be. In the bulk the relation of the disorder to the force constant as used previously is not applicable any more. However, using K as a proxy for the disorder allows the calculation of the disorder as a function of T without making alterations to the code.

Fig. 6.16 shows the optimised spectra for the different temperatures. Due to computational limitations the spectra did not fully converge, however differences are small.

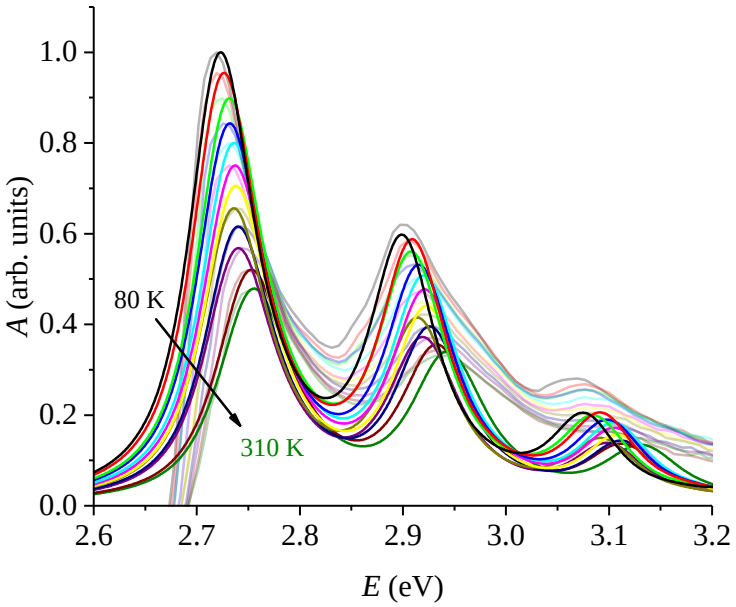


Figure 6.16.: Experimental (faded) and calculated (bold) spectra of MeLPPP at different temperatures from 80 K to 310 K. The spectra are not fully converged, however the features are reproduced: a blue-shift of the peaks with increasing energy, an increase in the 0-0 to 1-0 absorption ratio, and an overall decrease of the intensity in the region shown.

Generally, the blue-shift with increasing temperature is reproduced well. While the experimental spectra show a 0-0 shift from 2.719 eV ($T = 80$ K) to 2.756 eV ($T = 310$ K), the calculated spectra show a shift from 2.723 eV ($T = 80$ K) to 2.756 eV ($T = 310$ K), slightly overestimating the 0-0 vibrational peak energy for low-T. As for the ratios, for the experimental spectra the ratio increases from 0.62 to 0.69 (1-0/0-0 ratio), and for the calculated spectra from 0.60 to 0.71, over-shooting on either end.

As the spectra are not fully converged, neither are the structural parameters presented in Fig. 6.17. The fitted data for the thin-film is presented along-side an ideal model for a polymer in solution in which the disorder scales as $T^{1/2}$ due to the thermal energy and the equilibrium angle is independent of T [83]. The disorder in a thin-film is significantly smaller than in a solution and only increases slowly with temperature, as expected due

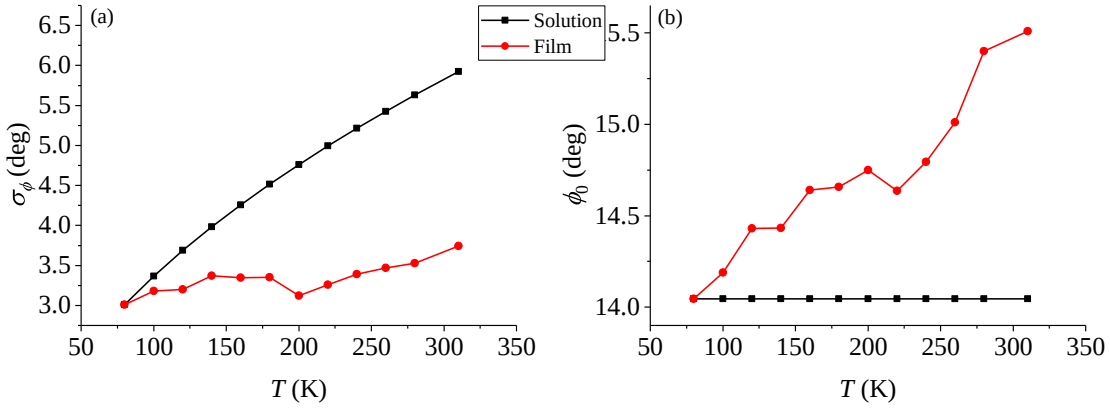


Figure 6.17.: Disorder, σ_ϕ, and equilibrium dihedral, ϕ_0, for a solution and a thin film of MeLPPP. The values for the thin film were obtained via the fitting of the calculated to the experimental spectra for the temperatures shown [149,150]. The fits did not fully converge, which explains the slight scattering of the values, however, the overall trend, increasing disorder and dihedral with temperatures, is easily seen.

to the tight packing of chains. σ_ϕ seems to increase more for higher T, while for $T \lesssim 200$ K it appears more or less constant (subject to convergence errors). The dihedral also increases with T, more or less monotonically (again, subject to convergence errors). Like the disorder, the increase with T seems to become larger for large T, however this is less pronounced. The increase in the dihedral is expected due to increased thermal energy and steric considerations due to the bulky side-chains of the polymer.

These results are, to our knowledge, the first attempt to elucidate structural data from linear spectra directly by using theoretical algorithms. While the data is not fully converged, the trends are clear and as expected and the results presented are therefore a proof-of-principle that optical spectra contain information about the multi-scale structure of polymer chains and aggregates. After a summary in the next chapter we will build on this observation to propose a scheme that is, in principle, able to act as a structure determination tool using the spectroscopic signature of polymers.

7

Conclusion and Outlook

The research interest in conjugated polymers has recently started to decline as the main focus is shifted towards a novel class of photovoltaics, the so called Perovskites. These materials are organic-inorganic hybrid materials which crystalise in a perovskite structure and have seen a large increase in efficiency over the past years. As such they have somewhat eclipsed conjugated polymers as desirable materials for photoelectric applications. This may be due to a lack of understanding of the quantum mechanical processes that occur within conjugated polymers under the interaction with light and as such a more thorough theoretical foundation for these processes might advance the research into conjugated polymers.

This work is a first step into this direction and a brief summary of the results of the previous chapters will follow before tying this work into a larger context of anticipated developments over the coming years.

7.1 Summary of Results

Using a Frenkel-Holstein model, directly coupling excitonic and vibrational degrees of freedom, closed formulae relating the local structure of a polymer to its optical signature have been derived. Electronic excitations in conjugated polymers can be treated as a single particle coupled to local normal modes within the monomers, which in turn can be treated quantum-mechanically as phonons. This gives rise to two models: a semi-classical model treating the normal modes classically and a fully-quantised model. While the former is a relatively simple model that is easily solvable even for large systems, the latter

is the more accurate one. As a trade-off for the accuracy, however, the computational cost increases significantly and its applicability is therefore limited to relatively small systems.

In Chapter 4 the fully quantised model was used to verify theoretical predictions derived from the Frenkel-Holstein model in the adiabatic limit. Using parameters that are generally applicable to conjugated polymers, the results were found to match the Born-Oppenheimer predictions very closely in the case of linear, non-disordered polymers. Furthermore, introducing random disorder into the systems, it was shown using this high-accuracy method, that the excitations localise to sections of the polymer chain. These sections show the same spectral features of ordered chains of the same lengths and for a given amount of disorder have a defined length. It is this feature that enabled the definition of a chromophore within a polymer and the direct link to quantum-mechanical phenomena.

Having established that the Born-Oppenheimer expression for the vibronic progression in conjugated polymers are generally valid, the semi-classical Frenkel-Holstein model, which does not compute the vibronic progression due to the lack of quantised normal modes, can be used to study larger systems, which are not feasible to study with the fully quantised model.

Following on from the discussion of linear systems with torsional disorder, the effect of the conformation of a polymer was studied. First, macrocycles, a relatively new class of compounds with many interesting electronic and optical features, was studied. Due to the symmetry of these systems the transitions between the electronic ground state and excited states are directly affected. The lowest energy transition is a dark transition as it is dipole forbidden. This means, within the Born-Oppenheimer and Condon approximation that the transitions and vibronic progressions observed stem from the second excited

state, the only allowed transition for an ordered cycle. However, due to the coupling between the electronic and vibrational degrees of freedom the symmetry selection rules are partially lifted and transitions that are forbidden within the Condon approximation become allowed, most notably the 1-0 absorption for the lowest excited state. This intensity borrowing from higher excited states can be quantified using perturbation theory within the adiabatic regime. This correction allows, once again, for the determination of the chromophore size and via that the for the calculation of the local disorder in the system by observing the optical properties.

The two limits, linear polymers and macrocycles, were then generalised to bent chains, i.e. polymers with arbitrary conformation and disorder. The theoretical methods developed in this case links the two extreme cases discussed previously and allows now the connection of the optical signature to (i) the local disorder within the chain and (ii) the conformation of the chain itself. This allows the calculation of the (averaged) nano-scale structure of an ensemble of polymer chains from the optical signature (and vice versa). It is found that the bending of chains transfers oscillator strength from the low-energy tail of the spectrum to the high-energy region. Thus, especially for OPVs, depending on the polymer used it may be more efficient to either straighten the chains or to let them coil up as to maximise the spectral absorption in the UV-Vis region. This theoretical model might be the first model that can establish that link and explain the associated experimental observations.

Following on from this general discussion of the theoretical predictions, experimental spectra were modelled using the approach introduced previously. With the use of the Born-Oppenheimer predictions long chains can be modelled using the semi-classical Frenkel-Holstein model. First general poly(*para*-phenylene) (PPP) and poly(*para*-phenylene

vinylene) is studied and the validity of the Born-Oppenheimer expressions is shown for shorter oligomers and polymers. Cyclo-poly(*para*-phenylene ethynylene) was modelled subsequently to demonstrate the effects of the conformation in the extreme case of macrocycles and how introduced disorder then leads to optical signatures typical of bent chromophores before, in the limit of a macrocycle with infinite diameter and/or infitinte disorder the behaviour of linear polymers was found, again.

After this more commonly explored systems, namely a ladder-type PPP polymer, MeLPPP, and an methoxy-substituted PPV (MEH-PPPV) were investigated and the spectra directly compared with experimental results obtained from the research group of Prof A Köhler at the University of Bayreuth, Germany. An optimisation protocol was used for the parameters of the model and following on from this the experimental data was reproduced very accurately, confirming the theoretical results once again. Additionally, in a proof-of-principle, conformational data were extracted from the spectra that match up with experimental evidence, as well.

7.2 Optical Spectroscopy of Conjugated Polymers and its Applications in the Future

The results of this thesis, especially the Chapter 6, show that there is a direct link between the conformation of a polymer and its optical signature and that it is possible to obtain the spectra once the conformation is known. Moreover, however, the conformation can be calculated using the optical spectra. In a direct extension to this project the question arises if a link can be made between the multiscale structures of a polymer and its optical properties. In a bulk or a thin film of a polymer, the direct environment of a single polymer will have a direct influence on its electrical and optical properties, something

that has been incorporated here by introducing random disorder. If the modelling of these multiscale structures can be refined, it could be possible to establish direct relationships of these structural features with the optical signature of a bulk of thin film. While this is a desirable outcome in itself, I propose to take it one step further: use the structure-property relationships established in prior research to devise a protocol capable of finding structural information from optical spectra. Such a protocol would necessarily involve molecular dynamics simulations of the bulk structure of the polymer. Progress on this front has been made and I propose to combine the results from this thesis with those in an iterative approach establishing feedback-loops between the experimental and simulated data. If this approach is to succeed polymer bulk structures can be obtained from spectroscopic measurements and as such a deeper insight into the relationship between structure and optical properties can be obtained, helping to guide future developments in this area and to increase the efficiency of OLEDs and OPs to help secure future energy conversion.

Bibliography

[1] H. Shirakawa, E. J. Louis, A. G. MacDiarmid, C. K. Chiang, A. J. Heeger, Synthesis of Electrically Conducting Organic Polymers: Halogen Derivatives of Polyacetylene, (CH)., *J. Chem. Soc., Chem. Commun.* **16**, 578 (1977).

[2] A. J. Heeger, S. Kivelson, J. R. Schrieffer, W. P. Su, Solitons in Conducting Polymers., *Rev. Mod. Phys.* **60**, 781 (1988).

[3] A. O. Patil, A. J. Heeger, F. Wudl, Optical Properties of Conducting Polymers., *Chem. Rev.* **88**, 183 (1988).

[4] J. H. Burroughes, D. D. C. Bradley, A. R. Brown, R. N. Marks, K. Mackay, R. H. Friend, P. L. Burns, A. B. Holmes, Light-Emitting Diodes Based on Conjugated Polymers., *Nature* **347**, 539 (1990).

[5] R. Peierls, *Quantum Theory of Solids.*, Oxford University Press, Oxford, (1955).

[6] P. W. Anderson, Absence of Diffusion in Certain Random Lattices., *Phys. Rev.* **109**, 1492 (1958).

[7] N. F. Mott, W. D. Twose, The Theory of Impurity Conduction., *Adv. Phys.* **10**, 107 (1961).

[8] K. Huang, A. Rhys, Theory of Light Absorption and Non-Radiative Transitions in F-Centres., *Proc. R. Soc. Lon. A* **204**, 406 (1950).

[9] Z. Shuai, J. L. Brédas, Relaxation of the First Bu Excited State in Linear Polyenes: From trans-Butadiene to Polyacetylene., *J. Chem. Phys.* , 5970 (1992).

[10] Z. Shuai, J. Brédas, W. Su, Nature of Photoexcitations in Poly(Paraphenylene Vinylene) and its Oligomers., *Chem. Phys. Lett.* **228**, 301 (1994).

[11] J. Cornil, D. Beljonne, C. Heller, I. Campbell, B. Laurich, D. Smith, D. Bradley, K. Müllen, J. Brédas, Photoluminescence Spectra of Oligo-Paraphenyllenevinylenes: A Joint Theoretical and Experimental Characterization., *Chem. Phys. Lett.* **278**, 139 (1997).

[12] J. Yu, M. Hayashi, S. Lin, K.-K. Liang, J. Hsu, W. Fann, C.-I. Chao, K.-R. Chuang, S.-A. Chen, Temperature Effect on the Electronic Spectra of Poly(p-Phenylenevinylene)., *Synth. Met.* **82**, 159 (1996).

[13] R. Chang, J. Hsu, W. Fann, K. Liang, C. Chang, M. Hayashi, J. Yu, S. Lin, E. Chang, K. Chuang, S. Chen, Experimental and Theoretical Investigations of Absorption and Emission Spectra of the Light-Emitting Polymer MEH-PPV in Solution., *Chem. Phys. Lett.* **317**, 142 (2000).

[14] F. C. Spano, The Spectral Signatures of Frenkel Polarons in H- and J-Aggregates., *Acc. Chem. Res.* **43**, 429 (2010).

[15] F. C. Spano, H. Yamagata, Vibronic Coupling in J-Aggregates and Beyond: A Direct Means of Determining the Exciton Coherence Length from the Photoluminescence Spectrum., *J. Phys. Chem. B* **115**, 5133 (2011).

[16] H. Yamagata, F. C. Spano, Vibronic Coupling in Quantum Qires: Applications to Polydiacetylene., *J. Chem. Phys.* **135**, 054906 (2011).

[17] H. Yamagata, F. C. Spano, Strong Photophysical Similarities between Conjugated Polymers and J-Aggregates., *Phys. Chem. Lett.* **5**, 622 (2014).

[18] W. Barford, E. R. Bittner, A. Ward, Exciton Dynamics in Disordered Poly(p-phenylenevinylene). 2. Exciton Diffusion., *J. Phys. Chem. A* **116**, 10319 (2012).

[19] W. Barford, Excitons in Conjugated Polymers: A Tale of Two Particles., *J. Phys. Chem. A* **117**, 2665 (2013).

[20] R. H. Mitchell, The Metacyclophanediene-Dihydropyrene Photochromic π Switch., *Eur. J. Org. Chem.* **1999**, 2695 (1999).

[21] M. Iyoda, M. Hasegawa, Y. Miyake, Bi-TTF, Bis-TTF, and Related TTF Oligomers., *Chem. Rev.* **104**, 5085 (2004).

[22] J. S. Kim, D. T. Quang, Calixarene-Derived Fluorescent Probes., *Chem Rev.* **107**, 3780 (2007).

[23] K. Becker, P. Lagoudakis, G. Gaefke, S. Höger, J. Lupton, Exciton Accumulation in π-Conjugated Wires Encapsulated by Light-Harvesting Macrocycles., *Angew. Chem. Int. Ed.* **46**, 3450 (2007).

[24] O. Mongin, A. Schuwey, M.-A. Vallot, A. Gossauer, Synthesis of a Macrocyclic Porphyrin Hexamer with a Nanometer-Sized Cavity as a Model for the Light-Harvesting Arrays of Purple Bacteria., *Tetrahedron Lett.* **40**, 8347 (1999).

[25] R. Herges, Organic Chemistry: Aromatics with a Twist., *Nature* **450**, 36 (2007).

[26] R. Herges, Topology in Chemistry:âĂĽ Designing Möbius Molecules., *Chem. Rev.* **106**, 4820 (2006).

[27] H. Meier, Areno-Condensed Annulenes - Extended Discotic Mesogens., *Synthesis* **2002**, 1213 (2002).

[28] K. S. Kim, J. M. Lim, A. Osuka, D. Kim, Various Strategies for Highly-Efficient Two-Photon Absorption in Porphyrin Arrays., *J. Photochem. Photobiol. C* **9**, 13 (2008).

[29] J. K. Sprafke, D. V. Kondratuk, M. Wykes, A. L. Thompson, M. Hoffmann, R. Drevinskas, W.-H. Chen, C. K. Yong, J. Kärnbratt, J. E. Bullock, M. Malfois, M. R. Wasielewski, B. Albinsson, L. M. Herz, D. Zigmantas, D. Beljonne, H. L. Anderson, Belt-Shaped π-Systems: Relating Geometry to Electronic Structure in a Six-Porphyrin Nanoring., *J. Am. Chem. Soc.* **133**, 17262 (2011).

[30] C.-K. Yong, P. Parkinson, D. V. Kondratuk, W.-H. Chen, A. Stannard, A. Summerfield, J. K. Sprafke, M. C. O'Sullivan, P. H. Beton, H. L. Anderson, L. M. Herz, Ultrafast Delocalization of Excitation in Synthetic Light-Harvesting Nanorings., *Chem. Sci.* **6**, 181 (2015).

[31] C. Camacho, T. A. Niehaus, K. Itami, S. Irle, Origin of the Size-Dependent Fluorescence Blueshift in [n]Cycloparaphenylenes., *Chem. Sci.* **4**, 187 (2013).

[32] L. Adamska, I. Nayyar, H. Chen, A. K. Swan, N. Oldani, S. Fernandez-Alberti, M. R. Golder, R. Jasti, S. K. Doorn, S. Tretiak, Self-Trapping of Excitons, Violation of Condon Approximation, and Efficient Fluorescence in Conjugated Cycloparaphenylenes., *Nano Lett.* **14**, 6539 (2014).

[33] A. V. Aggarwal, A. Thiessen, A. Idelson, D. Kalle, D. Würsch, T. Stangl, F. Steiner, S.-S. Jester, J. Vogelsang, S. J. M. L. Höger, Fluctuating Exciton Localization in Giant π-Conjugated Spoked-Wheel Macrocycles., *Nat. Chem.* **5**, 964 (2013).

[34] A. Thiessen, D. Würsch, S.-S. Jester, A. V. Aggarwal, A. Idelson, S. Bange, J. Vogelsang, S. Höger, J. M. Lupton, Exciton Localization in Extended π-Electron Systems: Comparison of Linear and Cyclic Structures., *J. Phys. Chem. B* **119**, 9949 (2015).

[35] B. M. Wong, Optoelectronic Properties of Carbon Nanorings: Excitonic Effects from Time-Dependent Density Functional Theory., *J. Phys. Chem. C* **113**, 21921 (2009).

[36] J. Yang, S. Ham, T.-W. Kim, K. H. Park, K. Nakao, H. Shimizu, M. Iyoda, D. Kim, Inhomogeneity in the Excited-State Torsional Disorder of a Conjugated Macrocycle., *J. Phys. Chem. B* **119**, 4116 (2015).

[37] M. S. Vezie, S. Few, I. Meager, G. Pieridou, B. Dörling, R. Shahid Ashraf, A. R. Goni, H. Bronstein, I. McCulloch, S. C. Hayes, M. Campoy-Quiles, J. Nelson, Exploring the Origin of High Optical Absorption in Conjugated Polymers., *Nature Mat.* (2016).

[38] B. Steinberg, L. Scott, New Strategies for Synthesizing Short Sections of Carbon Nanotubes., *Angew. Chem. Int. Ed.* **48**, 5400 (2009).

[39] N. J. Hestand, F. C. Spano, The Effect of Chain Bending on the Photophysical Properties of Conjugated Polymers., *J. Phys. Chem. B* **118**, 8352 (2014).

[40] M. Marcus, O. R. Tozer, W. Barford, Theory of Optical Transitions in Conjugated Polymers. II. Real Systems., *J. Chem. Phys.* **141**, 164102 (2014).

[41] M. Marcus, J. Coonjobeeharry, W. Barford, Theory of Optical Transitions in Conjugated Macrocycles., *J. Chem. Phys.* **144**, 154102 (2016).

[42] G. Herzberg, E. Teller, Schwingungsstruktur der Elektronenübergänge bei mehratomigen Molekülen., *Z. Phys. Chem. Abt. B* **21**, 410 (1933).

[43] W. Barford, *Electronic and Optical Properties of Conjugated Polymers.*, 2 Ed., Oxford University Press, Oxford, (2013).

[44] J. Gierschner, J. Cornil, H.-J. Egelhaaf, Optical Bandgaps of pi-Conjugated Organic Materials at the Polymer Limit: Experiment and Theory., *Adv. Mater.* **19**, 173 (2007).

[45] M. Rohlfing, S. G. Louie, Optical Excitations in Conjugated Polymers., *Phys. Rev. Lett.* **82**, 1959 (1999).

[46] Y. Shimoi, S. Abe, S. Kuroda, K. Murata, Electronic Properties of Neutral and Polaron States in Poly(p-Phenylene Vinylene)., *Synth. Met.* **85**, 1133 (1997).

[47] W. Barford, M. Y. Lavrentiev, R. J. Bursill, The Low Energy Electronic Structure of Poly(P-Phenylene Vinylene)., *Synth. Met.* **101**, 171 (1999).

[48] A. A. Ovchinnikov, I. I. Ukrainskii, G. V. Kventsel, Theory of One-Dimensional Mott Semiconductors and the Electronic Structure of Long Molecules Having Conjugated Bonds., *Soviet Physics - Uspekhi* **15**, 575 (1973).

[49] N. S. Bayliss, A Metallic Model for the Spectra of Conjugated Polyenes., *J. Chem. Phys.* **16**, 287 (1948).

[50] H. Kuhn, Elektronengasmodell zur Quantitativen Deutung der Lichtabsorption von Organischen Farbstoffen I., *Helv. Chim. Acta* **31**, 1441 (1948).

[51] N. F. Mott, R. Peierls, Discussion of the Paper by Boer and Verwey., *Proc. Phys. Soc.* **49**, 72 (1937).

[52] J. H. de Boer, E. J. W. Verwey, Semi-Conductors with Partially and with Completely Filled 3D-Lattice Bands., *Proc. Phys. Soc.* **49**, 59 (1937).

[53] S. Pleutin, J.-L. Fave, The Molecular Crystal Approach for π-Conjugated Polymers: From the Pariser-Parr-Pople Hamiltonian to the Holstein Model for Polaron States., *J. Phys: Cond. Mater.* **11**, 9629 (1999).

[54] R. Pariser, R. G. Parr, A Semi-Emperical Theory of the Electronic Spectra and Electronic Structure of Complex Unsaturated Molecules. I., *J. Chem. Phys.* **21**, 466 (1953).

[55] R. Pariser, R. G. Parr, A Semi-Emperical Theory of the Electronic Spectra and Electronic Structure of Complex Unsaturated Molecules. II., *J. Chem. Phys.* **21**, 767 (1953).

[56] J. A. Pople, Electron Interaction in Unsaturated Hydrocarbons., *Trans. Faraday Soc.* **49**, 1375 (1953).

[57] K. Ohno, Some Remarks on the Pariser-Parr-Pople Method., *Theo. Chim. Acta* **2**, 219 (1964).

[58] W. Su, J. R. Schrieffer, A. J. Heeger, Solitons in Polyacetylene., *Phys. Rev. Lett.* **42**, 1698 (1979).

[59] W. Su, J. R. Schrieffer, A. J. Heeger, Soliton Excitations in Polyacetylene., *Phys. Rev. B* **22**, 2099 (1980).

[60] N. S. Sariciftci, Primary Photoexcitations in Conjugated Polymers: Molecular Exciton Versus Semiconductor Band Model., *World Scientific* (1998).

[61] M. J. Rice, Y. N. Gartstein, Excitons and Interband Excitations in Conducting Polymers Based on Phenylene., *Phys. Rev. Lett.* **73**, 2504 (1994).

[62] M. Chandross, S. Mazumdar, S. Jeglinski, X. Wei, Z. V. Vardeny, E. W. Kwock, T. M. Miller, Excitons in Poly(Para-Phenylenevinylene)., *Phys. Rev. B.* **50**, 14702 (1994).

[63] A. Köhler, D. A. dos Santos, D. Beljonne, Z. Shuai, J.-L. Brédas, A. B. Holmes, A. Kraus, K. Müllen, R. H. Friend, Charge Separation in Localized and Delocalized Electronic States in Polymeric Semiconductors., *Nature* **392**, 903 (1998).

[64] W. Barford, N. Paiboonvorachat, Excitons in Conjugated Polymers: Wavefunctions, Symmetries and Quantum Numbers., *J. Chem. Phys.* **129**, 164716 (2008).

[65] S. Karabunarliev, E. R. Bittner, Polaron-Excitons and Electron-Vibrational Band Shapes in Conjugated Polymers., *J. Chem. Phys.* **118**, 4291 (2003).

[66] J. Frenkel, On the Transformation of Light into Heat in Solids. I., *Phys. Rev.* **37**, 17 (1931).

[67] J. Frenkel, On the Transformation of Light into Heat in Solids. II., *Phys. Rev.* **37**, 1276 (1931).

[68] V. I. Arkhipov, H. Bässler, Exciton Dissociation and Charge Photogeneration in Pristine and Doped Conjugated Polymers., *Phys. Stat. Sol. (A)* **201**, 1152 (2004).

[69] A. Moliton, R. C. Hiorns, Review of Electronic and Optical Properties of Semiconducting π-Conjugated Polymers: Applications in Optoelectronics., *Poly. Int.* **53**, 1397 (2004).

[70] I. G. Scheblykin, A. Yartsev, T. Pullerits, V. Gulbinas, V. Sundström, Excited State and Charge Photogeneration Dynamics in Conjugated Polymers., *J. Phys. Chem. B* **111**, 6303 (2007).

[71] W. Barford, D. Trembath, Exciton Localization in Polymers with Static Disorder., *Phys. Rev. B* **80**, 12 (2009).

[72] O. R. Tozer, W. Barford, Exciton Dynamics in Disordered Poly(p-phenylenevinylene). 1. Ultrafast Interconversion and Dynamical Localization., *J. Phys. Chem. A* **116**, 10310 (2012).

[73] M. Chandross, S. Mazumdar, Coulomb Interactions and Linear, Non-Linear and Triplet Absorption in Poly(para-Phenylenevinylene)., *Phys. Rev. B* **55**, 1497 (1997).

[74] R. Binder, S. Römer, J. Wahl, I. Burghardt, An Analytic Mapping of Oligomer Potential Energy Surfaces to an Effective Frenkel Model., *J. Chem. Phys.* **141**, 014101 (2014).

[75] E. Abrahams, P. W. Anderson, D. C. Licciardello, T. V. Ramakrishnan, Scaling Theory of Localization: Absence of Quantum Diffusion in Two Dimensions., *Phys. Rev. Lett.* **42**, 673 (1979).

[76] G. D. Scholes, D. S. Larsen, G. R. Fleming, G. Rumbles, P. L. Burn, Origin of Line Broadening in the Electronic Absorption Spectra of Conjugated Polymers: Three-Pulse-Echo Studies of MEH-PPV in Toluene., *Phys. Rev. B* **61**, 13670 (2000).

[77] S. T. Hoffmann, H. Bässler, A. Köhler, What Determines Inhomogeneous Broadening of Electronic Transitions in Conjugated Polymers?, *J. Phys. Chem.* **114**, 17037 (2010).

[78] J. M. Ziebarth, M. D. McGehee, Measuring the Refractive Indices of Conjugated Polymer Films with Bragg Grating Outcouplers., *App. Phys. Lett.* **134**, 5092 (2003).

[79] W. Barford, N. Paiboonvorachat, D. Yaron, Second-Order Dispersion Interactions in π-Conjugated Polymers., *J. Chem. Phys.* **134**, 234101 (2011).

[80] A. V. Malyshev, V. A. Malyshev, Statistics of Low Energy Levels of a One-Dimensional Weakly Localized Frenkel Exciton: A Numerical Study., *Phys. Rev. B* **63**, 195111 (2001).

[81] A. V. Malyshev, V. A. Malyshev, F. Domínguez-Adame, Low-Temperature Quenching of One-Dimensional Localized Frenkel Excitons., *Chem. Phys. Lett.* **371**, 417 (2003).

[82] A. V. Malyshev, V. A. Malyshev, F. Domínguez-Adame, On the Low-Temperature Diffusion of Localized Frenkel Excitons in Linear Molecular Aggregates., *J. Phys. Chem. B* **107**, 4418 (2003).

[83] D. V. Makhov, W. Barford, Local Exciton Ground States in Disordered Polymers., *Phys. Rev. B* **81**, 165201 (2010).

[84] W. Barford, M. Marcus, Theory of Optical Transitions in Conjugated Polymers. I. Ideal Systems., *J. Chem. Phys.* **141**, 164101 (2014).

[85] W. Barford, I. Baczarow, T. Wharram, Ulta-Fast Dynamical Localization of Photo-Excited States in Poly(para-Phenylenevinylene)., *J. Phys. Chem. A* **117**, 2665 (2011).

[86] T. Holstein, Studies of Polaron Motion: Part I. The Molecular-Crystal Model., *Ann. Phys.* **8**, 325 (1959).

[87] T. Holstein, Studies of Polaron Motion: Part II. The "Small" Polaron., *Ann. Phys.* **8**, 343 (1959).

[88] M. Y. Lavrentiev, W. Barford, Electron-Phonon Interactions in Poly(Para-Phenylene) Oligomers., *J. Chem. Phys.* **111**, 11177 (1999).

[89] R. E. Merrifield, Theory of the Vibrational Structure of Molecular Exciton States., *J. Chem. Phys.* **40**, 445 (1963).

[90] E. Ortiz Muniz, A Method for Deriving Various Formulas in Electrostatics and Electromagnetism Using Lagrange's Trigonometric Identities., *Am. J. Phys.* **21**, 140 (1953).

[91] A. Jeffrey, H.-H. Dai, *Handbook of Mathematical Formulas and Intgerals.*, 4 Ed., Academic Press, (2008).

[92] L. D. Landau, S. I. Pekar, Effective Mass of a Polaron., *Zh. Eksp. Teor. Fiz.* **18**, 419 (1948).

[93] S. I. Pekar, Research into Electron Theory of Crystals., *Gostekhizdat, Moskva* (1951).

[94] L. D. Landau, Electron Motion in Crystal Lattices., *Z. Phys.* **3**, 664 (1933).

[95] J.-L. Brédas, J. Cornil, A. J. Heeger, The Exciton Binding Energy in Luminescent Conjugated Polymers., *Adv. Mater.* **8**, 447 (1996).

[96] S. A. Schmid, R. Abbel, A. P. H. J. Schenning, E. W. Meijer, L. M. Herz, Impact of Nuclear Lattice Relaxation on the Excitation Energy Transfer Along a Chain of π-Conjugated Molecules., *Phys. Rev. B* **81**, 085438 (2012).

[97] E. I. Rashba, *Excitons.*, Elsevier Science, Amsterdam, (1982).

[98] B. Kramer, A. MacKinnon, Localization: Theory and Experiment., *Rep. Prog. Phys.* **56**, 1469 (1993).

[99] M. Capone, W. Stephan, M. Grilli, Small-Polaron Formation and Optical Absorption in Su-Schrieffer-Heeger and Holstein Models., *Phys. Rev. B* **56**, 4484 (1997).

[100] O. R. Tozer, W. Barford, Localization of Large Polarons in the Disordered Holstein Model., *Phys. Rev. B* **89** (2014).

[101] W. Barford, M. Marcus, O. R. Tozer, Polarons in π-Conjugated Polymers: Anderson or Landau?, *J. Phys. Chem. A* **120**, 615 (2016).

[102] S. R. White, R. M. Noack, Real-Space Quantum Renormalization Groups., *Phys. Rev. Lett.* **68**, 2863 (1992).

[103] K. G. Wilson, The Renormalization Group: Critical Phenomena and the Kondo Problem., *Rev. Mod. Phys.* **47**, 773 (1975).

[104] H. R. Krishna-Murthy, J. W. Wilkins, K. G. Wilson, Renomalization Group Approach to the Anderson Model of Dilute Magnetic Alloys. I. Static Properties for the Symmetric Case., *Phys. Rev. B* **21**, 1003 (1980).

[105] R. Bulla, T. A. Costi, T. Prushke, Numerical Renomalization Group Method for Quantum Impurity Systems., *Rev. Mod. Phys.* **80**, 395 (2008).

[106] S. Chui, J. W. Bray, Computer Renormalization Group Technique Applied to the Hubbard Model., *Phys. Rev. B* **18**, 2426 (1978).

[107] J. E. Hirsch, Renormalization Group Study of the Hubbard Model., *Phys. Rev. B* **22**, 5259 (1980).

[108] C. Dasgupta, P. Pfeuty, Real-Space Renormalization Group Study of the One-Dimensional Hubbard Model., *J. Phys. C: Solid State Physics.* **14**, 717 (1981).

[109] C. Y. Pan, X. Chen, Renormalization Group Study of High-Spin Heisenberg Antiferromagnets., *Phys. Rev. B* **36**, 8600 (1987).

[110] M. D. Kovarik, Numerical Solution of large $s = \frac{1}{2}$ and $s = 1$ Heisenberg Antiferromagnetic Spin Chains Using a Truncated Basis Expansion., *Phys. Rev. B* **41**, 6889 (1990).

[111] R. J. Baxter, Dimers on a Rectangular Lattice., *J. Math. Phys.* **9**, 650 (1968).

[112] S. Östlund, S. Rommer, Thermodynamic Limit of Density Matrix Renormalization., *Phys. Rev. Lett.* **75**, 3537 (1995).

[113] J. Dukelsky, M. A. Martin-Delgado, T. Nishino, G. Sierra, Equivalence of the Variational Matrix Product Method and the Density Matrix Renormalization Group Applied to Spin Chains., *Europhys. Lett.* **43**, 457 (1998).

[114] I. P. McCulloch, From Density-Matrix Renormalization Group to Matrix Product States., *J. Stat. Mech.: Theory and Experiment* **2007**, P10014 (2007).

[115] T. Nishino, Y. Hieida, K. Okunishi, N. Maeshima, Y. Akutsu, A. Genidar, Two-Dimensional Tensor Product Variational Formulation., *Prog. Theo. Phys.* **105**, 409 (2001).

[116] F. Verstraete, V. Murg, J. I. Cirac, Matrix Product States, Projected Entangled Pair States, and Variational Renormalization Group Methods for Quantum Spin Systems., *Adv. Phys.* **57**, 143 (2008).

[117] S. Al-Assam, S. R. Clark, C. J. Foot, D. Jaksch, Capturing Long Range Correlations in Two-Dimensional Quantum Lattice Systems Using Correlator Product States., *Phys. Rev. B* **84**, 205108 (2011).

[118] R. Orús, A Practical Introduction To Tensor Networks: Matrix Product States and Projected Entangled Pair States., *Ann. Phys.* **349**, 117 (2014).

[119] U. Schollwöck, The Density-Matrix Renormalization Group., *Rev. Mod. Phys.* **77**, 259 (2005).

[120] U. Schollwöck, The Density Matrix Renormalization Group in the Age of Matrix Product States., *Ann. Phys.* **326**, 96 (2011).

[121] S. R. White, Density-Matrix Algorithms for Quantum Renormalization Groups., *Phys. Rev. B* **48**, 10345 (1993).

[122] G. H. Golub, C. F. van Loan, *Matrix Computations.*, JHUP, (1996).

[123] W. H. Press, S. A. Teukolsky, W. T. Vetterling, B. P. Flannery, *Numerical Recipes in Fortran.*, Cambridge University Press, Cambridge, (1992).

[124] T. Azumi, K. Matsuzaki, What does the Term "Vibronic Coupling" Mean?, *Photochem. Photobiol.* **25**, 315 (1977).

[125] J. Franck, E. G. Dymond, Elementary Processes of Photochemical Reactions., *Trans. Faraday Soc.* **21**, 536 (1926).

[126] E. Condon, A Theory of Intensity Distribution in Band Systems., *Phys. Rev.* **28**, 1182 (1926).

[127] E. U. Condon, Nuclear Motions Associated with Electron Transitions in Diatomic Molecules., *Phys. Rev.* **32**, 858 (1928).

[128] M. M.-L. Grage, Y. Zaushitsyn, A. Yartsev, M. Chachisvilis, V. Sundström, T. Pullerits, Ultrafast Excitation Transfer and Trapping in a Thin Polymer Film., *Phys. Rev. B* **67**, 205207 (2003).

[129] W. J. D. Beenken, T. Pullerits, Excitonic Coupling in Polythiophenes: Comparison of Different Calculation Methods., *J. Chem. Phys.* **120**, 2490 (2004).

[130] R. P. Feynman, Forces in Molecules., *Phys. Rev.* **56**, 340 (1939).

[131] H. Hellmann, *Einführung in die Quantenchemie.*, Franz Deuticke, Leipzig, (1937).

[132] W. Demtröder, *Laser Spectroscopy: Basic Concepts and Instrumentation.*, Springer, (2003).

[133] M. J. Frisch, G. W. Trucks, H. B. S. et al., Gaussian 09 Revision D.01, gaussian Inc. Wallingford CT 2009.

[134] A. D. Becke, Density-Functional Thermochemistry. III. The Role of Exact Exchange., *J. Chem. Phys.* **98**, 5648 (1993).

[135] A. D. McLean, G. S. Chandler, Contracted Gaussian-Basis Sets for Molecular Calculations. 1. 2nd Row Atoms Z=11-18., *J. Chem. Phys.* **72**, 5639 (1980).

[136] K. Raghavachari, J. S. Binkley, R. Seeger, J. A. Pople, Self-Consistent Molecular Orbital Methods. 20. Basis Set for Correlated Wave-Functions., *J. Chem. Phys.* **72**, 650 (1980).

[137] P. Hohenberg, W. Kohn, Inhomogeneous Electron Gas., *Phys. Rev.* **136**, B864 (1964).

[138] W. Kohn, L. J. Sham, Self-Consistent Equations Including Exchange and Correlation Effects., *Phys. Rev.* **140**, A1133 (1965).

[139] N. Nijegorodov, W. Downey, M. Danailov, Systematic Investigation of Absorption, Fluorescence and Laser Properties of some p- and m-Oligophenylenes., *Spectro. Acta Part A: Molecular and Biomolecular Spectroscopy* **56**, 783 (2000).

[140] A. Piaggi, G. Lanzani, G. Bongiovanni, M. Loi, A. Mura, W. Graupner, F. Meghdadi, G. Leising, Optical Properties of Polycrystalline Films., *Optical Materials* **9**, 489 (1998).

[141] S. Wachsmann-Hogiu, L. A. Peteanu, L. A. Liu, D. J. Yaron, J. Wildeman, The Effects of Structural and Microenvironmental Disorder on the Electronic Properties of Poly[2-methoxy,5-(2'-ethyl-hexoxy)-1,4-phenylene vinylene] (MEH-PPV) and Related Oligomers., *J. Phys. Chem. B* **107**, 5133 (2003).

[142] C. Consani, F. Koch, F. Panzer, T. Unger, A. Köhler, T. Brixner, Relaxation Dynamics and Exciton Energy Transfer in the Low-Temperature Phase of MEH-PPV., *J. Chem. Phys.* **142**, 212429 (2015).

[143] H. Yamagata, N. Hestand, F. C. Spano, A. Köhler, C. Scharsich, S. T. Hoffmann, H. Bässler, The Red-Phase of Poly[2-methoxy-5-(2-ethylhexyloxy)-1,4-phenylenevinylene] (MEH-PPV): A Disordered HJ-Aggregate., *J. Chem. Phys.* **139**, 114903 (2013).

[144] T. Unger, F. Panzer, C. Consani, F. Koch, T. Brixner, H. Bässler, A. Köhler, Ultrafast Energy Transfer between Disordered and Highly Planarized Chains of Poly[2-methoxy-5-(2-ethylhexyloxy)-1,4-phenylenevinylene] (MEH-PPV)., *Macro Lett.* **4**, 412 (2015).

[145] E. Mulazzi, A. Ripamonti, L. Athouël, J. Wery, S. Lefrant, Theoretical and Experimental Investigation of the Optical Properties of Poly(Paraphenylene): Evidence of Chain-Length Distribution., *Phys. Rev. B* **65**, 085204 (2002).

[146] L. Athouël, J. Wéry, B. Dulieu, J. Bullot, J. Buisson, G. Froyer, Optical Properties of Polyparaphenyl Thin Films from Oligomers to Polymers., *Synth. Met.* **84**, 287 (1997).

[147] A. Köhler, S. T. Hoffmann, H. Bässler, An Order-Disorder Transition in the Conjugated Polymer MEH-PPV., *J. Am. Chem. Soc.* **134**, 11594 (2012).

[148] G. A. Sherwood, R. Cheng, T. M. Smith, J. H. Werner, A. P. Shreve, L. A. Peteanu, J. Wildeman, Aggregation Effects on the Emission Spectra and Dynamics of Model Oligomers of MEH-PPV., *J. Phys. Chem. C* **113**, 18851 (2009).

[149] A. Rudnick, K.-J. Kass, E. Preis, U. Scherf, H. Bässler, A. Köhler, Interplay of Localized Pyrene Chromophores and π-Conjugation in Novel Poly(2,7-pyrene) Ladder Polymers., *J. Chem. Phys.* **146**, 174903 (2017).

[150] S. T. Hoffmann, J. M. Koenen, U. Scherf, I. Bauer, P. Strohriegl, H. Bässler, A. Köhler, Triplet-Triplet Annihilation in a Series of Poly(p-Phenylene) Derivatives., *J. Phys. Chem. B* **115**, 8417 (2011).

A

Derivation of the Pariser-Parr-Pople Hamiltonian

Here the Pariser-Parr-Pople Hamiltonian, which is the basis for the exciton models used in this thesis, will be derived from first principles. To our knowledge there is no account of a complete first-principles derivation in the literature.

Consider a system S described by Hamiltonian $\hat{H}$ in the state $|\Psi\rangle_S$. The Hamiltonian has a set of eigenstates, $\{|\Phi_\lambda\rangle\}$ with eigenenergies E_λ, i.e.

$$\hat{H}\,|\Phi_\lambda\rangle = E_\lambda\,|\Phi_\lambda\rangle\,, \tag{A.1}$$

and the state, $|\Psi\rangle_S$ of the system can be expanded in the eigenbasis as,

$$|\Psi\rangle_S = \sum_\lambda \Psi_\lambda\,|\Phi_\lambda\rangle\,, \tag{A.2}$$

where Ψ_λ is the wavefunction. The systems under consideration are molecular and thus the particles investigated (principally) are electrons and nuclei and hence the Hamiltonian can be written in many-body form as,

$$\hat{H} = \sum_{i=1}^{n} \frac{p_i^2}{2m_\mathrm{e}} + \sum_{A=1}^{N} \frac{P_A^2}{2M_A} + \frac{1}{2}\sum_{i\neq j}^{n} \frac{\mathrm{e}^2}{4\pi\varepsilon_0\,|\mathbf{r}_i - \mathbf{r}_j|} + \frac{1}{2}\sum_{A\neq B}^{N} \frac{Q_A Q_B \mathrm{e}^2}{4\pi\varepsilon_0\,|\mathbf{r}_A - \mathbf{r}_B|} - \sum_{i}^{n}\sum_{A}^{N} \frac{Q_A \mathrm{e}^2}{4\pi\varepsilon_0\,|\mathbf{r}_i - \mathbf{r}_A|}, \tag{A.3}$$

where n and N are the numbers of electrons and nuclei, respectively. Capital letters $(A, B, ...)$ label the nuclei, whereas small letters $(i, j, ...)$ label the electrons. This general Hamiltonian will now be simplified by a series of approximations.

First, it is assumed that the Born-Oppenheimer approximation is valid, *i.e.* the nuclear and electronic degrees of freedom are separable, such that the eigenstate of the Hamiltonian can be factorized as,

$$|\Phi_\lambda\rangle = \left|\Phi_\lambda^{\mathrm{elec}}\right\rangle \otimes \left|\Phi_\lambda^{\mathrm{nucl}}\right\rangle. \tag{A.4}$$

The nuclei will now be treated classically such that only the electronic wavefunction is considered and to ease notation the superscript will be dropped.

The second approximation made is that the nuclei are stationary, that is, their kinetic energy vanishes. This is easily justified by the relative masses of electrons and nuclei and it will be shown that the approximation is generally valid. Hence the second term in eq. (A.3) vanishes.

As electrons are the particles of interest their fermionic nature needs to be considered. The eigenstate $|\Phi\rangle$ is easily expanded in a molecular spin-orbital basis, $\{|\phi_a\rangle\}$, in a Slater-

Determinant, as,

$$|\Phi\rangle = (n!)^{-\frac{1}{2}} \begin{vmatrix} \phi_a(1) & \phi_b(1) & \cdots & \phi_z(1) \\ \phi_a(2) & \phi_b(2) & \cdots & \phi_z(2) \\ \vdots & \vdots & \ddots & \vdots \\ \phi_a(n) & \phi_b(n) & \cdots & \phi_z(n) \end{vmatrix} = |\phi_a(1)\phi_b(2)\cdots\phi_z(n)\rangle\,. \tag{A.5}$$

$\phi_a(i)$ is the real-space projection of the state $|\phi_a\rangle$,

$$\phi_a = \langle \mathbf{r}|\,\phi_a\rangle\,, \tag{A.6}$$

containing electron i. Atomic units will now be used to ease notation (e.g. $\mathrm{e}^2/4\pi\epsilon_0 = 1$). Without loss of generality it is assumed that the basis $\{|\phi_a\rangle\}$ is orthonormal, i.e. $\langle\phi_a\,|\phi_b\rangle = \delta_{ab}$. Evaluating the energy of Eq. (A.5) with Eq. (A.3) gives,

$$E = \sum_i^n \sum_a^z t_i^{(a)} + \frac{1}{2}\sum_{i\neq j}^n \sum_{ab}^z [\langle ab\,|ab\rangle - \langle ab\,|ba\rangle] - \sum_i^n \sum_A^N \sum_a^z Q_A\,\langle a\,||\,a\rangle + \sum_{A\neq B}^N V_{AB}, \tag{A.7}$$

where,

$$t_i^{(a)} = \left\langle \phi_a(i) \left| \frac{p_i^2}{2m_\mathrm{e}} \right| \phi_a(i) \right\rangle, \tag{A.8}$$

is the transfer integral

$$\langle ab\,|cd\rangle = \iint \phi_a^*(i)\phi_b^*(j) r_{ij}^{-1} \phi_c(i)\phi_d(j)\mathrm{d}\tau_i \mathrm{d}\tau_j, \tag{A.9}$$

with τ_i being all coordinates of electron i (i.e. space and spin coordinates),

$$\langle a\,||\,a\rangle = \int \phi_a^*(i) r_{iA}^{-1} \phi_a(i)\mathrm{d}\tau_i, \tag{A.10}$$

is the electron-nucleus interaction and

$$V_{AB} = \frac{Q_A Q_B}{r_{AB}}, \tag{A.11}$$

is the nucleus-nucleus interaction. $\langle ab\,|ab\rangle \equiv J_{ab}$ is commonly called Coulomb-Integral and $\langle ab\,|ba\rangle \equiv K_{ab}$ Exchange-Integral.

The molecular spin-orbital basis itself can now be expressed in terms of an atomic basis in a familiar Linear-Combination-of-Atomic-Orbitals (LCAO) approach. Let $\left\{ \left|\chi_\mu^{(A)}\right\rangle \right\}$ be a local atomic basis on nucleus A. We can then expand the molecular orbital $|\phi_a\rangle$ as,

$$|\phi_a\rangle = \sum_\mu \sum_A \phi_{a\mu}^{(A)} \left|\chi_\mu^{(A)}\right\rangle, \tag{A.12}$$

then Eq. (A.7) becomes,

$$\begin{aligned} E = & \sum_{i}^{n}\sum_{a}^{z}\sum_{\mu\nu}\sum_{AB}\phi_{a\mu}^{(A)}\phi_{a\nu}^{(B)}t_{\mu\nu}^{(a)} \\ & + \frac{1}{2}\sum_{i\neq j}^{n}\sum_{ab}^{z}\sum_{\mu\nu\rho\kappa}\sum_{ABCD}\left(\phi_{a\mu}^{(A)}\right)^{*}\left(\phi_{b\nu}^{(B)}\right)^{*}\left[\phi_{a\rho}^{(C)}\phi_{b\kappa}^{(D)}\left\langle\mu\nu\,|\rho\kappa\right\rangle - \phi_{b\rho}^{(C)}\phi_{a\kappa}^{(D)}\left\langle\mu\nu\,|\kappa\rho\right\rangle\right] \\ & - \sum_{i}^{n}\sum_{A}^{N}\sum_{a}^{z}\sum_{\mu\nu}\sum_{A'B'}Q_{A}\left(\phi_{a\mu}^{(A')}\right)^{*}\phi_{a\nu}^{(B')}\left\langle\mu\,||\,\nu\right\rangle + \frac{1}{2}\sum_{A\neq B}^{N}V_{AB}, \end{aligned} \tag{A.13}$$

where equivalent definitions hold for the symbols as in Eq. (A.7).

To simplify Eq. (A.13) the Zero-Differential-Overlap (ZDO) approximation is made, i.e.

$$\left(\chi_{\mu}^{(A)}\right)^{*}(i)\chi_{\nu}^{(B)}(i) = 0 \quad \forall \quad A \neq B, \tag{A.14}$$

i.e. the overlap of orbitals on different nuclei vanishes. This reduces the energy expression to,

$$\begin{aligned} E = & \sum_{i}^{n}\sum_{a}^{z}\sum_{\mu\nu}\sum_{A}\phi_{a\mu}^{(A)}\phi_{a\nu}^{(B)}t_{\mu\nu}^{(a)} \\ & + \frac{1}{2}\sum_{i\neq j}^{n}\sum_{ab}^{z}\sum_{\mu\nu\rho\kappa}\sum_{AB}\left(\phi_{a\mu}^{(A)}\right)^{*}\left(\phi_{b\nu}^{(B)}\right)^{*}\phi_{a\rho}^{(A)}\phi_{b\kappa}^{(B)}\left\langle\mu\nu\,|\rho\kappa\right\rangle \\ & - \sum_{i}^{n}\sum_{A}^{N}\sum_{a}^{z}\sum_{\mu\nu}\sum_{A'}Q_{A}\left(\phi_{a\mu}^{(A')}\right)^{*}\phi_{a\nu}^{(A')}\left\langle\mu\,||\,\nu\right\rangle + \frac{1}{2}\sum_{A\neq B}^{N}V_{AB}. \end{aligned} \tag{A.15}$$

Note that the Exchange-Integrals vanish due to this approximation.

So far no assumptions about the system have been made aside from the approximations above (which are general) and that it is a molecule consisting of electrons and nuclei. The model will now be tailored to the systems under consideration. As these are π-conjugated polymers the molecular orbitals of interest can be expanded in a local atomic orbital basis consisting of a single p-orbital. Thus, only one atomic orbital per nucleus is taken into account, making the AO index (μ) redundant. For a similar reason the number of electrons is identical to the number of nuclei, as each carbon atom contributes one electron to the π-electron system, *i.e.* $n = N$ and also $z = n$. Then,

$$\begin{aligned} E = & \sum_{i}^{n}\sum_{a}^{n}\sum_{AB}^{N}\left(\phi_{a}^{(A)}\right)^{*}\phi_{a}^{(B)}t_{a}^{(AB)} \\ & + \frac{1}{2}\sum_{i\neq j}^{n}\sum_{ab}^{n}\sum_{AB}^{N}\left|\phi_{a}^{(A)}\right|^{2}\left|\phi_{b}^{(B)}\right|^{2}\left\langle AB\,|AB\right\rangle \\ & - \sum_{i}^{n}\sum_{A}^{n}\sum_{a}^{n}\sum_{A'}^{N}Q_{A}\left|\phi_{a}^{(A')}\right|^{2}\left\langle A'\,||\,A'\right\rangle + \frac{1}{2}\sum_{A\neq B}^{N}V_{AB}. \end{aligned} \tag{A.16}$$

Introduce,

$$t_{AB} = t_a^{(AB)} \quad \forall a, \tag{A.17}$$

$$V_{AB} \equiv \langle AB\,|AB\rangle\,, \tag{A.18}$$

and

$$V_{AB} \equiv Q_A\,\langle B\,||\,B\rangle\,, \tag{A.19}$$

and

$$\left|\phi_a^{(A)}(i)\right|^2 = n_a^{(A)}(i); \quad \left(\phi_a^{(A)}(i)\right)^* \phi_a^{(B)}(i) = n_a^{(AB)}(i). \tag{A.20}$$

Summing over the molecular orbitals (*i.e.* $\sum_a n_a^{(A)}(i) \equiv n_A(i)$) one obtains,

$$E = \sum_i^n \sum_{AB}^N n_{AB}(i) t_{AB} + \frac{1}{2} \sum_{i\neq j}^n \sum_{AB}^N n_A(i) n_B(j) V_{AB} - \sum_i^n \sum_{AB}^N n_B(i) V_{AB} + \frac{1}{2} \sum_{A\neq B}^N V_{AB}. \tag{A.21}$$

With $\sum_i n_{AB}(i) \equiv n_{AB}$ this reduces to,

$$E = \sum_{AB}^N n_{AB} t_{AB} + \frac{1}{2} \sum_{AB}^N n_A n_B V_{AB} - \sum_{AB}^N n_B V_{AB} + \frac{1}{2} \sum_{A\neq B}^N V_{AB} - \frac{1}{2} \sum_i^n \sum_{AB}^N n_A(i) n_B(i) V_{AB}, \tag{A.22}$$

where the last term is the correction term for the completion of the second summation over i and j. Each of these terms (with exception of the penultimate) can be either on-site ($A = B$) or off-site ($A \neq B$) contributions. Each term will now be investigated separately to ease discussion:

$$\sum_{AB}^N n_{AB} t_{AB} = \sum_A n_A t_{AA} + \sum_{A\neq B} n_{AB} t_{AB}, \tag{A.23}$$

gives the kinetic energy of the electron. This can be split in an on-site momentum, which is simply an off-set of the energy of nt if $t_{AA} \equiv t \quad \forall A$, which is correct within the model here and can thus be set to 0, and the off-site (hopping) term. Assuming only nearest-neighbour hopping, $B = A \pm 1$ and due to the arbitrariness of the indices, this rewrites as,

$$\sum_{AB}^N n_{AB} t_{AB} = \sum_A t_{AA+1} \left(n_{AA+1} + n_{A+1A}\right). \tag{A.24}$$

The second term in Eq. (A.22) gives the electron-electron interaction, which can be rewritten as,

$$\frac{1}{2} \sum_{AB}^N n_A n_B V_{AB} = \frac{U}{2} \sum_A n_A n_A + \frac{1}{2} \sum_{A\neq B} n_A n_B V_{AB}, \tag{A.25}$$

where $U \equiv V_{AA} \quad \forall A$. The second term is the off-site electron-electron correlation and the first term will partially cancel out (see below).

The third term can be rewritten as,

$$-\sum_{AB}^{N} n_B V_{AB} = -U\sum_{A} n_A - \sum_{A\neq B} V_{AB} n_A, \tag{A.26}$$

which quantifies the electron-nucleus attraction.

The fourth term is the nucleus-nucleus interaction and the last term can be rewritten as,

$$-\frac{1}{2}\sum_{i}\sum_{AB} = -\frac{U}{2}\sum_{i}\sum_{A} n_A(i)n_A(i) - \frac{1}{2}\sum_{i}\sum_{A\neq B} n_A(i)n_B(i)V_{AB}, \tag{A.27}$$

where the last term vanishes due to the ZDO approximation and the first term cancels out contributions in the term mentioned above in which the electrons are identical.

This leads to,

$$\begin{aligned} E = &\sum_{A} t_{AA+1}\left(n_{AA+1} + n_{A+1A}\right) + \frac{1}{2}\sum_{A\neq B} n_A n_B V_{AB} + \frac{U}{2}\sum_{i\neq j}\sum_{A} n_A(i)n_A(j) \\ &- U\sum_{A} n_A - \sum_{AB} V_{AB} n_A + \frac{1}{2}\sum_{A\neq B}^{N} V_{AB}. \end{aligned} \tag{A.28}$$

So far electron spin has been ignored. It is easy to introduce the spin-quantum number σ now, as it has only a small effect on the equation, however three aspects have to be discussed. Firstly, in the hopping term the spin has to be conserved, i.e.,

$$\sum_{A} t_{AA+1}\left(n_{AA+1} + n_{A+1A}\right) \rightarrow \sum_{A} t'_A\left(n_{AA+1,\sigma} + n_{A+1A,\sigma}\right) \tag{A.29}$$

where the factor of 2 arising from the new indiex has been incorporated into t'_A. Secondly, the on-site interaction has to be split into interactions arising from electrons with the same and the opposite spin. This is because $i \neq j$ and exchange effects have to be re-introduced. The term thus rewrites as,

$$\frac{U}{2}\sum_{i\neq j}\sum_{A} n_A(i)n_A(j) = 2\sum_{A} n_{A\uparrow}n_{A\downarrow} - \sum_{A}\frac{U}{4}, \tag{A.30}$$

where the first factor of 2 arises from the fact that $i = \uparrow$ or $i = \downarrow$ and j the opposite, respectively, and the second term is the exchange correction for the case that the spins are identical, which is only true for 50% of cases. The last effect is a halving of the contributions to the on-site energy. Hence,

$$\begin{aligned} E = &\sum_{A} t_A\left(n_{AA+1,\sigma} + n_{A+1A,\sigma}\right) + \frac{1}{2}\sum_{A\neq B} n_A n_B V_{AB} + U\sum_{A} n_{A\uparrow}n_{A\downarrow} \\ &- \sum_{A}\frac{U}{4} - \frac{U}{2}\sum_{A} n_A - \sum_{AB} V_{AB} n_A + \frac{1}{2}\sum_{A\neq B}^{N} V_{AB}. \end{aligned} \tag{A.31}$$

With this final energy expression a Hamiltonian in second quantization can be formulated. Let $\hat{c}^{\dagger}_{i\sigma}$ ($\hat{c}_{i\sigma}$) create (destroy) an electron on site i with spin σ. Then,

$$\hat{n}_i = \hat{n}_{i\uparrow} + \hat{n}_{i\downarrow} = \hat{c}^{\dagger}_{i\uparrow}\hat{c}_{i\uparrow} + \hat{c}^{\dagger}_{i\downarrow}\hat{c}_{i\downarrow},$$

and

$$\hat{n}_{ij\sigma} = \hat{c}^{\dagger}_{i\sigma}\hat{c_{j\sigma}},$$

are number operators with the respective densities as matrix elements. This leads to,

$$\begin{aligned}\hat{H} = &\sum_i t_i \left(\hat{c}^{\dagger}_{i\sigma}\hat{c}_{i+1\sigma} + \hat{c}^{\dagger}_{i+1\sigma}\hat{c_{i\sigma}}\right) + \frac{1}{2}\sum_{i\neq j} V_{ij}\hat{n}_i\hat{n}_j + U\sum_i \hat{n}_{i\uparrow}\hat{n}_{i\downarrow} \\ &- \sum_i \frac{U}{4} - \frac{U}{2}\sum_i \hat{n}_i - \sum_{i\neq j} V_{ij}\hat{n}_i + \frac{1}{2}\sum_{i\neq j} V_{ij},\end{aligned} \tag{A.32}$$

which can be rewritten as,

$$\begin{aligned}\hat{H} = &\sum_i t_i \left(\hat{c}^{\dagger}_{i\sigma}\hat{c}_{i+1\sigma} + \hat{c}^{\dagger}_{i+1\sigma}\hat{c_{i\sigma}}\right) + U\sum_i \left(\hat{n}_{i\uparrow} - \frac{1}{2}\right)\left(\hat{n}_{i\downarrow} - \frac{1}{2}\right) \\ &+ \sum_{i\neq j} V_{ij}\left(\hat{n}_i - 1\right)\left(\hat{n}_j - 1\right) + \frac{1}{2}\sum_{i\neq j} V_{ij},\end{aligned} \tag{A.33}$$

which is the Pariser-Parr-Pople Hamiltonian.

B

Intrapolating between Adiabatic and Antiadiabatic Limits

As observed by Spano and co-workers there are strong photophysical similarities between conjugated polymers and molecular J-aggregates[1]. However, J-aggregates lie within the anti-adiabatic regime, $\hbar\omega/|J| \gg 1$, of the Frenkel-Holstein model, while conjugated polymers are within the adiabatic regime, $\hbar\omega/|J| \ll 1$. The two regimes are shown schematically in Fig. B.1 and the purpose of this chapter is to show how that affects the photophysical properties of the two systems and that they are, in fact, behave very differently.

In the anti-adiabatic limit the nuclear energy scale is much larger than the excitonic kinetic energy, *i.e.* the nuclei adapt instantaneous to the presence of the exciton. As shown in Fig. 1.3 the nuclear displacement for a monomer with the exciton present is $\sim \sqrt{2}g_1$. We can define the Lang-Firsov basis in this regime as,

$$|n, \{\upsilon\}\rangle = |n\rangle \, |\upsilon_1, \upsilon_2, \ldots, \tilde{\upsilon}_n, \ldots, \upsilon_{N-1}, \upsilon_N\rangle\rangle \, , \tag{B.1}$$

where the exciton is on monomer n and the corresponding oscillator is displaced ($\tilde{\upsilon}_n$), while the others are not. We can define the corresponding oscillator states as,

$$|\upsilon\rangle\rangle = \frac{\left(b^\dagger\right)^\upsilon}{\sqrt{\upsilon!}} \, |0\rangle\rangle \, , \tag{B.2}$$

and

$$|\tilde{\upsilon}\rangle\rangle = \frac{\left(\tilde{b}^\dagger\right)^\upsilon}{\sqrt{\upsilon!}} \, |0\rangle\rangle \, , \tag{B.3}$$

where $\tilde{b}^\dagger \equiv b^\dagger - g_1$.

Spano used a two-particle basis set, *i.e.* the system contains each one electronic and vibrational excitation[2] In the anti-adiabatic limit they are situated on the same site (as argued above) and the corresponding basis simplifies to,

$$|n, \nu_n\rangle = |n\rangle \, |0_1, 0_2, \ldots, \nu_n, \ldots, 0_{N-1}, 0_N\rangle\rangle \, . \tag{B.4}$$

[1] H. Yamagata, F. C. Spano, Strong Photophysical Similarities between Conjugated Polymers and J-Aggregates., *Phys. Chem. Lett.* **5**, 622 (2014).

[2] F. C. Spano, Modeling Disorder in Polymer Aggregates: The Optical Spectroscopy of Regioregular Poly(3-Hexylthiophene) Thin Films., *J. Chem. Phys.* **122**, 234701 (2005).

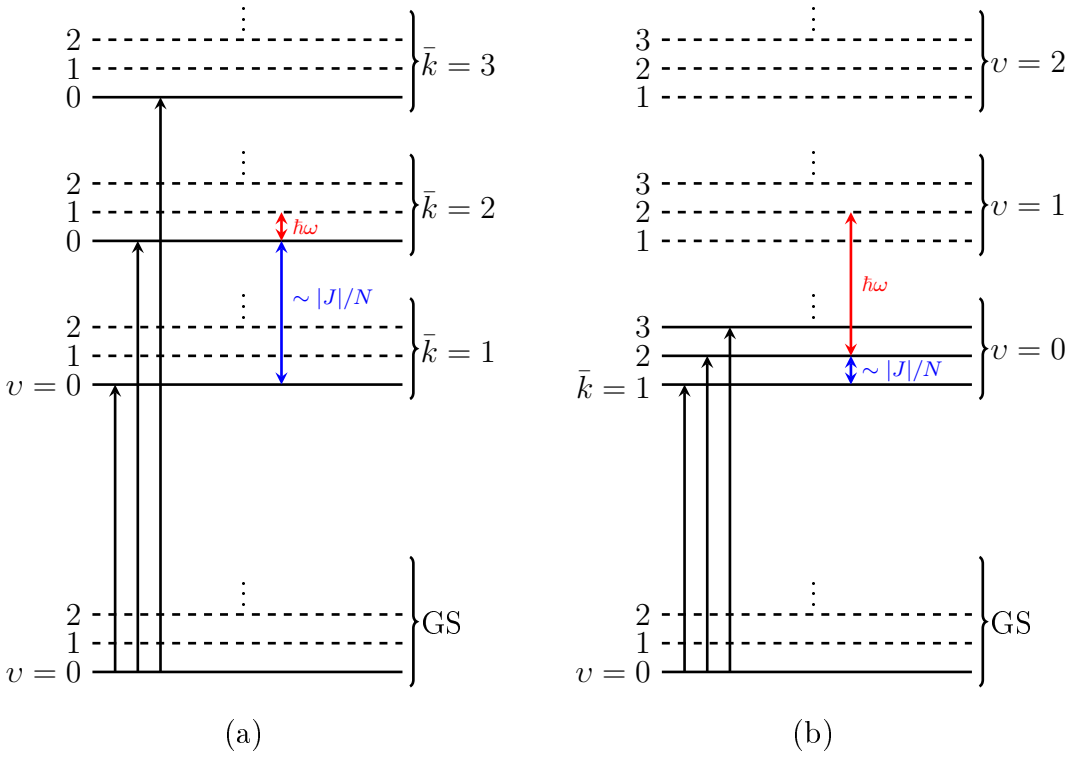


Figure B.1.: Schematic representation of the adiabatic (a) and anti-adiabatic (b) regime of the Frenkel-Holstein model. For $\hbar\omega/|J| \ll 1$ the states are grouped according to the exciton momentum with the vibronic states forming ladders of these. For $\hbar\omega/|J| \gg 1$ the states are grouped according to the number of phonons present with the excitonic states forming ladders of these.

With this basis the absorption intensity ratio can be obtained, namely,

$$\frac{A^{00}}{A^{10}} = \left(\frac{1 + 0.96|J|/\hbar\omega}{1 - 0.29|J|/\hbar\omega}\right)^2 : \quad g_1^2 = 1. \tag{B.5}$$

This result for the anti-adiabatic limit differs significantly from our result for the adiabatic regime for linear polymers (cf. Eq. (4.50)),

$$\frac{A^{00}}{A^{01}} = \mathrm{PN} = \left(\sum_{n=1}^{N} |\Psi_n|^4\right)^{-1} : \quad g_1^2 = 1. \tag{B.6}$$

PN is a proxy for the chromophore length and for ordered, linear chains under PBC PN $\equiv N$ in the adiabatic limit. We thus expect a strong dependency on the chain length within the adiabatic limit, while for the anti-adiabatic limit Eq. (B.5) indicates an independence on the chain length.

We have performed DMRG calculations on the (virtually exact) fully-quantised Frenkel-Holstein model to intrapolate between these two limits. Due to the ordering of the states in the anti-adiabatic limit a large number of system states has to be calculated to cap-

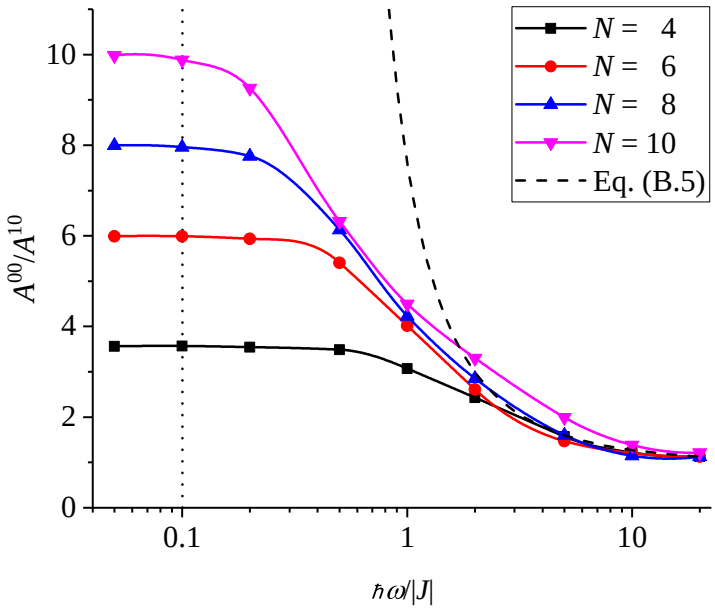


Figure B.2.: Intrapolation of the 0-0/1-0 absorption intensity ratio from the adiabatic regime to the anti-adiabatic regime for $N = 4, 6, 8, 10$ as well as a two data points for $N = 20$ (see text). The dashed line is Eq. (B.5) and the dotted line indicates a parameter value typical for a conjugated polymer ($\hbar\omega/|J| \approx 0.1$).

ture the 1-0 absorption entirely. For a chain of length N about $4N$ states have to be calculated. Due to the set up of the DMRG routine, this requires a large number of augmented block states and phonons in order to achieve reasonable accuracy, even with sweeps. This, unfortunately, means that the system size is strongly restricted in order to make the calculations computationally affordable. Calculations were performed for chains up to a length of $N = 10$ to full accuracy, while for $N = 20$ calculations yielded satisfying results in the adiabatic limit while in the anti-adiabatic limit computational limitations prohibited an accurate calculation. The results are shown in Fig. B.2.

As can be seen the results converge towards the prediction made by Spano (Eq. (B.5)) in the anti-adiabatic regime and do become independent of the length of the chain/chromophore. In the adiabatic regime our prediction is recovered with all results indicating $A^{00}/A^{10} \to N$ as $\hbar\omega/|J| \to 0$. It can also be seen that for a typical value of $\hbar\omega/|J|$ in a conjugated polymer the result obtained in this thesis is a very reasonable approximation as a typical chromophore length within a conjugated polymer is about 13 moieties[3,4].

[3] M. Marcus, O. R. Tozer, W. Barford, Theory of Optical Transitions in Conjugated Polymers. II. Real Systems., *J. Chem. Phys.* **141**, 164102 (2014)

[4] M. Marcus, J. Coonjobeeharry, W. Barford, Theory of Optical Transitions in Conjugated Macrocycles., *J. Chem. Phys.* **144**, 154102 (2016).

C

Parameters for Polymer Modelling

C.1 PPP

Equilibrium Dihedral The dihedral angle was obtained using the Gaussian09 programme package[1] using standard Hartree-Fock Self-Consistent Field (HF-SCF)[2] calculations and the three split-valence basis sets 3-21G, 6-31G, and 6-311G[3]. The number n gives the number of phenylene units in the chain. For $n \geq 3$ the phenylene units can be in different conformations to each other. To account for the resulting (minor) fluctuations in the dihedral the average over the staggered and the alternating conformation was taken.

n \ Basis	3-21G	6-31G	6-311G
2	0.8871	0.7788	0.7933
3	0.8765	0.7677	0.7819
4	0.8727	0.7629	0.7767
5	0.8706	0.7608	0.7739
6	0.8695	0.7592	0.7727
∞	0.8691	0.7585	0.7716

The values for polymer chains were obtained with an asymptotic fit of the values calculated explicitly for each basis set. The values obtained for the larger basis sets (43.5°) are in agreement with experimental gas-phase angles. The values used in this thesis take into account planarisation in solution and the solid, as confirmed by experiment.

Torsional Force Constant The force constant was computed with the same methods as used for the equilibrium angle. For the growing chains the innermost dihedral angle was taken as the angle to be scanned. A relaxed surface scan was performed around the equilibrium angle in steps o.f 0.5° and the resulting surface was fitted to a parabolic surface (harmonic oscillator model) in the vicinity of the equilibrium angle. The force constant is then given as the factor in $V(\phi) = 0.5K\phi^2$. For chains with more than two phenylene units two conformations were calculated, staggered and alternating, and the average was taken.

[1] M. J. Frisch, G. W. Trucks, H. B. Schlegel *et al.*, gaussian 09, Revision D.01, Gaussian Inc., Wallingford, CT, 2009.
[2] C. C. J. Roothaan, *Rev. Mod. Phys.* **23**, 69 (1951).
[3] J. S. Binkley, J. A. Pople, and W. J. Hehre, *J. Am. Chem. Soc.* **102**, 9393 (1980).

n \ Basis	3-21G	6-31G	6-311G
2	0.5192	0.6571	0.5992
3	0.5196	0.6573	0.5990
4	0.5198	0.6574	0.5995
5	0.5199	0.6576	0.5997
6	0.5198	0.6573	0.5993

The results are given in the table above for the various basis sets and chain lengths.

Exciton-Phonon Coupling Constant The method described in Section 2.2.2.1 to calculate the exciton-phonon coupling constant has been applied to find the constant for PPP. This was done using, again, the Gaussian 09 program package, using HF-SCF and DFT[4] methods, using Becke's B3LYP[5] and the Perdew-Burke-Ernzerhof GGA[6] functional. For small oligomers a series of basis sets was used to test for convergence, namely the Pople 3-21G and 6-31G basis sets as well as Dunning's correlation-consistent double-zeta basis sets[7]. Fig. C.2 shows the results for the calculations for different oligomer length.

The value of the exciton-phonon coupling constant, A, can then be calculated as,

$$A = \frac{\beta\Gamma^{(1)}}{\sqrt{\mu\hbar\omega^3}},$$

where μ is the reduced mass and ω the frequency of the normal mode under consideration, here $\mu = 5.5$ u and $\omega = 1730$ cm^{-1}. With $\alpha = 2.9$ eV/Å(see section 2.2.2.1) and $\beta = 2$ then gives $A \simeq 1.36$ or $g_1^2 = 0.933$.

C.2 PPV

Equilibrium Dihedral The same methods were used for the equilibrium dihedral in [n]PPV, where n here is the number of vinylene units. The chains were capped with phenylene units to emulate realistic oligomers. Due to the multitude of possible structures when including *cis-trans* defects and the relatively shallow torsional potential only *all-trans* structures were calculated without alternation in the dihedrals, leading to chains taking the form of a helix.

[4] W. Kohn and L. J. Sham, *Phys. Rev.* **140**, A1133 (1965).
[5] A. D. Becke, *J. Chem. Phys.* **98**, 5648 (1993).
[6] J. P. Perdew, K. Burke, and M. Ernzerhof, *Phys. Rev. Lett.* **77**, 3865 (1996).
[7] T. H. Dunning Jr., *J. Chem. Phys.* **90**, 1007 (1989).

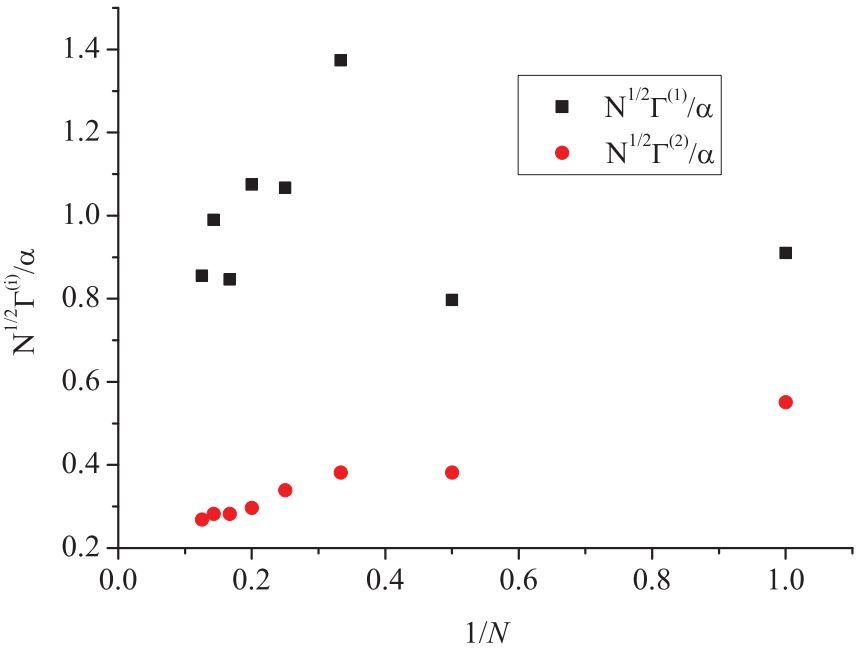


Figure C.1.: $\sqrt{N}\Gamma^{(i)}/\alpha$ against $\sqrt{N}$ as defined in Section 2.2.2.1.. For large N the values converge to 0.85 for $i = 1$ and 0.28 for $i = 2$, despite being subject to some scatter. This is consitent with the ratio of these values for t-polyacteylene, which is $\Gamma^{(1)}/\Gamma^{(2)} = 3$. The scaling of $\sqrt{N}$ is due to the delocalisation of the normal modes along the entire chain. The values shown here are therefore appropriate for a *localised* vibration.

n \ Basis	3-21G	6-31G	6-311G
1	0.4743	0.3769	0.3435
2	0.4570	0.3604	0.3235
3	0.4506	0.3548	0.3160
4	0.4475	0.3518	0.3122
∞	0.4459	0.3506	0.3102

The equilibrium dihedrals are reported in the table above and it can be seen that the range from 25.5° to 17.8° depending on the basis set used. The angle of $\phi_0 = 15°$ was chosen for solid state calculations, while for chains in solution we used an angle of $\phi_0 = 27°$, which is in line with experimental findings and in reasonable agreement with our calculations presented here.

Torsional Force Constant Again, similar procedures were used for the torsional force constants as for PPP. The results are reported below.

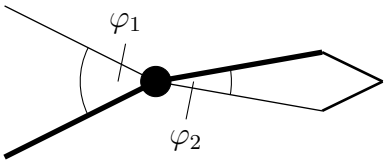


Figure C.2.: MeLPPP unit viewed along the molecular axis indicating the two different dihedral angles between neighbouring phenylene units and showing the bridging =CRR' unit constraining the phenylene rings.

Basis / n	3-21G	6-31G	6-311G
1	0.2532	0.2418	0.2390
2	0.2435	0.2314	0.1837
3	0.2407	0.2298	0.1801
4	0.2402	0.2295	0.1798

For the calculations in this thesis we have chosen a value of 0.46 eV rad^{-2} to account for differences arising from *cis-trans* defects which will have a stiffening effect on the torsional potentials. Moreover, for substituted PPV, like MEH-PPV, to which spectra are often compared, the torsional potential will be stiffer and the dihedral angles will be larger due to extended side chains acting as steric anchors.

C.3 MeLPPP

The ladder-type polymer MeLPPP (Fig. 6.1) is a fairly rigid polymer with respect to the torsional angles due to the bridging =CRR' units between neighbouring phenylene sites. This is expected to increase the force constant significantly. Due to the large side chains in this polymer, the dihedral angles between neighbouring phenylene sites is not expected to be 0. In order to obtain the realistic values for these angles, the die chains have to be considered explicitly which makes a computation of a polymer beyond n=2 computationally inefficient due to the large number of atoms involved (53 carbon and 84 hydrogen atoms for n=2). We have thus calculated the equilibrium angle using an $n = 1$ monomer and modelling the side chains explicitly, while for the force constant the side chains were approximated by a methyl group, significantly lowering the computational effort while retaining a reasonable accuracy.

Equilibrium Dihedral The equilibrium angles were obtained performing geometry optimisation using the gaussian09 programme package. The Hartree-Fock SCF formalism has been used with the basis sets indicated in the table. Due to the linking of neighbouring phenylene units on one side of the molecular axis the phenyl ring is subject to out-of-plane strain causing a de-planarisation of the ring. As a result there are two different dihedral angles for the same phenyl-phenyl pair as depicted in Fig. C.2.

φ_n \ Basis	STO-3G	3-21G	6-31G
$n = 1$	0.5341	0.5407	0.5501
$n = 2$	0.2597	0.2597	0.2691
avg.	0.3969	0.3989	0.4096

Torsional Force constant The constants were calculated by performing a relaxed surface scan of the dihedral angle between two neighbouring sites of the polymer with the same method as for the equilibrium angles. The dihedral closest to the centre of the chain was chosen to reduce surface effects and bulky side chains were approximated by methyl groups to speed up calculations. The table lists the obtained values (in eV rad^{-2}) using the harmonic approximation.

n \ Basis	3-21G	6-31G	6-311G
3	2.0412	2.1568	2.1398
4	2.0601	2.1845	2.1418
5	2.0751	2.1941	2.1458

D

DMRG Convergence Tables

The following are convergence tables for the fully-quantised Frenkel-Holstein Hamiltonian using the DMRG routine to solve the model. The convergence parameters are the number of states per augmented block, M, the number of sweeps performed at the target chain length, N_{sweep}, and the number of phonons per site, N_{phon}. The tables show the 0-0 absorption/emission, 1-0 absorption, and 0-1 emission intensity as well as the 0-0/1-0 absorption and 0-0/0-1 emission intensity ratios. The tables are for fixed parameters $(\hbar\omega/|J|, g_1^2)$ and fixed N_{phon} with M and N_{sweep} being varied within the table.

Table D.1.: 1 phonon, PBC, linear: $\hbar\omega/J = 1, g_1^2 = 1$

		$N = 10$			$N = 20$		
M	N_{sweep}	A^{00}	A^{10}	I^{01}	A^{00}	A^{10}	I^{01}
10	0	8.376257	0.261050	0.566679	16.158147	0.253954	0.552579
20	0	8.371407	0.262510	0.566190	16.765222	0.118169	0.565223
40	0	8.371073	0.263609	0.565773	16.743702	0.139862	0.565874
80	0	8.371086	0.263675	0.565690	16.744009	0.138811	0.565727
10	1	8.389878	0.257894	0.564585	16.520323	0.188260	0.543862
20	1	8.370924	0.263622	0.565857	16.781309	0.112441	0.563407
40	1	8.371086	0.267387	0.565689	16.745014	0.134916	0.565816
80	1	8.371086	0.264009	0.565690	16.743944	0.138223	0.565793
10	2	8.389479	0.257932	0.564619	16.532531	0.183192	0.535927
20	2	8.370927	0.264756	0.565853	16.781562	0.112617	0.563394
40	2	8.371086	0.266413	0.565689	16.744060	0.138535	0.565821
80	2	8.371086	0.263620	0.565690	16.744127	0.138719	0.565768
10	3	8.391141	0.258082	0.564421	16.526095	0.181175	0.538168
20	3	8.370921	0.263622	0.565856	16.781531	0.112519	0.563390
40	3	8.371086	0.264558	0.565690	16.744060	0.138535	0.565821
80	3	8.371086	0.262878	0.565690	16.744111	0.138630	0.565772

Table D.2.: 2 phonons, PBC, linear: $\hbar\omega/J = 1, N = 10, g_1^2 = 1$

		$N = 10$			$N = 20$		
M	N_{sweep}	A^{00}	A^{10}	I^{01}	A^{00}	A^{10}	I^{01}
10	0	7.678534	0.503893	0.720468	14.536685	0.467893	0.698565
20	0	7.650904	0.510173	0.715237	15.315925	0.338009	0.718666
40	0	7.650551	0.510508	0.715515	15.303915	0.387947	0.715301
80	0	7.650928	0.509683	0.715262	15.304497	0.386575	0.715174
10	1	7.672623	0.503172	0.719287	14.872921	0.251914	0.685991
20	1	7.650944	0.509642	0.715454	15.313854	0.350674	0.719248
40	1	7.651270	0.509626	0.715064	15.304006	0.419389	0.715323
80	1	7.651270	0.509627	0.715062	15.304565	0.367008	0.715166
10	2	7.670482	0.502333	0.719502	14.911180	0.220098	0.661603
20	2	7.650984	0.509542	0.715349	15.312370	0.350976	0.719206
40	2	7.651270	0.509616	0.715063	15.304645	0.386105	0.715248
80	2	7.651257	0.509818	0.715077	15.304451	0.386796	0.715204
10	3	7.670482	0.502336	0.719503	14.885289	0.238356	0.656122
20	3	7.650944	0.509642	0.715454	15.312760	0.352178	0.719171
40	3	7.651270	0.509626	0.715063	15.304577	0.386676	0.715248
80	3	7.651270	0.509626	0.715064	15.304518	0.387008	0.715184

Table D.3.: 4 phonons, PBC, linear: $\hbar\omega/J = 1, N = 10, g_1^2 = 1$

		$N = 10$			$N = 20$		
M	N_{sweep}	A^{00}	A^{10}	I^{01}	A^{00}	A^{10}	I^{01}
10	0	7.412548	0.643734	0.751002	13.887194	0.561768	0.693369
20	0	7.392645	0.716984	0.738740	14.784684	0.571775	0.743456
40	0	7.393276	0.715977	0.738299	14.789949	0.688359	0.738344
80	0	7.393098	0.715391	0.739377			
10	1	7.405254	0.711390	0.744178	14.090705	0.343986	0.685612
20	1	7.392818	0.715662	0.738785	14.785870	0.658925	0.741252
40	1	7.393520	0.715819	0.738090	14.788456	0.696499	0.738463
80	1	7.393099	0.714439	0.737859			
10	2	7.404795	0.714138	0.744196	14.276259	0.395725	0.678066
20	2	7.392773	0.712257	0.738813	14.785906	0.664688	0.741785
40	2	7.393511	0.715628	0.738112	14.788451	0.696500	0.738461
80	2	7.393360	0.717888	0.738173			
10	3	7.404788	0.714199	0.744198	14.239348	0.355440	0.677689
20	3	7.392773	0.715382	0.738804	14.786570	0.664457	0.741799
40	3	7.391709	0.717355	0.738374	14.788451	0.696500	0.738461
80	3	7.393317	0.715048	0.738200			

Table D.4.: 8 phonons, PBC, linear: $\hbar\omega/J = 1, N = 10, g_1^2 = 1$

		$N = 10$			$N = 20$		
M	N_{sweep}	A^{00}	A^{10}	I^{01}	A^{00}	A^{10}	I^{01}
10	0	7.404675	0.718547	0.747155	13.556362	0.511520	0.687619
20	0	7.382268	0.740078	0.739188	14.760124	0.569804	0.743468
40	0	7.383385	0.738366	0.738325	14.769565	0.727742	0.738749
80	0	7.383068	0.743598	0.738616			
10	1	7.383656	0.700082	0.742691	12.841375	0.688882	0.777094
20	1	7.382609	0.738363	0.739048	14.767308	0.695769	0.741568
40	1	7.383069	0.738857	0.738462	14.768610	0.736480	0.738695
80	1	7.383080	0.743710	0.738571			
10	2	7.383849	0.699915	0.742728	11.871522	0.584538	0.770250
20	2	7.382610	0.738370	0.739047	14.766332	0.703519	0.741872
40	2	7.383084	0.748059	0.738271	14.768610	0.737667	0.735545
80	2	7.383282	0.740458	0.738396			
10	3	7.383849	0.699916	0.742728	11.718290	0.703854	0.780050
20	3	7.382610	0.738370	0.739047	14.766816	0.703453	0.741847
40	3	7.383349	0.738342	0.738429	14.768456	0.738116	0.738624
80	3	7.383321	0.740032	0.738354			